

1 **The Sensitivity to Oscillation Parameters**
2 **from a Simultaneous Beam and**
3 **Atmospheric Neutrino Analysis that**
4 **combines the T2K and SK Experiments**



6 Daniel Robert Clement Barrow
7 Magdalen College
8 University of Oxford

9 A thesis submitted for the degree of
10 *Doctor of Philosophy*
11 Trinity 2022

Abstract

12

13 A simultaneous beam and atmospheric oscillation analysis that combines the
14 T2K and SK experiments has been presented. The first sensitivities of the joint
15 analysis are reported, with the intention for the two collaborations to publish a
16 data analysis in the near-future. This analysis leverages the different energies
17 and baselines of the two experiments and provides strong sensitivities on δ_{CP} ,
18 $\sin^2(\theta_{23})$ and Δm_{32}^2 . To do this, a Bayesian Markov Chain Monte Carlo technique
19 is utilised to generate parameter estimates and credible intervals. Constraints
20 from the T2K near detector are also used to constrain the uncertainties of both
21 beam and atmospheric predictions.

22 For a known set of oscillation parameters close to the preferred values from
23 a T2K-only data fit, the sensitivity of the joint analysis to $\sin^2(\theta_{23})$ is increased
24 compared to the beam-only analysis. Furthermore, the sensitivity of the joint
25 analysis to select the correct mass hierarchy hypothesis is drastically improved
26 compared to the beam-only analysis, culminating in a substantial preference as
27 classified by Jeffrey's scale. This statement is stronger than the sensitivity of the
28 beam-only analysis, either with or without external constraints on $\sin^2(\theta_{13})$. The
29 sensitivities of the beam-only and joint beam-atmospheric analyses have also been
30 compared for a known set of oscillation parameters which are CP-conserving.
31 The joint analysis displays an improved ability to select the correct phase of δ_{CP}
32 and octant of $\sin^2(\theta_{23})$ compared to the beam-only analysis. This thesis illustrates
33 the benefit of the combined beam and atmospheric analysis, which could also be
34 extended for use in the next-generation Hyper-Kamiokande experiment.

Acknowledgements

³⁶ Personal

³⁷ This is where you thank your advisor, colleagues, and family and friends.

³⁸ Lorem ipsum dolor sit amet, consectetur adipiscing elit. Vestibulum feugiat
³⁹ et est at accumsan. Praesent sed elit mattis, congue mi sed, porta ipsum. In
⁴⁰ non ullamcorper lacus. Quisque volutpat tempus ligula ac ultricies. Nam sed
⁴¹ erat feugiat, elementum dolor sed, elementum neque. Aliquam eu iaculis est,
⁴² a sollicitudin augue. Cras id lorem vel purus posuere tempor. Proin tincidunt,
⁴³ sapien non dictum aliquam, ex odio ornare mauris, ultrices viverra nisi magna
⁴⁴ in lacus. Fusce aliquet molestie massa, ut fringilla purus rutrum consectetur.
⁴⁵ Nam non nunc tincidunt, rutrum dui sit amet, ornare nunc. Donec cursus
⁴⁶ tortor vel odio molestie dignissim. Vivamus id mi erat. Duis porttitor diam
⁴⁷ tempor rutrum porttitor. Lorem ipsum dolor sit amet, consectetur adipiscing
⁴⁸ elit. Sed condimentum venenatis consectetur. Lorem ipsum dolor sit amet,
⁴⁹ consectetur adipiscing elit.

⁵⁰ Aenean sit amet lectus nec tellus viverra ultrices vitae commodo nunc. Mauris
⁵¹ at maximus arcu. Aliquam varius congue orci et ultrices. In non ipsum vel
⁵² est scelerisque efficitur in at augue. Nullam rhoncus orci velit. Duis ultricies
⁵³ accumsan feugiat. Etiam consectetur ornare velit et eleifend.

⁵⁴ Suspendisse sed enim lacinia, pharetra neque ac, ultricies urna. Phasellus sit
⁵⁵ amet cursus purus. Quisque non odio libero. Etiam iaculis odio a ex volutpat, eget
⁵⁶ pulvinar augue mollis. Mauris nibh lorem, mollis quis semper quis, consequat
⁵⁷ nec metus. Etiam dolor mi, cursus a ipsum aliquam, eleifend venenatis ipsum.
⁵⁸ Maecenas tempus, nibh eget scelerisque feugiat, leo nibh lobortis diam, id laoreet
⁵⁹ purus dolor eu mauris. Pellentesque habitant morbi tristique senectus et netus
⁶⁰ et malesuada fames ac turpis egestas. Nulla eget tortor eu arcu sagittis euismod
⁶¹ fermentum id neque. In sit amet justo ligula. Donec rutrum ex a aliquet egestas.

⁶² Institutional

⁶³ If you want to separate out your thanks for funding and institutional support,
⁶⁴ I don't think there's any rule against it. Of course, you could also just remove
⁶⁵ the subsections and do one big traditional acknowledgement section.

⁶⁶ Lorem ipsum dolor sit amet, consectetur adipiscing elit. Ut luctus tempor ex at
⁶⁷ pretium. Sed varius, mauris at dapibus lobortis, elit purus tempor neque, facilisis
⁶⁸ sollicitudin felis nunc a urna. Morbi mattis ante non augue blandit pulvinar.
⁶⁹ Quisque nec euismod mauris. Nulla et tellus eu nibh auctor malesuada quis
⁷⁰ imperdiet quam. Sed eget tincidunt velit. Cras molestie sem ipsum, at faucibus
⁷¹ quam mattis vel. Quisque vel placerat orci, id tempor urna. Vivamus mollis,
⁷² neque in aliquam consequat, dui sem volutpat lorem, sit amet tempor ipsum felis
⁷³ eget ante. Integer lacinia nulla vitae felis vulputate, at tincidunt ligula maximus.
⁷⁴ Aenean venenatis dolor ante, euismod ultrices nibh mollis ac. Ut malesuada
⁷⁵ aliquam urna, ac interdum magna malesuada posuere.

Statement of Originality

77 The work, and associated interpretation, presented within this thesis are
78 my own and were produced by myself. Where applicable, results and figures
79 taken from others have been attributed and referenced. This work has not been
80 submitted for any other qualification, at this university or any other.

81 The background of neutrino physics history and a description of the T2K and
82 SK experiments are provided in Chapters 2 and 3, respectively. The Bayesian
83 fitting techniques and MaCh3 framework used throughout this analysis are de-
84 tailed in Chapter 4. These chapters present entirely background knowledge
85 relevant for understanding the work presented within this thesis. Chapter 5
86 documents the simulation and reconstruction of neutrino events. This includes a
87 section of work done by myself to validate the `fiTQun` reconstruction software
88 for use on SK-V data.

89 Chapter 6 details the event selections and systematics used within this oscilla-
90 tion analysis. The selections were developed by others within the T2K and SK
91 collaborations and have been appropriately referenced. The implementation and
92 validation of the simultaneous support for the beam and atmospheric samples,
93 selected by the SK detector, in the MaCh3 fitting framework has been entirely my
94 own work. The systematic models invoked within this analysis were developed
95 by others, and relevant references have been included. The implementation
96 of these systematics within the MaCh3 fitting framework has been entirely my
97 own work and includes generating the systematic response functions for each
98 systematic from the Super-Kamiokande Monte Carlo. The implementation and
99 validation of the near detector samples and systematics were performed by
100 Clarence Wret on behalf of the MaCh3 working group.

101 Chapter 7 documents a new method of calculating the oscillation probabilities
102 for atmospheric neutrinos at SK. The method and validation of the ‘smearing’
103 technique were entirely my own. The methodology for including effects from
104 production height systematics was developed by others but the implementation
105 and validation were my own. Several performance increases, including the
106 interfacing of an alternative oscillation calculation engine, were my own work.
107 The sensitivities, and interpretation, provided within Chapter 8 are produced
108 entirely by myself.

Contents

109

110	1 Introduction	1
111	2 Neutrino Oscillation Physics	4
112	2.1 Discovery of Neutrinos	5
113	2.2 Theory of Neutrino Oscillation	6
114	2.3 Neutrino Oscillation Measurements	10
115	2.4 Summary Of Oscillation Parameter Measurements	19
116	2.5 Overview of Oscillation Effects	21
117	3 T2K and SK Experiment Overview	29
118	3.1 The Super-Kamiokande Experiment	29
119	3.2 The Tokai to Kamioka Experiment	39
120	4 Bayesian Statistics and Markov Chain Monte Carlo Techniques	54
121	4.1 Bayesian Statistics	55
122	4.2 Monte Carlo Simulation	57
123	4.3 Understanding the MCMC Results	65
124	5 Simulation, Reconstruction, and Event Reduction	70
125	5.1 Simulation	70
126	5.2 Event Reconstruction at SK	76
127	5.3 Event Reduction at SK	87
128	6 Sample Selections and Systematics	92
129	6.1 Atmospheric Samples	94
130	6.2 Near Detector Beam Samples	102
131	6.3 Far Detector Beam Samples	104
132	6.4 Systematic Uncertainties	109
133	6.5 Likelihood Calculation	130
134	7 Oscillation Probability Calculation	133
135	7.1 Treatment of Fast Oscillations	134
136	7.2 Calculation Engine	141
137	7.3 Matter Density Profile	145
138	7.4 Production Height Averaging	150

¹³⁹	8 Oscillation Analysis	153
¹⁴⁰	8.1 Monte Carlo Prediction	154
¹⁴¹	8.2 Likelihood Scans	155
¹⁴²	8.3 Sensitivity Studies	167
¹⁴³	8.4 Summary of Sensitivity Studies	219
¹⁴⁴	9 Conclusions and Outlook	221

1

145

146

Introduction

147 Current astrophysical measurements show that the universe is matter-dominated,
148 despite current theoretical models suggesting that an equal amount of matter
149 and antimatter were created in the Big Bang. For an imbalance to occur, the
150 Sakharov conditions [1] require the violation of charge parity (CP) symmetries.
151 CP violation has been observed in quark mixing but is insufficient to explain
152 the observed asymmetry. As the Standard Model relates the neutrino and the
153 antineutrino through these symmetries, CP violation could be found in the
154 neutrino sector. This would be observed as a difference between neutrino and
155 antineutrino oscillation. Current neutrino oscillation measurements contain hints
156 of CP violation [2] but no conclusive measurement has been achieved. One of the
157 main goals of neutrino oscillation experiments is to continue the search for CP
158 violation, requiring a precise measurement of all oscillation parameters.

159 The Super-Kamiokande (SK) detector observes atmospheric neutrinos emitted
160 from the subsequent decays of cosmic rays. It is also situated as the far detector
161 of the Tokai-to-Kamioka (T2K) experiment and measures the interactions of
162 neutrinos produced from the J-PARC (anti-)neutrino beam facility. Previous
163 oscillation analyses published by these two experiments have treated the datasets
164 independently. However, due to the different energies, path lengths, and density
165 of matter in which the neutrinos pass through, a combined analysis can leverage

166 the constraints from both datasets and may be able to improve measurements
167 of neutrino oscillation parameters.

168 This thesis introduces a joint beam and atmospheric neutrino analysis using
169 beam samples observed at the near and far detectors of the T2K experiment and
170 atmospheric samples present in SK. It combines the beam analysis presented in
171 [2] and the atmospheric analysis documented in [3]. This corresponds to run1-10
172 of the T2K experiment with approximately equal exposure taken in neutrino
173 and antineutrino beam modes, alongside more than 3000 days of atmospheric
174 events. The results in this thesis are presented as sensitivities to the δ_{CP} , $\sin^2(\theta_{13})$,
175 $\sin^2(\theta_{23})$, and Δm_{32}^2 oscillation parameters. Crucially, the combination of beam
176 and atmospheric neutrinos gives strong sensitivity to the mass hierarchy due to
177 the correlation between the matter resonance and $\sin^2(\theta_{23})$. The sensitivities are
178 generated by the MaCh3 Bayesian Markov Chain Monte Carlo fitting framework.

179 Chapter 2 provides a concise overview of neutrino physics history including
180 the discovery of the neutrino along with the first evidence for neutrino oscillation.
181 It also includes a brief discussion of the theory underpinning the PMNS formal-
182 ism of neutrino oscillation alongside a summary of the current measurements
183 of each oscillation parameter.

184 The T2K and SK experiments are detailed in Chapter 3. This includes the
185 design and calibration of the SK detector along with a brief description of the
186 composition and detection techniques of T2K's two near detectors. The neutrino
187 beamline, and the 'off-axis' technique, are also briefly summarised.

188 This thesis presents a Bayesian neutrino oscillation analysis that uses Markov
189 Chain Monte Carlo techniques. This analysis strategy, along with a summary
190 of the fundamental concepts of Bayesian inference, is described in Chapter 4.
191 This includes a discussion about the conditions that are required to correctly
192 sample the parameter space along with the methods used to calculate parameter
193 estimations and build credible intervals.

194 Chapter 5 details the simulations and reconstruction tools used to build Monte
195 Carlo predictions of each sample used within this analysis. This includes the

196 models used to provide flux predictions of the beam and atmospheric neutrinos
197 as well as the models invoked with this analysis to simulate neutrino interactions.

198 A description of the beam samples used at the near and far detector and the
199 atmospheric samples used at the SK detector is presented in Chapter 6. These
200 include energy and interaction mode comparisons along with documenting the
201 event selection cuts. This chapter also describes the systematic models used
202 to quantify the uncertainty in the flux predictions of both beam and atmo-
203 spheric neutrinos, the interaction models, and the response of the detectors
204 used within this analysis.

205 A novel atmospheric neutrino oscillation probability calculation method
206 is documented in Chapter 7. This is required to ensure reliable Monte Carlo
207 sampling of a rapidly varying region of oscillation parameter space. This chapter
208 also documents the uncertainties related to the Earth’s density as well as the
209 production height of neutrinos in the upper atmosphere.

210 Chapter 8 presents the sensitivities of this joint beam and atmospheric neu-
211 trino oscillation analysis. The results are provided for two different sets of known
212 values. The application of the external constraints on $\sin^2(\theta_{13})$ has also been
213 considered. The sensitivities of the joint analysis are compared to the beam-only
214 analysis and show the benefits of the combined analysis. These results have been
215 presented by the T2K and SK collaborations at the Neutrino 2022 conference [4].

216 A summarised discussion of the sensitivity results and the outlook for the
217 analysis, including the implications of this analysis on the next generation of
218 neutrino experiments, is provided in Chapter 9.

2

219

220

Neutrino Oscillation Physics

221 When first proposed, neutrinos were expected to be approximately massless
222 fermions that only interact through weak and gravitational forces. This meant
223 they were very difficult to detect as they can pass through significant amounts
224 of matter without interacting. Despite this, experimental neutrino physics has
225 developed many different detection techniques and observed neutrinos from
226 both natural and artificial sources. In direct tension with Standard Model physics,
227 neutrinos have been determined to oscillate between different lepton flavours,
228 requiring them to have mass.

229 The observation techniques which led to the discovery of the neutrino are doc-
230 umented in section 2.1. The theory underpinning neutrino oscillation is described
231 in section 2.2 and includes the approximations which can be made to simplify
232 the understanding of neutrino oscillation in the two-flavour approximation. Past,
233 current, and future neutrino experiments are detailed in section 2.3, including the
234 reactor, atmospheric, and long-baseline accelerator neutrino sources that have
235 been used to successfully constrain oscillation parameters. Finally, the current
236 state of oscillation parameter measurements are summarised in section 2.4.

2.1 Discovery of Neutrinos

At the start of the 20th century, the electrons emitted from the β -decay of the nucleus were found to have a continuous energy spectrum [5, 6]. This observation seemingly broke the energy conservation invoked within that period's nuclear models. In 1930, Pauli provided a solution to this problem in the form of a new particle, the neutrino (originally termed "neutron"). It was theorized to be an electrically neutral spin-1/2 fermion with a mass smaller than that of the electron [7]. This neutrino was emitted with the electron in β -decay to alleviate the apparent breaking of energy conservation. As a predecessor of today's weak interaction model, Fermi's theory of β -decay developed the understanding by coupling the four constituent particles: electron, proton, neutron, and neutrino, into a quantitative model [8].

Whilst Pauli was not convinced of the ability to detect neutrinos, the first observations of the particle were made in the mid-1950s when neutrinos from a reactor were observed via the inverse β -decay (IBD) process, $\bar{\nu}_e + p \rightarrow n + e^+$ [9, 10]. The detector consisted of two parts: a neutrino interaction medium and a liquid scintillator. The interaction medium was built from two water tanks, loaded with cadmium chloride to allow for increased efficiency in the detection of neutron capture. The positron emitted from IBD annihilates, $e^+ + e^- \rightarrow 2\gamma$, generating a prompt signal and the neutron is captured on the cadmium via $n + ^{108}Cd \rightarrow ^{109*}Cd \rightarrow ^{109}Cd + \gamma$, producing a delayed signal. An increase in the coincidence rate was observed when the reactor was operating which was interpreted as interactions from neutrinos generated in the reactor.

After the discovery of the ν_e , the question of how many flavours of neutrino exist was asked. In 1962, a measurement of the ν_μ was conducted at the Brookhaven National Laboratory [11]. A proton beam was directed at a beryllium target, generating pions which then decayed via $\pi^\pm \rightarrow \mu^\pm + (\nu_\mu, \bar{\nu}_\mu)$, and the subsequent interactions of the ν_μ were observed. As the interaction of the neutrino generated muons rather than electrons, it was determined that

the ν_μ was fundamentally different from ν_e . The final observation to be made was that of the ν_τ from the DONUT experiment [12]. Three neutrinos seem the obvious solution as it mirrors the known number of charged leptons (as they form weak isospin doublets) but there could be evidence of more. Several neutrino experiments have found anomalous results [13, 14] which could be attributed to “sterile” neutrinos. These hypothesised particles are not affected by gauge interactions in the Standard Model so their presence can only be inferred through the observation of non-standard oscillation modes. However, cosmological observations indicate the number of neutrino species $N_{eff} = 2.99 \pm 0.17$ [15], as measured from the cosmic microwave background power spectrum. LEP also measured the number of active neutrino flavours to be $N_\nu = 2.9840 \pm 0.0082$ [16] from measurements of the Z-decay width, but this does not strongly constrain the number of sterile neutrinos.

2.2 Theory of Neutrino Oscillation

A neutrino generated with lepton flavour α can change into a different lepton flavour β after propagating some distance. This phenomenon is called neutrino oscillation and requires that neutrinos must have a non-zero mass. This behaviour has been characterised by the Pontecorvo-Maki-Nakagawa-Sakata (PMNS) [17–19] mixing matrix which describes how the flavour and mass of neutrinos are associated. This is analogous to the Cabibbo-Kobayashi-Maskawa (CKM) [20] matrix measured in quark physics.

2.2.1 Three Flavour Oscillations

The PMNS parameterisation defines three flavour eigenstates, ν_e , ν_μ and ν_τ (indexed ν_α), which are eigenstates of the weak interaction and three mass eigenstates, ν_1 , ν_2 and ν_3 (indexed ν_i). Each mass eigenstate is the superposition

²⁹¹ of all three flavour states,

$$|\nu_i\rangle = \sum_{\alpha} U_{\alpha i} |\nu_{\alpha}\rangle. \quad (2.1)$$

²⁹² Where U is the 3×3 unitary PMNS matrix and connects the mass and
²⁹³ flavour eigenstates.

²⁹⁴ The weak interaction, when interacting via a W^{\pm} boson, couples to flavour
²⁹⁵ eigenstates so neutrinos interact with leptons of the same flavour. The prop-
²⁹⁶ agation of a neutrino flavour eigenstate, in a vacuum, can be re-written as a
²⁹⁷ plane-wave solution to the time-dependent Schrödinger equation,

$$|\nu_{\alpha}(t)\rangle = \sum_i U_{\alpha i}^{*} |\nu_i\rangle e^{-i\phi_i}. \quad (2.2)$$

²⁹⁸ The ϕ_i term can be expressed in terms of the energy, E_i , and magnitude of the
²⁹⁹ three momenta, p_i , of the neutrino, $\phi_i = E_i t - p_i x$ (t and x being time and position
³⁰⁰ coordinates). The probability of observing a neutrino of flavour eigenstate β from
³⁰¹ one which originated as flavour α can be calculated as,

$$P(\nu_{\alpha} \rightarrow \nu_{\beta}) = |\langle \nu_{\beta} | \nu_{\alpha}(t) \rangle|^2 = \sum_{i,j} U_{\alpha i}^{*} U_{\beta i} U_{\alpha j} U_{\beta j}^{*} e^{-i(\phi_j - \phi_i)}. \quad (2.3)$$

³⁰² The term within the exponential can be represented as,

$$\phi_j - \phi_i = E_j t - E_i t - p_j x + p_i x. \quad (2.4)$$

³⁰³ For a relativistic particle, $E_i \gg m_i$, a Taylor series expansion means,

$$p_i = \sqrt{E_i^2 - m_i^2} \approx E_i - \frac{m_i^2}{2E_i}. \quad (2.5)$$

³⁰⁴ Making the approximations that neutrinos are relativistic, the mass eigenstates
³⁰⁵ were created with the same energy, and that $x = L$, where L is the distance
³⁰⁶ travelled by the neutrino, Equation 2.4 then becomes

$$\phi_j - \phi_i = \frac{\Delta m_{ij}^2 L}{2E}, \quad (2.6)$$

307 where $\Delta m_{ij}^2 = m_i^2 - m_j^2$. This, combined with further use of unitarity relations
 308 results in Equation 2.3 becoming

$$\begin{aligned} P(\nu_\alpha \rightarrow \nu_\beta) &= \delta_{\alpha\beta} - 4 \sum_{i>j} \Re \left(U_{\alpha i}^* U_{\beta i} U_{\alpha j} U_{\beta j}^* \right) \sin^2 \left(\frac{\Delta m_{ij}^2 L}{4E} \right) \\ &\quad + (-) 2 \sum_{i>j} \Im \left(U_{\alpha i}^* U_{\beta i} U_{\alpha j} U_{\beta j}^* \right) \sin \left(\frac{\Delta m_{ij}^2 L}{2E} \right). \end{aligned} \quad (2.7)$$

309 Where $\delta_{\alpha\beta}$ is the Kronecker delta function and the negative sign on the last
 310 term is included for the oscillation probability of antineutrinos. As an important
 311 point to note, the observation of oscillation probability requires a non-zero value
 312 of Δm_{ij}^2 , which in turn requires that neutrinos have differing masses.

313 Typically, the PMNS matrix is parameterised into three mixing angles, a
 314 charge parity (CP) violating phase δ_{CP} , and two Majorana phases $\alpha_{1,2}$,

$$U = \underbrace{\begin{pmatrix} 1 & 0 & 0 \\ 0 & c_{23} & s_{23} \\ 0 & -s_{23} & c_{23} \end{pmatrix}}_{\text{Atmospheric, Accelerator}} \underbrace{\begin{pmatrix} c_{13} & 0 & s_{13}e^{-i\delta_{CP}} \\ 0 & 1 & 0 \\ -s_{13}e^{-i\delta_{CP}} & 0 & c_{13} \end{pmatrix}}_{\text{Reactor, Accelerator}} \times \underbrace{\begin{pmatrix} c_{12} & s_{12} & 0 \\ -s_{12} & c_{12} & 0 \\ 0 & 0 & 1 \end{pmatrix}}_{\text{Reactor, Solar}} \underbrace{\begin{pmatrix} e^{i\alpha_1/2} & 0 & 0 \\ 0 & e^{i\alpha_2/2} & 0 \\ 0 & 0 & 1 \end{pmatrix}}_{\text{Majorana}}. \quad (2.8)$$

315 Where $s_{ij} = \sin(\theta_{ij})$ and $c_{ij} = \cos(\theta_{ij})$. The oscillation parameters are often
 316 grouped: (1,2) as “solar”, (2,3) as “atmospheric” and (1,3) as “reactor”. Many
 317 neutrino experiments aim to measure the PMNS parameters from a wide array
 318 of origins, as is the purpose of this thesis.

319 The Majorana phase, $\alpha_{1,2}$, included within the fourth matrix in Equation 2.8
 320 is only included for completeness. For an oscillation analysis experiment, any
 321 terms containing this phase disappear due to taking the expectation value of the
 322 PMNS matrix. Measurements of these phases can be performed by experiments
 323 searching for neutrino-less double β -decay [21].

324 A two-flavour approximation can be obtained when one assumes the third
325 mass eigenstate is degenerate with another. This results in the two-flavour
326 approximation being reasonable for understanding the features of the oscillation.
327 In this two-flavour case, the mixing matrix becomes,

$$U_{\text{2 Flav.}} = \begin{pmatrix} \cos(\theta) & \sin(\theta) \\ -\sin(\theta) & \cos(\theta) \end{pmatrix}. \quad (2.9)$$

328 This culminates in the oscillation probability,

$$\begin{aligned} P(\nu_\alpha \rightarrow \nu_\alpha) &= 1 - \sin^2(2\theta) \sin^2\left(\frac{\Delta m^2 L}{4E}\right), \\ P(\nu_\alpha \rightarrow \nu_\beta) &= \sin^2(2\theta) \sin^2\left(\frac{\Delta m^2 L}{4E}\right). \end{aligned} \quad (2.10)$$

329 Where $\alpha \neq \beta$. For a fixed neutrino energy, the oscillation probability is
330 a sinusoidal function depending upon the distance over which the neutrino
331 propagates. The frequency and amplitude of oscillation are dependent upon
332 $\Delta m^2 / 4E$ and $\sin^2 2\theta$, respectively. The oscillation probabilities presented thus far
333 assume $c = 1$, where c is the speed of light in a vacuum. In more familiar units, the
334 maximum oscillation probability for a fixed value of θ is given at $L[\text{km}] / E[\text{GeV}] \sim$
335 $1.27 / \Delta m^2$. It is this calculation that determines the best L/E value for a given
336 experiment to be designed around for measurements of a specific value of Δm^2 .

337 2.2.2 The MSW Effect

338 The theory of neutrino oscillation in a vacuum has been described in subsec-
339 tion 2.2.1. However, the beam neutrinos and atmospheric neutrinos originating
340 from below the horizon propagate through the matter in the Earth. The coherent
341 scattering of neutrinos from a material target modifies the Hamiltonian of the
342 system. This results in a change of the oscillation probability. This modification
343 is termed the Mikheyev-Smirnov-Wolfenstein (MSW) effect [22–24]. This occurs
344 because charged current scattering ($\nu_e + e^- \rightarrow \nu_e + e^-$, propagated by a W^\pm
345 boson) only affects electron neutrinos whereas the neutral current scattering

³⁴⁶ ($\nu_l + l^- \rightarrow \nu_l + l^-$, propagated by a Z^0 boson) interacts through all neutrino
³⁴⁷ flavours equally. In the two-flavour approximation, the effective mixing pa-
³⁴⁸ rameter becomes

$$\sin^2(2\theta) \rightarrow \sin^2(2\theta_m) = \frac{\sin^2(2\theta)}{(A/\Delta m^2 - \cos(2\theta))^2 + \sin^2(2\theta)}, \quad (2.11)$$

³⁴⁹ where $A = 2\sqrt{2}G_F N_e E$, N_e is the electron density of the medium and G_F
³⁵⁰ is Fermi's constant. It is clear that there exists a value of $A = \Delta m^2 \cos(2\theta)$ for
³⁵¹ $\Delta m^2 > 0$ which forces $\sin^2(2\theta)$ to be equal to unity. This is colloquially called
³⁵² the matter resonance and regenerates the electron neutrino component of the
³⁵³ neutrino flux [22–24]. The density at which the resonance occurs is given by

$$N_e = \frac{\Delta m^2 \cos(2\theta)}{2\sqrt{2}G_F E}. \quad (2.12)$$

³⁵⁴ At densities lower than this critical value, the oscillation probability will
³⁵⁵ be much closer to that of vacuum oscillation. For antineutrinos, the $N_e \rightarrow$
³⁵⁶ $-N_e$ substitution is made [25].

³⁵⁷ The resonance occurring from the MSW effect depends on the sign of Δm^2 .
³⁵⁸ Therefore, any neutrino oscillation experiment which observes neutrinos and
³⁵⁹ antineutrinos which have propagated through matter can have some sensitivity
³⁶⁰ to the ordering of the neutrino mass eigenstates.

³⁶¹ 2.3 Neutrino Oscillation Measurements

³⁶² As evidence of beyond Standard Model physics, the 2015 Nobel Prize in Physics
³⁶³ was awarded to the Super-Kamiokande (SK) [26] and Sudbury Neutrino Ob-
³⁶⁴ servatory (SNO) [27] collaborations for the first definitive observation of solar
³⁶⁵ and atmospheric neutrino oscillation [28]. Since then, the field has seen a wide
³⁶⁶ array of oscillation measurements from a variety of neutrino sources. As seen
³⁶⁷ in subsection 2.2.1, the neutrino oscillation probability is dependent on the ratio
³⁶⁸ of the propagation baseline, L , to the neutrino energy, E . It is this ratio that
³⁶⁹ determines the type of neutrino oscillation a particular experiment is sensitive to.

As illustrated in Figure 2.1, there are many neutrino sources that span a wide range of energies. The least energetic neutrinos are from reactor and terrestrial sources at $O(1)$ MeV whereas the most energetic neutrinos originate from atmospheric and galactic sources with energies $> O(1)$ TeV.

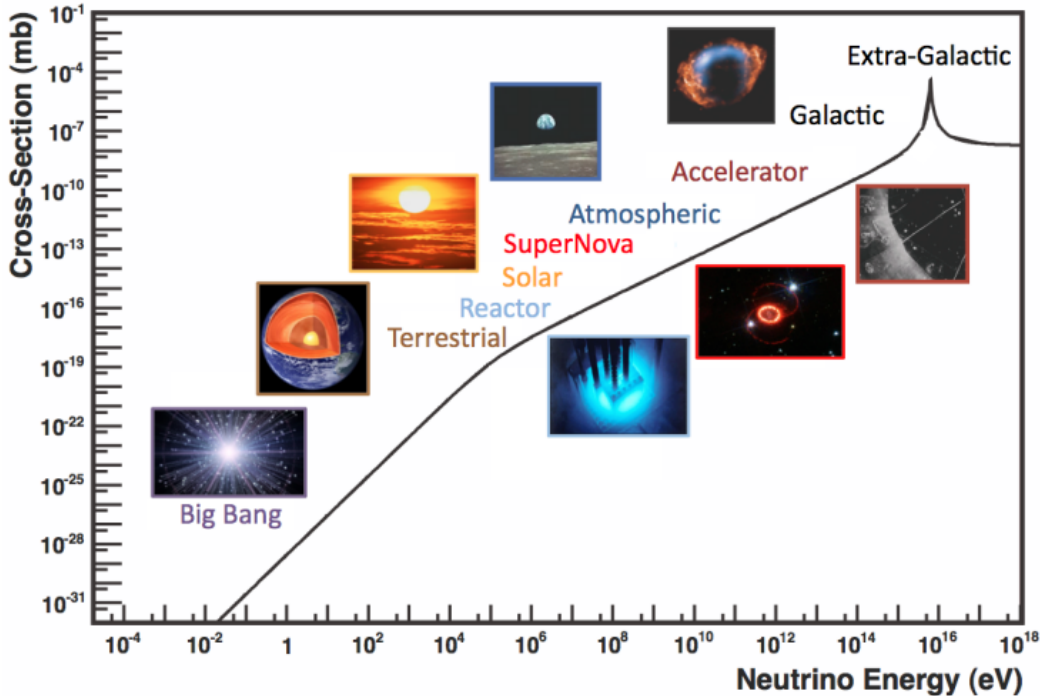


Figure 2.1: The electro-weak cross-section for $\bar{\nu}_e + e^- \rightarrow \bar{\nu}_e + e^-$ scattering on free electrons from various natural and man-made neutrino sources, as a function of neutrino energy. Taken from [29].

2.3.1 Solar Neutrinos

Solar neutrinos are emitted from fusion reaction chains at the centre of the Sun. The solar neutrino flux, given as a function of neutrino energy for different fusion and decay chains, is illustrated in Figure 2.2. Whilst proton-proton fusion generates the largest flux of neutrinos, the neutrinos are low energy and are difficult to reconstruct due to the IBD interaction threshold of 1.8MeV [30]. Consequently, most experiments focus on the neutrinos from the decay of 8B (via ${}^8B \rightarrow {}^8Be^* + e^+ + \nu_e$), which are higher energy.

The first measurements of solar neutrinos observed a significant reduction in the event rate compared to predictions from the Standard Solar Model [32, 33]. A

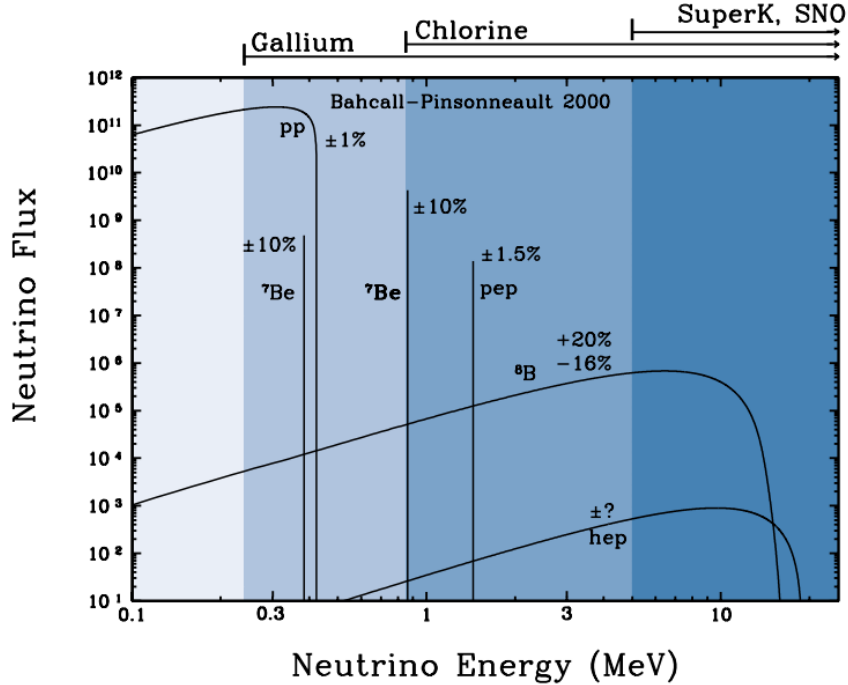
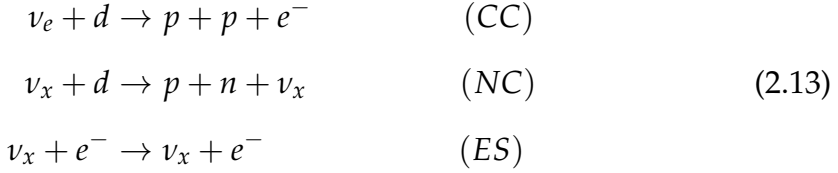


Figure 2.2: The solar neutrino flux as a function of neutrino energy for various fusion reactions and decay chains as predicted by the Standard Solar Model. Taken from [31].

384 proposed solution to this “solar neutrino problem” was $\nu_e \leftrightarrow \nu_\mu$ oscillations in a
 385 precursory version of the PMNS model [34]. The Kamiokande [35], Gallex [36]
 386 and Sage [37] experiments confirmed the ~ 0.5 factor deficit of solar neutrinos.

387 The conclusive solution to this problem was determined by the SNO col-
 388 laboration [27]. Using a deuterium water target to observe 8B neutrinos, the
 389 event rate of charged current (CC), neutral current (NC), and elastic scattering
 390 (ES) interactions (given in Equation 2.13) was simultaneously measured. CC
 391 events can only occur for electron neutrinos, whereas the NC channel is agnostic
 392 to neutrino flavour, and the ES channel has a small excess sensitivity for the
 393 detection of electron neutrino interactions. This meant that there were direct
 394 measurements of the ν_e and ν_x neutrino flux. It was concluded that the CC and
 395 ES interaction rates were consistent with the deficit previously observed. Most
 396 importantly, the NC reaction rate was only consistent with the others under the

³⁹⁷ hypothesis of flavour transformation.



³⁹⁸ 2.3.2 Accelerator Neutrinos

³⁹⁹ The concept of using an artificial “neutrino beam” was first realised in 1962 [11].
⁴⁰⁰ Since then, many experiments have adopted the same fundamental concepts.
⁴⁰¹ Typically, a proton beam is aimed at a target producing charged mesons that decay
⁴⁰² to neutrinos. The mesons can be sign-selected by the use of magnetic focusing
⁴⁰³ horns to generate a neutrino or antineutrino beam. Pions are the primary mesons
⁴⁰⁴ that decay and depending on the orientation of the magnetic field, a muon (anti-
⁴⁰⁵)neutrino beam is generated via $\pi^+ \rightarrow \mu^+ + \nu_\mu$ or $\pi^- \rightarrow \mu^- + \bar{\nu}_\mu$. The decay of
⁴⁰⁶ muons and kaons results in an irreducible intrinsic electron neutrino background.
⁴⁰⁷ In the Tokai-to-Kamioka (T2K) experiment, this background contamination is
⁴⁰⁸ $O(< 1\%)$ [38]. There is also an approximately $\sim 5\%$ “wrong-sign” background
⁴⁰⁹ of $\bar{\nu}_\mu$ generated via the same decays, when operating in neutrino mode. As the
⁴¹⁰ beam is generated by proton interactions (rather than anti-proton interactions),
⁴¹¹ the wrong-sign component in the antineutrino beam is larger when operating
⁴¹² in neutrino mode.

⁴¹³ Tuning the proton energy in the beam and using beam focusing techniques
⁴¹⁴ allows the neutrino energy to be set to a value that maximises the disappear-
⁴¹⁵ ance oscillation probability in the L/E term in Equation 2.10. This means that
⁴¹⁶ accelerator experiments are typically more sensitive to the mixing parameters as
⁴¹⁷ compared to a natural neutrino source. However, the disadvantage compared
⁴¹⁸ to atmospheric neutrino experiments is the cost of building a facility to provide
⁴¹⁹ high-energy neutrinos, with a high flux, which is required for longer baselines.
⁴²⁰ Consequently, there is typically less sensitivity to matter effects and the ordering
⁴²¹ of the neutrino mass eigenstates.

422 A neutrino experiment measures

$$R(\vec{x}) = \Phi(E_\nu) \times \sigma(E_\nu) \times \epsilon(\vec{x}) \times P(\nu_\alpha \rightarrow \nu_\beta), \quad (2.14)$$

423 where $R(\vec{x})$ is the event rate of neutrinos at position \vec{x} , $\Phi(E_\nu)$ is the flux of
 424 neutrinos with energy E_ν , $\sigma(E_\nu)$ is the cross-section of the neutrino interaction and
 425 $\epsilon(\vec{x})$ is the efficiency and resolution of the detector. In order to leverage the most
 426 out of an accelerator neutrino experiment, the flux and cross-section systematics
 427 need to be constrained. This is typically done via the use of a “near detector”,
 428 situated at a baseline of $O(1)$ km. This detector observes the unoscillated neutrino
 429 flux and constrains the parameters used within the flux and cross-section model.

430 The first accelerator experiments to precisely measure oscillation parameters
 431 were MINOS [39] and K2K [40]. These experiments confirmed the ν_μ disappear-
 432 ance seen in atmospheric neutrino experiments by finding consistent parameter
 433 values for $\sin^2(\theta_{23})$ and Δm_{32}^2 . The current generation of accelerator neutrino
 434 experiments, T2K and NO ν A extended this field by observing $\bar{\nu}_\mu \rightarrow \bar{\nu}_e$ oscillations
 435 and lead the sensitivity to atmospheric mixing parameters as seen in Figure 2.6
 436 [41]. The two experiments differ in their peak neutrino energy, baseline, and
 437 detection technique. The NO ν A experiment is situated at a baseline of 810km
 438 from the NuMI beamline which delivers 2GeV neutrinos. The T2K neutrino beam
 439 is peaked around 0.6GeV and propagates 295km [42]. Additionally, the NO ν A
 440 experiment uses functionally identical detectors (near and far) whereas T2K uses
 441 a plastic scintillator technique at the near detector and a water Cherenkov far
 442 detector. The future generation experiments DUNE [43] and Hyper-Kamiokande
 443 [44] will succeed these experiments as the high-precision era of neutrino oscil-
 444 lation parameter measurements develops.

445 Several anomalous results have been observed in the LSND [13] and Mini-
 446 BooNE [14] detectors which were designed with purposefully short baselines.
 447 Parts of the neutrino community attributed these results to oscillations induced
 448 by a fourth “sterile” neutrino [45] but several searches in other experiments,

⁴⁴⁹ MicroBooNE [46] and KARMEN [47], found no hints of additional neutrino
⁴⁵⁰ species. The solution to these anomalous results is still being determined.

⁴⁵¹ 2.3.3 Atmospheric Neutrinos

⁴⁵² The interactions of primary cosmic ray protons in the Earth's upper atmosphere
⁴⁵³ generate showers of energetic hadrons. These are mostly pions and kaons that
⁴⁵⁴ decay to produce a natural source of neutrinos spanning energies of MeV to
⁴⁵⁵ TeV [48]. The main decay is via,

$$\begin{aligned} \pi^\pm &\rightarrow \mu^\pm + (\nu_\mu, \bar{\nu}_\mu), \\ \mu^\pm &\rightarrow e^\pm + (\nu_\mu, \bar{\nu}_\mu) + (\nu_e, \bar{\nu}_e), \end{aligned} \tag{2.15}$$

⁴⁵⁶ such that for a single pion decay, three neutrinos can be produced. The
⁴⁵⁷ atmospheric neutrino flux energy spectra as predicted by the Bartol [49], Honda
⁴⁵⁸ [50–52], and FLUKA [53] models are illustrated in Figure 2.3. The flux distribution
⁴⁵⁹ peaks at an energy of $O(10)$ GeV. The uncertainties associated with these models
⁴⁶⁰ are dominated by the hadronic production of kaon and pions as well as the
⁴⁶¹ primary cosmic flux.

⁴⁶² Unlike long-baseline experiments which have a fixed baseline, the distance
⁴⁶³ atmospheric neutrinos propagate is dependent upon the zenith angle, relative to
⁴⁶⁴ the detector, at which they interact. This is illustrated in Figure 2.4. Neutrinos that
⁴⁶⁵ are generated directly above the detector ($\cos(\theta) = 1.0$) have a baseline equivalent
⁴⁶⁶ to the height of the atmosphere, whereas neutrinos that interact directly below
⁴⁶⁷ the detector ($\cos(\theta) = -1.0$) have to travel a length equal to the diameter of
⁴⁶⁸ the Earth. This means atmospheric neutrinos have a baseline that varies from
⁴⁶⁹ $O(20)$ km to $O(6 \times 10^3)$ km. Any neutrino generated at or below the horizon will
⁴⁷⁰ be subject to MSW matter resonance as they propagate through the Earth.

⁴⁷¹ Figure 2.5 highlights the atmospheric neutrino flux as a function of the zenith
⁴⁷² angle for different slices of neutrino energy. For medium to high-energy neutrinos
⁴⁷³ (and to a lesser degree for low-energy neutrinos), the flux is approximately
⁴⁷⁴ symmetric around $\cos(\theta) = 0$. To the accuracy of this approximation, the

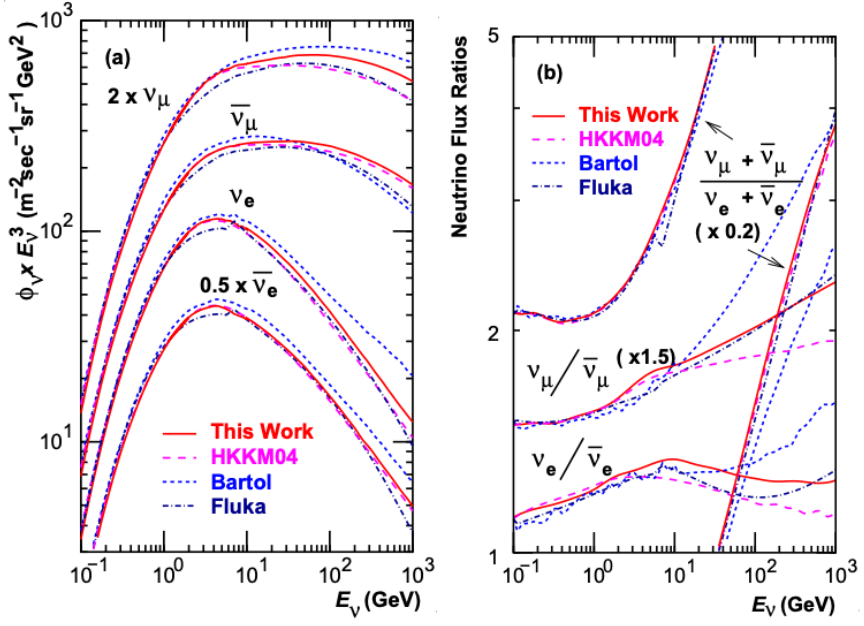


Figure 2.3: Left panel: The atmospheric neutrino flux for different neutrino flavours as a function of neutrino energy as predicted by the 2007 Honda model (“This work”) [50], the 2004 Honda model (“HKKM04”)[51], the Bartol model [49] and the FLUKA model [53]. Right panel: The ratio of the muon to electron neutrino flux as predicted by all the quoted models. Both figures taken from [50].

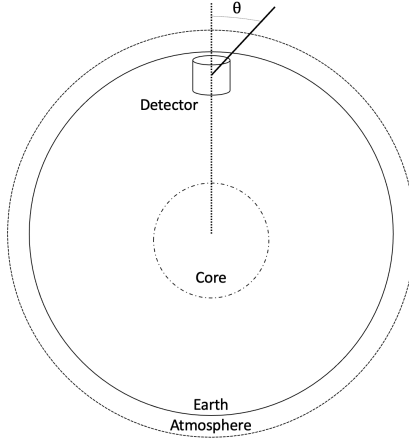


Figure 2.4: A diagram illustrating the definition of zenith angle as used in the Super Kamiokande experiment [54].

systematic uncertainties associated with atmospheric flux for comparing upward-going and down-going neutrino cancels. This allows the down-going events, which are mostly insensitive to oscillation probabilities, to act as an unoscillated prediction (similar to a near detector in an accelerator neutrino experiment).

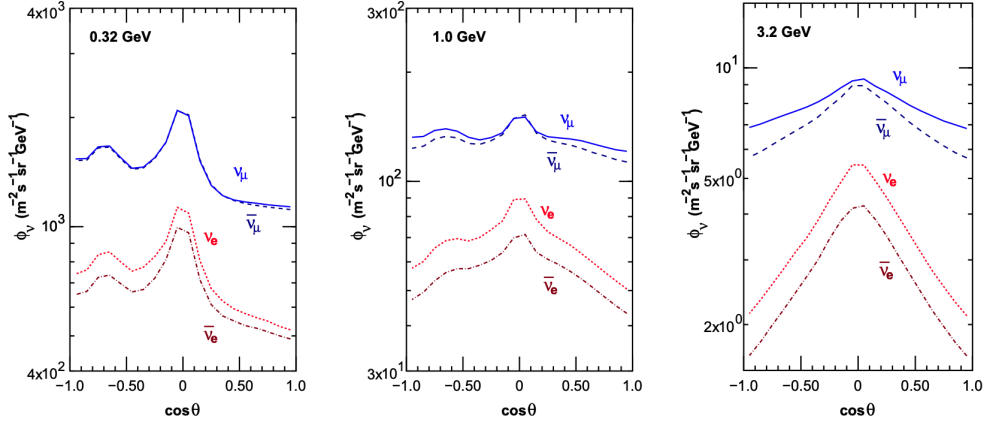


Figure 2.5: Prediction of $\nu_e, \bar{\nu}_e, \nu_\mu, \bar{\nu}_\mu$ fluxes as a function of zenith angle as calculated by the HKKM model [52]. The left, middle and right panels represent three values of neutrino energy, 0.32GeV, 1.0GeV and 3.2GeV respectively. Predictions for other models including Bartol [49], Honda [50] and FLUKA [53] are given in [54].

479 Precursory hints of atmospheric neutrinos were observed in the mid-1960s
 480 searching for $\nu_\mu + X \xrightarrow{(-)} X^* + \mu^\pm$ [55]. This was succeeded by the IMB-3 [56]
 481 and Kamiokande [57] experiments which measured the double ratio of muon
 482 to electron neutrinos in data to Monte Carlo, $R(\nu_\mu/\nu_e) = (\mu/e)_{Data}/(\mu/e)_{MC}$.
 483 Both experiments were found to have a consistent deficit of muon neutrinos,
 484 with $R(\nu_\mu/\nu_e) = 0.67 \pm 0.17$ and $R(\nu_\mu/\nu_e) = 0.658 \pm 0.016 \pm 0.035$, respectively.
 485 Super-Kamiokande (SK) [54] extended this analysis by fitting oscillation pa-
 486 rameters in $P(\nu_\mu \rightarrow \nu_\tau)$ which found best fit parameters $\sin^2(2\theta) > 0.92$ and
 487 $1.5 \times 10^{-3} < \Delta m^2 < 3.4 \times 10^{-3} eV^2$.

488 Since then, atmospheric neutrino experiments have been making precision
 489 measurements of the $\sin^2(\theta_{23})$ and Δm^2_{32} oscillation parameters. Atmospheric
 490 neutrino oscillation is dominated by $P(\nu_\mu \rightarrow \nu_\tau)$, where SK observed a 4.6σ
 491 discovery of ν_τ appearance [58]. Figure 2.6 illustrates the current estimates on
 492 the atmospheric mixing parameters, from a wide range of atmospheric and
 493 accelerator neutrino observatories.

494 2.3.4 Reactor Neutrinos

495 As illustrated in the first discovery of neutrinos (section 2.1), nuclear reactors
 496 are a very useful artificial source of electron antineutrinos. For reactors that use

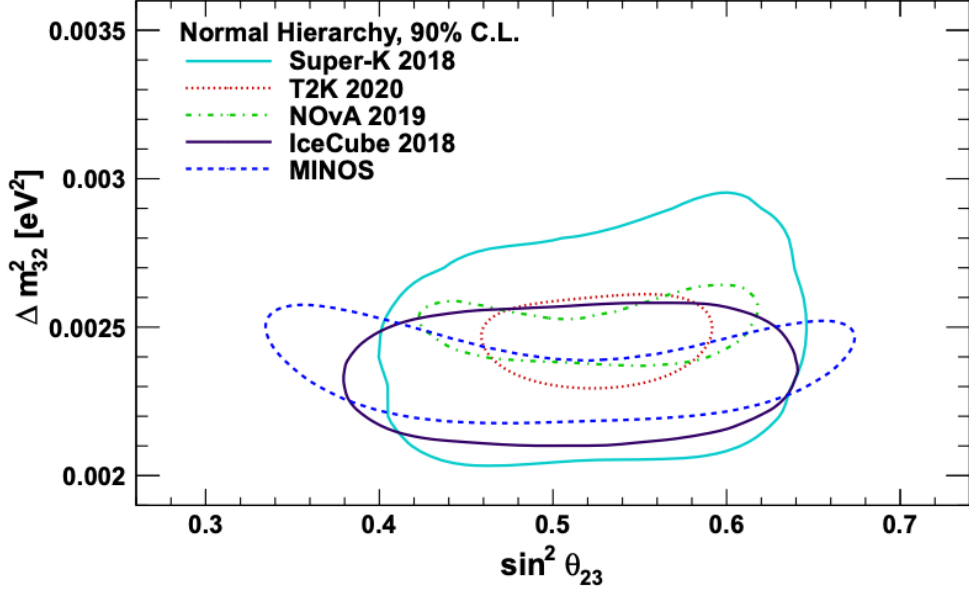


Figure 2.6: Constraints on the atmospheric oscillation parameters, $\sin^2(\theta_{23})$ and Δm_{32}^2 , from atmospheric and long-baseline experiments: SK [59], T2K [60], NOvA [61], IceCube [62] and MINOS [63]. Figure taken from [64].

497 low-enriched uranium ^{235}U as fuel, the antineutrino flux is dominated by the
 498 β -decay fission of ^{235}U , ^{238}U , ^{239}Pu and ^{241}Pu [65] as illustrated in Figure 2.7.

499 Due to their low energy, reactor electron antineutrinos predominantly interact
 500 via the inverse β -decay (IBD) interaction. The typical signature contains two
 501 signals delayed by $O(200)\mu\text{s}$; firstly the prompt photons from positron annihila-
 502 tion, and secondly the photon emitted ($E_{tot}^\gamma = 2.2\text{MeV}$) from de-excitation after
 503 neutron capture on hydrogen. Searching for both signals improves the detector's
 504 ability to distinguish between background and signal events [66].

505 There are many short baseline experiments ($L \sim O(1)\text{km}$) that have mea-
 506 sured the $\sin^2(\theta_{13})$ and Δm_{32}^2 oscillation parameters. Daya Bay [67], RENO [68]
 507 and Double Chooz [69] have all provided precise measurements, with the first
 508 discovery of a non-zero θ_{13} made by Daya Bay and RENO (and complemented
 509 by T2K [69]). The constraints on $\sin^2(\theta_{13})$ by the reactor experiments lead the
 510 field. They are often used as external inputs to accelerator neutrino experiments
 511 to improve their sensitivity to δ_{CP} and mass hierarchy determination.

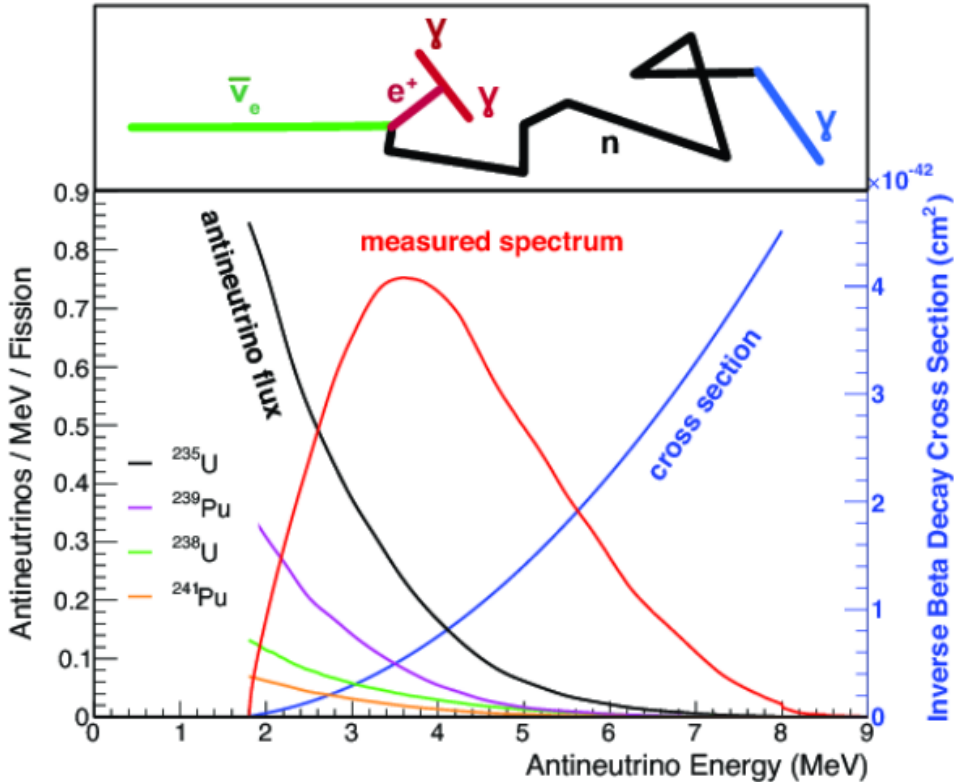


Figure 2.7: Reactor electron antineutrino fluxes for ^{235}U (Black), ^{238}U (Green), ^{239}Pu (Purple), and ^{241}Pu (Orange) isotopes. The inverse β -decay cross-section (Blue) and corresponding measurable neutrino spectrum (Red) are also given. Top panel: Schematic of Inverse β -decay interaction including the eventual capture of the emitted neutron. This capture emits a γ -ray which provides a second signal of the event. Taken from [64].

Kamland [70] is the only experiment to have observed reactor neutrinos using a long baseline (flux weighted averaged baseline of $L \sim 180\text{km}$) which allows it to have sensitivity to Δm_{21}^2 . Combined with the SK solar neutrino experiment, the combined analysis puts the most stringent constraint on Δm_{21}^2 [71].

2.4 Summary Of Oscillation Parameter Measurements

Since the first evidence of neutrino oscillations, numerous measurements of the mixing parameters have been made. Many experiments use neutrinos as a tool for the discovery of new physics (diffuse supernova background, neutrinoless double beta decay and others) so the PMNS parameters are summarised in the Particle Data Group (PDG) review tables. The analysis presented in this thesis

522 focuses on the 2020 T2K oscillation analysis presented in [2] which uses the 2020
523 PDG constraints [72]. These constraints are outlined in Table 2.1.

Parameter	2020 Constraint
$\sin^2(\theta_{12})$	0.307 ± 0.013
Δm_{21}^2	$(7.53 \pm 0.18) \times 10^{-5} \text{ eV}^2$
$\sin^2(\theta_{13})$	$(2.18 \pm 0.07) \times 10^{-2}$
$\sin^2(\theta_{23})$ (I.H.)	0.547 ± 0.021
$\sin^2(\theta_{23})$ (N.H.)	0.545 ± 0.021
Δm_{32}^2 (I.H.)	$(-2.546^{+0.034}_{-0.040}) \times 10^{-3} \text{ eV}^2$
Δm_{32}^2 (N.H.)	$(2.453 \pm 0.034) \times 10^{-3} \text{ eV}^2$

Table 2.1: The 2020 Particle Data Group constraints of the oscillation parameters taken from [72]. The value of Δm_{32}^2 is given for both normal hierarchy (N.H.) and inverted hierarchy (I.H.) and $\sin^2(\theta_{23})$ is broken down by whether its value is below (Q1) or above (Q2) 0.5.

524 The $\sin^2(\theta_{13})$ measurement stems from the electron antineutrino disappearance,
525 $P(\bar{\nu}_e \rightarrow \bar{\nu}_e)$, and is taken as the average best-fit from the combination of
526 Daya Bay, Reno and Double Chooz. It is often used as a prior uncertainty within
527 other neutrino oscillation experiments, typically termed the reactor constraint.
528 The $\sin^2(\theta_{12})$ parameter is predominantly measured through electron neutrino
529 disappearance, $P(\nu_e \rightarrow \nu_{\mu,\tau})$, in solar neutrino experiments. The long-baseline
530 reactor neutrino experiment Kamland also has a sensitivity to this parameter
531 and is used in a joint fit to solar data from SNO and SK, using the reactor con-
532 straint. Measurements of $\sin^2(\theta_{23})$ are made by long-baseline and atmospheric
533 neutrino experiments. The PDG value is a joint fit of T2K, NO ν A, MINOS and
534 IceCube DeepCore experiments. The latest T2K-only measurement, provided at
535 Neutrino2020 and is the basis of this thesis, is given as $\sin^2(\theta_{23}) = 0.546^{+0.024}_{-0.046}$ [2].
536 The PDG constraint on Δm_{21}^2 is provided by the KamLAND experiment using
537 solar and geoneutrino data. This measurement utilised a $\sin^2(\theta_{13})$ constraint
538 from accelerator (T2K, MINOS) and reactor neutrino (Daya Bay, RENO, Double
539 Chooz) experiments. Accelerator measurements make some of the most stringent
540 constraints on Δm_{32}^2 although atmospheric experiments have more sensitivity to
541 the mass hierarchy determination. The PDG performs a joint fit of accelerator and

atmospheric data, in both normal and inverted hierarchies separately. The latest T2K-only result is $\Delta m_{32}^2 = 2.49^{+0.058}_{-0.082} \times 10^{-3} \text{ eV}^2$ favouring normal hierarchy [2]. The value of δ_{CP} is largely undetermined. CP-conserving values of 0 and π were rejected with $\sim 2\sigma$ intervals, as published in Nature [73]. Since the 2020 PDG publication, there has been a new measurement of $\sin^2(\theta_{13}) = (2.20 \pm 0.07) \times 10^{-2}$ [74], alongside updated Δm_{32}^2 and $\sin^2(\theta_{23})$ measurements.

Throughout this thesis, several sample spectra predictions and contours are presented, which require oscillation parameters to be assumed. Table 2.2 defines two sets of oscillation parameters, with “Asimov A” set being close to the preferred values from a previous T2K-only fit [75] and “Asimov B” being CP-conserving and further from maximal θ_{23} mixing.

Parameter	Asimov A	Asimov B
Δm_{12}^2	$7.53 \times 10^{-5} \text{ eV}^2$	
Δm_{32}^2	$2.509 \times 10^{-3} \text{ eV}^2$	
$\sin^2(\theta_{12})$	0.304	
$\sin^2(\theta_{13})$	0.0219	
$\sin^2(\theta_{23})$	0.528	0.45
δ_{CP}	-1.601	0.0

Table 2.2: Reference values of the neutrino oscillation parameters for two different oscillation parameter sets.

2.5 Overview of Oscillation Effects

The analysis presented within this thesis focuses on the determination of oscillation parameters from a joint atmospheric and beam analysis which combines the SK and T2K experiments. Whilst subject to the same oscillation formalism, the way in which the two samples have sensitivity to the different oscillation parameters differs significantly.

Atmospheric neutrinos have a varying baseline, or “path length” L , such that the distance each neutrino travels before interacting is dependent upon the zenith angle, θ_Z . As primary cosmic rays can interact anywhere between the Earth’s

surface and $\sim 50\text{km}$ above that, the height, h , in the atmosphere at which the neutrino was generated also affects the path length,

$$L = \sqrt{(R_E + h)^2 - R_E^2 (1 - \cos^2(\theta_Z))} - R_E \cos(\theta_Z). \quad (2.16)$$

Where $R_E = 6,371\text{km}$ is the Earth's radius. This assumes a spherically symmetric Earth model. Therefore, the oscillation probability is dependent upon two parameters, $\cos(\theta_Z)$ and E_ν .

The oscillation probability used within this analysis is based on [25]. The neutrino wavefunction in the vacuum Hamiltonian evolves in each layer of constant matter density via

$$i \frac{d\psi_j(t)}{dt} = \frac{m_j^2}{2E_\nu} \psi_j(t) - \sum_k \sqrt{2} G_F N_e U_{ej} U_{ke}^\dagger \psi_k(t), \quad (2.17)$$

where m_j^2 is the square of the j^{th} vacuum eigenstate mass, E_ν is the neutrino energy, G_F is Fermi's constant, N_e is the electron number density and U is the PMNS matrix. The transformation $N_e \rightarrow -N_e$ and $\delta_{CP} \rightarrow -\delta_{CP}$ is applied for antineutrino propagation. Thus, a model of the Earth's density is required for neutrino propagation. Following the SK methodology [76], this analysis uses the Preliminary Reference Earth Model (PREM) [77] which provides piecewise cubic polynomials as a function of the Earth's radius. This density profile is illustrated in Figure 2.8. As the propagator requires layers of constant density, the SK methodology approximates the PREM model by using four layers of constant density [76], detailed in Table 2.3.

Layer	Outer Radius [km]	Density [g/cm ³]	Chemical composition (Z/A)
Inner Core	1220	13	0.468 ± 0.029
Outer Core	3480	11.3	0.468 ± 0.029
Lower Mantle	5701	5.0	0.496
Transition Zone	6371	3.3	0.496

Table 2.3: Description of the four layers of the Earth invoked within the constant density approximation of the PREM model [77].

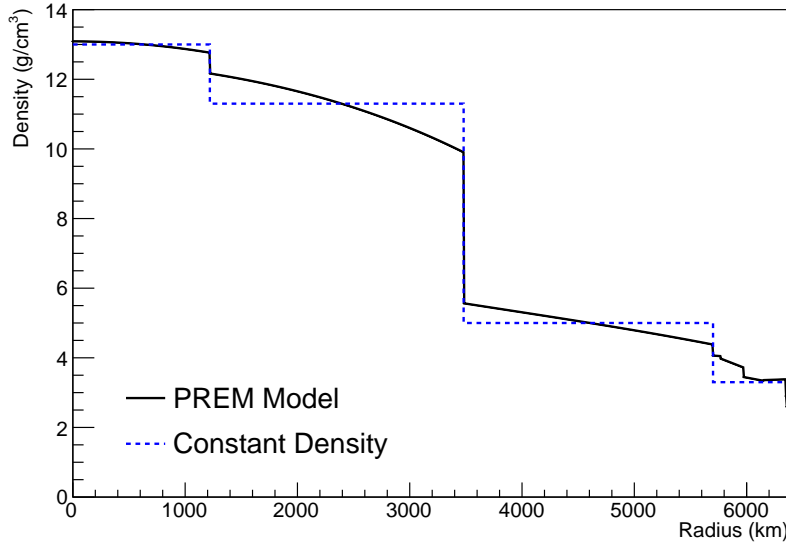


Figure 2.8: The density of the Earth given as a function of the radius, as provided by the PREM model (Black), and the constant density four-layer approximation (Blue), as used in the official SK-only analysis.

580 The atmospheric neutrino oscillation probabilities can be presented as two di-
 581 mensional “oscillograms” as illustrated in Figure 2.9. The distinct discontinuities,
 582 as a function of $\cos(\theta_Z)$, are due to the discontinuous density in the PREM model.

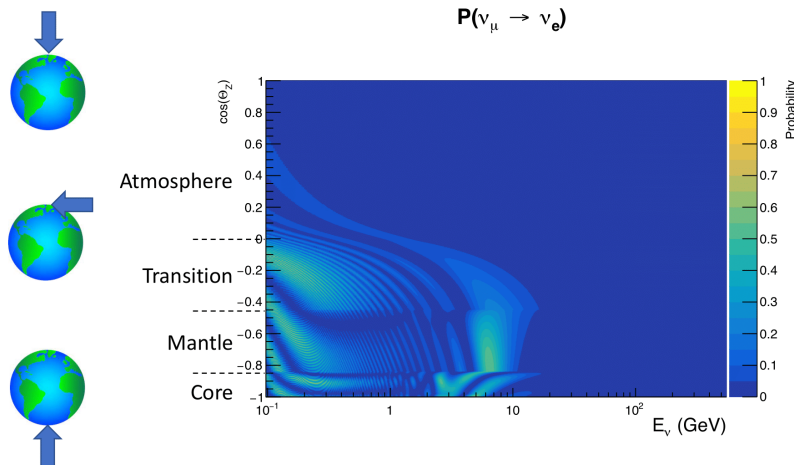


Figure 2.9: An “oscillogram” that depicts the $P(\nu_\mu \rightarrow \nu_e)$ oscillation probability as a function of neutrino energy and cosine of the zenith angle. The zenith angle is defined such that $\cos(\theta_Z) = 1.0$ represents neutrinos that travel from directly above the detector. The four-layer constant density PREM model approximation is used and Asimov A oscillation parameters are assumed (Table 2.2).

Atmospheric neutrinos have sensitivity to δ_{CP} through the overall event rate. Figure 2.10 illustrates the difference in oscillation probability between CP-conserving ($\delta_{CP} = 0.$) and a CP-violating ($\delta_{CP} = -1.601$) value taken from Asimov A oscillation parameter set (Table 2.2). The result is a complicated oscillation pattern in the appearance probability for sub-GeV upgoing neutrinos. The detector does not have sufficient resolution to resolve these individual patterns so the sensitivity to δ_{CP} for atmospheric neutrinos comes via the overall normalisation of these events.

The presence of matter means that the effect δ_{CP} has on the oscillation probability is not equal between neutrinos and antineutrinos. Furthermore, the interaction cross-section for neutrinos is larger than for antineutrinos so the two effects have to be disentangled. All of these effects lead to a difference in the number of neutrinos detected compared to antineutrinos. This changes how the δ_{CP} normalisation term is observed, resulting in a very complex sensitivity to δ_{CP} .

The vacuum and matter oscillation probabilities for $P(\nu_e \rightarrow \nu_e)$ and $P(\bar{\nu}_e \rightarrow \bar{\nu}_e)$ are presented in Figure 2.11, where the PREM model has been assumed. The oscillation probability for both neutrinos and antineutrinos is affected in the presence of matter. However, the resonance effects around $O(5)\text{GeV}$ only occur for neutrinos in the normal mass hierarchy and antineutrinos in the inverse mass hierarchy. The exact position and amplitude of the resonance depend on $\sin^2(\theta_{23})$, further increasing the atmospheric neutrinos' sensitivity to the parameter.

As the T2K beam flux is centered at the first oscillation maximum ($E_\nu = 0.6\text{GeV}$) [42], the sensitivity to δ_{CP} is predominantly observed as a change in the event-rate of e-like samples in $\nu/\bar{\nu}$ modes. Figure 2.12 illustrates the $P(\nu_\mu \rightarrow \nu_e)$ oscillation probability for a range of δ_{CP} values. A circular modulation of the first oscillation peak (in both magnitude and position) is observed when varying throughout the allowable values of δ_{CP} . The CP-conserving values of $\delta_{CP} = 0, \pi$ have a lower(higher) oscillation maximum than the CP-violating values of $\delta_{CP} = -\pi/2(\delta_{CP} = \pi/2)$. A sub-dominant shift in the energy of the oscillation peak is also present, which aids in separating the two CP-conserving values of δ_{CP} .

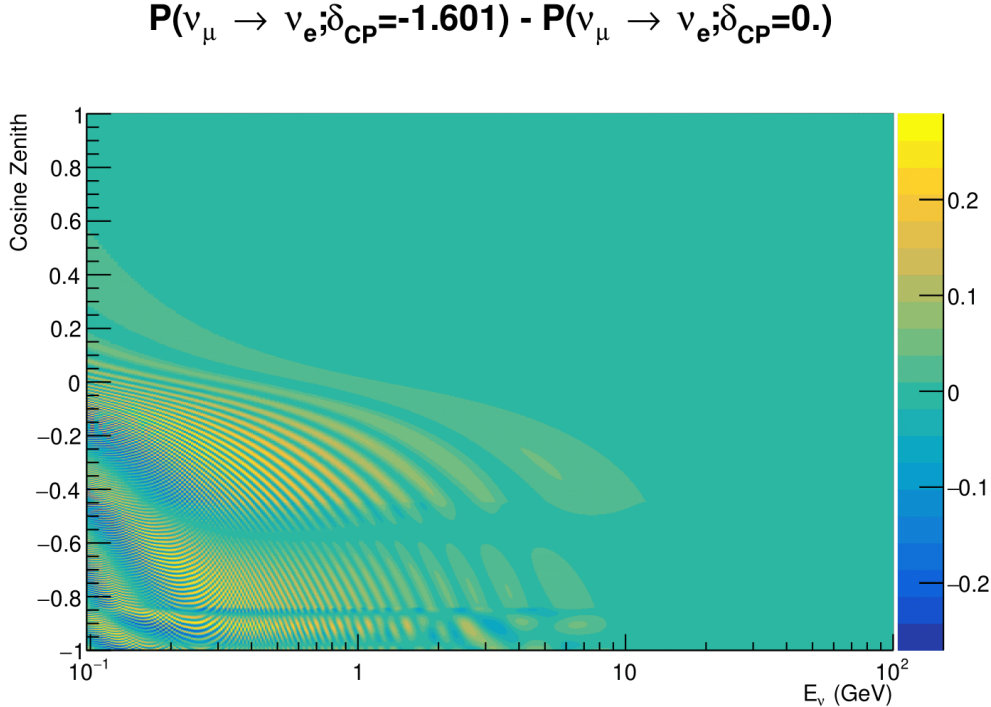


Figure 2.10: The effect of δ_{CP} for atmospheric neutrinos given in terms of the neutrino energy and zenith angle. This oscillogram compares the $P(\nu_\mu \rightarrow \nu_e)$ oscillation probability for a CP conserving ($\delta_{CP} = 0.0$) and a CP violating ($\delta_{CP} = -1.601$) value taken from the Asimov A parameter set. The other oscillation parameters assume the Asimov A oscillation parameter set given in Table 2.2.

613 T2K's sensitivity to $\sin^2(\theta_{23})$ and Δm_{32}^2 is observed as a shape-based variation
 614 of the muon-like samples, as illustrated in Figure 2.12. The value of Δm_{32}^2 laterally
 615 shifts the position of the oscillation dip (around $E_\nu \sim 0.6\text{GeV}$) in the $P(\nu_\mu \rightarrow \nu_\mu)$.
 616 A variation of $\sin^2(\theta_{23})$ is predominantly observed as a vertical shift of the
 617 oscillation dip with second-order horizontal shifts being due to matter effects.
 618 The beam neutrinos have limited sensitivity to matter effects due to the relatively
 619 shorter baseline as well as the Earth's mantle being a relatively low-density
 620 material (as compared to the Earth's core). For some values of δ_{CP} , the degeneracy
 621 in the number of e-like events allows the mass hierarchy to be broken. This leads
 622 to a δ_{CP} -dependent mass hierarchy sensitivity which can be seen in Figure 2.13.
 623 Whilst all oscillation channels should be included for completeness, the
 624 computational resources required to run a fit are limited and any reasonable
 625 approximations which reduce the number of oscillation probability calculations

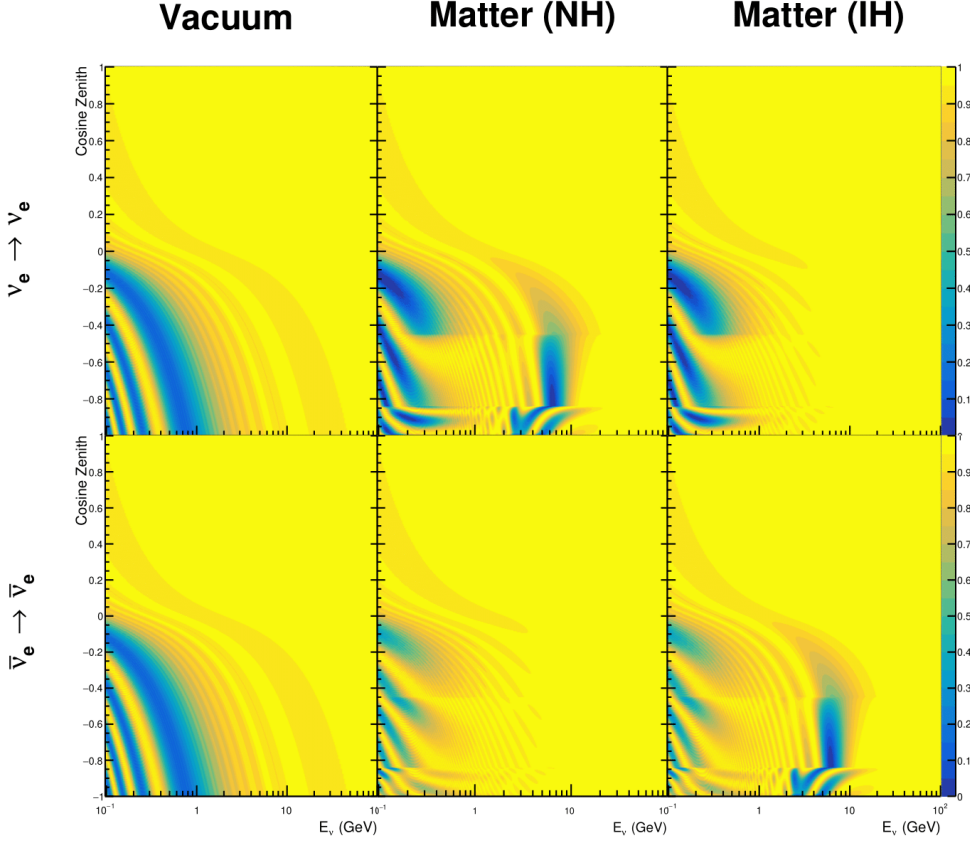


Figure 2.11: An illustration of the matter-induced effects on the oscillation probability, given as a function of neutrino energy and zenith angle. The top row of panels gives the $P(\nu_e \rightarrow \nu_e)$ oscillation probability and the bottom row illustrates the $P(\bar{\nu}_e \rightarrow \bar{\nu}_e)$ oscillation probability. The left column highlights the oscillation probability in a vacuum, whereas the middle and right column represents the oscillation probabilities when the four-layer fixed density PREM model is assumed. All oscillation probabilities assume the “Asimov A” set given in Table 2.2, but importantly, the right column sets an inverted mass hierarchy. The “matter resonance” effects at $E_\nu \sim 5\text{GeV}$ can be seen in the $P(\nu_e \rightarrow \nu_e)$ for normal mass hierarchy and $P(\bar{\nu}_e \rightarrow \bar{\nu}_e)$ for inverted hierarchy.

that need to be made should be applied. The $\nu_e \rightarrow \nu_{e,\mu,\tau}$ (and antineutrino equivalent) oscillations can be ignored for beam neutrinos as the $\nu_e/\bar{\nu}_e$ fluxes are approximately two orders of magnitude smaller than the corresponding $\nu_\mu/\bar{\nu}_\mu$ flux [78]. Furthermore, as the peak neutrino energy of the beam is well below the threshold for charged current tau production ($E_\nu = 3.5\text{GeV}$ [58]), only a small proportion of the neutrinos produced in the beam have the required energy. For the few neutrinos that have sufficient energy, the oscillation probability

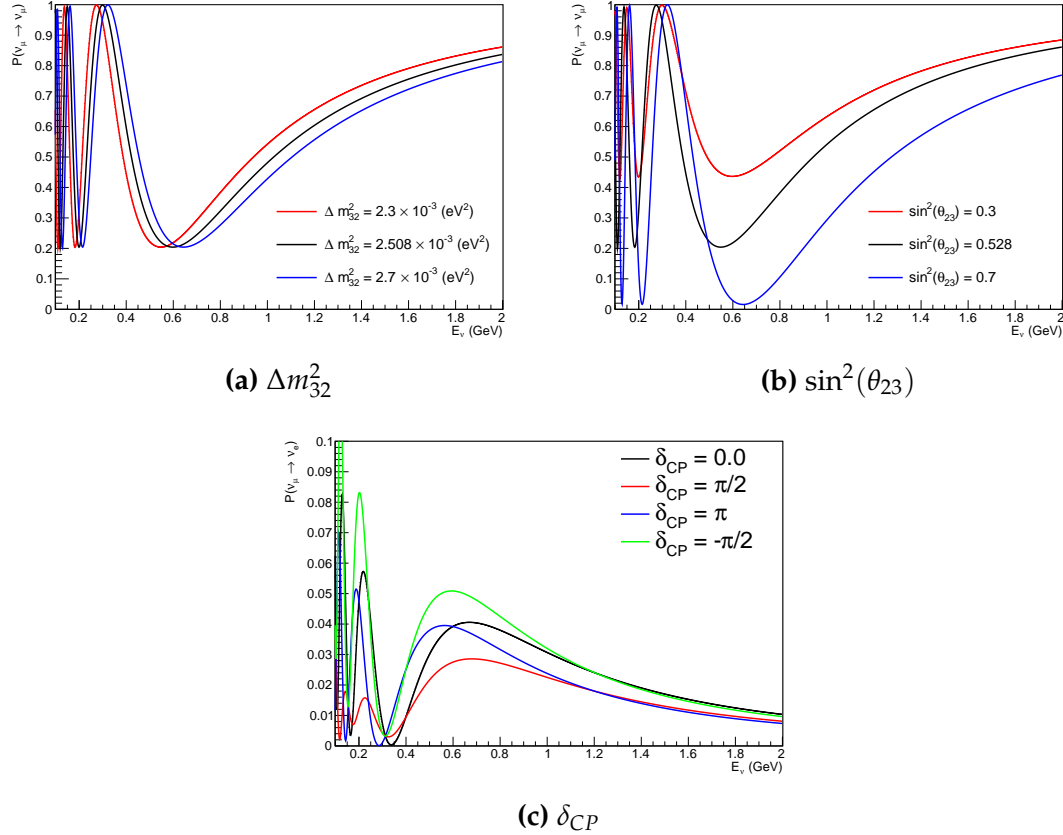


Figure 2.12: The oscillation probability for beam neutrino events given as a function of neutrino energy. All oscillation parameters assume the “Asimov A” set given in Table 2.2 unless otherwise stated. A path-length of 295km is assumed. Each panel represents a change in one of the oscillation parameters whilst keeping the remaining parameters fixed.

is very small due to their energy being well above the oscillation maximum (small value of L/E). Whilst these approximations have been made for the beam neutrinos, the atmospheric flux of ν_e is of the same order of magnitude as the ν_μ flux and the energy distribution of atmospheric neutrinos extends well above the tau production threshold. These events can have non-negligible oscillation probabilities due to the further distance they travel.

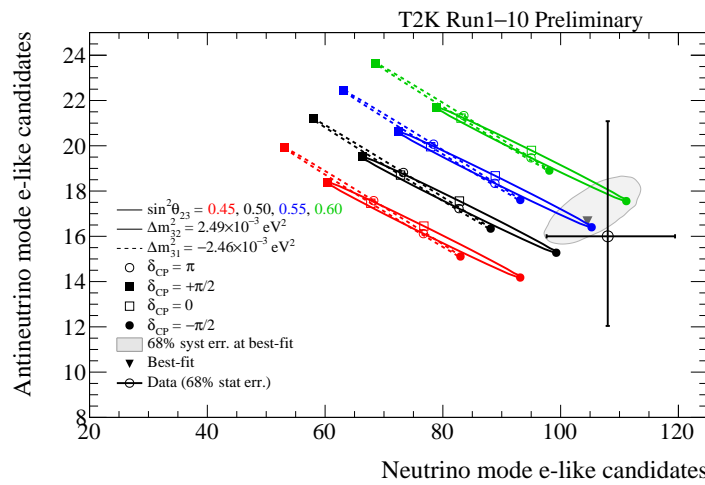


Figure 2.13: The number of electron-like events in the FHC and RHC operating mode of the beam, as a function of the oscillation probabilities. Both normal hierarchy (Solid) and inverse hierarchy (Dashed) values of Δm_{32}^2 are given.

3

639

640

T2K and SK Experiment Overview

641 As the successor of the Kamiokande experiment, the Super-Kamiokande (SK)
642 collaboration has been leading atmospheric neutrino oscillation analyses for
643 over two decades. The detector has provided some of the strongest constraints
644 on proton decay and the first precise measurements of the Δm_{32}^2 and $\sin^2(\theta_{23})$
645 neutrino oscillation parameters. The history, detection technique, and operation
646 of the SK detector is described in section 3.1.

647 The Tokai-to-Kamioka (T2K) experiment was one of the first long-baseline
648 experiments to use both neutrino and antineutrino beams to precisely measure
649 charge parity violation within the neutrino sector. The T2K experiment observed
650 the first hints of a non-zero $\sin^2(\theta_{13})$ measurement and continues to lead the
651 field with the constraints it provides on $\sin^2(\theta_{13})$, $\sin^2(\theta_{23})$, Δm_{32}^2 and δ_{CP} . In
652 section 3.2, the techniques that T2K use to generate the neutrino beam and
653 constrain systematic parameter through near detector constraints are described.

654 3.1 The Super-Kamiokande Experiment

655 The SK experiment began taking data in 1996 [79] and has had many modifi-
656 cations throughout its operation. There have been seven defined periods of
657 data taking as noted in Table 3.1. Data taking began in SK-I which ran for five

years. Between the SK-I and SK-II periods, approximately 55% of the PMTs were damaged during maintenance [80]. Those that survived were equally distributed throughout the detector in the SK-II era, which resulted in a reduced 19% photo-coverage. From SK-III onwards, repairs to the detector meant the full suite of PMTs was operational recovering the 40% photo-coverage. Before the start of SK-IV, the data acquisition and electronic systems were upgraded. Between SK-IV and SK-V, a significant effort was placed into tank open maintenance and repair/replacement of defective PMTs in preparation for the Gadolinium upgrade; a task for which the author of this thesis was required. Consequently, the detector conditions were significantly changed from this point. SK-VI marked the start of the SK-Gd era, with the detector being doped with gadolinium at a concentration of 0.01% by concentration. SK-VII, which started during the writing of this thesis, has increased the gadolinium concentration to 0.03% for continued operation [81].

The oscillation analysis presented within this thesis focuses on the SK-IV period of running and the data taken within it. This follows from the recent SK analysis presented in [82]. Therefore, the information presented within this section focuses on that period.

Period	Start Date	End Date	Live-time (days)
I	April 1996	July 2001	1489.19
II	October 2002	October 2005	798.59
III	July 2006	September 2008	518.08
IV	September 2008	May 2018	3244.4
V	January 2019	July 2020	461.02
VI	July 2020	May 2022	583.3
VII	May 2022	Ongoing	N/A

Table 3.1: The various SK periods and their respective live-time. The SK-VI live-time is calculated until 1st April 2022. SK-VII started during the writing of this thesis.

3.1.1 The SK Detector

The basic structure of the Super-Kamiokande (SK) detector is a cylindrical tank, with diameter 39.3m and height 41.1m, filled with ultrapure water [80]. A diagram of the significant components of the SK detector is given in Figure 3.1.

679 The SK detector is situated in the Kamioka mine in Gifu, Japan. The mine is under-
 680 ground with roughly 1km rock overburden (2.7km water equivalent overburden)
 681 [83]. At this depth, the rate of cosmic ray muons is significantly decreased to a
 682 value of $\sim 2\text{Hz}$ (net rate). The top of the tank is covered with stainless steel which
 683 is designed as a working platform for maintenance, calibration, and location for
 684 high voltage and data acquisition electronics.

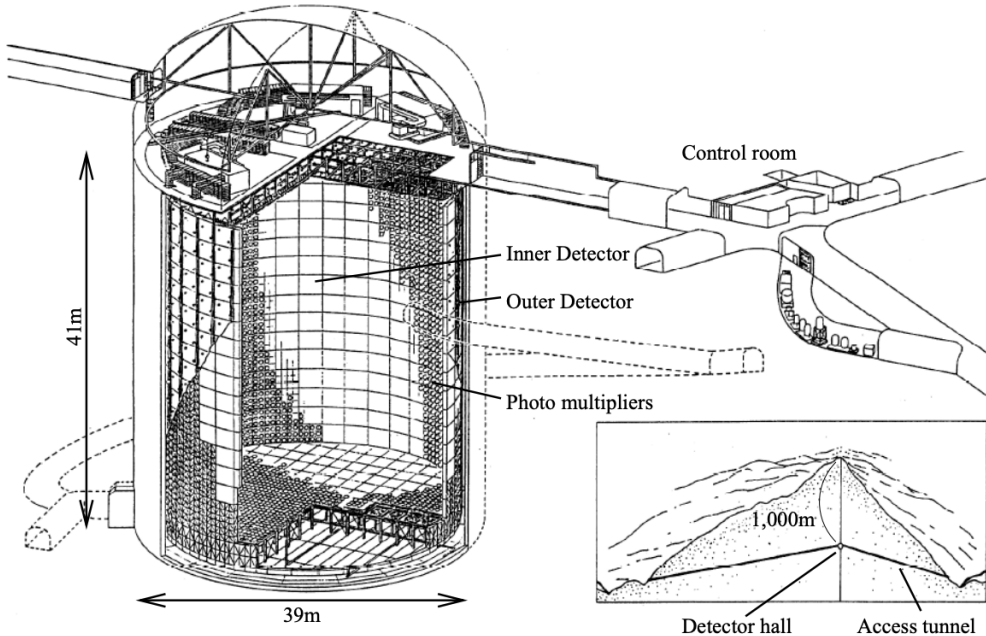


Figure 3.1: A schematic diagram of the Super-Kamiokande Detector. Taken from [84].

685 A smaller cylindrical structure (36.2m diameter, 33.8m height) is situated
 686 inside the tank, with an approximate 2m gap between this structure and the outer
 687 tank wall. The purpose of this structure is to support the photomultiplier tubes
 688 (PMTs). The volume inside and outside the support structure is referred to as the
 689 inner detector (ID) and outer detector (OD), respectively. In the SK-IV era, the
 690 ID and OD are instrumented by 11,129 50cm and 1,885 20cm PMTs, respectively
 691 [80]. The ID contains a 32kton mass of water. Many analyses performed at SK
 692 use a “fiducial volume” defined by the volume of water inside the ID excluding
 693 some distance to the ID wall. This reduces the volume of the detector which is
 694 sensitive to neutrino events but reduces radioactive backgrounds and allows for

695 better reconstruction performance. The nominal fiducial volume is defined as the
696 area contained inside 2m from the ID wall for a total of 22.5kton water [3].

697 The two regions of the detector (ID and OD) are optically separated with
698 opaque black plastic hung from the support structure. The purpose of this is
699 to determine whether an event entered or exited the ID. This allows cosmic ray
700 muons and partially contained events to be tagged and separated from neutrino
701 events entirely contained within the ID. This black plastic is also used to cover
702 the area between the ID PMTs to reduce photon reflection from the ID walls.
703 Opposite to this, the OD is lined with a reflective material to allow photons to
704 reflect around inside the OD until collected by one of the PMTs. Furthermore,
705 each OD PMT is optically coupled with $50 \times 50\text{cm}$ plates of wavelength shifting
706 acrylic which increases the efficiency of light collection [83].

707 In the SK-IV data-taking period, the photocathode coverage of the detector, or
708 the fraction of the ID wall instrumented with PMTs, is $\sim 40\%$ [83]. The PMTs have
709 a quantum efficiency (the ratio of detected electrons to incident photons) of $\sim 21\%$
710 for photons with wavelengths of $360\text{nm} < \lambda < 390\text{nm}$ [85, 86]. The proportion
711 of photoelectrons that produce a signal in the dynode of a PMT, termed the
712 collection efficiency, is $> 70\%$ [83]. The PMTs used within SK are most sensitive
713 to photons with wavelength $300\text{nm} \leq \lambda \leq 600\text{nm}$ [83]. One disadvantage of
714 using PMTs as the detection media is that the Earth's geomagnetic field can
715 modify its response. Therefore, a set of compensation coils is built around the
716 inner surface of the detector to mitigate this effect [83].

717 The SK detector is filled with ultrapure water, which in a perfect world, con-
718 tains no impurities. However, bacteria and organic compounds can significantly
719 degrade the water quality. This decreases the attenuation length, which reduces
720 the total number of photons that hit a PMT. To combat this, a sophisticated water
721 treatment system has been developed [83, 87]. UV lights, mechanical filters, and
722 membrane degasifiers are used to reduce the bacteria, suspended particulates,
723 and radioactive materials from the water. The flow of water within the tank
724 is also critical as it can remove stagnant bacterial growth or build-up of dust

725 on the surfaces within the tank. Gravity drifts impurities in the water towards
726 the bottom of the tank which, if left uncontrolled, can create asymmetric water
727 conditions between the top and bottom of the tank. Typically, the water entering
728 the tank is cooled below the ambient temperature of the tank to control convection
729 and inhibit bacteria growth. Furthermore, the rate of dark noise hits within PMTs
730 is sensitive to the PMT temperature [88]. Therefore controlling the temperature
731 gradients within the tank is beneficial for stable measurements.

732 SK-VI is the first phase of the SK experiment to use gadolinium dopants
733 within the ultrapure water [81]. As such, the SK water system had to be replaced
734 to avoid removing the gadolinium concentrate from the ultrapure water [66]. For
735 an inverse β -decay (IBD) interaction on a water target, the emitted neutron is
736 thermally captured on hydrogen. This process releases a 2.2MeV γ ray which is
737 difficult to detect as the resulting Compton scattered electrons are very close to the
738 Cherenkov threshold, limiting detection capability. Thermal capture of neutrons
739 on gadolinium generates γ rays with higher energy (8MeV [66]) meaning they
740 are more easily detected and reconstructed. SK-VI has 0.01% Gd loading (0.02%
741 gadolinium sulphate by mass) which causes $\approx 50\%$ of neutrons emitted by IBD
742 to be captured on gadolinium[89]. Whilst predominantly useful for low energy
743 analyses, Gd loading allows better $\nu/\bar{\nu}$ separation for atmospheric neutrino
744 event selections [90]. Efforts are currently in place to increase the gadolinium
745 concentrate to 0.03% for $\approx 75\%$ neutron capture efficiency on gadolinium [91].
746 The final stage of loading targets 0.1% concentrate for $\approx 90\%$ neutron capture
747 efficiency on gadolinium.

748 3.1.2 Calibration

749 The calibration of the SK detector is documented in [80] and summarised below.
750 The analysis presented within this thesis is dependent upon ‘high energy events’
751 (Charged particles with $O(> 100)\text{MeV}$ momenta). These are events that are
752 expected to generate a larger number of photons such that each PMT will
753 be hit with multiple photons. The reconstruction of these events depends

upon the charge deposited within each PMT and the timing response of each individual PMT. Therefore, the most relevant calibration techniques to this thesis are outlined.

Before installation, 420 PMTs were calibrated to have identical charge responses and then distributed throughout the tank in a cross-shape pattern (As illustrated by Figure 3.2). These are used as a standardised measure for the rest of the PMTs installed at similar geometric positions within SK to be calibrated against. To perform this calibration, a xenon lamp is located at the center of the SK tank which flashes uniform light at 1Hz. This allows for geometrical effects, water quality variation, and timing effects to be measured in situ throughout normal data-taking periods.

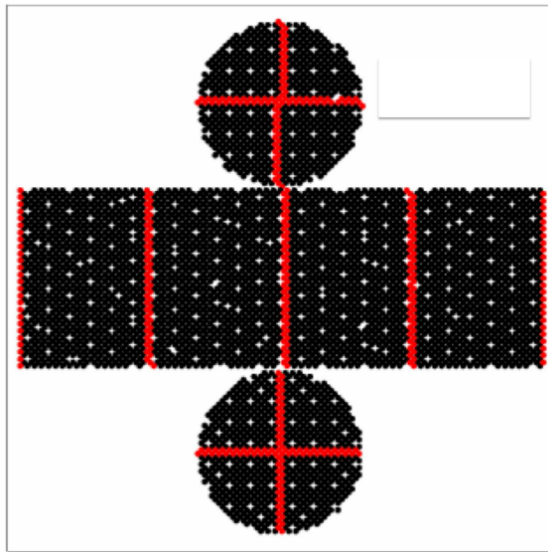


Figure 3.2: The location of “standard PMTs” (red) inside the SK detector. Taken from [80].

When specifically performing calibration of the detector (in out-of-data taking mode), the water in the tank was circulated to avoid top/bottom asymmetric water quality. Any non-uniformity within the tank significantly affects the PMT hit probability through scattering or absorption. This becomes a dominant effect for very low-intensity light sources that are designed such that only one photon is incident upon a given PMT.

771 The gain of a PMT is defined as the ratio of the total charge of the signal
 772 produced compared to the charge of photoelectrons emitted by the photocathodes
 773 within the PMT. To calibrate the signal of each PMT, the “relative” and “absolute”
 774 gain values are measured. The relative gain is the variation of gain among each
 775 of the PMTs whereas the absolute gain is the average gain of all PMTs.

776 The relative gain is calibrated as follows. A laser is used to generate two
 777 measurements: a high-intensity flash that illuminates every PMT with a sufficient
 778 number of photons, and a low-intensity flash in which only a small number
 779 of PMTs collect light. The first measurement creates an average charge, $Q_{obs}(i)$
 780 on PMT i , whereas the second measurement ensures that each hit PMT only
 781 generates a single photoelectron. For the low-intensity measurement, the number
 782 of times each PMT records a charge larger than 1/4 photoelectrons, $N_{obs}(i)$, is
 783 counted. The values measured can be expressed as

$$\begin{aligned} Q_{obs}(i) &\propto I_H \times f(i) \times \epsilon(i) \times G(i), \\ N_{obs}(i) &\propto I_L \times f(i) \times \epsilon(i). \end{aligned} \tag{3.1}$$

784 Where I_H and I_L is the intensity of the high and low flashes, $f(i)$ is the
 785 acceptance efficiency of the i^{th} PMT, $\epsilon(i)$ is the product of the quantum and
 786 collection efficiency of the i^{th} PMT and $G(i)$ is the gain of the i^{th} PMT. The relative
 787 gain for each PMT can be determined by taking the ratio of these quantities.

788 The absolute gain calibration is performed by observing fixed energy γ -rays
 789 of $E_\gamma \sim 9\text{MeV}$ emitted isotropically from neutron capture on a NiCf source
 790 situated at the center of the detector. This generates a photon yield of about 0.004
 791 photoelectrons/PMT/event, meaning that $> 99\%$ of PMT signals are generated
 792 from single photoelectrons. A charge distribution is generated by performing
 793 this calibration over all PMTs, and the average value of this distribution is taken
 794 to be the absolute gain value.

795 As mentioned in subsection 3.1.1, the average quantum and collection effi-
 796 ciency for the SK detector PMTs is $\sim 21\%$ and $> 70\%$ respectively. However,
 797 these values do differ between each PMT and need to be calibrated accordingly.

798 Consequently, the NiCf source is also used to calibrate the “quantum \times collection”
799 efficiency (denoted “QE”) value of each PMT. The NiCf low-intensity source is
800 used as the PMT hit probability is proportional to the QE ($N_{obs}(i) \propto \epsilon(i)$ in
801 Equation 3.1). A Monte Carlo prediction which includes photon absorption,
802 scattering, and reflection is made to estimate the number of photons incident on
803 each PMT and the ratio of the number of predicted to observed hits is calculated.
804 The difference is attributed to the QE efficiency of that PMT. This technique is
805 extended to calculate the relative QE efficiency by normalizing the average of
806 all PMTs which removes the dependence on the light intensity.

807 Due to differing cable lengths and readout electronics, the timing response
808 between a photon hitting the PMT and the signal being captured by the data
809 acquisition can be different between each PMT. Due to threshold triggers (De-
810 scribed in subsection 3.1.3), the time at which a pulse reaches a threshold is
811 dependent upon the size of the pulse. This is known as the ‘time-walk’ effect
812 and also needs to be accounted for in each PMT. To calibrate the timing response,
813 a pulse of light with width 0.2ns is emitted into the detector through a diffuser.
814 Two-dimensional distributions of time and pulse height (or charge) are made
815 for each PMT and are used to calibrate the timing response. This is performed
816 in-situ during data taking with the light source pulsing at 0.03Hz.

817 The top/bottom water quality asymmetry is measured using the NiCf calibra-
818 tion data and cross-referencing these results to the “standard PMTs”. The water
819 attenuation length is continuously measured by the rate of vertically-downgoing
820 cosmic-ray muons which enter via the top of the tank.

821 Dark noise is where a PMT registers a pulse that is consistent with a single
822 photoelectron emitted from photon detection despite the PMT being in complete
823 darkness. This is predominately caused by two processes. Firstly there is
824 intrinsic dark noise which is where photoelectrons gain enough thermal energy
825 to be emitted from the photocathode, and secondly, the radioactive decay of
826 contaminants inside the structure of the PMT. Typical dark noise rate for PMTs
827 used within SK are $O(3)\text{kHz}$ [83]. This is lower than the expected number of

828 photons generated for a ‘high energy event’ (As described in subsection 3.1.4)
829 but instability in this value can cause biases in reconstruction. Dark noise is
830 related to the gain of a PMT and is calibrated using hits inside a time window
831 recorded before an event trigger [92].

832 3.1.3 Data Acquisition and Triggering

833 As the analysis presented in this thesis will only use the SK-IV period of the
834 SK experiment so this subsection focuses on the relevant points of the data
835 acquisition and triggering systems to that SK period. The earlier data acquisition
836 and triggering systems are documented in [93, 94].

837 Before the SK-IV period started, the existing front-end electronics were re-
838 placed with “QTC-Based Electronics with Ethernet, QBEE” systems [95]. When
839 the QBEE observes a signal above a 1/4 photoelectron threshold, the charge-to-
840 time (QTC) converter generates a rectangular pulse. The start of the rectangular
841 pulse indicates the time at which the analog photoelectron signal was received
842 and the width of the pulse indicates the total charge integrated throughout
843 the signal. This is then digitized by time-to-digital converters and sent to the
844 “front-end” PCs.

845 The software trigger (described in [96]) operates by determining the number
846 of PMT hits within a 200ns sliding window, N_{200} . This window coincides with the
847 maximum time that a Cherenkov photon would take to traverse the length of the
848 SK tank [94]. For lower energy events that generate fewer photons, this technique
849 is useful for eliminating background processes like dark noise and radioactive
850 decay which would be expected to be separated in time. When the value of
851 N_{200} exceeds some pre-defined threshold, a software trigger is issued. There are
852 several trigger thresholds used within the SK-IV period which are detailed in
853 Table 3.2. If one of these thresholds is met, the PMT hits within an extended time
854 window are also read out and saved to disk. In the special case of an event that
855 exceeds the SHE trigger but does not exceed the OD trigger, the AFT trigger looks
856 for delayed coincidences of 2.2MeV gamma rays emitted from neutron capture in

857 a $535\mu\text{s}$ window after the SHE trigger. A similar but more complex “Wideband
858 Intelligent Trigger (WIT)” has been deployed and is described in [97].

Trigger	Acronym	Condition	Extended time window (μs)
Super Low Energy	SLE	>34/31 hits	1.3
Low Energy	LE	>47 hits	40
High Energy	HE	>50 hits	40
Super High Energy	SHE	>70/58 hits	40
Outer Detector	OD	>22 hits in OD	N/A

Table 3.2: The trigger thresholds and extended time windows saved around an event which were utilised throughout the SK-IV period. The exact thresholds can change and the values listed here represent the thresholds at the start and end of the SK-IV period.

3.1.4 Cherenkov Radiation

860 Cherenkov light is emitted from any highly energetic charged particle traveling
861 with relativistic velocity, β , greater than the local speed of light in a medium [98].
862 Cherenkov light is formed at the surface of a cone with a characteristic pitch angle,

$$\cos(\theta) = \frac{1}{\beta n}. \quad (3.2)$$

863 Where n is the refractive index of the medium. Consequently, the Cherenkov
864 momentum threshold, P_{thres} , is dependent upon the mass, m , of the charged
865 particle moving through the medium,

$$P_{\text{thres}} = \frac{m}{\sqrt{n^2 - 1}}. \quad (3.3)$$

866 For water, where $n = 1.33$, the Cherenkov threshold momentum and energy
867 for various particles are given in Table 3.3. In contrast, γ -rays are detected
868 indirectly via the combination of photons generated by Compton scattering
869 and pair production. The threshold for detection in the SK detector is typically
870 higher than the threshold for photon production. This is due to the fact that the
871 attenuation of photons in the water means that typically $\sim 75\%$ of Cherenkov
872 photons reach the ID PMTs. Then the collection and quantum efficiencies

873 described in subsection 3.1.1 result in the number of detected photons being
874 lower than the number of photons which reach the PMTs.

Particle	Threshold Momentum (MeV)	Threshold Energy (MeV)
Electron	0.5828	0.7751
Muon	120.5	160.3
Pion	159.2	211.7
Proton	1070.0	1423.1

Table 3.3: The threshold momentum and total energy for a particle to generate Cherenkov light in ultrapure water, as calculated in Equation 3.2 in ultrapure water which has refractive index $n = 1.33$.

875 The Frank-Tamm equation [99] describes the relationship between the number
876 of Cherenkov photons generated per unit length, dN/dx , the wavelength of the
877 photons generated, λ , and the relativistic velocity of the charged particle,

$$\frac{d^2N}{dx d\lambda} = 2\pi\alpha \left(1 - \frac{1}{n^2\beta^2}\right) \frac{1}{\lambda^2}. \quad (3.4)$$

878 Where α is the fine structure constant. For a 100MeV momentum electron,
879 approximately 330 photons will be produced per centimeter in the $300\text{nm} \leq \lambda \leq$
880 700nm region which the ID PMTs are most sensitive to [83].

881 3.2 The Tokai to Kamioka Experiment

882 The Tokai-to-Kamioka (T2K) experiment is a long-baseline neutrino oscillation
883 experiment located in Japan. Proposed in the early 2000s [84, 100] to replace
884 K2K [101], T2K was designed to observe electron neutrino appearance whilst
885 precisely measuring the oscillation parameters associated with muon neutrino
886 disappearance [102]. The experiment consists of a neutrino beam generated
887 at the Japan Proton Accelerator Research Complex (J-PARC), a suite of near
888 detectors situated 280m from the beam target, and the Super Kamiokande far
889 detector positioned at a 295km baseline. The cross-section view of the T2K
890 experiment is drawn in Figure 3.3.

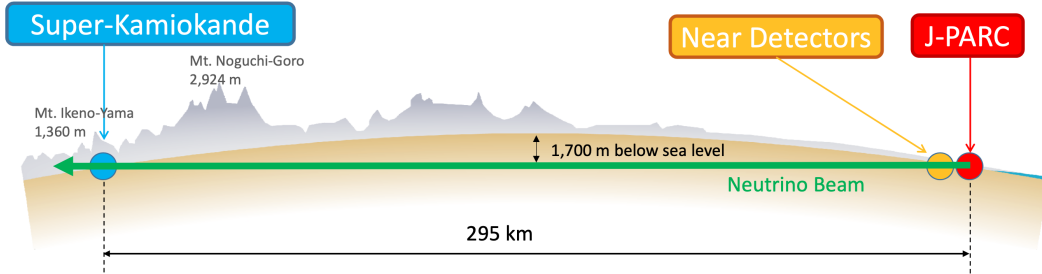


Figure 3.3: The cross-section view of the Tokai to Kamioka experiment illustrating the beam generation facility at J-PARC, the near detector situated at a baseline of 280m and the Super Kamiokande far detector situated 295km from the beam target.

891 The T2K collaboration makes world-leading measurements of the $\sin^2(\theta_{23})$,
 892 Δm_{32}^2 , and δ_{CP} oscillation parameters. Improvements in the precision and accu-
 893 racy of parameter estimates are still being made by including new data samples
 894 and developing the models which describe the neutrino interactions and detector
 895 responses [4]. Electron neutrino appearance was first observed at T2K in 2014
 896 [103] with 7.3σ significance.

897 The near detectors provide constraints on the beam flux and cross-section
 898 model parameters used within the oscillation analysis by observing the unoscil-
 899 lated neutrino beam. There are a host of detectors situated in the near detector hall
 900 (as illustrated in Figure 3.4): ND280 (subsection 3.2.3), INGRID (subsection 3.2.4),
 901 NINJA [104], WAGASCI [105], and Baby-MIND [106]. The latter three are not
 902 currently used within the oscillation analysis presented in this thesis.

903 Whilst this thesis presents the ND280 in terms of its purpose for the oscillation
 904 analysis, the detector can also make many cross-section measurements at neutrino
 905 energies of $O(1)\text{GeV}$ for the different targets within the detector [107, 108]. These
 906 measurements are of equal importance as they can lead the way in determining
 907 the model parameters used in the interaction models for the future high-precision
 908 era of neutrino physics.

909 3.2.1 Analysis Overview

910 There are two independent fitters, MaCh3 and BANFF, which perform the near
 911 detector fit. MaCh3 uses a bayesian Markov Chain Monte Carlo fitting technique,

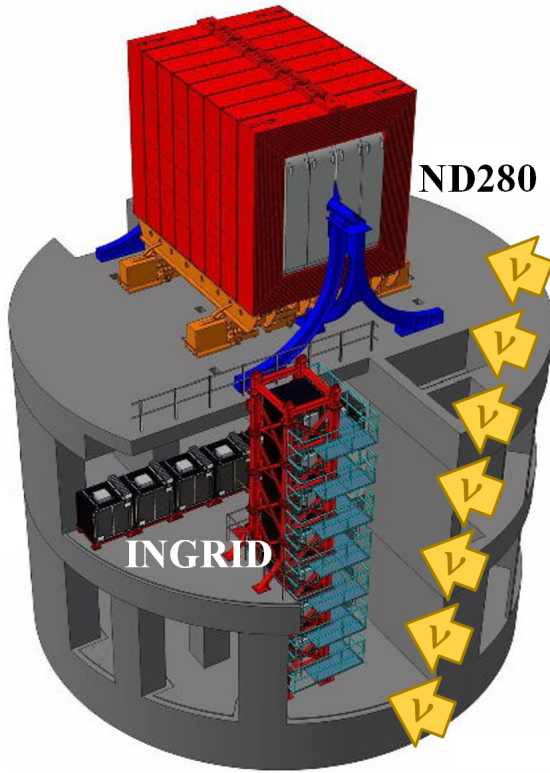


Figure 3.4: The near detector suite for the T2K experiment showing the ND280 and INGRID detectors. The distance between the detectors and the beam target is 280m.

912 whereas BANFF uses a frequentist gradient descent technique. The output of
 913 each fitter is compared as a method of cross-checking the behaviour of the two
 914 fitters. This is done by comparing: the Monte Carlo predictions using various
 915 tunes, the likelihood that is calculated in each fitter, and the post-fit constraint
 916 associated with every parameter used in the fit. Once validated, the output is
 917 converted into a covariance matrix to describe the error and correlations between
 918 all the flux and cross-section parameters. This is then propagated to the far-
 919 detector oscillation analysis group.

920 The far detector group has three independent fitters: P-Theta, VALOR and
 921 MaCh3. The first two fitters use a hybrid frequentist fitting technique where the
 922 likelihood is minimised with respect to the parameters of interest and marginalised
 923 over all other parameters. These fitters use the covariance provided by the near
 924 detector fitters as a basis for implementing the near detector constraints. The
 925 MaCh3 fitter uses a simultaneous fit of all near and far detector samples. This

removes any Gaussian assumptions when making the covariance matrix from the near detector results. The results for all three fitters are compared using a technique similar to the validation of the near detector fitters.

There are three particular tunes of the T2K flux and cross section model typically considered. Firstly, the “generated” tune which is the set of dial values with which the Monte Carlo was generated. Secondly, the set of dial values which are taken from external data measurements and used as inputs. These are the “pre-fit” dial values. The reason these two sets of dial values are different is that the external data measurements are continually updated but it is very computationally intensive to regenerate a Monte Carlo prediction after each update. The final tune is the “post-fit”, “post-ND fit” or “post-BANFF” dial values. These are the values taken from the constraints provided by the near detector.

3.2.2 The Neutrino Beam

The neutrino beam used within the T2K experiment is described in [38, 42] and summarised below. The accelerator facility at J-PARC is composed of two sections; the primary and secondary beamlines. Figure 3.5 illustrates a schematic of the beamline, focusing mostly on the components of the secondary beamline. The primary beamline has three accelerators that progressively accelerate protons; a linear accelerator, a rapid-cycling synchrotron, and the main-ring (MR) synchrotron. Once fully accelerated by the MR, the protons have a kinetic energy of 30GeV. Eight bunches of these protons, separated by 500ns, are extracted per “spill” from the MR and directed towards a graphite target (a rod of length 91.4cm and diameter 2.6cm). Spills are extracted at 0.5Hz with $\sim 3 \times 10^{14}$ protons contained per spill.

The secondary beamline consists of three main components: the target station, the decay volume, and the beam dump. The target station is comprised of the target, beam monitors, and three magnetic focusing horns. The proton beam interacts with the graphite target to form a secondary beam of mostly pions

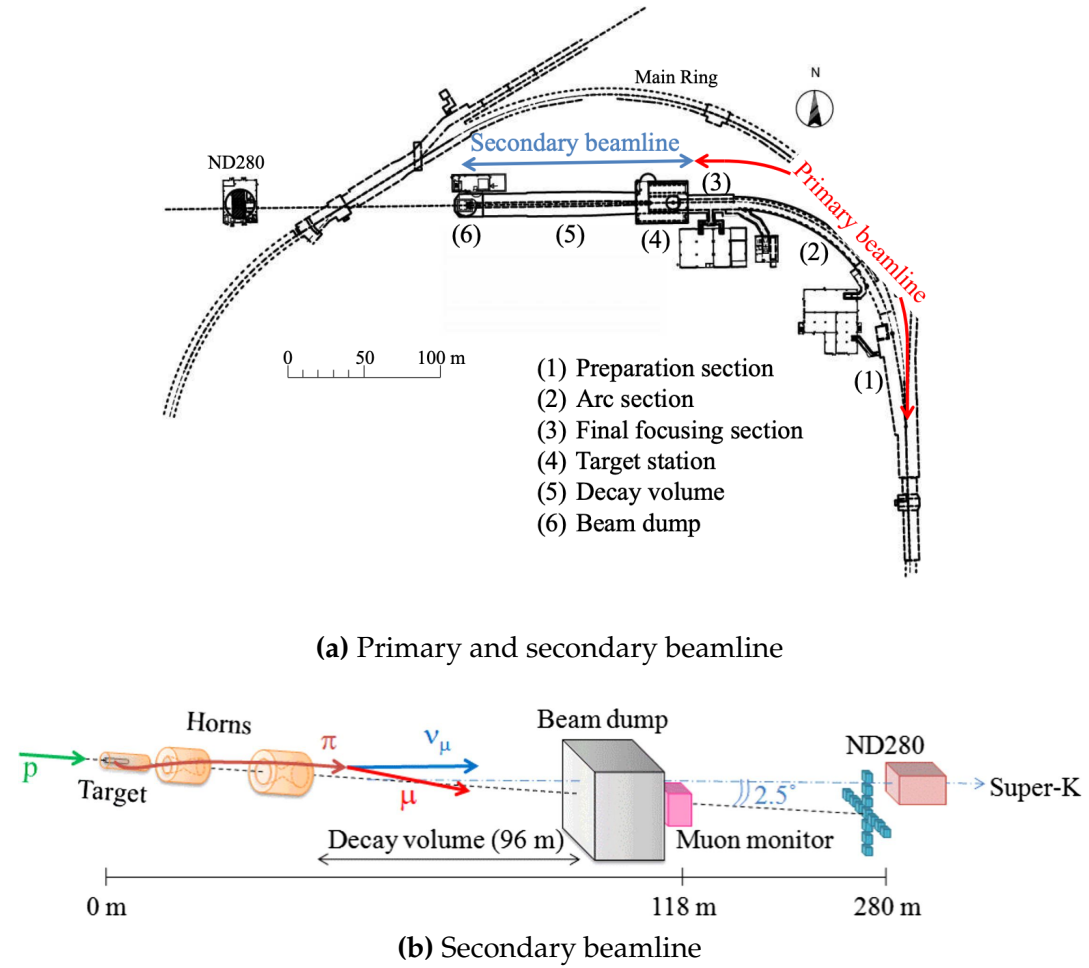


Figure 3.5: Top panel: Bird's eye view of the most relevant part of primary and secondary beamline used within the T2K experiment. The primary beamline is the main-ring proton synchrotron, kicker magnet, and graphite target. The secondary beamline consists of the three focusing horns, decay volume, and beam dump. Figure taken from [42]. Bottom panel: The side-view of the secondary beamline including the focusing horns, beam dump and neutrino detectors. Figure taken from [109].

and kaons. The secondary beam travels through a 96m long decay volume, generating neutrinos through the following decays [38],

$$\begin{aligned}
 \pi^+ &\rightarrow \mu^+ + \nu_\mu & \pi^- &\rightarrow \mu^- + \bar{\nu}_\mu \\
 K^+ &\rightarrow \mu^+ + \nu_\mu & K^- &\rightarrow \mu^- + \bar{\nu}_\mu \\
 &\rightarrow \pi^0 + e^+ + \nu_e & &\rightarrow \pi^0 + e^- + \bar{\nu}_e \\
 &\rightarrow \pi^0 + \mu^+ + \nu_\mu & &\rightarrow \pi^0 + \mu^- + \bar{\nu}_\mu \\
 K_L^0 &\rightarrow \pi^- + e^+ + \nu_e & K_L^0 &\rightarrow \pi^+ + e^- + \bar{\nu}_e \\
 &\rightarrow \pi^- + \mu^+ + \nu_\mu & &\rightarrow \pi^+ + \mu^- + \bar{\nu}_\mu \\
 \mu^+ &\rightarrow e^+ + \bar{\nu}_\mu + \nu_e & \mu^- &\rightarrow e^- + \nu_\mu + \bar{\nu}_e.
 \end{aligned}$$

The electrically charged component of the secondary beam is focused towards the far detector by the three magnetic horns. These horns direct charged particles of a particular polarity towards SK whilst defocusing the oppositely charged particles. This allows a mostly neutrino or mostly antineutrino beam to be used within the experiment, denoted as “forward horn current (FHC)” or “reverse horn current (RHC)” respectively.

Figure 3.6 illustrates the different contributions to the FHC and RHC neutrino flux. The low energy flux is dominated by the decay of pions whereas kaon decay becomes the dominant source of neutrinos for $E_\nu > 3\text{GeV}$. The “wrong-sign” component, which is the $\bar{\nu}_\mu$ background in a ν_μ beam, and the intrinsic irreducible ν_e background, are predominantly due to muon decay for $E_\nu < 2\text{GeV}$. As the antineutrino production cross-section is smaller than the neutrino cross-section, the wrong-sign component is more dominant in the RHC beam as compared to that in the FHC beam.

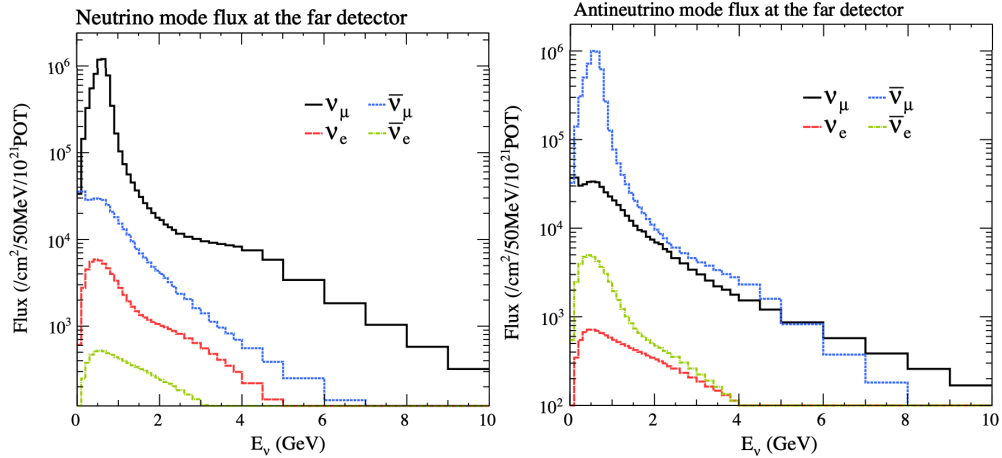


Figure 3.6: The Monte Carlo prediction of the energy spectrum for each flavour of neutrino (ν_e , $\bar{\nu}_e$, ν_μ and $\bar{\nu}_\mu$) in the neutrino dominated beam FHC mode (Left) and antineutrino dominated beam RHC mode (Right) expected at SK. Taken from [78].

The beam dump, situated at the end of the decay volume, stops all charged particles other than highly energetic muons ($p_\mu > 5\text{GeV}$). The MuMon detector monitors the penetrating muons to determine the beam direction and intensity which is used to constrain some of the beam flux systematics within the analysis [109, 110].

977 The T2K experiment uses an off-axis beam to narrow the neutrino energy
 978 distribution. This was the first implementation of this technique in a long-
 979 baseline neutrino oscillation experiment after its original proposal [111]. Pion
 980 decay, $\pi \rightarrow \mu + \nu_\mu$, is a two-body decay. Consequently, the neutrino energy,
 981 E_ν , can be determined based on the pion energy, E_π , and the angle at which
 982 the neutrino is emitted, θ ,

$$E_\nu = \frac{m_\pi^2 - m_\mu^2}{2(E_\pi - p_\pi \cos(\theta))}, \quad (3.5)$$

983 where m_π and m_μ are the mass of the pion and muon respectively. For a fixed
 984 energy pion, the neutrino energy distribution is dependent upon the angle at
 985 which the neutrinos are observed from the initial pion beam direction. For the
 986 295km baseline at T2K, $E_\nu = 0.6\text{GeV}$ maximises the electron neutrino appearance
 987 probability, $P(\nu_\mu \rightarrow \nu_e)$, whilst minimising the muon disappearance probability,
 988 $P(\nu_\mu \rightarrow \nu_\mu)$. Figure 3.7 illustrates the neutrino energy distribution for a range of
 989 off-axis angles, as well as the oscillation probabilities most relevant to T2K.

990 3.2.3 The Near Detector at 280m

991 Whilst all the near detectors are situated in the same “pit” located 280m from
 992 the beam target, the “ND280” detector is the off-axis detector which is situated
 993 at the same off-axis angle as the Super-Kamiokande far detector. It has two
 994 primary functions; firstly it measures the neutrino flux and secondly, it counts the
 995 event rates of different types of neutrino interactions. Both of these constrain the
 996 flux and cross-section systematics invoked within the model for a more accurate
 997 prediction of the expected event rate at the far detector.

998 As illustrated in Figure 3.8, the ND280 detector consists of several sub-
 999 detectors. The most important part of the detector for this analysis is the tracker
 1000 region. This is comprised of two-time projection chambers (TPCs) sandwiched
 1001 between three fine grain detectors (FGDs). The FGDs contain both hydrocarbon
 1002 plastic and water targets for neutrino interactions and provide track recon-
 1003 struction near the interaction vertex. The emitted charged particles can then

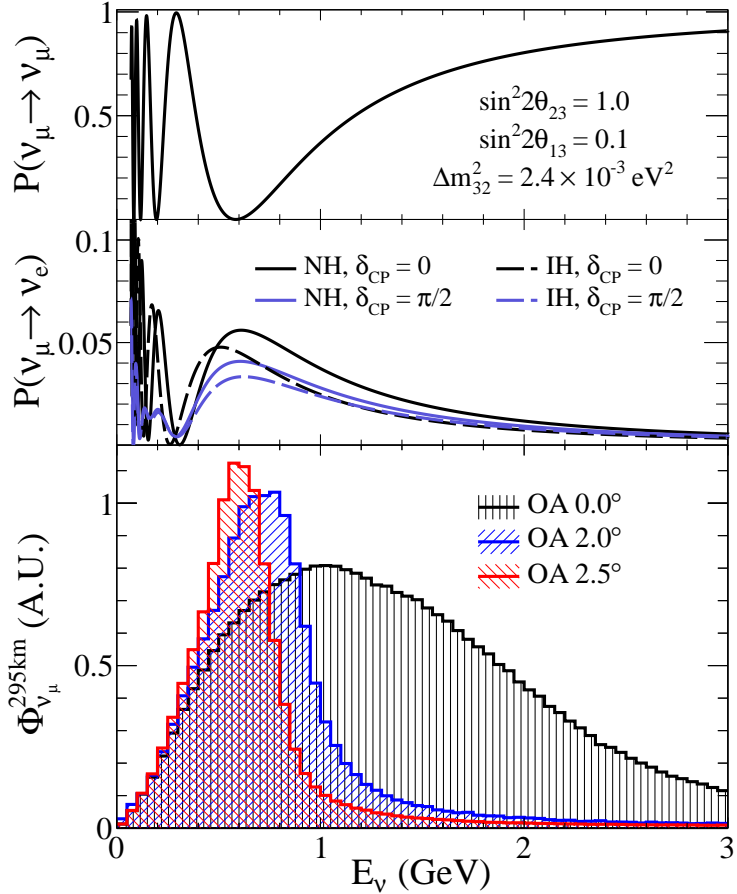


Figure 3.7: Top panel: T2K muon neutrino disappearance probability as a function of neutrino energy. Middle panel: T2K electron neutrino appearance probability as a function of neutrino energy. Bottom panel: The neutrino flux distribution for three different off-axis angles (Arbitrary units) as a function of neutrino energy.

1004 propagate into the TPCs which provide particle identification and momentum
 1005 reconstruction. The FGDs and TPCs are further described in subsubsection 3.2.3.1
 1006 and subsubsection 3.2.3.2, respectively. The electromagnetic calorimeter (ECAL)
 1007 encapsulates the tracker region alongside the π^0 detector (P0D). The ECAL
 1008 measures the deposited energy from photons emitted from interactions within
 1009 the FGD. The P0D constrains the cross-section of neutral current interactions
 1010 which generate neutral pions, which is one of the largest backgrounds in the
 1011 electron neutrino appearance oscillation channel. The P0D and ECAL detectors
 1012 are detailed in subsubsection 3.2.3.3 and subsubsection 3.2.3.4, respectively.
 1013 The entire detector is located within a large yoke magnet which produces a
 1014 0.2T magnetic field. This design of the magnet also includes a scintillating

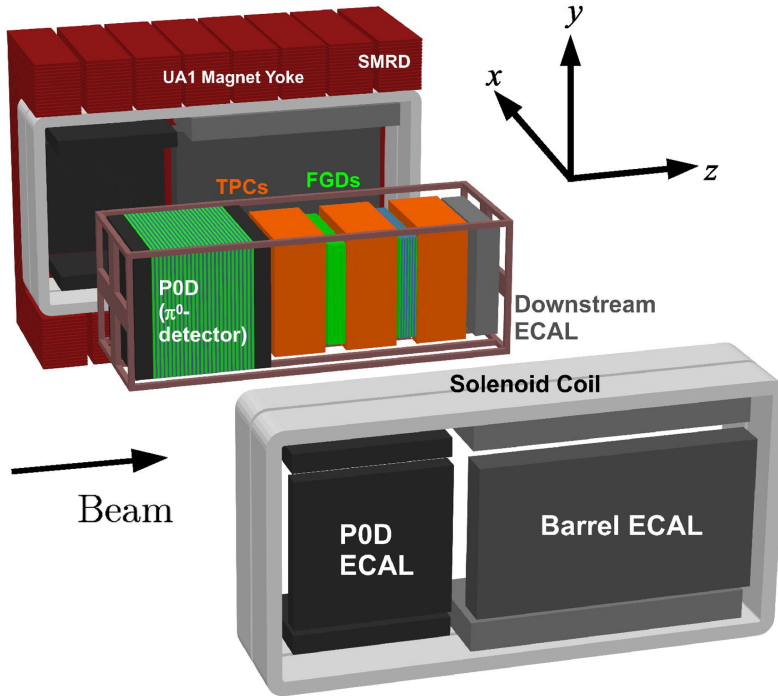


Figure 3.8: The components of the ND280 detector. The neutrino beam travels from left to right. Taken from [42].

1015 detector called the side muon range detector (SMRD), which is used to track
 1016 high-angle muons as well as acting as a cosmic veto. The SMRD is described
 1017 in subsubsection 3.2.3.5.

1018 3.2.3.1 Fine Grained Detectors

1019 The T2K tracker region is comprised of two fine-grained detectors (FGD) and
 1020 three Time Projection Chambers (TPC). A detailed description of the FGD design,
 1021 construction, and assembly is found in [112] and summarised below. The FGDs
 1022 are the primary target for neutrino interactions with a mass of 1.1 tonnes per
 1023 FGD. Alongside this, the FGDs are designed to be able to track short-range
 1024 particles which do not exit the sub-detector. Typically, short-range particles are
 1025 low momentum and are observed as tracks that deposit a large amount of energy
 1026 per unit length. This means the FGD needs good granularity to resolve these
 1027 particles. The FGDs have the best timing resolution ($\sim 3\text{ns}$) of any of the sub-
 1028 detectors of the ND280 detector. As such, the FGDs are used for time of flight
 1029 measurements to distinguish forward-going positively charged particles from

1030 backward-going negatively charged particles. Finally, any tracks which pass
1031 through multiple sub-detectors are required to be track matched to the FGD.

1032 Both FGDs are made from square scintillator planes of side length 186cm and
1033 width 2.02cm. Each plane consists of two layers of 192 scintillator bars in an
1034 X or Y orientation. A wavelength-shifting fiber is threaded through the center
1035 of each bar and is read out by a multi-pixel photon counter (MPPC). FGD1 is
1036 the most upstream of the two FGDs and contains 15 planes of carbon plastic
1037 scintillator which is a common target in external neutrino scattering data. As
1038 the far detector is a pure water target, 7 of the 15 scintillator planes in FGD2
1039 have been replaced with a hybrid water-scintillator target. Due to the complexity
1040 of the nucleus, nuclear effects can not be extrapolated between different nuclei.
1041 Therefore having the ability to take data on one target which is the same as
1042 external data and another target which is the same as the far detector target is
1043 beneficial for reliable model parameter estimates.

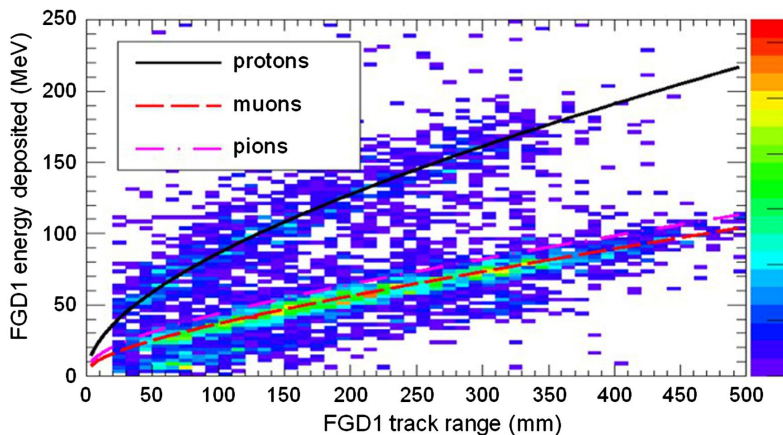


Figure 3.9: Comparison of data to Monte Carlo prediction of integrated deposited energy as a function of track length for particles that stopped in FGD1. Taken from [112].

1044 The integrated deposited energy is used for particle identification in the FGD.
1045 The sub-detector can distinguish protons from other charged particles by com-
1046 paring this quantity from data to Monte Carlo prediction, as seen in Figure 3.9.

1047 3.2.3.2 Time Projection Chambers

1048 The majority of particle identification and momentum measurements within
 1049 ND280 are provided by three Time Projection Chambers (TPCs) [113]. The TPCs
 1050 are located on either side of the FGDs. They are located inside the magnetic
 1051 field meaning the momentum of a charged particle can be determined from
 1052 the bending of the track.

1053 Each TPC module consists of two gas-tight boxes, as shown in Figure 3.10,
 1054 which are made of non-magnetic material. The outer box is filled with CO₂
 1055 which acts as an electrical insulator between the inner box and the ground. The
 1056 inner box forms the field cage which produces a uniform electric drift field of
 1057 $\sim 275\text{V/cm}$ and is filled with an argon gas mixture. Charged particles moving
 1058 through this gas mixture ionize the gas and the subsequent charge is drifted
 1059 towards micromegas detectors. The time and position information in the readout
 1060 allows a three-dimensional image of the neutrino interaction.

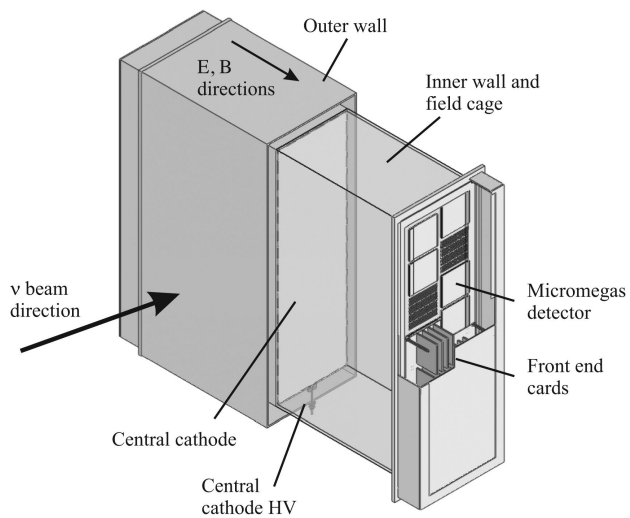


Figure 3.10: Schematic design of a Time Projection Chamber detector. Taken from [113].

1061 The particle identification of tracks that pass through the TPCs is performed
 1062 using dE/dx measurements. Figure 3.11 illustrates the data to Monte Carlo
 1063 distributions of the energy lost by a charged particle passing through the TPC as
 1064 a function of the reconstructed particle momentum. The resolution is $7.8 \pm 0.2\%$

1065 meaning that electrons and muons can be distinguished. This allows reliable
 1066 measurements of the intrinsic ν_e component of the beam.

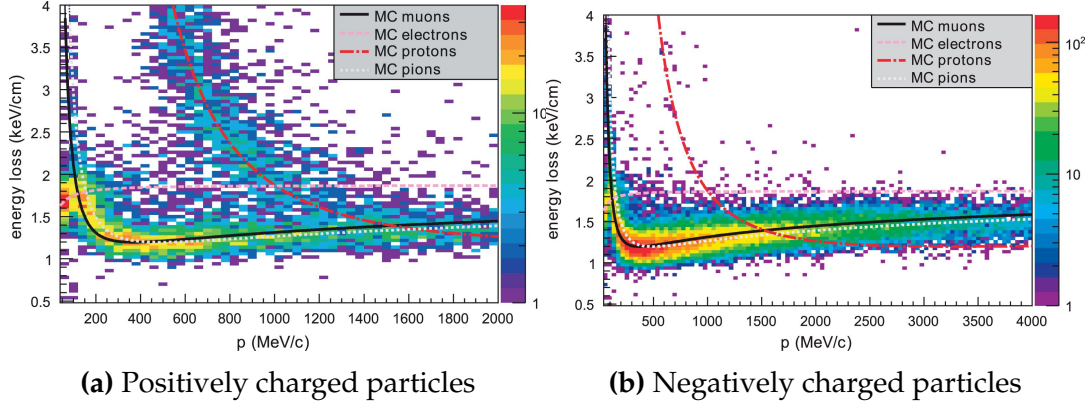


Figure 3.11: The distribution of energy loss as a function of reconstructed momentum for charged particles passing through the TPC, comparing data to Monte Carlo prediction. Taken from [113].

1067 3.2.3.3 π^0 Detector

1068 If one of the γ -rays from a $\pi^0 \rightarrow 2\gamma$ decay is missed at the far detector, the
 1069 reconstruction algorithm could determine that event to be a charge current ν_e -like
 1070 event. This is one of the main backgrounds hindering the electron neutrino
 1071 appearance searches. The π^0 detector (P0D) measures the cross-section of the
 1072 neutral current induced neutral pion production on a water target to constrain
 1073 this background.

1074 The P0D is a cube of approximately 2.5m length consisting of layers of scin-
 1075 tillating bars, brass and lead sheets, and water bags as illustrated in Figure 3.12.
 1076 Two electromagnetic calorimeters are positioned at the most upstream and most
 1077 downstream position in the sub-detector and the water target is situated between
 1078 them. The scintillator layers are built from two triangular bars orientated in
 1079 opposite directions to form a rectangular layer. Each triangular scintillator bar is
 1080 threaded with optical fiber which is read out by MPPCs. The high-Z brass and
 1081 lead regions produce electron showers from the photons emitted in π^0 decay.

1082 The sub-detector can generate measurements of NC1 π^0 cross-sections on a
 1083 water target by measuring the event rate both with and without the water target,

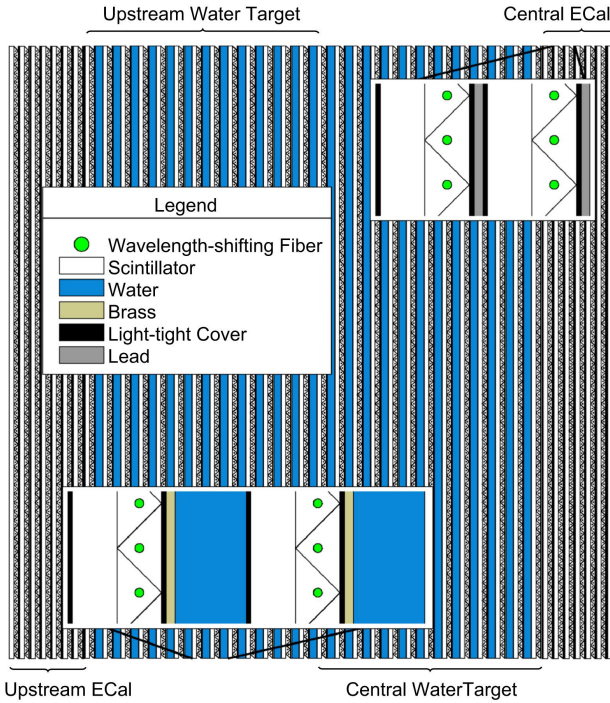


Figure 3.12: A schematic of the P0D side-view. Taken from [114].

1084 with the cross-section on a water target being determined as the difference. The to-
 1085 tal active mass is 16.1 tonnes when filled with water and 13.3 tonnes when empty.

1086 3.2.3.4 Electromagnetic Calorimeter

1087 The electromagnetic calorimeter [115] (ECal) encapsulates the P0D and tracking
 1088 sub-detectors. Its primary purpose is to aid π^0 reconstruction from any interac-
 1089 tion in the tracker. To do this, it measures the energy and direction of photon
 1090 showers from $\pi^0 \rightarrow 2\gamma$ decays. It can also distinguish pion and muon tracks
 1091 depending on the shape of the photon shower deposited.

1092 The ECal is comprised of three sections; the P0D ECal which surrounds the
 1093 P0D, the barrel ECal which encompasses the tracking region, and the downstream
 1094 ECal which is situated downstream of the tracker region. The barrel and down-
 1095 stream ECals are tracking calorimeters that focus on electromagnetic showers
 1096 from high-angle particles emitted from the tracking sub-detectors. Particularly in
 1097 the TPC, high-angle tracks (those which travel perpendicularly to the beam-axis)
 1098 can travel along a single scintillator bar resulting in very few hits. The width of

1099 the barrel and downstream ECal corresponds to ~ 11 electron radiation lengths
1100 to ensure a significant amount of the π^0 energy is contained. As the P0D has
1101 its own calorimetry which reconstructs showers, the P0D ECal determines the
1102 energy which escapes the P0D.

1103 Each ECal is constructed of multiple layers of scintillating bars sandwiched
1104 between lead sheets. The scintillating bars are threaded with optical fiber and read
1105 out by MPPCs. Each sequential layer of the scintillator is orientated perpendicular
1106 to the previous which allows a three-dimensional event reconstruction. The
1107 target mass of the P0D ECal, barrel ECal, and downstream ECal are 1.50, 4.80,
1108 and 6.62 tonnes respectively.

1109 3.2.3.5 Side Muon Range Detector

1110 As illustrated in Figure 3.8, the ECal, FGDs, P0D, and TPCs are enclosed within
1111 the UA1 magnet. Reconditioned after use in the UA1 [116] and NOMAD [117]
1112 experiments, this magnet provides a uniform horizontal magnetic field of 0.2T
1113 with an uncertainty of 2×10^{-4} T.

1114 Built into the UA1 magnet, the side muon range detector (SMRD)[118] moni-
1115 tors high-energy muons which leave the tracking region and permeate through
1116 the ECal. It additionally acts as a cosmic muon veto and trigger.

1117 3.2.4 The Interactive Neutrino GRID

1118 The Interactive Neutrino GRID (INGRID) detector is situated within the same
1119 “pit” as the other near detectors. It is aligned with the beam in the “on-axis”
1120 position and measures the beam direction, spread, and intensity. The detector
1121 was originally designed with 16 identical modules [42] (two modules have since
1122 been decommissioned) and a “proton” module. The design of the detector is 14
1123 modules oriented in a cross with length and height $10\text{m} \times 10\text{m}$, as illustrated
1124 in Figure 3.13.

1125 Each module is composed of iron sheets interlaced with eleven tracking
 1126 scintillator planes for a total target mass of 7.1 tonnes per module. The scin-
 1127 tillator design is an X-Y pattern of 24 bars in both orientations, where each
 1128 bar contains wave-length shifting fibers which are connected to MPPCs. Each
 1129 module is encapsulated inside veto planes to aid the rejection of charged particles
 1130 entering the module.

1131 The proton module is different from the other modules in that it consists
 1132 of entirely scintillator planes with no iron target. The scintillator bars are also
 1133 smaller than those used in the other modules to increase the granularity of
 1134 the detector and improve tracking capabilities. The module sits in the center
 1135 of the beamline and is designed to give precise measurements of quasi-elastic
 1136 charged current interactions to evaluate the performance of the Monte Carlo
 1137 simulation of the beamline.

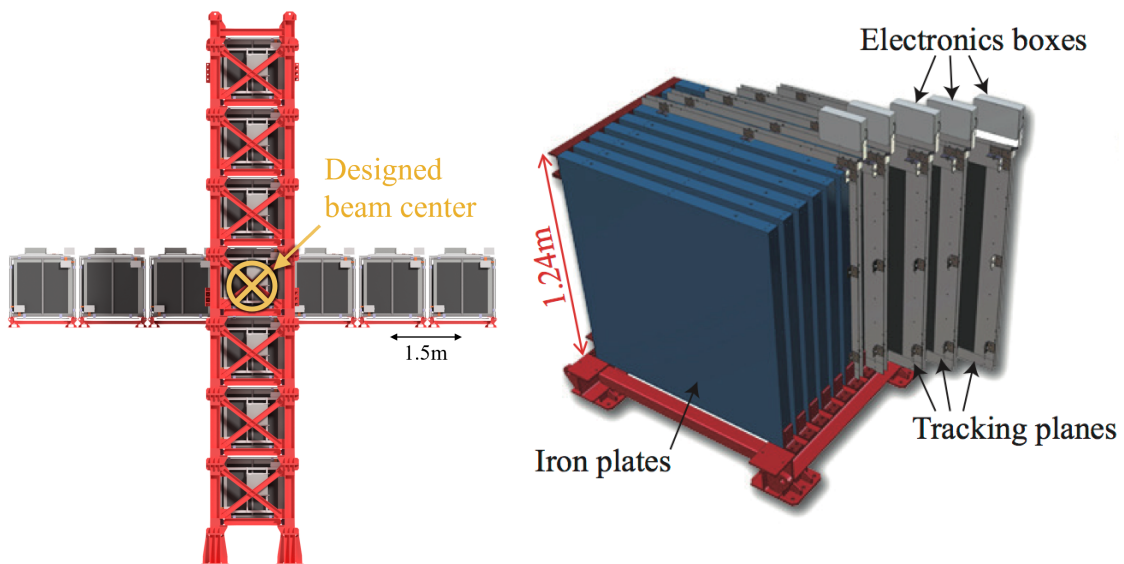


Figure 3.13: Left panel: The Interactive Neutrino GRID on-axis Detector. 14 modules are arranged in a cross-shape configuration, with the center modules being directly aligned with the on-axis beam. Right panel: The layout of a single module of the INGRID detector. Both figures are recreated from [42].

1138 The INGRID detector can measure the beam direction to an uncertainty of
 1139 0.4mrad and the beam centre within a resolution of 10cm [42]. The beam direction
 1140 in both the vertical and horizontal directions is discussed in [119] and it is found
 1141 to be in good agreement with the MUMON monitor described in subsection 3.2.2.

4

1142

1143

1144

Bayesian Statistics and Markov Chain Monte Carlo Techniques

1145 This thesis presents a Bayesian oscillation analysis. To extract the oscillation
1146 parameters, a Markov Chain Monte Carlo (MCMC) method is used. This chapter
1147 explains the theory of how parameter estimates can be determined using this
1148 technique and condenses the material found in the literature [120–123].

1149 The oscillation parameter determination presented here is built upon a simultaneous
1150 fit to neutrino beam samples in the near detector, beam samples at SK,
1151 and atmospheric samples at SK. In total, there are four oscillation parameters of
1152 interest ($\sin^2(\theta_{23})$, $\sin^2(\theta_{13})$, Δm_{32}^2 , and δ_{CP}), two oscillation parameters to which
1153 this study will not be sensitive ($\sin^2(\theta_{12})$, Δm_{21}^2) and many nuisance parameters
1154 that control the systematic uncertainty models.

1155 This analysis uses a Monte Carlo technique to generate a multi-dimensional
1156 probability distribution across all of the model parameters used in the fit. To
1157 determine an estimate for each parameter, this multi-dimensional object is in-
1158 tegrated over all other parameters. This process is called Marginalisation and
1159 is described in subsection 4.3.1. Monte Carlo techniques approximate the prob-
1160 ability distribution of each parameter within the limit of generating infinite
1161 samples. As ever, generating a large number of samples is time and resource-

1162 dependent. Therefore, an MCMC technique is utilised within this analysis to
1163 reduce the required number of steps to sufficiently sample the parameter space.
1164 This technique is described in further detail in subsection 4.2.1.

1165 The Bayesian analysis techniques used within this thesis are built within the
1166 MaCh3 framework [124]. This uses a custom MCMC library package exclusively
1167 supported and developed by the MaCh3 collaborators (which includes the author
1168 of this thesis).

1169 4.1 Bayesian Statistics

1170 Bayesian inference treats observable data, D , and model parameters, $\vec{\theta}$, on equal
1171 footing such that a probability model of both data and parameters is required.
1172 This is the joint probability distribution $P(D, \vec{\theta})$ and can be described by the
1173 prior distribution for model parameters $P(\vec{\theta})$ and the likelihood of the data given
1174 the model parameters $P(D|\vec{\theta})$,

$$P(D, \vec{\theta}) = P(D|\vec{\theta})P(\vec{\theta}). \quad (4.1)$$

1175 The prior distribution, $P(\vec{\theta})$, describes all previous knowledge about the
1176 parameters within the model. For example, if the risk of developing health
1177 problems is known to increase with age, the prior distribution would describe the
1178 increase. For the purpose of this analysis, the prior distribution is typically
1179 the best-fit values taken from external data measurements with a Gaussian
1180 uncertainty. The prior distribution can also contain correlations between model
1181 parameters. In an analysis using Monte Carlo techniques, the likelihood of
1182 measuring some data assuming some set of model parameters is calculated
1183 by comparing the Monte Carlo prediction generated at that particular set of
1184 model parameters to the data.

1185 It is parameter estimation that is important for this analysis and as such, Bayes'
1186 theorem [125] is applied to calculate the probability for each parameter to have a

₁₁₈₇ certain value given the observed data, $P(\vec{\theta}|D)$, which is known as the posterior
₁₁₈₈ distribution (often termed the posterior). This can be expressed as

$$P(\vec{\theta}|D) = \frac{P(D|\vec{\theta})P(\vec{\theta})}{\int P(D|\vec{\theta})P(\vec{\theta})d\vec{\theta}}. \quad (4.2)$$

₁₁₈₉ The denominator in Equation 4.2 is the integral of the joint probability distri-
₁₁₉₀ bution over all values of all parameters used within the fit. For brevity, the
₁₁₉₁ posterior distribution is

$$P(\vec{\theta}|D) \propto P(D|\vec{\theta})P(\vec{\theta}). \quad (4.3)$$

₁₁₉₂ For the purposes of this analysis, it is acceptable to neglect the normalisation
₁₁₉₃ term and focus on this proportional relationship.

₁₁₉₄ 4.1.1 Application of Prior Knowledge

₁₁₉₅ The posterior distribution is proportional to the prior uncertainty applied to
₁₁₉₆ each parameter, as illustrated by Equation 4.3. This means that it is possible
₁₁₉₇ to change the prior after the posterior distribution has been determined. The
₁₁₉₈ prior uncertainty of a particular parameter can be ‘divided’ out of the posterior
₁₁₉₉ distribution and the resulting distribution can be reweighted using the new
₁₂₀₀ prior uncertainty that is to be applied. The methodology and implementation
₁₂₀₁ of changing the prior follows that described in [126].

₁₂₀₂ An example implementation that is useful for this analysis is the application
₁₂₀₃ of the “reactor constraint”. As discussed in section 2.4, an external constraint
₁₂₀₄ on $\sin^2(\theta_{13})$ is determined from measurements taken from reactor experiments.
₁₂₀₅ However, the sensitivities from just using the T2K and SK samples is equally
₁₂₀₆ as important. Without this technique, two fits would have to be run, doubling
₁₂₀₇ the required resources. Therefore, the key benefit for this analysis is the fact
₁₂₀₈ that only a single ‘fit’ has to be performed to provide the results both with and
₁₂₀₉ without the reactor constraint applied.

1210 4.2 Monte Carlo Simulation

1211 Monte Carlo techniques are used to numerically solve a complex problem that
1212 does not necessarily have an analytical solution. These techniques rely on
1213 building a large ensemble of samples from an unknown distribution and then
1214 using the ensemble to approximate the properties of the distribution.

1215 An example that uses Monte Carlo techniques is to calculate the area under-
1216 neath a curve. For example, take the problem of calculating the area under a
1217 straight line with gradient $M = 0.4$ and intercept $C = 1.0$. Analytically, one can
1218 calculate the area under the line is equal to 30 units for $0 \leq x \leq 10$. Using Monte
1219 Carlo techniques, one can calculate the area under this line by throwing many
1220 random values for the x and y components of each sample and then calculating
1221 whether that point falls below the line. The area can then be calculated by the
1222 ratio of points below the line to the total number of samples thrown multiplied by
1223 the total area in which samples were scattered. The study is shown in Figure 4.1
1224 highlights this technique and finds the area under the curve to be 29.9 compared
1225 to an analytical solution of 30.0. The deviation of the numerical to analytical
1226 solution can be attributed to the number of samples used in the study. The
1227 accuracy of the approximation in which the properties of the Monte Carlo samples
1228 replicate those of the desired distribution is dependent on the number of samples
1229 used. Replicating this study with a differing number of Monte Carlo samples
1230 used in each study (As shown in Figure 4.2) highlights how the Monte Carlo
1231 techniques are only accurate within the limit of a high number of samples.

1232 Whilst the above example has an analytical solution, these techniques are just
1233 as applicable to complex solutions. Clearly, any numerical solution is only as
1234 useful as its efficiency. As discussed, the accuracy of the Monte Carlo technique is
1235 dependent upon the number of samples generated to approximate the properties
1236 of the distribution. Furthermore, if the positions at which the samples are
1237 evaluated are not ‘cleverly’ picked, the efficiency of the Monte Carlo technique
1238 significantly drops. Given the example in Figure 4.1, if the region in which the

1239 samples are scattered significantly extends passed the region of interest, many
1240 calculations will be calculated but do not add to the ability of the Monte Carlo
1241 technique to achieve the correct result. For instance, any sample evaluated at
1242 $y \geq 5$ could be removed without affecting the final result. This does bring in
1243 an aspect of the ‘chicken and egg’ problem in that to achieve efficient sampling,
1244 one needs to know the distribution beforehand.

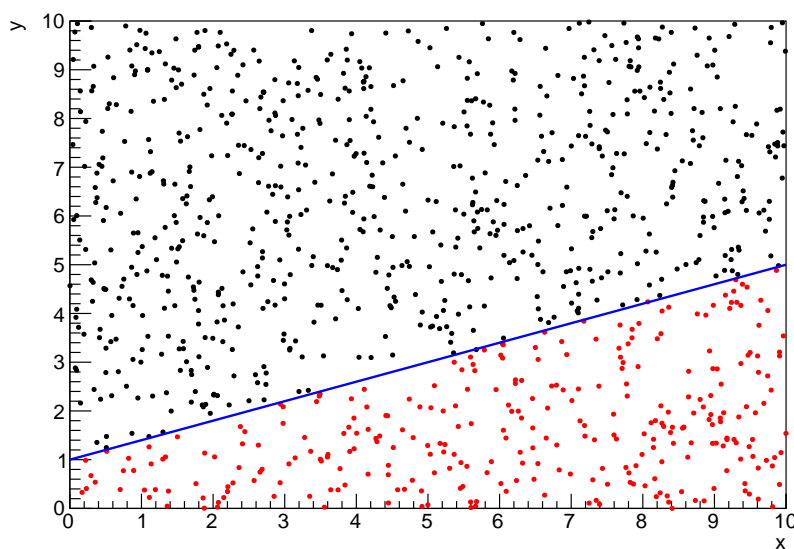


Figure 4.1: Example of using Monte Carlo techniques to find the area under the blue line. The gradient and intercept of the line are 0.4 and 1.0 respectively. The area found to be under the curve using one thousand samples is 29.9 units.

1245 4.2.1 Markov Chain Monte Carlo

1246 This analysis utilises a multi-dimensional probability distribution, with some
1247 dimensions being significantly more constrained than others. These constraints
1248 can be from prior knowledge of parameter distributions from external data or
1249 un-physical regions in which parameters can not exist. To maximise the efficiency
1250 of building the posterior distribution, a Markov Chain Monte Carlo (MCMC)
1251 technique is used. This employs a Markov chain to select the points at which
1252 to sample the posterior distribution. It performs a semi-random stochastic walk
1253 through the allowable parameter space. This builds a posterior distribution

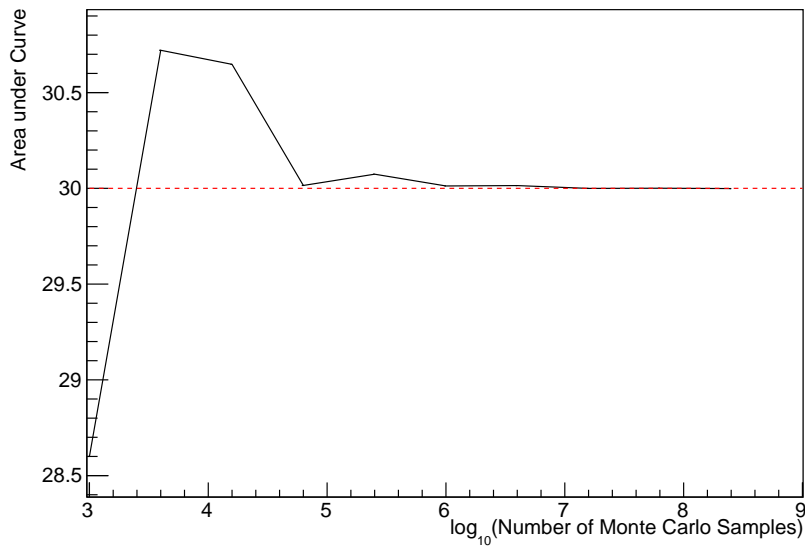


Figure 4.2: The area under a line of gradient 0.4 and intercept 1.0 for the range $0 \leq x \leq 10$ as calculated using Monte Carlo techniques as a function of the number of samples used in each repetition. The analytical solution to the area is 30 units as given by the red line.

1254 which has the property that the density of sampled points is proportional to the
 1255 probability density of that parameter. This means that the samples produced by
 1256 this technique are not statistically independent but they will cover the space
 1257 of the distribution.

1258 A Markov chain functions by selecting the position of step \vec{x}_{i+1} based on the
 1259 position of \vec{x}_i . The space in which the Markov chain selects samples is dependent
 1260 upon the total number of parameters utilised within the fit, where a discrete point
 1261 in this space is described by the N-dimensional vector \vec{x} . In a perfectly operating
 1262 Markov chain, the position of the next step depends solely on the previous step
 1263 and not on the further history of the chain (\vec{x}_0, \vec{x}_1 , etc.). However, in solving
 1264 the multi-dimensionality of the fit used within this analysis, each step becomes
 1265 correlated with several of the steps preceding itself. Providing the MCMC chain is
 1266 well optimised, it will begin to converge towards a unique stationary distribution.
 1267 The period between the chain's initial starting point and the convergence to the
 1268 unique stationary distribution is colloquially known as the burn-in period. Once
 1269 the chain reaches the stationary distribution, all points sampled after that point

1270 will look like samples from that distribution.

1271 Further details of the theories underpinning MCMC techniques are discussed
1272 in [121] but can be summarised by the requirement that the chain satisfies the
1273 three ‘regularity conditions’:

- 1274 • Irreducibility: From every position in the parameter space \vec{x} , there must
1275 exist a non-zero probability for every other position in the parameter space
1276 to be reached.
- 1277 • Recurrence: Once the chain arrives at the stationary distribution, every step
1278 following from that position must be samples from the same stationary
1279 distribution.
- 1280 • Aperiodicity: The chain must not repeat the same sequence of steps at any
1281 point throughout the sampling period.

1282 The output of the chain after burn-in (i.e. the sampled points after the chain
1283 has reached the stationary distribution) can be used to approximate the posterior
1284 distribution and model parameters $\vec{\theta}$. To achieve the requirement that the unique
1285 stationary distribution found by the chain be the posterior distribution, one
1286 can use the Metropolis-Hastings algorithm. This guides the stochastic process
1287 depending on the likelihood of the current proposed step compared to that
1288 of the previous step.

1289 4.2.2 Metropolis-Hastings Algorithm

1290 As a requirement for MCMCs, the Markov chain implemented in this technique
1291 must have a unique stationary distribution that is equivalent to the posterior
1292 distribution. To ensure this requirement and that the regularity conditions are
1293 met, this analysis utilises the Metropolis-Hastings (MH) algorithm [127, 128].
1294 For the i^{th} step in the chain, the MH algorithm determines the position in the
1295 parameter space to which the chain moves to based on the current step, \vec{x}_i , and
1296 the proposed step, \vec{y}_{i+1} . The proposed step is randomly selected from some

1297 proposal function $f(\vec{x}_{i+1}|\vec{x}_i)$, which depends solely on the current step (ie. not
1298 the further history of the chain). The next step in the chain \vec{x}_{i+1} can be either the
1299 current step or the proposed step, determined by whether the proposed step is
1300 accepted or rejected. To decide if the proposed step is selected, the acceptance
1301 probability, $\alpha(\vec{x}_i, \vec{y}_i)$, is calculated as

$$\alpha(\vec{x}_i, \vec{y}_{i+1}) = \min\left(1, \frac{P(\vec{y}_{i+1}|D)f(\vec{x}_i|\vec{y}_{i+1})}{P(\vec{x}_i|D)f(\vec{y}_{i+1}|\vec{x}_i)}\right). \quad (4.4)$$

1302 Where $P(\vec{y}_{i+1}|D)$ is the posterior probability distribution as introduced in
1303 section 4.1. To simplify this calculation, the proposal function is required to
1304 be symmetric such that $f(\vec{x}_i|\vec{y}_{i+1}) = f(\vec{y}_{i+1}|\vec{x}_i)$. In practice, a multi-variate
1305 Gaussian distribution centered on \vec{x}_i is used to throw parameter proposals. This
1306 reduces Equation 4.4 to

$$\alpha(\vec{x}_i, \vec{y}_{i+1}) = \min\left(1, \frac{P(\vec{y}_{i+1}|D)}{P(\vec{x}_i|D)}\right). \quad (4.5)$$

1307 After calculating this quantity, a random number, β , is generated uniformly
1308 between 0 and 1. If $\beta \leq \alpha(\vec{x}_i, \vec{y}_{i+1})$, the proposed step is accepted. Otherwise,
1309 the chain sets the next step equal to the current step. This procedure is repeated
1310 for subsequent steps. This can be interpreted as if the posterior probability
1311 of the proposed step is greater than that of the current step, ($P(\vec{y}_{i+1}|D) \geq$
1312 $P(\vec{x}_i|D)$), the proposed step will always be accepted. If the opposite is true,
1313 ($P(\vec{y}_{i+1}|D) \leq P(\vec{x}_i|D)$), the proposed step will be accepted with probability
1314 $P(\vec{x}_i|D)/P(\vec{y}_{i+1}|D)$. This ensures that the Markov chain does not get trapped
1315 in any local minima in the potentially non-Gaussian posterior distribution. The
1316 outcome of this technique is that the density of steps taken in a discrete region
1317 is directly proportional to the probability density in that region.

1318 4.2.3 MCMC Optimisation

1319 As discussed in subsection 4.2.2, the proposal function invoked within the MH
1320 algorithm can take any form and the chain will still converge to the stationary
1321 distribution. At each set of proposed parameter values, a prediction of each

sample spectra has to be generated which requires significant computational resources. Therefore, the number of steps taken before the unique stationary distribution is found should be minimised as only steps after convergence add information to the oscillation analysis. Furthermore, the chain should entirely cover the allowable parameter space to ensure that all values have been considered. Tuning the distance that the proposal function jumps between steps on a parameter-by-parameter basis can both minimise the length of the burn-in period and ensure that the correlation between step \vec{x}_i and \vec{x}_j is sufficiently small.

The effect of changing the width of the proposal function is highlighted in Figure 4.3. Three scenarios, each with the same underlying stationary distribution (A Gaussian of width 1.0 and mean 0.), are presented. The only difference between the three scenarios is the width of the proposal function, colloquially known as the ‘step size, σ ’. Each scenario starts at an initial parameter value of 10.0 which would be considered an extreme variation. For the case where $\sigma = 0.1$, it is clear to see that the chain takes a long time to reach the expected region of the parameter. This indicates that this chain would have a large burn-in period and does not converge to the stationary distribution until step ~ 500 . Furthermore, whilst the chain does move towards the expected region, each step is significantly correlated with the previous. Considering the case where $\sigma = 5.0$, the chain approaches the expected parameter region almost instantly meaning that the burn-in period is not significant. However, there are clearly large regions of steps where the chain does not move. This is likely due to the chain proposing steps in the tails of the distribution which have a low probability of being accepted. Consequently, this chain would take a significant number of steps to fully span the allowable parameter region. For the final scenario, where $\sigma = 0.5$, you can see a relatively small burn-in period of approximately 100 steps. Once the chain reaches the stationary distribution, it moves throughout the expected region of parameter values many times, sufficiently sampling the full parameter region. This example is a single parameter varying across a continuous distribution and does not fully reflect the difficulties in the many-hundred multi-variate parameter

1352 distribution used within this analysis. However, it does give a conceptual idea of
1353 the importance of selecting the proposal function and associated step size.

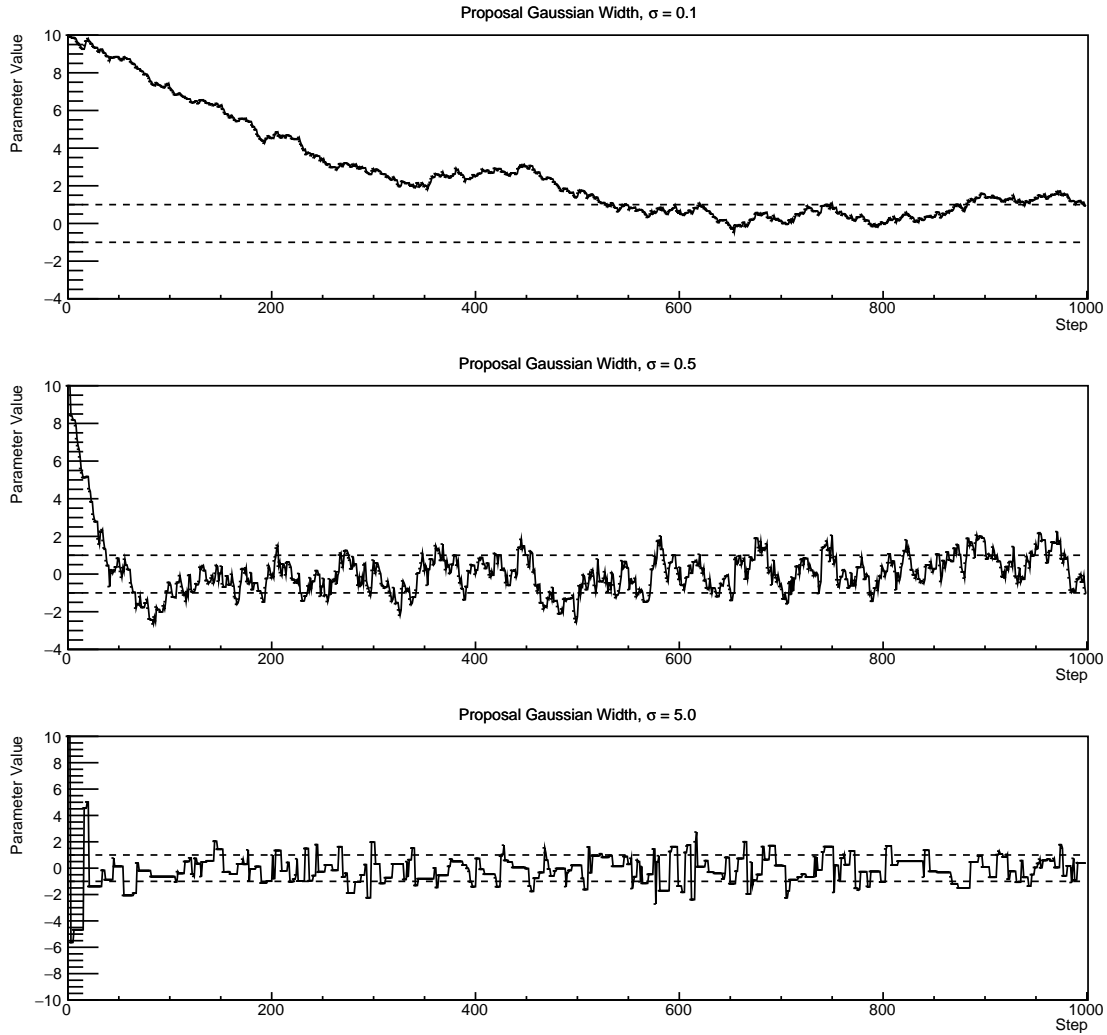


Figure 4.3: Three MCMC chains, each with a stationary distribution equal to a Gaussian centered at 0 and width 1 (As indicated by the black dotted lines). All of the chains use a Gaussian proposal function but have different widths (or ‘step size σ ’). The top panel has $\sigma = 0.1$, middle panel has $\sigma = 0.5$ and the bottom panel has $\sigma = 5.0$.

1354 As discussed, step size tuning directly correlates to the average step accep-
1355 tance rate. If the step size is too small, many steps will be accepted but the
1356 chain moves slowly. If the opposite is true, many steps will be rejected as the
1357 chain proposes steps in the tails of the distribution. Discussion in [129] suggests
1358 that the ‘ideal’ acceptance rate of a high dimension MCMC chain should be

¹³⁵⁹ approximately $\sim 25\%$. An “ideal” step size [129] of

$$\sigma = \frac{2.4}{N_p}, \quad (4.6)$$

¹³⁶⁰ where N_p is the number of parameters included in the MCMC fit. However,
¹³⁶¹ the complex correlations between systematics mean that some parameters have
¹³⁶² to be hand-tuned and many efforts have been taken to select a set of parameter-
¹³⁶³ by-parameter step sizes to approximately reach the ideal acceptance rate.

¹³⁶⁴ Figure 4.4 highlights the likelihood as calculated by the fit in subsection 8.3.4
¹³⁶⁵ as a function of the number of steps in each chain. In practice, many independent
¹³⁶⁶ MCMC chains are run simultaneously to parallelise the task of performing the
¹³⁶⁷ fit. This figure overlays the distribution found in each chain. As seen, the
¹³⁶⁸ likelihood decreases from its initial value and converges towards a stationary
¹³⁶⁹ distribution after $\sim 1 \times 10^5$ steps.

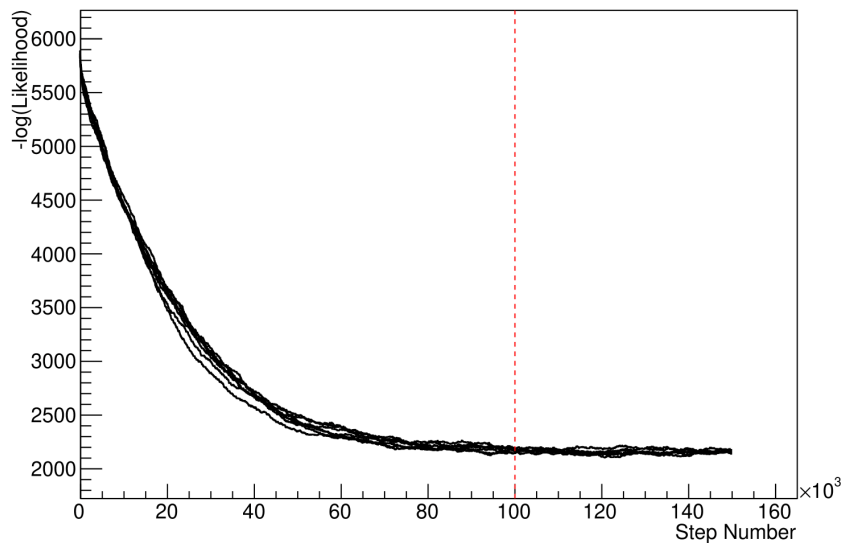


Figure 4.4: The log-likelihood from the fit detailed in subsection 8.3.4 as a function of the number of steps accumulated in each fit. Many independent MCMC chains were run in parallel and overlaid on this plot. The red line indicates the 1×10^5 step burn-in period after which the log-likelihood becomes stable.

¹³⁷⁰ Multiple configurations of this analysis have been performed throughout this
¹³⁷¹ thesis where different samples or systematics have been used. For all of these
¹³⁷² configurations, it was found that a burnin period of 1×10^5 was sufficient.

1373 4.3 Understanding the MCMC Results

1374 The previous sections have described how to generate the posterior probability
1375 distribution using Bayesian MCMC techniques. However, this analysis focuses
1376 on oscillation parameter determination. The posterior distribution output from
1377 the chain is a high-dimension object, with as many dimensions as there are
1378 parameters included in the oscillation analysis. However, this multi-dimensional
1379 object is difficult to conceptualize so parameter estimations are often presented
1380 in one or two-dimensional projections of this probability distribution. To do
1381 this, marginalisation techniques are invoked.

1382 4.3.1 Marginalisation

1383 The output of the MCMC chain is a highly dimensional probability distribution
1384 which is very difficult to interpret. From the standpoint of an oscillation analysis
1385 experiment, the one or two-dimensional ‘projections’ of the oscillation parameters
1386 of interest are most relevant. Despite this, the best fit values and uncertainties on
1387 the oscillation parameters of interest should correctly encapsulate the correlations
1388 to the other systematic uncertainties (colloquially called ‘nuisance’ parameters).
1389 For this joint beam and atmospheric analysis, the oscillation parameters of
1390 interest are $\sin^2(\theta_{23})$, $\sin^2(\theta_{13})$, Δm_{32}^2 , and δ_{CP} . All other parameters (includ-
1391 ing the oscillation parameters this fit is insensitive to) are deemed nuisance
1392 parameters. To generate these projections, the posterior distribution is integrated
1393 over all nuisance parameters. This is called marginalisation. This technique
1394 also explains why it is acceptable to neglect the normalisation constant of the
1395 posterior distribution, which was discussed in section 4.1.

1396 A simple example of the marginalisation technique is to imagine the scenario
1397 where two coins are flipped. To determine the probability that the first coin
1398 returned a ‘head’, the exact result of the second coin flip is disregarded and
1399 simply integrated over. For the parameters of interest, $\vec{\theta}_i$, the marginalised

1400 posterior is calculated by integrating over the nuisance parameters, $\vec{\theta}_n$. In this
1401 case, Equation 4.2 becomes

$$P(\vec{\theta}_i|D) = \frac{\int P(D|\vec{\theta}_i, \vec{\theta}_n)P(\vec{\theta}_i, \vec{\theta}_n)d\vec{\theta}_n}{\int P(D|\vec{\theta})P(\vec{\theta})d\vec{\theta}}. \quad (4.7)$$

1402 Where $P(\vec{\theta}_i, \vec{\theta}_n)$ encodes the prior knowledge about the uncertainty and
1403 correlations between the parameters of interest and the nuisance parameters.
1404 In practice, this is simply taking the one or two-dimensional projection of the
1405 multi-dimensional probability distribution.

1406 While in principle an easy solution to a complex problem, correlations be-
1407 tween the interesting and nuisance parameters can bias the marginalised results.
1408 A similar effect is found when the parameters being marginalised over have
1409 non-Gaussian probability distributions. For example, Figure 4.5 highlights
1410 the marginalisation bias in the probability distribution found for a parameter
1411 when requiring a correlated parameter to have a positive value. Due to the
1412 complex nature of the oscillation parameter fit presented in this thesis, there
1413 are correlations occurring between the oscillation parameters of interest and the
1414 other nuisance parameters included in the fit.

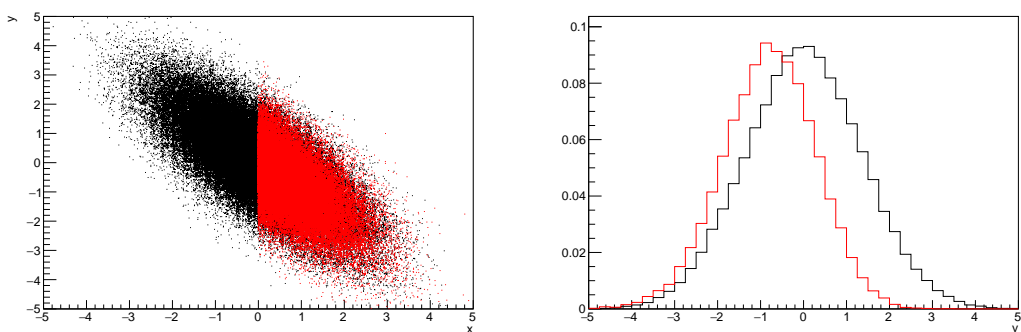


Figure 4.5: Left: The two-dimensional probability distribution for two correlated parameters x and y . The red distribution shows the two-dimensional probability distribution when $0 \leq x \leq 5$. Right: The marginalised probability distribution for the y parameter found when requiring the x to be bound between $-5 \leq x \leq 5$ and $0 \leq x \leq 5$ for the black and red distribution, respectively.

4.3.2 Parameter Estimation and Credible Intervals

The purpose of this analysis is to determine the best fit values for the oscillation parameters that the beam and atmospheric samples are sensitive to: $\sin^2(\theta_{23})$, $\sin^2(\theta_{13})$, Δm_{32}^2 , and δ_{CP} . The posterior probability density, taken from the output MCMC chain, is binned in these parameters. The parameter best-fit point is then taken to be the value that has the highest posterior probability. This is performed in both one and two-dimensional projections.

However, the single best-fit point in a given parameter is not of much use on its own. The uncertainty on the best-fit point must also be presented using credible intervals. The definition of the 1σ credible interval is that there is 68% belief that the parameter is within those bounds. For a more generalised definition, the credible interval is the region, R , of the posterior distribution that contains a specific fraction of the total probability, such that

$$\int_R P(\theta|D)d\theta = \alpha. \quad (4.8)$$

Where θ is the parameter being evaluated. This technique then calculates the $\alpha \times 100\%$ credible interval.

In practice, this analysis uses the highest posterior density (HPD) credible intervals which are calculated through the following method. First, the probability distribution is area-normalised such that it has an integrated area equal to 1.0. The bins of probability are then summed from the highest to lowest until the sum exceeds the 1σ level (0.68 in this example). This process is repeated for a range of credible intervals, notably the 1σ , 2σ and 3σ along with other levels where the critical values for each level can be found in [72]. This process can be repeated for the two-dimensional probability distributions by creating two-dimensional contours rather than one-dimensional credible intervals.

¹⁴³⁹ 4.3.3 Bayesian Model Comparisons

¹⁴⁴⁰ Due to the matter resonance, this analysis has some sensitivity to the mass
¹⁴⁴¹ hierarchy of neutrino states (whether Δm_{32}^2 is positive or negative) and the
¹⁴⁴² octant of $\sin^2(\theta_{23})$. The Bayesian approach utilised within this analysis gives an
¹⁴⁴³ intuitive method of model comparison by determining which hypothesis is most
¹⁴⁴⁴ favourable. Taking the ratio of Equation 4.3 for the two hypotheses of normal
¹⁴⁴⁵ hierarchy, NH , and inverted hierarchy, IH , gives

$$\frac{P(\vec{\theta}_{NH}|D)}{P(\vec{\theta}_{IH}|D)} = \frac{P(D|\vec{\theta}_{NH})}{P(D|\vec{\theta}_{IH})} \times \frac{P(\vec{\theta}_{NH})}{P(\vec{\theta}_{IH})}. \quad (4.9)$$

¹⁴⁴⁶ The middle term defines the Bayes factor, $B(NH/IH)$, which is a data-driven
¹⁴⁴⁷ interpretation of how strong the data prefers one hierarchy to the other. For this
¹⁴⁴⁸ analysis, equal priors on both mass hierarchy hypotheses are chosen ($P(\vec{\theta}_{NH}) =$
¹⁴⁴⁹ $P(\vec{\theta}_{IH}) = 0.5$). In practice, the MCMC chain proposes a value of $|\Delta m_{32}^2|$ and
¹⁴⁵⁰ then applies a 50% probability that the value is sign flipped. Consequently,
¹⁴⁵¹ the Bayes factor can be calculated from the ratio of the probability density in
¹⁴⁵² either hypothesis. This equates to counting the number of steps taken in the
¹⁴⁵³ normal and inverted hierarchies and taking the ratio. The same approach can be
¹⁴⁵⁴ taken to compare the upper octant (UO) compared to the lower octant (LO)
¹⁴⁵⁵ hypothesis of $\sin^2(\theta_{23})$.

$\log_{10}(B_{AB})$	B_{AB}	Strength of Preference
< 0.0	< 1	No preference for hypothesis A (Supports hypothesis B)
0.0 – 0.5	1.0 – 3.16	Preference for hypothesis A is weak
0.5 – 1.0	3.16 – 10.0	Preference for hypothesis A is substantial
1.0 – 1.5	10.0 – 31.6	Preference for hypothesis A is strong
1.5 – 2.0	31.6 – 100.0	Preference for hypothesis A is very strong
> 2.0	> 100.0	Decisive preference for hypothesis A

Table 4.1: Jeffreys scale for strength of preference for two models A and B as a function of the calculated Bayes factor ($B_{AB} = B(A/B)$) between the two models [130]. The original scale is given in terms of $\log_{10}(B(A/B))$ but converted to linear scale for easy comparison throughout this thesis.

¹⁴⁵⁶ Whilst the value of the Bayes factor should always be shown, the Jeffreys scale
¹⁴⁵⁷ [130] (highlighted in Table 4.1) gives an indication of the strength of preference

¹⁴⁵⁸ for one model compared to the other. Other interpretations of the strength of
¹⁴⁵⁹ preference of a model exist, e.g. the Kass and Raferty Scale [131].

¹⁴⁶⁰ 4.3.4 Comparison of MCMC Output to Expectation

¹⁴⁶¹ To ensure the fit is performing well, a best-fit spectrum is produced using the
¹⁴⁶² posterior probability distribution and compared with the data, allowing easy
¹⁴⁶³ by-eye comparisons to be made. A simple method of doing this is to perform a
¹⁴⁶⁴ comparison in the fitting parameters (e.g. the reconstructed neutrino energy for
¹⁴⁶⁵ T2K far detector beam samples) of the spectra generated by the MCMC chain to
¹⁴⁶⁶ ‘data’. This ‘data’ could be true data or some variation of Monte Carlo prediction.
¹⁴⁶⁷ This allows easy comparison of the MCMC probability distribution to the data. To
¹⁴⁶⁸ perform this, N steps from the post-burnin MCMC chain are randomly selected.
¹⁴⁶⁹ From these, the Monte Carlo prediction at each step is generated by reweighting
¹⁴⁷⁰ the model parameters to the values specified at that step. Due to the probability
¹⁴⁷¹ density being directly correlated with the density of steps in a certain region,
¹⁴⁷² parameter values close to the best fit value are most likely to be selected.

¹⁴⁷³ In practice, for each bin of the fitting parameters has a probability distribution
¹⁴⁷⁴ of event rates, with one entry per sampled MCMC step. This distribution is
¹⁴⁷⁵ binned where the bin with the highest probability is selected as the mean and an
¹⁴⁷⁶ error on the width of this probability distribution is calculated using the HPD
¹⁴⁷⁷ approach highlighted in subsection 4.3.2. Consequently, the best fit distribution in
¹⁴⁷⁸ the fit parameter is not necessarily that which would be attained by reweighting
¹⁴⁷⁹ the Monte Carlo prediction to the most probable parameter values.

¹⁴⁸⁰ A similar study can be performed to illustrate the freedom of the model
¹⁴⁸¹ parameter space prior to the fit. This can be done by throwing parameter values
¹⁴⁸² from the prior uncertainty of each parameter.

5

1483

1484

1485

Simulation, Reconstruction, and Event Reduction

1486 As a crucial part of the oscillation analysis, an accurate prediction of the expected
1487 neutrino spectrum at the far detector is required. This includes modeling the
1488 flux generation, neutrino interactions, and detector effects. All of the simulation
1489 packages required to do this are briefly described in section 5.1. The reconstruc-
1490 tion of neutrino events in the far detector, including the `fitQun` algorithm, is
1491 documented in section 5.2. This also includes data quality checks of the SK-V
1492 data which the author performed for the T2K oscillation analysis presented at the
1493 Neutrino 2020 conference [2]. Finally, section 5.3 describes the steps taken in the
1494 SK detector to trigger on events of interest whilst removing the comparatively
1495 large rate of cosmic ray muon events.

1496 5.1 Simulation

1497 In order to generate a Monte Carlo prediction of the expected event rate at
1498 the far detector, all the processes in the beam and atmospheric fluxes, neutrino
1499 interaction, and detector need to be modeled.

5.1.1 Neutrino Flux

The beamline simulation consists of three distinct parts: the initial hadron interaction modeled by FLUKA [132], the target station geometry and particle tracking performed by JNUBEAM, [38, 133] and any hadronic re-interactions simulated by GCALOR [134]. The primary hadronic interactions are $O(10)\text{GeV}$, where FLUKA matches external cross-section data better than GCALOR [135]. However, FLUKA is not very adaptable so a small simulation is built to model the interactions in the target and the output is then passed to JNUBEAM and GCALOR for propagation. The hadronic interactions are tuned to data from the NA61/SHINE [136–138] and HARP [139] experiments. The tuning is done by reweighting the FLUKA and GCALOR predictions to match the external data and cross-section measurements, based on final state particle kinematics [135]. The culmination of this simulation package generates the predicted flux for neutrino and antineutrino beam modes which are illustrated in Figure 3.6.

The atmospheric neutrino flux is simulated by the HKKM model [50, 52]. The primary cosmic ray flux is tuned to AMS [140] and BESS [141] data assuming the US-standard atmosphere '76 [142] density profile and includes geomagnetic field effects. The primary cosmic rays interact to generate pions and muons. The interaction of these secondary particles to generate neutrinos is handled by DPMJET-III [143] for energies above 32GeV and JAM [52, 144] for energies below that value [48]. These hadronic interactions are tuned to BESS and L3 data [145, 146] using the same methodology as the tuning of the beamline simulation. The energy and cosine zenith predictions of $\nu_e, \bar{\nu}_e, \nu_\mu, \bar{\nu}_\mu$ flux are given in Figure 2.3 and Figure 2.5, respectively. The flux is approximately symmetrical and peaked around the horizon ($\cos(\theta_Z) = 0.0$). This is because horizontally-going pions and kaons can travel further than their vertically-going counterparts resulting in a larger probability of decaying to neutrinos. The symmetry is broken in lower-energy neutrinos due to geomagnetic effects, which modify the track of the primary cosmic rays. Updates to the HKKM model are currently ongoing [147].

1529 5.1.2 Neutrino Interaction

1530 Once a flux prediction has been made for all three detectors, NEUT 5.4.0 [148, 149]
 1531 models the interactions of the neutrinos in the detectors. For the purposes of this
 1532 analysis, quasi-elastic (QE), meson exchange (MEC), single meson production
 1533 (PROD, RES), coherent pion production (COH), and deep inelastic scattering
 1534 (DIS) interactions are simulated. These interaction categories can be further
 1535 broken down by whether they were propagated via a W^\pm boson in Charged
 1536 Current (CC) interactions or via a Z^0 boson in Neutral Current (NC) interactions.
 1537 CC interactions have a charged lepton in the final state, which can be flavour-
 1538 tagged in reconstruction to determine the flavour of the neutrino. In contrast, NC
 1539 interactions have a neutrino in the final state so no flavour information can be
 1540 determined from the observables left in the detector after an interaction. This
 1541 is the reason why neutrinos that interact through NC modes are assumed to
 1542 not oscillate within this analysis. Both CC and NC interactions are modeled
 1543 for all the above interaction categories, other than MEC interactions which are
 1544 only modeled for CC events.

1545 As illustrated in Figure 5.1, CCQE interactions dominate the cross-section of
 1546 neutrino interactions around $E_\nu \sim 0.5\text{GeV}$. The NEUT implementation adopts
 1547 the Llewellyn Smith [150] model for neutrino-nucleus interactions, where the
 1548 nuclear ground state of any bound nucleons (neutrino-oxygen interactions) is
 1549 approximated by a spectral-function [151] model that simulates the effects of
 1550 Fermi momentum and Pauli blocking. The cross-section of QE interactions is
 1551 controlled by vector and axial-vector form factors parameterised by the BBBA05
 1552 [152] model and a dipole form factor with $M_A^{QE} = 1.21\text{GeV}$ fit to external data
 1553 [153], respectively. NEUT implements the Valencia [154] model to simulate MEC
 1554 events, where two nucleons and two holes in the nuclear target are produced
 1555 (often called 2p2h interactions).

1556 For neutrinos of energy $O(1)\text{GeV}$, PROD interactions become dominant.
 1557 These predominantly produce charged and neutral pions although γ , kaon,

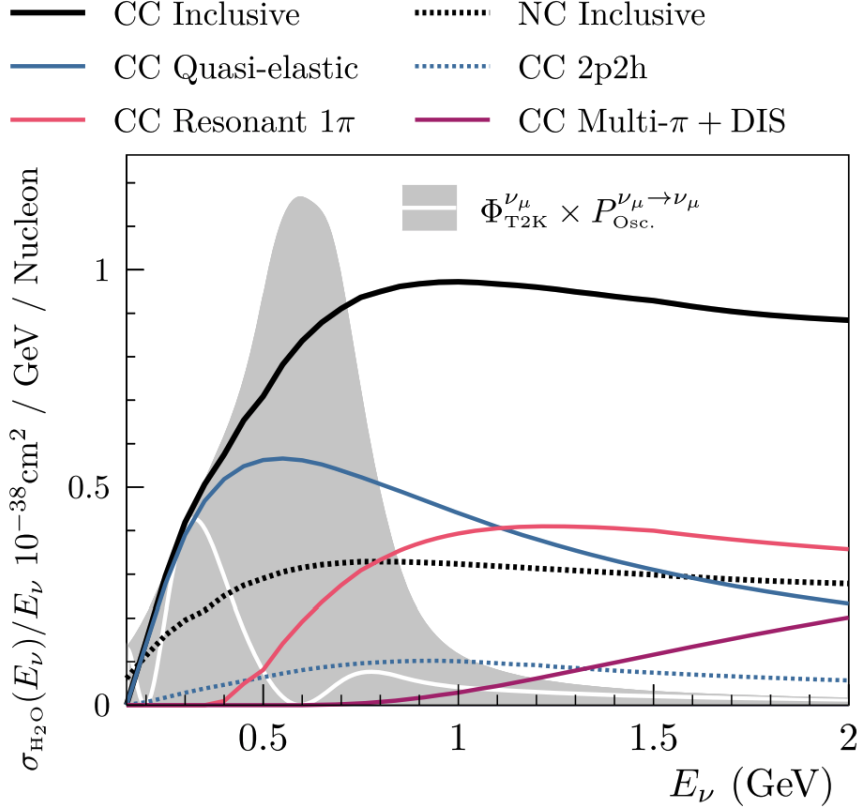


Figure 5.1: The NEUT prediction of the ν_μ -H₂O cross-section overlaid on the T2K ν_μ flux. The charged current (black, solid) and neutral current (black, dashed) inclusive, charged current quasi-elastic (blue, solid), charged current 2p2h (blue, dashed), charged current single pion production (pink), and charged current multi- π and DIS (Purple) cross-sections are illustrated. Figure taken from [148].

and η production is also considered. To simulate these interactions, the Berger-Sehgal [155] model is implemented within NEUT. It simulates the excitation of a nucleon from a neutrino interaction, production of an intermediate baryon, and the subsequent decay to a single meson or γ . Pions can also be produced through COH interactions, which occur when the incoming neutrino interacts with the entire oxygen nucleus leaving a single pion outside of the nucleus. NEUT utilises the Berger-Sehgal [156] model to simulate these COH interactions.

DIS and multi- π producing interactions become the most dominant for energies $> O(5)$ GeV. PYTHIA [157] is used to simulate any interaction with invariant mass $W > 2\text{GeV}/c^2$, which produces at least one meson. For any interaction which produces at least two mesons but has $W < 2\text{GeV}/c^2$, the

₁₅₆₉ Bronner model is used [158]. Both of these models use Parton distribution
₁₅₇₀ functions based on the Bodek-Yang model [159–161].

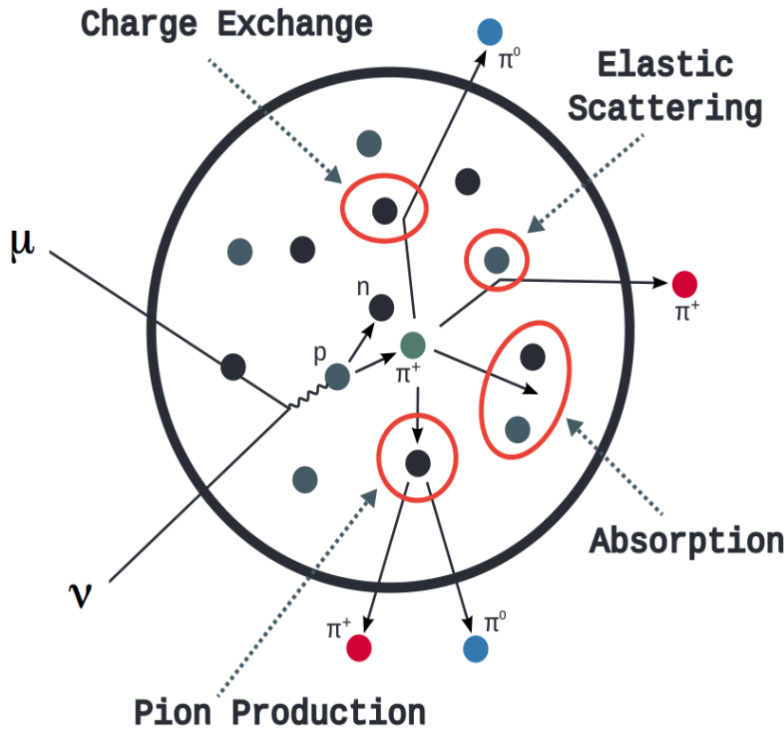


Figure 5.2: Illustration of the various processes which a pion can undergo before exiting the nucleus. Taken from [162].

₁₅₇₁ Any pion that is produced within the nucleus can re-interact through final
₁₅₇₂ state interactions before it exits, as illustrated by the scattering, absorption,
₁₅₇₃ production, and exchange interactions in Figure 5.2. These re-interactions alter
₁₅₇₄ the observable particles within the detector. For instance, if the charged pion
₁₅₇₅ from a CC PROD interaction is absorbed, the observables would mimic a CC QE
₁₅₇₆ interaction. To simulate these effects, NEUT uses a semi-classical intranuclear
₁₅₇₇ cascade model [148]. This cascade functions by stepping the pion through the
₁₅₇₈ nucleus in fixed-length steps equivalent to $dx = R_N/100$, where R_N is the radius
₁₅₇₉ of the nucleus. At each step, the simulation allows the pion to interact through
₁₅₈₀ scattering, charged exchange, absorption, or production with an interaction-
₁₅₈₁ dependent probability calculated from a fit to external data [163]. This cascade
₁₅₈₂ continues until the pion is absorbed or exits the nucleus.

1583 5.1.3 Detector

1584 Once the final state particle kinematics have been determined by NEUT, they
1585 are passed into the detector simulation. The near detectors, ND280 and INGRID,
1586 are simulated using a GEANT4 package [42, 164] to simulate the detector geom-
1587 etry, particle tracking, and energy deposition. The response of the detectors is
1588 simulated using the elecSim package [42].

1589 The far detector simulation, based upon the original Kamiokande experiment
1590 software, uses the GEANT3-based SKDETSIM [42, 165] package. This simulates the
1591 interactions of particles in the water as well as Cherenkov light production. The
1592 water quality and PMT calibration measurements detailed in subsection 3.1.2
1593 are also used within this simulation to make accurate predictions of the de-
1594 tector response.

1595 Any event which generates optical photons that occurs in SK will be observed
1596 by the PMT array, where each PMT records the time and accumulated charge.
1597 This recorded information is shown in event displays similar to those illustrated
1598 in Figure 5.3 for simulated Monte Carlo events. To be useful for physics analyses,
1599 this series of PMT hit information needs to be reconstructed to determine the
1600 number and identity of particles and their kinematics (or track parameters): four-
1601 vertex, direction, and momentum. The reconstruction uses the fact that the charge
1602 and timing distribution of photons generated by a particular particle in an event is
1603 dependent upon its initial kinematics. Electron and muon rings are distinguished
1604 by their “fuzziness”. Muons are heavier and less affected by scattering or
1605 showering meaning they typically produce “crisp” rings. Electrons are more
1606 likely to interact via electromagnetic showering or scattering which results in
1607 larger variations of their direction from the initial direction. Consequently,
1608 electrons typically produce “fuzzier” rings compared to muons.

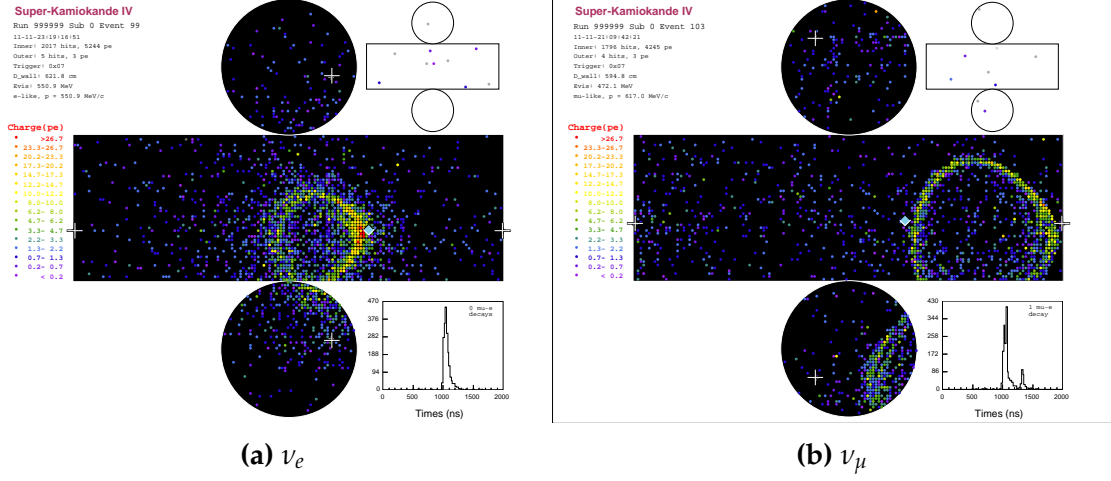


Figure 5.3: Event displays from Monte Carlo simulation at Super Kamiokande illustrating the “crisp” ring from a muon and the typically “fuzzy” electron ring. Each pixel represents a PMT and the color scheme denotes the accumulated charge deposited on that PMT. Figures taken from [166].

5.2 Event Reconstruction at SK

For the purposes of this analysis, the `fitQun` reconstruction algorithm [167] is utilised. Its core function is to compare a prediction of the accumulated charged and timing distribution from each PMT, generated for a particular particle identity, vertex, and momentum, to that observed in the neutrino event. It determines the preferred values by maximising a likelihood function (or minimising a log-likelihood function) which includes information from PMTs which were hit and those that were not hit. The `fitQun` algorithm is based on the key concepts of the MiniBooNE reconstruction algorithm [168].

The `fitQun` algorithm improves upon the previous `APFit` algorithm [169] which has been used for many previous SK analyses. `APFit` fits the vertex from timing information and then fits the direction of the particle from PMT hits within a 43 deg Cherenkov cone (assuming an ultra-relativistic particle) using a fitting estimator. A Hough transformation is used to find the radius of a ring (related to the momentum through Equation 3.2) as well as the number of rings contained within the event. The analysis presented here uses the `fitQun` algorithm as it improves both the accuracy of the fit parameters and the rejection of neutral

1626 current π^0 events as compared to APFit [170, 171].

1627 Any event in SK can consist of prompt (or primary) and decay (or secondary)
1628 particles. For example, a charged current muon neutrino interaction can generate
1629 two particles that have the potential of generating Cherenkov photons (assuming
1630 the proton is below the Cherenkov threshold): the prompt muon, and the
1631 secondary decay-electron from the muon, approximately $2\mu\text{s}$ later. To correctly
1632 reconstruct all particles within an event, it is divided into time clusters which are
1633 called “subevents”. Subevents after the primary subevent are considered to
1634 be decay electrons.

1635 The main steps of the `fitQun` reconstruction algorithm are:

- 1636 • **Vertex pre-fitting:** An estimate of the vertex is made using a goodness-of-fit
1637 metric based on PMT hit times
- 1638 • **Peak finding:** The initial time of each subevent is determined by clustering
1639 events by time residuals
- 1640 • **Single-ring fits:** Given the pre-fit vertex and estimated time of interaction,
1641 a maximum likelihood technique searches for a single particle generating
1642 light. Electron, muon, charged pion, and proton hypotheses are considered
- 1643 • **Multi-ring fits:** Seeded from the single-ring fits, hypotheses with multiple
1644 light-producing particles are considered using the same maximum likeli-
1645 hood technique. Electron-like or charged pion-like rings are added until
1646 the likelihood stops improving

1647 To find all the subevents in an event, a vertex goodness metric is calculated
1648 for some vertex position \vec{x} and time t ,

$$G(\vec{x}, t) = \sum_i^{\text{hit PMTs}} \exp \left(-\frac{1}{2} \left(\frac{T_{Res}^i(\vec{x}, t)}{\sigma} \right)^2 \right), \quad (5.1)$$

1649 where

$$T_{Res}^i(\vec{x}, t) = t^i - t - |R_{PMT}^i - \vec{x}| / c_n, \quad (5.2)$$

1650 is the residual hit time. It is the difference in time between the PMT hit
1651 time t^i , of the i^{th} PMT, and the expected time of the PMT hit if the photon was
1652 emitted at the vertex. R_{PMT}^i is the position of the i^{th} PMT, c_n is the speed of light
1653 in water and $\sigma = 4\text{ns}$ which is comparable to the time resolution of the PMT.
1654 When the proposed fit values of time and vertex are close to the true values,
1655 $T_{Res}^i(\vec{x}, t)$ tends to zero resulting in subevents appearing as spikes in the goodness
1656 metric. The proposed fit vertex and time are grid-scanned, and the values which
1657 maximise the goodness metric are selected as the “pre-fit vertex”. Whilst this
1658 predicts a vertex for use in the clustering algorithm, the final vertex is fit using
1659 the higher-precision maximum likelihood method described below.

1660 Once the pre-fit vertex has been determined, the goodness metric is scanned as
1661 a function of t to determine the number of subevents. A peak-finding algorithm
1662 is then used on the goodness metric. This requires the goodness metric to exceed
1663 some threshold and drop below a reduced threshold before any subsequent
1664 additional peaks are considered. The thresholds are set such that the rate of
1665 false peak finding is minimised while still attaining good data to Monte Carlo
1666 agreement. To improve performance, the pre-fit vertex for each delayed subevent
1667 is re-calculated after PMT hits from the previous subevent are masked. This
1668 improves the decay-electron tagging performance. Once all subevents have
1669 been determined, the time window around each subevent is then defined by the
1670 earliest and latest time which satisfies $-180 < T_{Res}^i < 800\text{ns}$. The subevents and
1671 associated time windows are then used as seeds for further reconstruction.

1672 For a given subevent, the `fitQun` algorithm constructs a likelihood based on
1673 the accumulated charge q_i and time information t_i from the i^{th} PMT,

$$L(\Gamma, \vec{\theta}) = \prod_j^{\text{unhit}} P_j(\text{unhit}|\Gamma, \vec{\theta}) \prod_i^{\text{hit}} \{1 - P_i(\text{unhit}|\Gamma, \vec{\theta})\} f_q(q_i|\Gamma, \vec{\theta}) f_t(t_i|\Gamma, \vec{\theta}). \quad (5.3)$$

1674 Where $\vec{\theta}$ defines the track parameters: vertex position, direction vector and
 1675 momenta, and Γ represents the particle hypothesis. $P_i(\text{unhit}|\Gamma, \vec{\theta})$ is the proba-
 1676 bility of the i^{th} tube to not register a hit given the track parameters and particle
 1677 hypothesis. The charge likelihood, $f_q(q_i|\Gamma, \vec{\theta})$, and time likelihood, $f_t(t_i|\Gamma, \vec{\theta})$,
 1678 represents the probability density function of observing charge q_i and time t_i on
 1679 the i^{th} PMT given the specified track parameters and particle hypothesis.

1680 The predicted charge is calculated based on contributions from both the
 1681 direct light and the scattered light. The direct light contribution is determined
 1682 based on the integration of the Cherenkov photon profile along the track. PMT
 1683 angular acceptance, water quality, and calibration measurements discussed in
 1684 subsection 3.1.2 are included to accurately predict the charge probability density
 1685 at each PMT. The scattered and reflected light is calculated in a similar way,
 1686 although it includes a scattering function that depends on the vertex of the
 1687 particle and the position of the PMT. The charge likelihood is calculated by
 1688 comparing the prediction to the observed charge in the PMT, where the prediction
 1689 is tuned to the PMT simulation.

1690 The time likelihood is approximated to depend on the vertex \vec{x} , direction \vec{d} ,
 1691 and time t of the track as well as the particle hypothesis. The expected time
 1692 for PMT hits is calculated by assuming unscattered photons being emitted from
 1693 the midpoint of the track, S_{mid} ,

$$t_{\text{exp}}^i = t + S_{\text{mid}}/c + |R_{\text{PMT}}^i - \vec{x} - S_{\text{mid}}\vec{d}|/c_n, \quad (5.4)$$

1694 where c is the speed of light in a vacuum. The time likelihood is then expressed
 1695 in terms of the residual difference between the PMT hit time and the expected
 1696 hit time, $t_{\text{Res}}^i = t^i - t_{\text{exp}}^i$. The particle hypothesis and momentum also affect the
 1697 Cherenkov photon distribution. These parameters modify the shape of the time
 1698 likelihood density since in reality not all photons are emitted at the midpoint of
 1699 the track. As with the charge likelihood, the contributions from both the direct
 1700 and scattered light to the time likelihood density are calculated separately, which
 1701 are both calculated from particle gun Monte Carlo studies.

1702 The track parameters and particle identity which maximise $L(\Gamma, \vec{\theta})$ are defined
 1703 as the best-fit parameters. In practice MINUIT [172] is used to minimise the value
 1704 of $-\ln L(\Gamma, \vec{\theta})$. The `fitQun` algorithm considers an electron-like, muon-like, and
 1705 charged pion-like hypothesis for events with a single final state particle, denoted
 1706 “single-ring events”. The particle’s identity is determined by taking the ratio of
 1707 the likelihood of each of the hypotheses. For instance, electrons and muons are
 1708 distinguished by considering the value of $\ln(L(e, \vec{\theta}_e)/L(\mu, \vec{\theta}_\mu))$ in comparison
 1709 to the reconstructed momentum of the electron hypothesis, as illustrated by
 1710 Figure 5.4. The coefficients of the discriminator between electron-like and muon-
 1711 like events are determined from Monte Carlo studies [167]. Similar distributions
 1712 exist for distinguishing electron-like events from π^0 -like events, and muon-like
 1713 events from pion-like events. The cuts are defined as,

$$\begin{aligned} \text{Electron/Muon} : & \ln(L_e/L_\mu) > 0.2 \times p_e^{rec} [\text{MeV}], \\ \text{Electron}/\pi^0 : & \ln(L_e/L_{\pi^0}) < 175 - 0.875 \times m_{\gamma\gamma} [\text{MeV}], \\ \text{Muon/Pion} : & \ln(L_\mu/L_{\pi^\pm}) < 0.15 \times p_\mu^{rec} [\text{MeV}], \end{aligned} \quad (5.5)$$

1714 as taken from [173], where p_e^{rec} and p_μ^{rec} are the reconstructed momentum of the
 1715 single-ring electron and muon fits, respectively. $m_{\gamma\gamma}$ represents the reconstructed
 1716 invariant mass of the two photons emitted from π^0 decay. Typically, the distance
 1717 between a particular entry in these two-dimensional distributions and the cut-line
 1718 is termed the PID parameter and is illustrated in Figure 5.5.

1719 The `fitQun` algorithm also considers a π^0 hypothesis. To do this, it performs
 1720 a fit looking for two standard electron-hypothesis tracks which point to the
 1721 same four-vertex. This assumes the electron tracks are generated from photon-
 1722 conversion so the electron tracks actually appear offset from the proposed π^0
 1723 vertex. For these fits, the conversion length, direction, and momentum of each
 1724 photon are also considered as track parameters which are then fit in the same
 1725 methodology as the standard single-ring hypotheses.

1726 Whilst lower energy events are predominantly single-ring events, higher
 1727 energy neutrino events can generate final states with multiple particles which

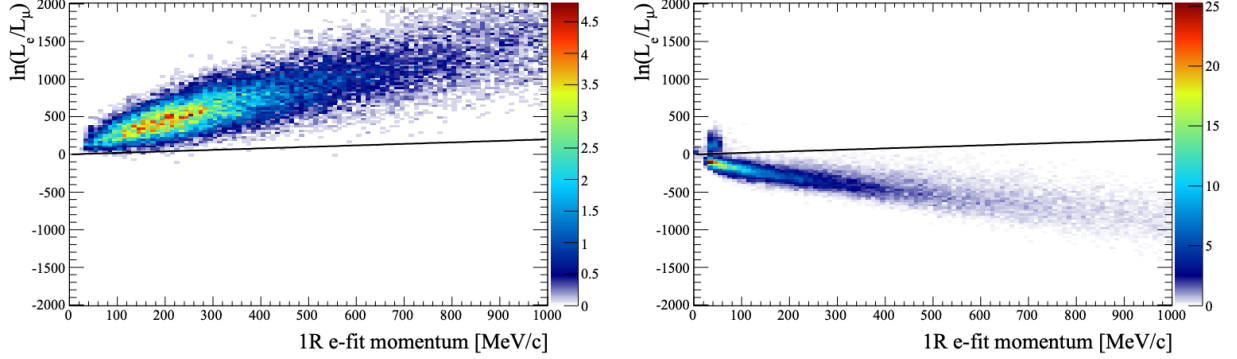


Figure 5.4: The difference of the electron-like and muon-like log-likelihood compared to the reconstructed single-ring fit momentum for atmospheric ν_e (left) and ν_μ (right) samples. The black line represents the cut used to discriminate electron-like and muon-like events, with coefficients obtained from Monte Carlo studies. Figures from [167].

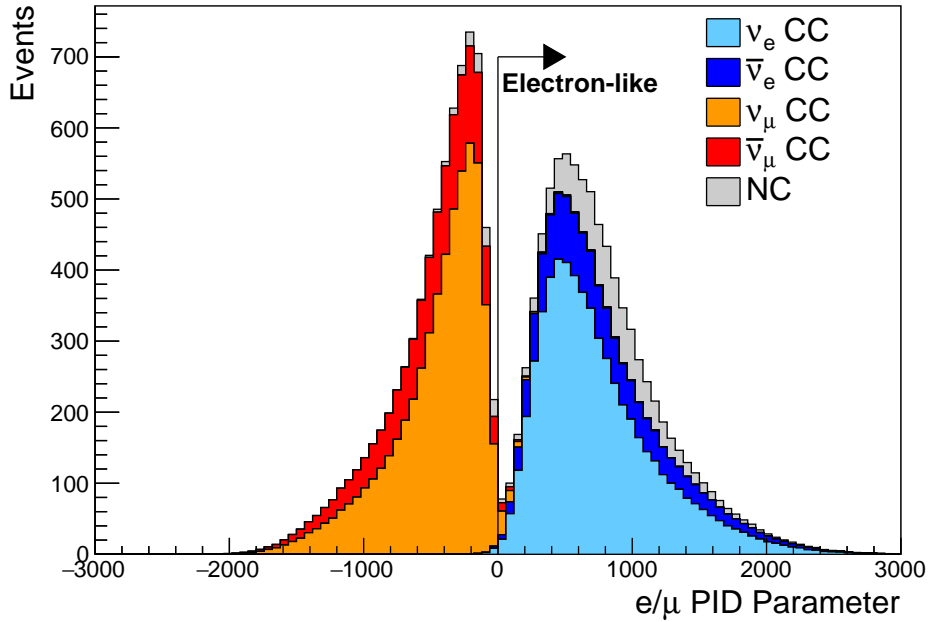


Figure 5.5: The electron/muon PID separation parameter for all sub-GeV single-ring events in SK-IV. The charged current (CC) component is broken down in four flavours of neutrino (ν_μ , $\bar{\nu}_\mu$, ν_e and $\bar{\nu}_e$). Events with positive values of the parameter are determined to be electron-like.

1728 generate Cherenkov photons. These “multi-ring” hypotheses are also considered
 1729 in the `fitQun` algorithm. When calculating the charge likelihood density, the
 1730 predicted charge associated with each ring is calculated separately and then
 1731 summed to calculate the total accumulated charge on each PMT. Similarly, the
 1732 time likelihood for the multi-ring hypothesis is calculated assuming each ring

is independent. Each track is time-ordered based on the time of flight from the center of the track to the PMT and the direct light from any ring incident on the PMT is assumed to arrive before any scattered light. To reduce computational resource usage, the multi-ring fits only consider electron-like and charged pion-like rings as the pion fit can be used as a proxy for a muon fit due to their similar mass. Due to the pions ability to interact through the strong force, they are more likely to hard-scatter. That means a single charged pion can produce multiple rings in different directions. There is an additional freedom, the fraction of kinetic energy lost in a single ring segment, which is added into the `fitQun` pion fit to cover this difference. Pion and muon rings are indistinguishable when this fraction tends to unity.

Multi-ring fits proceed by proposing another ring to the previous fit and then fitting the parameters in the method described above. Typically, multi-ring fits have the largest likelihood because of the additional degrees of freedom introduced. A likelihood value is calculated for the n -ring and $(n + 1)$ -ring hypotheses, where the additional ring is only included if the likelihood value is above 9.35, based on Monte Carlo studies in [174].

5.2.1 Validation of Reconstruction in SK-V

Understanding how the modelling of the detector conditions and stability effects the reconstruction is critical for ensuring accurate measurements. It is important to note that the detector systematics used in the 2020 T2K-only [2] oscillation analysis are determined using data-to-Monte Carlo comparisons of the SK-IV data [175]. Due to tank-open maintenance occurring between SK-IV and SK-V, the dark rate of each PMT was observed to increase in SK-V due to light exposure for a significant time during the repairs. This increase can be seen in Figure 5.6. Run-10 of the T2K experiment was conducted in the SK-V period, so the consistency of SK-IV and SK-V data needs to be studied to determine whether the SK-IV-defined systematics can be applied to the run-10 data. Consequently, the author of this thesis assessed the quality of `fitQun` event reconstruction for SK-V data.

This comparison study was performed using the stopping muon data set for both the SK-IV and SK-V periods. This data sample is used due to the high rate of interactions as well as having similar energies to muons from CCQE ν_μ interactions from beam interactions. The rate of cosmic muons does depend on the solar activity cycle [176] but this effect has been neglected in this comparison study. This is because the shape of the distributions is most important for the purposes of being compared to the detector systematics. The SK-IV and SK-V data samples consist of 2398.42 and 626.719 hours of data which equates to 686k and 192k events respectively. These samples do not correspond to the full data sets of either period but do contain enough events to be systematics limited rather than statistics limited.

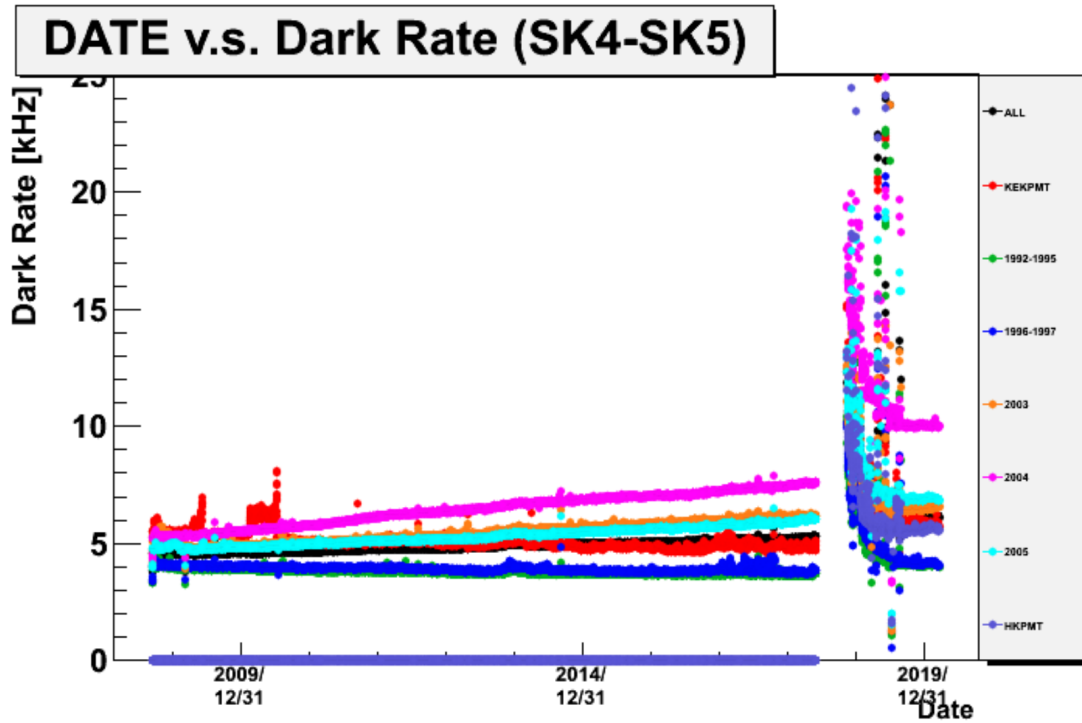


Figure 5.6: The variation of the measured dark rate as a function of date, broken down by PMT type. The SK-IV and SK-V periods span September 2008 to May 2018 and January 2019 to July 2020, respectively. The break in measurement in 2018 corresponds to the period of tank repair and refurbishment. Figure adapted from [175].

The predicted charge calculated in the `fitQun` algorithm includes a contribution from the photoelectron emission due to dark noise. Therefore, the increase

in the SK-V dark rate needs to be accounted for. In practice, the average dark rate in each SK period is calculated and used as an input in the reconstruction. This is calculated by averaging the dark rate per run for each period separately, using the calibration measurements detailed in subsection 3.1.2. The average dark rate from SK-IV and SK-V were found to be 4.57kHz and 6.30kHz, respectively. The charges associated with the muon and decay electron subevents are illustrated in Figure 5.7. The photoelectron emission from dark noise is more significant for events that have lower energy. This is because this contribution becomes more comparable to the number of photoelectrons emitted from incident photons in lower-energy events. This behaviour is observed in the data, where the charge deposited by the muon subevent is mostly unaffected by the increase in dark rate, whilst the charge associated with the decay-electron is clearly affected.

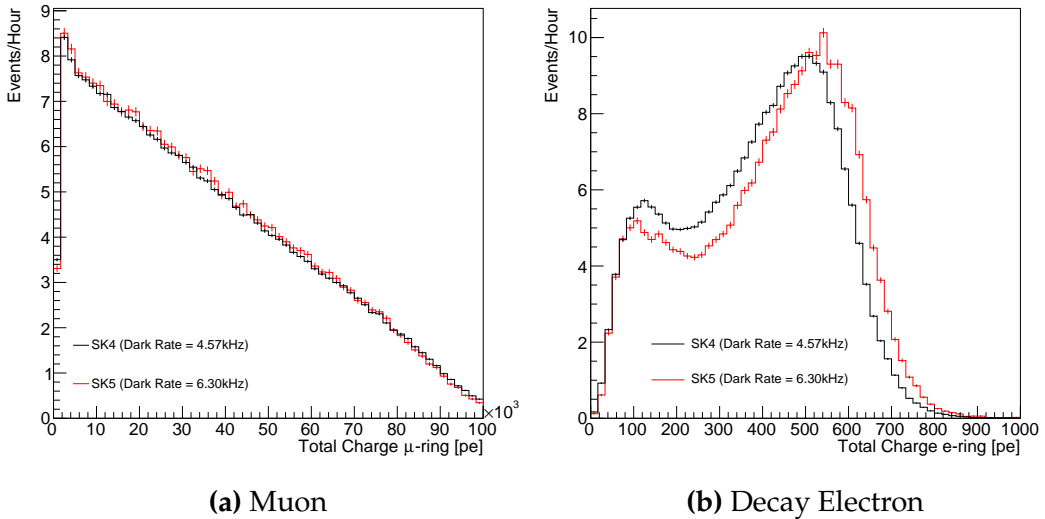


Figure 5.7: Comparison of the measured raw charge deposited per event from the stopping muon data samples between SK-IV (Blue) and SK-V (Red), split by the primary muon subevent (left) and the associated decay electron subevent (right).

The energy scale systematic is estimated from data-to-Monte Carlo differences in the stopping muon sample in [59] and found to be 2.1%. To determine the consistency of SK-IV and SK-V with respect to the energy scale systematic, the muon momentum distribution is compared between the two SK periods. As the total number of Cherenkov photons is integrated across the track length,

₁₇₉₂ the reconstructed momentum divided by track length (or range) is compared
₁₇₉₃ between SK-IV and SK-V as illustrated in Figure 5.8.

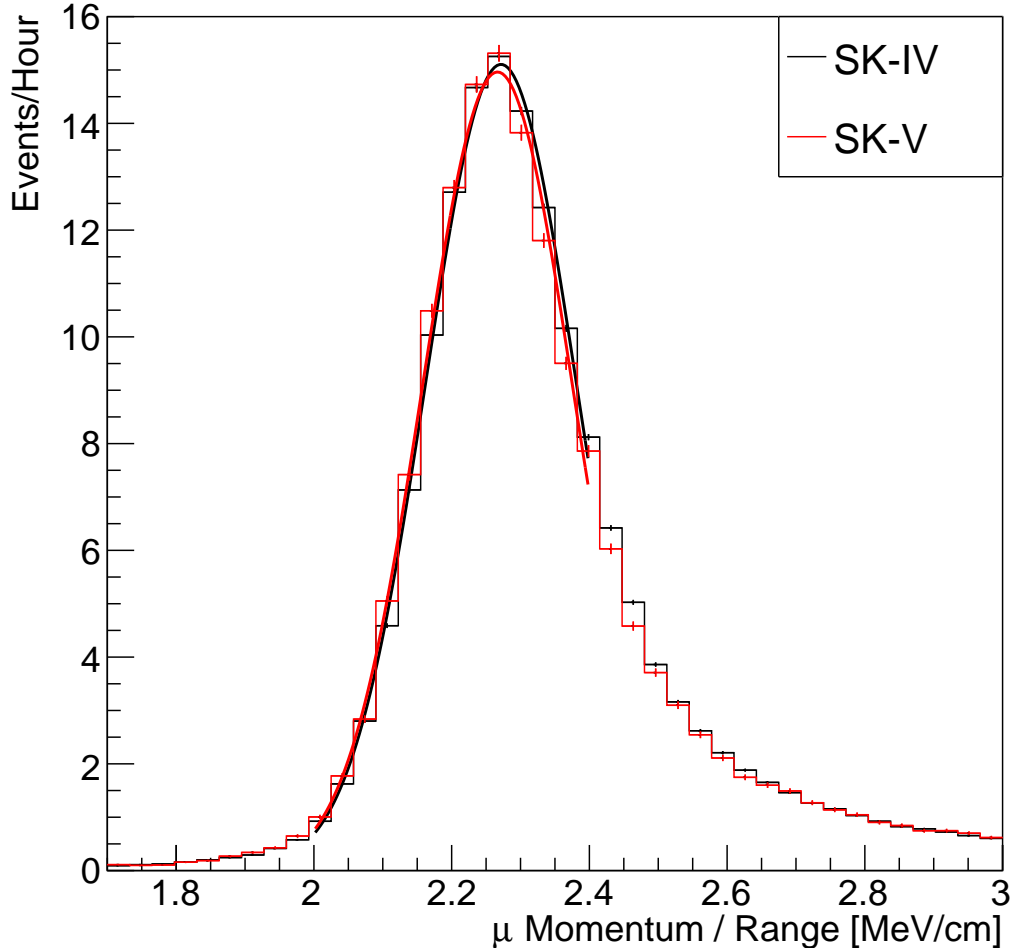


Figure 5.8: The distribution of the reconstructed momentum from the muon ring divided by the distance between the reconstructed muon and decay electron vertices as found in the stopping muon data sets of SK-IV (Black) and SK-IV (Red). Only events with one tagged decay electron are considered. A Gaussian fit is considered in the range $[2.0, 2.4]\text{MeV}/\text{cm}$ and illustrated as the solid curve.

₁₇₉₄ The consistency between these muon distributions has been computed in two
₁₇₉₅ ways. Firstly, a Gaussian is fit to the peak of each distribution separately, whose
₁₇₉₆ mean is found to be $(2.272 \pm 0.003)\text{MeV}/\text{cm}$ and $(2.267 \pm 0.006)\text{MeV}/\text{cm}$ for SK-
₁₇₉₇ IV and SK-V respectively. The ratio of these is equal to 1.002 ± 0.003 . The means of
₁₇₉₈ the Gaussian fits are consistent with the expected stopping power of a minimum

1799 ionising muon for a target material (water) with $Z/A \sim 0.5$ [177]. The second
 1800 consistency check is performed by introducing a nuisance parameter, α , which
 1801 modifies the SK-V distribution. The value of α which minimises the χ^2 value
 1802 between the SK-IV and SK-V is determined by scanning across a range of values.
 1803 This is repeated by applying the nuisance parameter as both a multiplicative
 1804 factor and an additive shift. The χ^2 distributions for different values of α is
 1805 illustrated in Figure 5.9. The values which minimise the χ^2 are found to be 0.0052
 1806 and 1.0024 for the additive and multiplicative implementations, respectively. No
 1807 evidence of shifts larger than the 2.1% uncertainty on the energy scale systematic
 1808 has been found in the reconstructed momentum distribution of SK-IV and SK-V.

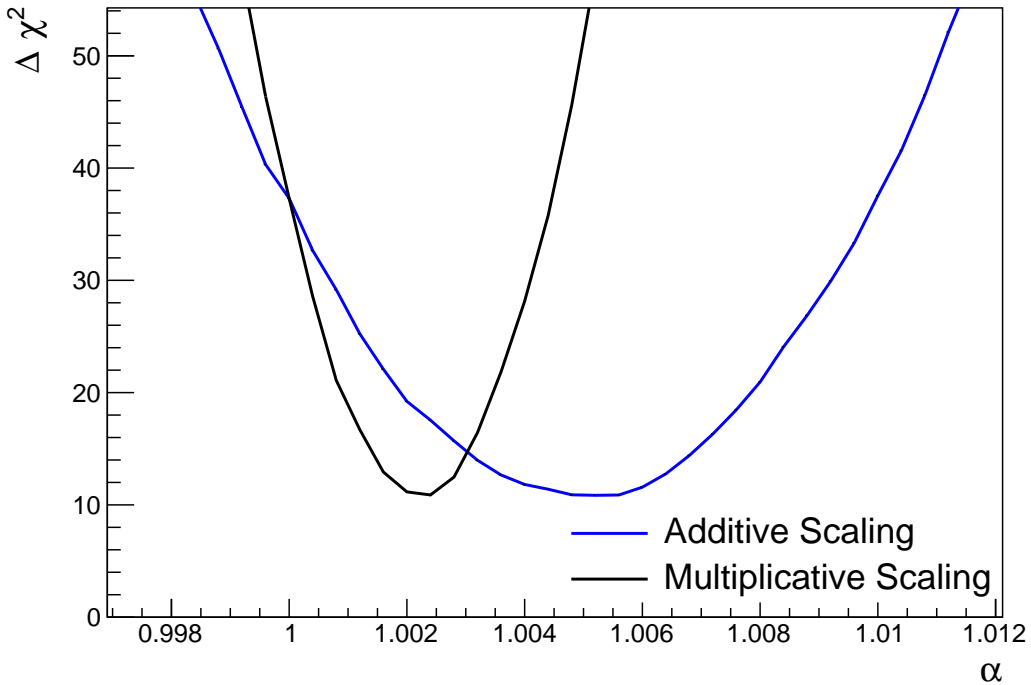


Figure 5.9: The χ^2 difference between the SK-IV and SK-V reconstructed muon momentum divided by range when the SK-V is modified by the scaling parameter α . Both additive (Blue) and multiplicative (Black) scaling factors have been considered. In practice, the additive scaling factor actually uses the value of $(\alpha - 1.0)$ but is illustrated like this so the results can be shown on the same axis range.

1809 5.3 Event Reduction at SK

1810 In normal data-taking operations, the SK detector observes many background
 1811 events alongside the beam and atmospheric neutrino signal events of physics
 1812 interest for this thesis. Cosmic ray muons and flasher events, which are the spon-
 1813 taneous discharge of a given PMT, contribute the largest amount of background
 1814 events in the energy range relevant to this thesis. Therefore the data recorded
 1815 is reduced with the aim of removing these background events. The reduction
 1816 process is detailed in [3, 54] and briefly summarised below.

1817 Atmospheric neutrino events observed in the SK detector are categorised
 1818 into three different types of samples: fully contained (FC), partially contained
 1819 (PC) and up-going muon (Up- μ), using PMT hit signatures in the inner and
 1820 outer detector (ID and OD, respectively). To identify FC neutrino events, it is
 1821 required that the neutrino interacts inside the fiducial volume of the ID and that
 1822 no significant OD activity is observed. For this analysis, an event is defined to be
 1823 in the fiducial volume provided the event vertex is at least 0.5m away from the
 1824 ID walls. PC events have the same ID requirements but can have a larger signal
 1825 present inside the OD. Typically, only high energy muons from ν_μ interactions can
 1826 penetrate the ID wall. The Up- μ sample contains events where muons are created
 1827 from neutrino interactions in the OD water or rock below the tank. They then
 1828 propagate upwards through the detector. Downward-going muons generated
 1829 from neutrino interactions above the tank are neglected because of the difficulty
 1830 in separating their signature from the cosmic muon shower background. The
 1831 sample categories are visually depicted in Figure 5.10.

1832 Based on the event characteristics, as defined by the `fitQun` event reconstruc-
 1833 tion software, the FC events are categorised by

- 1834 • **Visible Energy:** equal to the sum of the reconstructed kinetic energy of
 1835 particles above the Cerenkov threshold for all rings present in the event.
 1836 The purpose is to separate events into sub-GeV and multi-GeV categories.

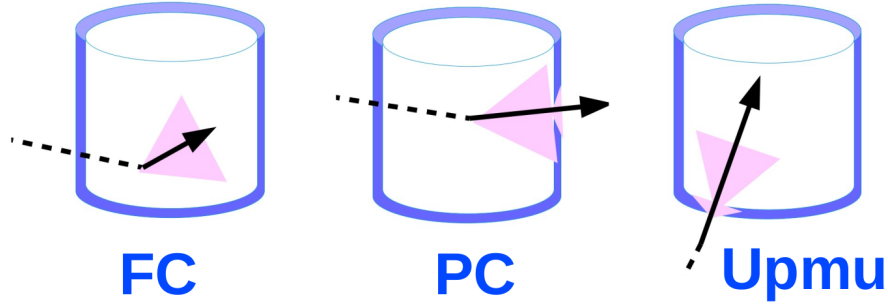


Figure 5.10: A depiction of the topology patterns for fully-contained (FC), partially-contained (PC), and up-going muon ($\text{Up-}\mu$) samples included in this analysis.

- **Number of observed Cerenkov rings.** The purpose is to separate single-ring and multi-ring events, where single-ring events predominantly consist of quasi-elastic interactions and multi-ring events are typically resonant pion production or deep inelastic scattering events.
- **Particle identification parameter of the most energetic ring:** A value determined from the maximum likelihood value based on `fitQun`'s electron, muon, or pion hypothesis. The purpose is to separate electron-like and muon-like events.
- **Number of decay electrons:** The purpose is to separate quasi-elastic events (which have one decay electron emitted from the muon decay) and resonant pion production events (which have two decay electrons emitted from the muon and pion).

The PC and Up- μ categories are broken down into “through-going” and “stopping” samples depending on whether the muon leaves the detector. This is because stopping events deposit the entire energy of the interaction into the detector, resulting in better reconstruction. The energy of events that exit the detector has to be estimated, with a typically worse resolution, which introduces much larger systematic uncertainties. Through-going Up- μ samples are further broken down by whether any hadronic showering was observed in the event which typically indicates DIS interactions. The expected neutrino energy for the different categories is given in Figure 5.11. FC sub-GeV and multi-GeV events

¹⁸⁵⁸ peak around 0.7GeV and 3GeV respectively, with slightly different peak energies
¹⁸⁵⁹ for ν_e and ν_μ oscillation channels. PC and Up- μ are almost entirely comprised
¹⁸⁶⁰ of ν_μ events and peak around 7GeV and 100GeV, respectively.

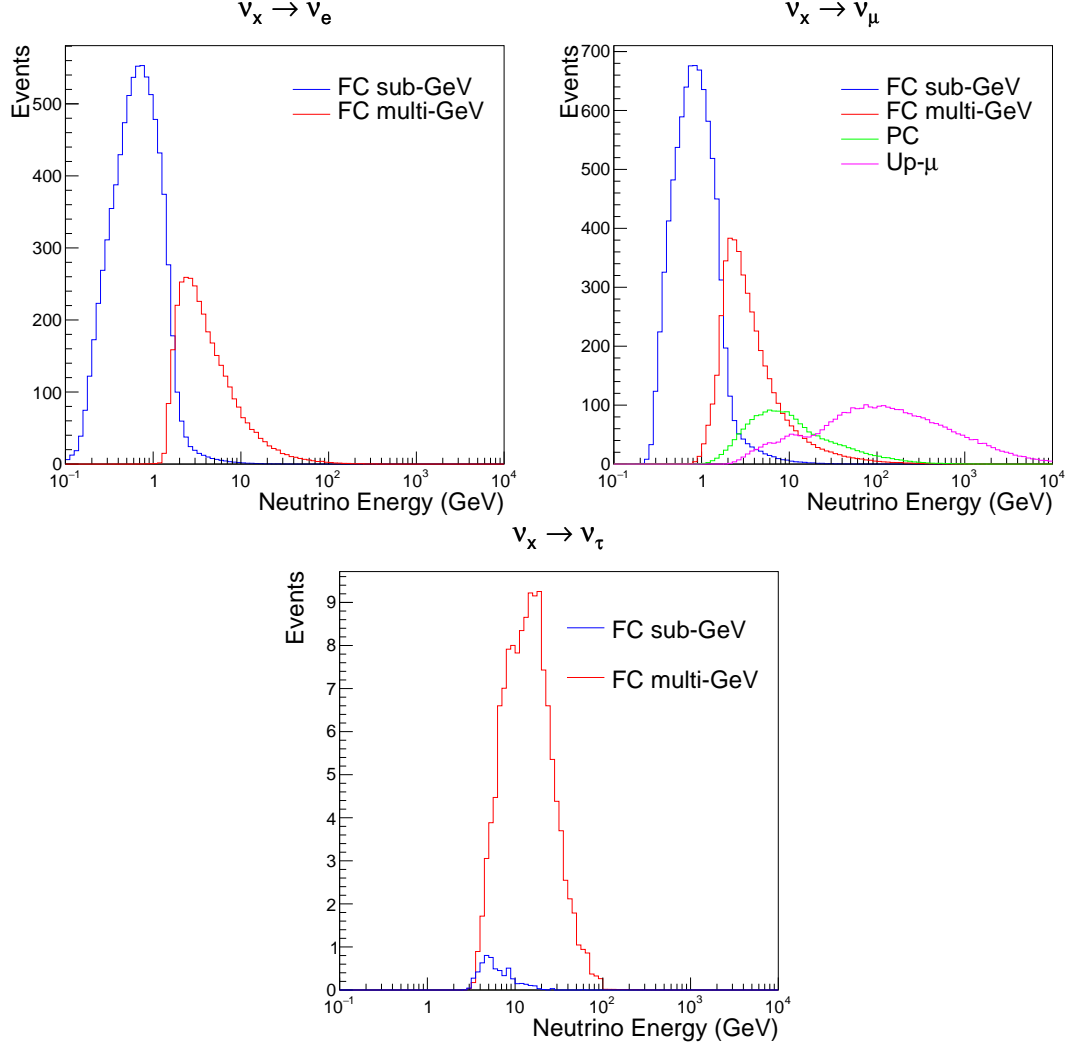


Figure 5.11: The predicted neutrino flux of the fully contained (FC) sub-GeV and multi-GeV, partially contained (PC), and upward-going muon (Up- μ) events. The prediction is broken down by the $\nu_x \rightarrow \nu_e$ prediction (top left), $\nu_x \rightarrow \nu_\mu$ prediction (top right) and $\nu_x \rightarrow \nu_\tau$ prediction (bottom). ν_x represents the flavours of neutrinos produced in the cosmic ray showers (electron and muon). Asimov A oscillation parameters are assumed (given in Table 2.2).

¹⁸⁶¹ The first two steps in the FC reconstruction remove the majority of cosmic
¹⁸⁶² ray muons by requiring a significant amount of ID activity compared to that
¹⁸⁶³ measured in the OD. Events that pass this cut are typically very high momentum
¹⁸⁶⁴ muons or events that leave very little activity in the OD. Consequently, a third

reduction step is then applied to select cosmic-ray muons that pass the initial reduction step. A purpose-built cosmic muon fitter is used to determine the entrance (or exit) position of the muon and a cut is applied to OD activity contained within 8m of this position. Flasher events are removed in the fourth reduction step which is based on the close proximity of PMT hits surrounding the PMT producing the flash. Events that pass all these reduction steps are reconstructed with the APFit algorithm. The fifth step of the reduction uses information from this more precise fitter to repeat the previous two steps with tighter cuts. Muons below the Cherenkov threshold can not generate optical photons in the ID but the associated decay electron can due to its lower mass. These are the types of events targeted in the fifth reduction step. The final cuts require the event vertex to be within the fiducial volume (0.5m from the wall), visible energy $E_{vis} > 30\text{MeV}$ and fewer than 16 hits within the higher energy OD cluster. The culmination of the fully contained reduction results in 8.09 events/day in the nominal fiducial volume [82]. The uncertainty in the reduction is calculated by comparing Monte Carlo prediction to data. The largest discrepancy is found to be 1.3% in the fourth reduction step.

The PC and Up- μ events are processed through their own reduction processes detailed in [54]. Both of these samples are reconstructed with the APFit algorithm rather than `fitQun`. This is because the efficiency of reconstructing events that leave the detector has not been sufficiently studied for reliable systematic uncertainties with `fitQun`. The PC and Up- μ samples acquire events at approximately 0.66 and 1.44 events/day.

Beam neutrinos events undergo the same reduction steps as FC events and are then subject to further cuts [178]. The GPS system that links the timing between the beam facility and SK needs to be operating correctly and there should be no activity within the detector in the previous $100\mu\text{s}$ before the trigger. The events then need to triggered between $-2\mu\text{s}$ and $10\mu\text{s}$ of the expected spill timing.

The beam neutrino samples are not split by visible energy since their energy range is smaller than the atmospheric neutrino events. Following the T2K

1895 analysis in [2], only single-ring beam neutrino events are considered. Similar to
1896 atmospheric event selection, the number of decay electrons is used as a proxy for
1897 distinguishing CCQE and CCRES events. The expected neutrino energy, broken
1898 down by the number of decay electrons, is given in Figure 5.12.

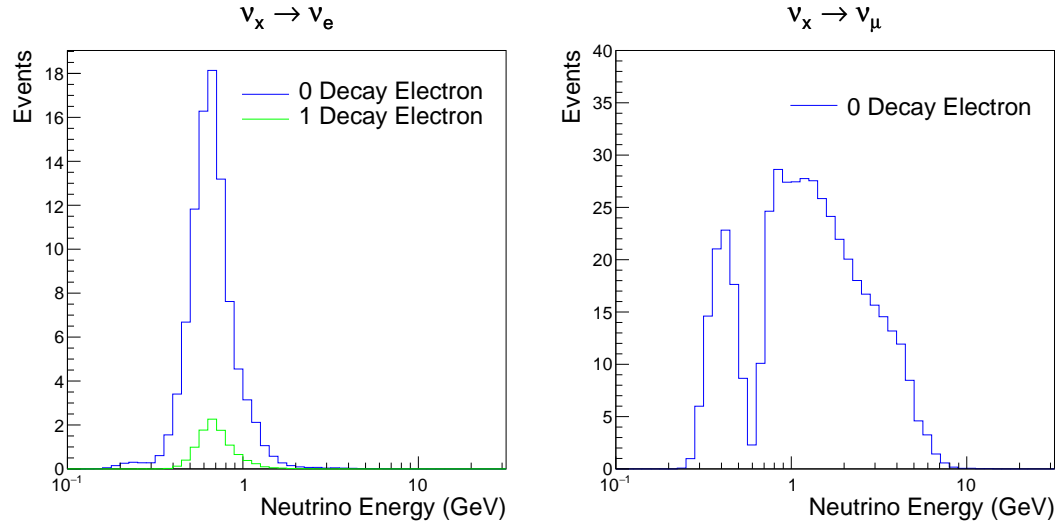


Figure 5.12: The predicted flux of beam neutrinos, as a function of neutrino energy. The predictions are broken down by the number of decay electrons associated with the particular events. Asimov A oscillation parameters are assumed (given in Table 2.2).

6

1899

1900

Sample Selections and Systematics

1901 The oscillation analysis presented within this thesis is built upon a simultaneous
1902 fit to atmospheric samples at SK, neutrino beam samples in the near detector,
1903 and beam samples at SK. The definitions of the samples are documented in
1904 section 6.1, section 6.2, and section 6.3, respectively. The data collected and
1905 used within this analysis is detailed in Table 6.1. This is the first simultaneous
1906 oscillation analysis of beam and atmospheric samples supported by the T2K
1907 and SK collaborations. Notably, the author of this thesis has been responsible
1908 for building and developing the MaCh3 framework to support all far-detector
1909 samples simultaneously. The near and far detector data corresponds to T2K
1910 runs 2-9 and runs 1-10, respectively. The accumulated POT and beam power
1911 for runs 1 – 10 are illustrated in Figure 6.1.

Data Type	Total
Near Detector FHC	1.15×10^{21} POT
Near Detector RHC	8.34×10^{20} POT
Far Detector FHC	1.97×10^{21} POT
Far Detector RHC	1.63×10^{21} POT
Atmospheric SK-IV	3244.4 days

Table 6.1: The amount of data collected in each detector used within this analysis. The data collected at the near and far detector, for both neutrino beam (FHC) and antineutrino beam (RHC), is measured as the number of protons on target (POT).

The difference in POT recorded at the near and far detector is due to the difference in downtime. The SK detector is very stable with almost 100% of data recorded during beam operation. Due to various technical and operational issues, the downtime of the near detector is significantly higher due to its more complex design and operating requirements.

The systematic parameters invoked within the flux, detector, and interaction models used within this analysis are documented in section 6.4. The standard configuration of the joint beam and atmospheric data fit utilises far detector systematics provided in the official inputs from the two experiments. Additionally, a correlated detector model concept, which fits the parameters used in event selections, has been considered and documented in subsection 6.4.5.

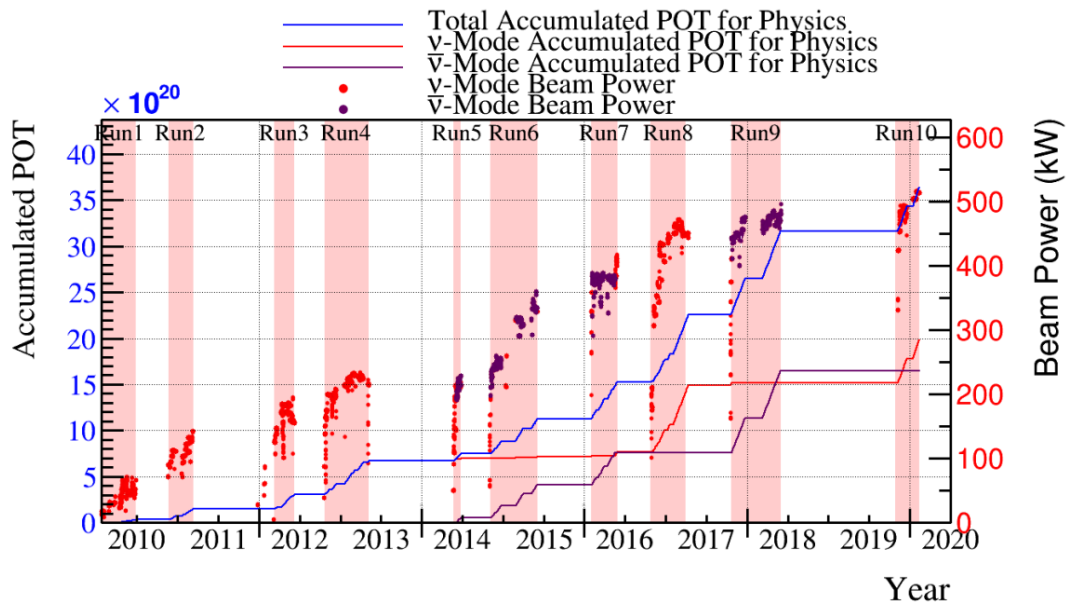


Figure 6.1: The accumulated beam data, measured as the number of protons on target (POT). The total data (blue) is given which comprises of the neutrino beam (red) and antineutrino (purple) components. The beam power for neutrino and antineutrino beams is given as the markers using the same colour scheme. The timescale runs from Run 1 which started in January 2010 until Run 10 which ended in February 2020. The ratio of accumulated data in neutrino and antineutrino beam is 54.7% : 45.3%.

1923 6.1 Atmospheric Samples

1924 The atmospheric event selection follows the official SK-IV analysis presented
1925 in [3] and is documented below. The Monte Carlo prediction used within this
1926 analysis corresponds to 500 years worth of neutrino events, which is scaled down
1927 to match the SK-IV livetime of 3244.4 days.

1928 The fully contained (FC), partially contained (PC), and upward going muon
1929 events ($\text{up-}\mu$) which pass the reduction cuts discussed in section 5.3 are further
1930 broken down into different samples based on reconstruction information. This
1931 section details the samples used within this oscillation analysis, alongside the
1932 chosen binning.

1933 FC events are first separated by the visible energy deposited within the
1934 detector. This is calculated as the sum of the reconstructed kinetic energy
1935 above the Cherenkov threshold for all rings present in the event. Events are
1936 separated by whether they were above or below $E_{\text{vis}} = 1.33\text{GeV}$. This separates
1937 “subGeV” and “multiGeV” events. Typically, lower energy events consist of
1938 charged current quasi-elastic (CCQE) interactions which are better understood
1939 and simpler to reconstruct resulting in smaller systematic uncertainties. Events
1940 are further separated by the number of rings associated with the event due to
1941 similar reasoning. As the oscillation probability is dependant upon the flavour
1942 of neutrino, electron and muon events are separated using a similar likelihood
1943 method to that discussed in section 5.2. To reduce computational resources
1944 required for the reconstruction, only electron and pion hypotheses are considered
1945 so this separation cut depends on the ratio of the electron to pion likelihoods,
1946 $\ln(L_e/L_\pi)$. Finally, the number of decay electrons is used to classify events.
1947 Charged current resonant pion production (CCRES) interactions generate a final-
1948 state pion. This can decay, mostly likely through a muon, into a decay electron.
1949 Therefore any electron-like event with one decay electron or muon-like event
1950 with two decay electrons was most likely produced by a CCRES interaction.
1951 Consequently, the number of decay electrons can be used to distinguish CCQE

¹⁹⁵² and CCRES interaction modes. Ultimately, FC subGeV events are separated
¹⁹⁵³ into the samples listed in Table 6.2.

Sample Name	Description
SubGeV- <i>e</i> like-0dcy	Single ring <i>e</i> -like events with zero decay electrons
SubGeV- <i>e</i> like-1dcy	Single ring <i>e</i> -like events with one or more decay electrons
SubGeV- <i>μ</i> like-0dcy	Single ring <i>μ</i> -like events with zero decay electrons
SubGeV- <i>μ</i> like-1dcy	Single ring <i>μ</i> -like events with one decay electrons
SubGeV- <i>μ</i> like-2dcy	Single ring <i>μ</i> -like events with two or more decay electrons
SubGeV- <i>π</i> 0like	Two <i>e</i> -like ring events with zero decay electrons and reconstructed π^0 mass $85 \leq m_{\pi^0} < 215$ MeV

Table 6.2: The fully contained subGeV samples, defined as events with visible energy $E_{vis} < 1.33$ GeV, used within this oscillation analysis.

¹⁹⁵⁴ In addition to the cuts discussed above, multiGeV samples also have addi-
¹⁹⁵⁵ tional cuts to separate samples which target neutrino and antineutrino events.
¹⁹⁵⁶ As discussed in section 2.5, the matter resonance only occurs for neutrinos in the
¹⁹⁵⁷ normal hierarchy and antineutrinos in the inverted mass hierarchy. Therefore,
¹⁹⁵⁸ having flavour-enriched samples aids in the determination of the mass hierarchy.
¹⁹⁵⁹ For a CCRES interaction,

$$\begin{aligned}
 \bar{\nu}_e + N &\rightarrow e^+ + N' + \pi^-, \\
 \nu_e + N &\rightarrow e^- + N' + \pi^+ \\
 &\quad \downarrow \mu^+ + \nu_\mu \\
 &\quad \downarrow e^+ + \nu_e + \bar{\nu}_\mu.
 \end{aligned} \tag{6.1}$$

¹⁹⁶⁰ The π^- emitted from a $\bar{\nu}_e$ interaction is more likely to be captured by an
¹⁹⁶¹ oxygen nucleus than the π^+ from ν_e interactions [179]. These pions then decay,
¹⁹⁶² mostly through muons, to electrons. Therefore the number of tagged decay
¹⁹⁶³ electrons associated with an event gives an indication of whether the interaction
¹⁹⁶⁴ was due to a neutrino or antineutrino: zero for $\bar{\nu}_e$ events, and one for ν_e events.
¹⁹⁶⁵ The ability to separate neutrino from antineutrino events is illustrated in Table 6.4,
¹⁹⁶⁶ where the MultiGeV-*e*like-nue has 78% purity of CC neutrino interactions with
¹⁹⁶⁷ only 7% antineutrino background, the rest consisting of NC backgrounds.

1968 The number of decay electrons discriminator works reasonably well for single-
1969 ring events. However, this is not the case for multi-ring events. A multiGeV
1970 multiring electron-like (MME) likelihood cut was introduced in [180, 181]. This
1971 is a two-stage likelihood selection cut. Four observables are used in the first
1972 likelihood cut to distinguish $CC\nu_e$ and $CC\bar{\nu}_e$ events from background:

- 1973 • The number of decay electrons
1974 • The maximum distance between the vertex of the neutrino and the decay
1975 electrons
1976 • The energy deposited by the highest energy ring
1977 • The particle identification of that highest energy ring

1978 Background events consist of $CC\nu_\mu$ and NC interactions. Typically, the
1979 majority of the energy in background events is carried by the hadronic system.
1980 Additionally, muons tend to travel further than the pions from $CC\nu_e$ interactions
1981 before decaying. Thus, the parameters used within the likelihood cut target these
1982 typical background interaction kinematics.

Sample Name	Description
MultiGeV-elike-nue	Single ring e -like events with zero decay electrons
MultiGeV-elike-nuebar	Single ring e -like events with one or more decay electrons
MultiGeV-mulike	Single ring μ -like events
MultiRing-elike-nue	Two or more ring events with leading energy e -like ring and passed both MME and $\nu/\bar{\nu}$ separation cuts
MultiRing-elike-nuebar	Two or more ring events with leading energy e -like ring and passed MME and failed $\nu/\bar{\nu}$ separation cuts
MultiRing-mulike	Two or more ring events with leading energy μ -like ring and only requires $E_{vis} > 0.6\text{GeV}$
MultiRing-Other1	Two or more ring events with leading energy e -like ring and failed the MME likelihood cut

Table 6.3: The fully contained multiGeV samples used within this oscillation analysis. Both the sample name and description are given.

1983 Neutrino and antineutrino events are then separated by a second likelihood
1984 method ($\nu/\bar{\nu}$ separation) detailed in [59]. This uses the number of decay electrons,

1985 the number of reconstructed rings, and the event’s transverse momentum. The
1986 last two parameters are used because higher-energy samples tend to have more
1987 pions produced above the Cherenkov threshold which results in more rings
1988 compared to an antineutrino interaction. Furthermore, the angular distribution
1989 also tends to be more forward peaked in antineutrino interactions as compared
1990 to neutrino interactions [3]. These FC multiGeV sample definitions are de-
1991 tailed in Table 6.3.

1992 The PC and up- μ samples are split by the amount of energy deposited within
1993 the outer detector, into “stopping” and “through-going” samples. If an event
1994 leaves the detector, the energy it takes with it has to be estimated which increases
1995 the systematic uncertainty compared to events entirely contained within the
1996 inner detector. This estimation is particularly poor at high energies, thus the
1997 up- μ through-going events are not binned in reconstructed momentum. The
1998 through-going up- μ are further separated by the presence of any electromagnetic
1999 showering in the event, as the assumption of non-showering muon does not give
2000 reliable reconstruction for these types of events [54]. In total, 13 FC, 2 PC, and
2001 3 up- μ atmospheric samples are included within this analysis.

2002 The atmospheric samples are binned in direct observables: reconstructed
2003 lepton momentum and direction, as given by Table 6.5. The distribution of
2004 the reconstructed lepton momentum (for samples that only have one bin in
2005 reconstructed zenith angle) and reconstructed direction for each atmospheric
2006 sample used within this analysis is illustrated in Figure 6.2.

2007 The reconstructed lepton momemtum, illustrated by interaction mode break-
2008 down, of some representative atmospheric samples is given in Figure 6.3. The
2009 equivalent distributions of all atmospheric samples used within this analy-
2010 sis can be found in [182]. The low energy samples tend to be dominated by
2011 the interaction mode they target (CCQE for SubGeV-elike-0dcy and CC1 π for
2012 SubGeV-elike-1dcy samples). The higher energy samples include much more
2013 CCOther interactions, especially at larger reconstructed lepton momentum.

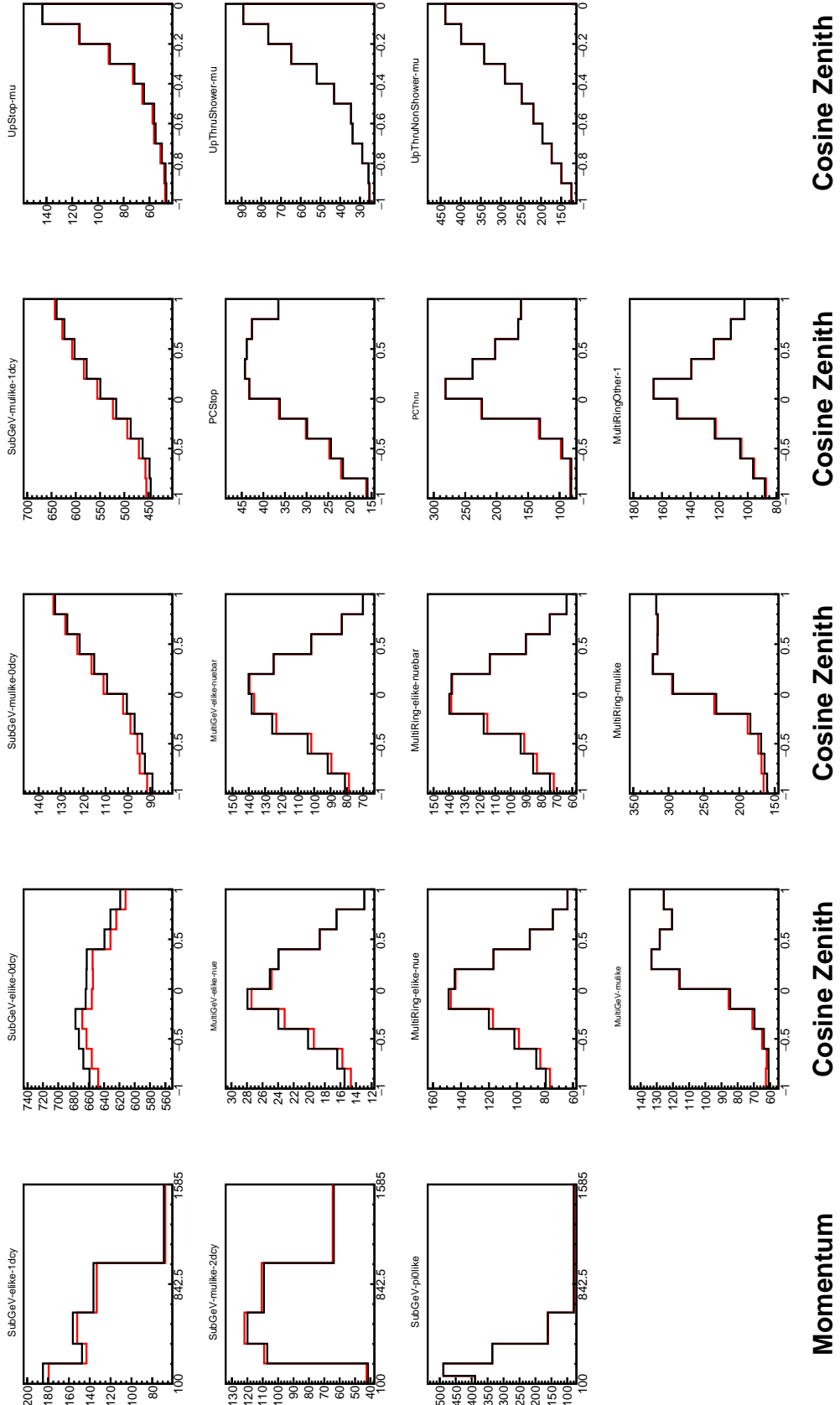


Figure 6.2: Comparison of the SK-IV atmospheric samples between predictions made with the CP-violating Asimov A (Black) and CP-conserving Asimov B (Red) oscillation parameter sets (given in Table 2.2). The subGeV samples CCRES and π^0 -like samples are given in their reconstructed lepton momentum. All other samples are presented in their reconstructed zenith angle projection.

Sample	$CC\nu_e$	$CC\bar{\nu}_e$	$CC(\nu_\mu + \bar{\nu}_\mu)$	$CC(\nu_\tau + \bar{\nu}_\tau)$	NC
SubGeV- <i>elike</i> -0dcy	72.17	23.3	0.724	0.033	3.77
SubGeV- <i>elike</i> -1dcy	86.81	1.773	7.002	0.062	4.351
SubGeV- <i>mulike</i> -0dcy	1.003	0.380	90.07	0.036	8.511
SubGeV- <i>mulike</i> -1dcy	0.023	0.	98.46	0.029	1.484
SubGeV- <i>mulike</i> -2dcy	0.012	0.	99.25	0.030	0.711
SubGeV- <i>pi0like</i>	6.923	2.368	0.928	0.011	89.77
MultiGeV- <i>elike</i> -nue	78.18	7.041	3.439	1.886	9.451
MultiGeV- <i>elike</i> -nuebar	56.68	37.81	0.174	0.614	4.718
MultiGeV- <i>mulike</i>	0.024	0.005	99.67	0.245	0.058
MultiRing- <i>elike</i> -nue	59.32	12.39	4.906	3.385	20
MultiRing- <i>elike</i> -nuebar	52.39	31.03	1.854	1.585	13.14
MultiRing- <i>mulike</i>	0.673	0.080	97.33	0.342	1.578
MultiRingOther-1	27.98	2.366	34.93	4.946	29.78
PCStop	8.216	3.118	84.45	0.	4.214
PCThru	0.564	0.207	98.65	0.	0.576
UpStop-mu	0.829	0.370	98.51	0.	0.289
UpThruNonShower-mu	0.206	0.073	99.62	0.	0.103
UpThruShower-mu	0.128	0.054	99.69	0.	0.132

Table 6.4: The purity of each atmospheric sample used within this analysis, broken down by charged current (CC) and neutral current (NC) interactions and which neutrino flavour interacted within the detector. Each row sums to 100% by definition. Asimov A oscillation parameter sets are assumed (given in Table 2.2). Electron neutrino and antineutrino events are separated to illustrate the ability of the separation likelihood cuts used within the multiGeV and multiring sample selections.

Sample	$\cos(\theta_Z)$ Bins	Momentum Bin Edges ($\log_{10}(P)$ MeV)
SubGeV- <i>elike</i> -0dcy	10	2.0, 2.4, 2.6, 2.8, 3.0, 3.2
SubGeV- <i>elike</i> -1dcy	1	2.0, 2.4, 2.6, 2.8, 3.0, 3.2
SubGeV- <i>mulike</i> -0dcy	10	2.0, 2.4, 2.6, 2.8, 3.0, 3.2
SubGeV- <i>mulike</i> -1dcy	10	2.0, 2.4, 2.6, 2.8, 3.0, 3.2
SubGeV- <i>mulike</i> -2dcy	1	2.0, 2.4, 2.6, 2.8, 3.0, 3.2
SubGeV- <i>pi0like</i>	1	2.0, 2.2, 2.4, 2.6, 2.8, 3.2
MultiGeV- <i>elike</i> -nue	10	3.0, 3.4, 3.7, 4.0, 5.0
MultiGeV- <i>elike</i> -nuebar	10	3.0, 3.4, 3.7, 4.0, 5.0
MultiGeV- <i>mulike</i>	10	3.0, 3.4, 5.0
MultiRing- <i>elike</i> -nue	10	3.0, 3.4, 3.7, 5.0
MultiRing- <i>elike</i> -nuebar	10	3.0, 3.4, 3.7, 5.0
MultiRing- <i>mulike</i>	10	2.0, 3.124, 3.4, 3.7, 5.0
MultiRing- <i>Other1</i>	10	3.0, 3.4, 3.7, 4.0, 5.0
PC-Stop	10	2.0, 3.4, 5.0
PC-Through	10	2.0, 3.124, 3.4, 3.7, 5.0
Upmu-Stop	10	3.2, 3.4, 3.7, 8.0
Upmu-Through-Showering	10	2.0, 8.0
Upmu-Through-NonShowering	10	2.0, 8.0

Table 6.5: The reconstructed cosine zenith and lepton momentum binning assigned to the atmospheric samples. The “ $\cos(\theta_Z)$ Bins” column illustrates the number of bins uniformly distributed over the $-1.0 \leq \cos(\theta_Z) \leq 1.0$ region for fully and partially contained samples and $-1.0 \leq \cos(\theta_Z) \leq 0.0$ region for up- μ samples.

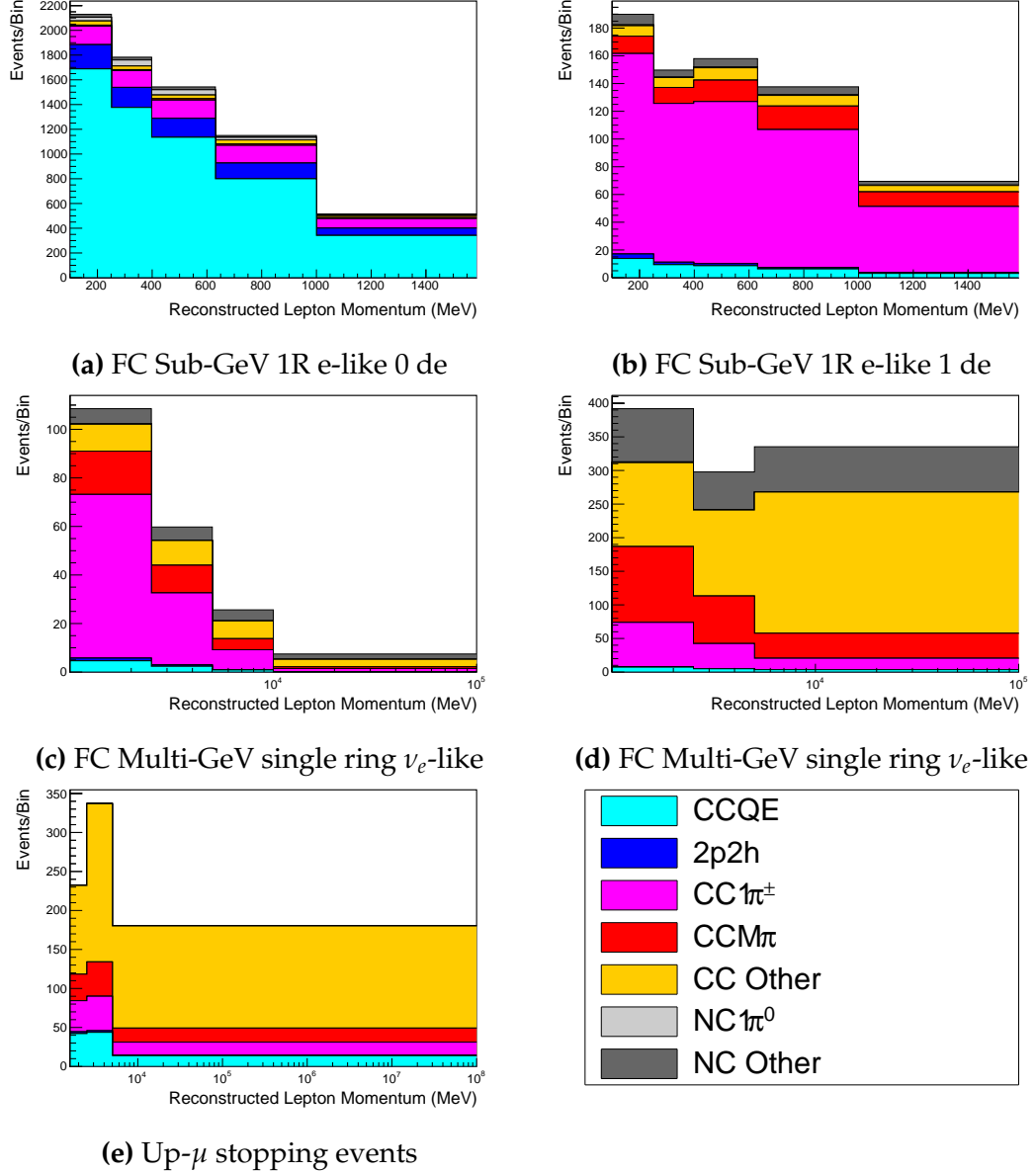


Figure 6.3: Breakdown by interaction mode of some representative atmospheric samples used within this analysis, illustrated as a function of reconstructed lepton momentum. The binning is provided in Table 6.5. Asimov A oscillation parameters are used to generate these plots. The interaction mode breakdown of all atmospheric samples used within this analysis can be found in [182].

2014 6.2 Near Detector Beam Samples

2015 The near detector sample selections are documented in detail within [183] and
2016 summarised below. Samples are selected based upon which of the two Fine
2017 Grained Detectors (FGD) the vertex is reconstructed in, as well as the operating
2018 mode of the beam: FHC or RHC. Wrong-sign neutrino background samples are
2019 considered in the RHC mode in order to add additional constraints on model
2020 parameters. Samples from the wrong-sign component of the FHC beam mode
2021 are not included as they are statistically insignificant compared to those samples
2022 already listed.

2023 The reconstruction algorithm uses a clustering algorithm to group hits within
2024 the TPC. It then adds this information together to form a track. In FHC(RHC),
2025 the highest momentum negative(positive) curvature track is defined as the muon
2026 candidate. Before being assigned a sample, these candidate muon events must
2027 pass CC-inclusive cuts, as defined in [184]:

- 2028 • Event Timing: The DAQ must be operational and the event must occur
2029 within the expected beam time window consistent with the beam spill
- 2030 • TPC Requirement: The muon-candidate track path must intercept one or
2031 more TPCs
- 2032 • Fiducial volume: The event must originate from within the fiducial volume
2033 defined in [185]
- 2034 • Upstream Background: Remove events that have muon tracks that originate
2035 upstream of the FGDs by requiring no high-momentum tracks within
2036 150mm upstream of the candidate vertex. Additionally, events that occur
2037 within the downstream FGD are vetoed if a secondary track starts within
2038 the upstream FGD
- 2039 • Broken track removal: All candidates where the muon candidate is broken
2040 in two are removed

- 2041 • Muon PID: Measurements of dE/dx in a TPC are used to distinguish muon-
2042 like events, from electron-like or proton-like, using a likelihood cut

2043 In addition to these cuts, RHC neutrino events also have to undergo the
2044 following cuts to aid in the separation of neutrino and antineutrino events [186]:

- 2045 • TPC Requirement: The track path must intercept TPC2
2046 • Positive Track: The highest momentum track must have a positive recon-
2047 structed charge
2048 • TPC1 Veto: Remove any events originating upstream of TPC1

2049 Once all CC-inclusive events have been determined, they are further split by
2050 pion multiplicity: CC0 π , CC1 π , and CCOther. Pions in the TPCs are selected by
2051 requiring a second track to be observed, which is separate from the muon track
2052 and is in the same beam spill window and sub-detector. The number of FGD
2053 pions is equal to the number of Michel electrons which were tagged within the
2054 same sub-detector and spill window. If this value is equal to zero, the number
2055 of FGD pions is equivalent to the number of pion-like tracks which have dE/dx
2056 measurements consistent with the pion hypothesis. The pion tracks from both
2057 FGD and TPC events are required to have a vertex consistent with that of the
2058 muon candidate. The Michel electron tagging is preferential as a delayed Michel
2059 is almost always a pion meaning this cut has a higher purity [184, 187], whereas a
2060 track in the FGD that is consistent with a pion could be another particle resulting
2061 in a lower purity. Michel electrons are neglected in the TPC as the pions very
2062 rarely stop due to the low density.

2063 CC0 π , CC1 π , and CCOther samples are defined with the following cuts:

- 2064 • ν_μ CC0 π Selection: No electrons in TPC and no charged pions or decay
2065 electrons within the TPC or FGD
- 2066 • ν_μ CC1 π Selection: Exactly one charged pion in either the TPC or FGD

- 2067 • ν_μ **CCOther Selection:** All events which are not classified into the above
 2068 two selections

2069 Counting the three selections for each FGD in FHC and RHC running, includ-
 2070 ing the wrong-sign background in RHC, 18 near detector samples are used within
 2071 this analysis. These samples are binned in reconstructed lepton momentum
 2072 (illustrated in Figure 6.4) and direction with respect to the beam. The binning
 2073 is chosen such that each event has at least 20 Monte Carlo events in each bin
 2074 [185]. This is to ensure that the bins are coarse enough to ensure the reduction
 2075 of statistical errors, whilst also being fine enough to sample the high-resolution
 2076 peak regions. The exact binning is detailed in [185].

2077 6.3 Far Detector Beam Samples

2078 The beam neutrino events which occur at the SK detector, which pass the
 2079 reduction cuts detailed in section 5.3, are separated based on whether the beam
 2080 was operating in FHC or RHC mode. The events are then separated into three
 2081 samples: electron-like ($1Re$), muon-like ($1R\mu$), and CC1 π^+ -like ($1Re1de$) which
 2082 are observed as electron-like events with an associated decay electron [175].
 2083 As discussed in section 6.1, positively charged pions emitted from neutrino
 2084 interactions are more likely to produce decay electrons than negatively charged
 2085 pions emitted from antineutrino interactions. Consequently, the CC1 π^+ -like
 2086 sample is only selected when the beam is operating in FHC mode. Therefore,
 2087 five beam samples measured at SK are used in this analysis.

2088 The fiducial volume definition for beam samples is slightly different from that
 2089 used for the atmospheric samples. It uses both the distance to the closest wall
 2090 (`dWall`) and the distance to the wall along the trajectory of the particle (`toWall`).
 2091 This allows events that originate close to the wall but are facing into the tank to be
 2092 included within the analysis, which would have otherwise been removed. These
 2093 additional events are beneficial for a statistics-limited experiment. The exact

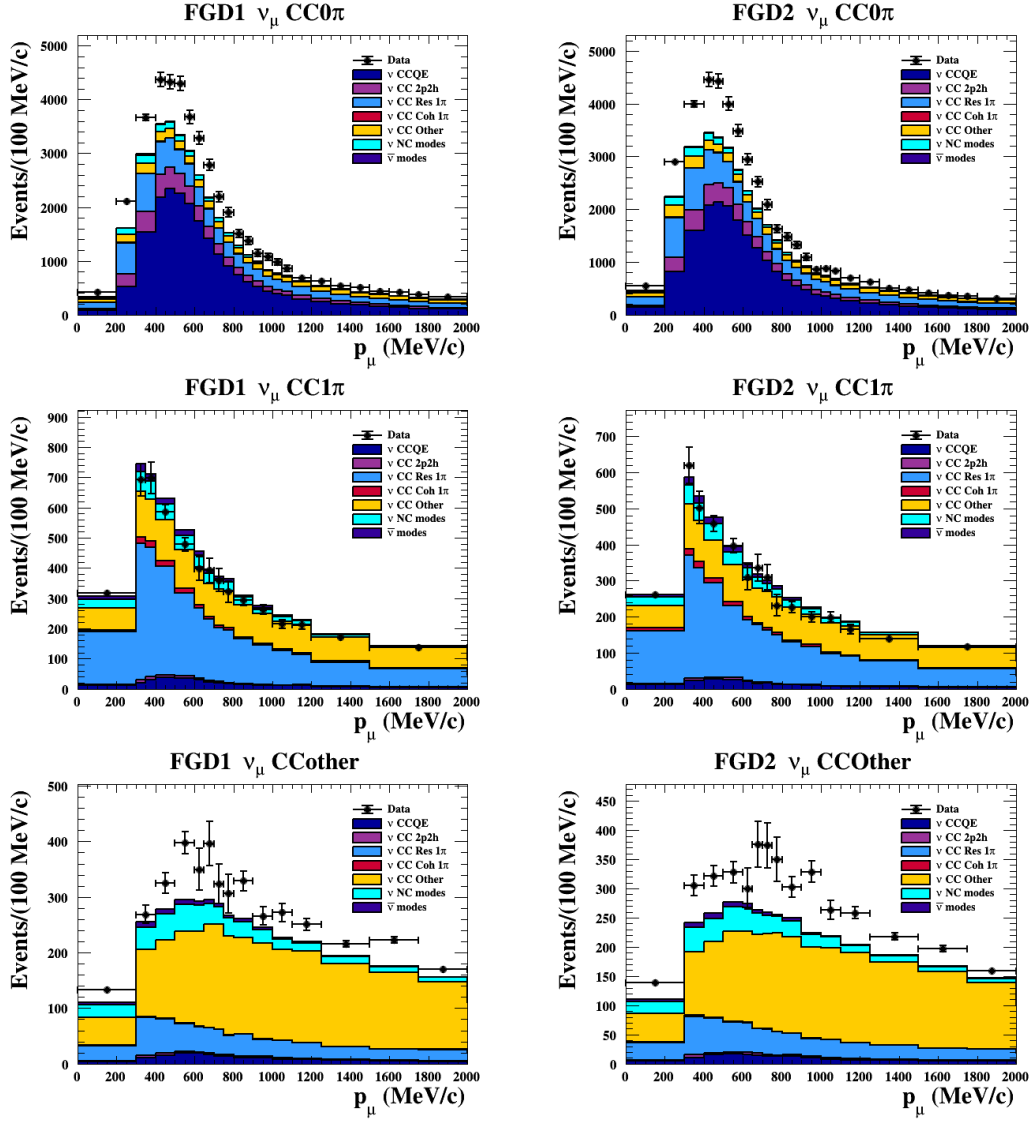


Figure 6.4: The nominal Monte Carlo predictions compared to data for the FGD1 and FGD2 samples in neutrino beam mode, broken down into the $CC\nu_\mu 0\pi$, $CC\nu_\mu 1\pi$ and $CC\nu_\mu$ Other categories. Figures taken from [183].

2094 cut values for both `dWall` and `tWall` are different for each of the three types of
 2095 sample and are optimised based on T2K sensitivity to δ_{CP} [173, 188]. They are:

2096 **1Re event selection** For an event to be classified as a 1Re-like, the event must sat-
 2097 isfy:

- 2098 • Fully-contained and have $dWall > 80\text{cm}$ and $tWall > 170\text{cm}$
- 2099 • Total of one ring which is reconstructed as electron-like with reconstructed

2100 momentum $P_e > 100\text{MeV}$

2101 • Zero decay electrons are associated with the event

2102 • Passes π^0 rejection cut discussed in section 5.2

2103 **CC1 π^+ event selection** This event selection is very similar to that of the 1Re
 2104 sample. The only differences are that the dWall and toWall criteria are changed
 2105 to $> 50\text{cm}$ and $> 270\text{cm}$, respectively, and exactly one decay electron is required
 2106 from the π^+ decay.

2107 **1R μ event selection** A 1R μ -like event is determined by the following cuts:

2108 • Fully-contained and have dWall $> 50\text{cm}$ and toWall $> 250\text{cm}$

2109 • Total of one ring which is reconstructed as muon-like with reconstructed
 2110 momentum $P_\mu > 200\text{MeV}$

2111 • Fewer than two decay electrons are associated with the event

2112 • Passes π^+ rejection cut discussed in section 5.2

2113 All of these samples are binned in reconstructed neutrino energy. This is
 2114 possible under a particular interaction mode assumption, as the direction from
 2115 the source is known extremely well. For the 1Re-like and 1R μ -like samples,

$$E_\nu^{rec} = \frac{(M_N - V_{nuc})E_l - m_l^2/2 + M_N V_{nuc} - V_{nuc}^2/2 + (M_P^2 + M_N^2)/2}{M_N - V_{nuc} - E_l + P_l \cos(\theta_{beam})}. \quad (6.2)$$

2116 Where M_N , M_P and m_l are the masses of the neutron, proton and outgoing
 2117 lepton, respectively. $V_{nuc} = 27\text{MeV}$ is the binding energy of the oxygen nucleus
 2118 [175], θ_{beam} is the angle between the beam and the direction of the outgoing
 2119 lepton, and E_l and P_l are the energy and momentum of that outgoing lepton.

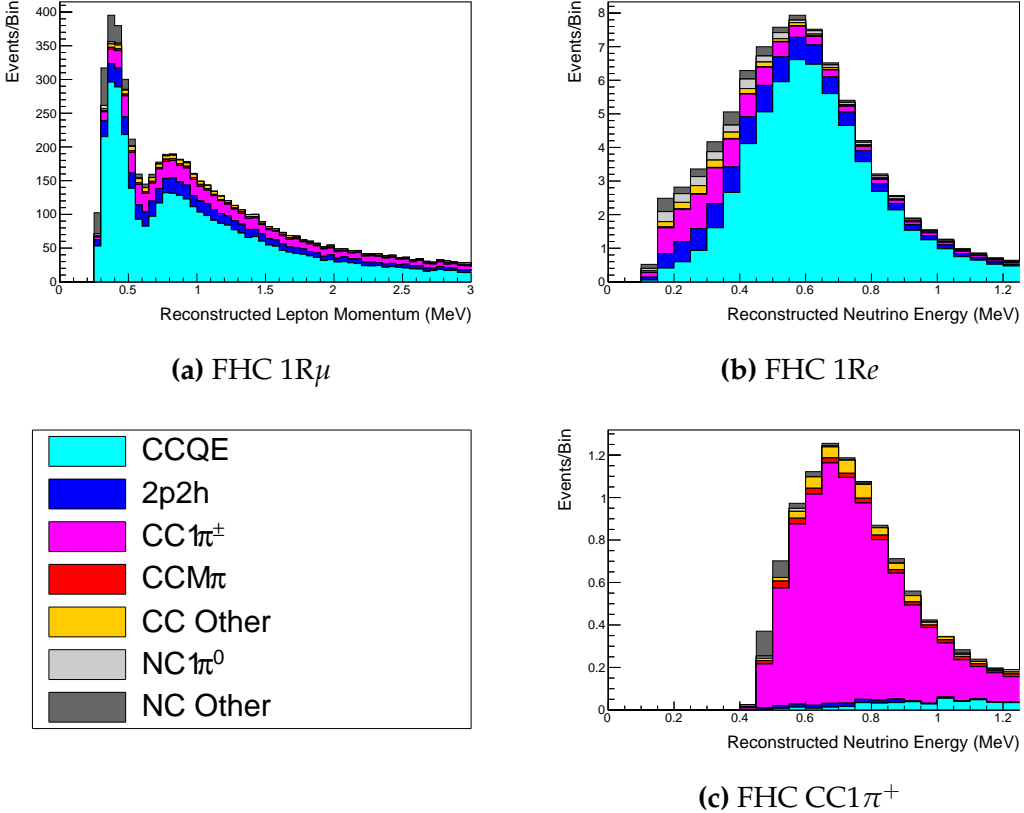


Figure 6.5: The reconstructed neutrino energy, as defined by Equation 6.2 and Equation 6.3, for the 1R μ -like, 1Re-like, and CC1 π^+ -like samples. The AsimovA oscillation parameters are assumed (given in Table 2.2). These samples are the FHC mode samples. For ease of viewing, the 1R μ sample only shows the $0 \leq E_\nu^{rec} < 3.0\text{GeV}$ but the binning extends to 30.0GeV.

2120 The reconstructed neutrino energy of the CC1 π^+ -like events also accounts
 2121 for the delta resonance produced within the interaction,

$$E_\nu^{rec} = \frac{2M_N E_l + M_{\Delta^{++}}^2 - M_N^2 - m_l^2}{2(M_N - E_l + P_l \cos(\theta_{beam}))}. \quad (6.3)$$

2122 Where $M_{\Delta^{++}}$ is the mass of the delta baryon. Binding energy effects are not
 2123 considered as a two-body process, with the delta baryon, is assumed. This follows
 2124 the T2K oscillation analysis presented in [2], although recent developments of
 2125 the interaction model in the latest T2K oscillation analysis do include effects
 2126 from binding energy in this calculation [189].

2127 The reconstructed neutrino energy for the FHC samples is illustrated in
 2128 Figure 6.5. As expected, the 1R μ -like and 1Re-like samples are heavily dominated

2129 by CCQE interactions, with smaller contributions from 2p2h meson exchange and
 2130 resonant pion production interactions. The CC1 π^+ -like sample predominantly
 2131 consists of charged current resonant pion production interactions. The 1Re-like
 2132 and CC1 π^+ -like samples are also binned by the angle between the neutrino beam
 2133 and the reconstructed lepton momentum. This is to aid in charged current and
 2134 neutral current separation, as indicated in Figure 6.6. This is because the neutral
 2135 current backgrounds are predominantly due to π^0 -decays, which decay into two
 2136 γ rays. The opening angle of which (alongside the different final state kinematics)
 2137 can produce a slightly broader angular distribution compared to the final state
 2138 particles originating from charged current ν_e interactions.

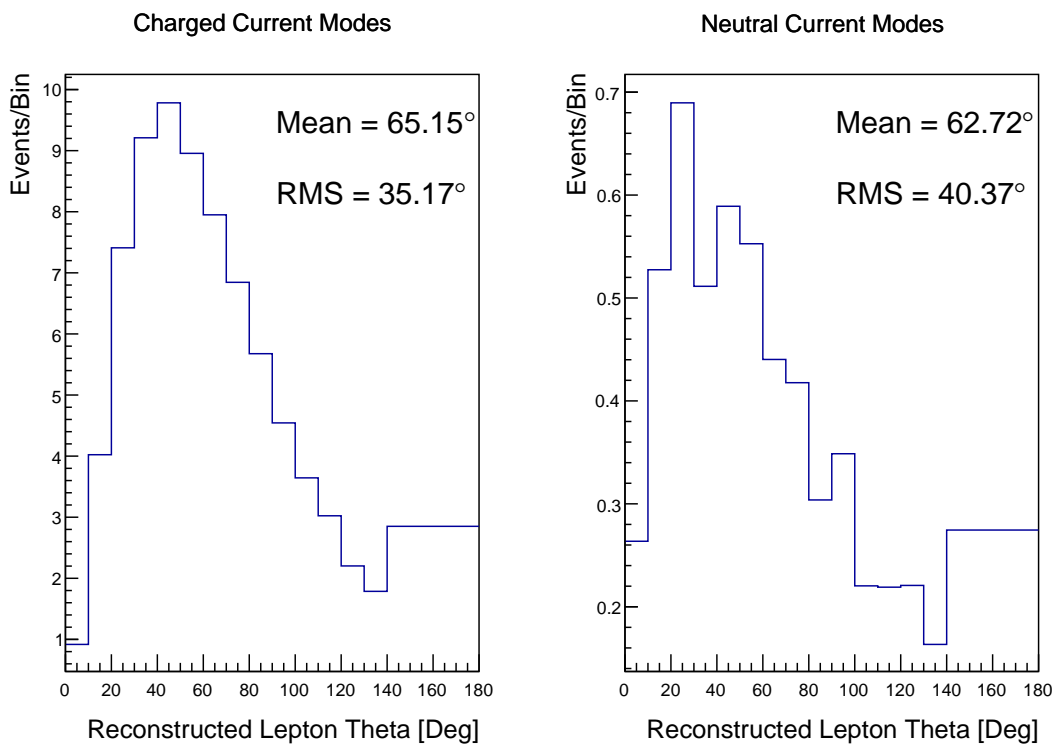


Figure 6.6: The distribution of the angle between the neutrino beam direction and the reconstructed final state lepton, for the FHC 1Re-like sample. The distribution is broken down by neutrino interaction mode into charged current (left) and neutral current (right) components. Asimov A oscillation parameter sets are assumed (given in Table 2.2). The RMS of the charged and neutral current plots are 35.17° and 40.37° , respectively.

2₁₃₉ 6.4 Systematic Uncertainties

2₁₄₀ The systematic model parameters for this analysis are split into groups, or blocks,
2₁₄₁ depending on their purpose. They consist of flux uncertainties, neutrino-matter
2₁₄₂ interaction systematics, and detector efficiencies. There are also uncertainties on
2₁₄₃ the oscillation parameters to which this analysis is not sensitive, namely Δm_{21}^2
2₁₄₄ and $\sin^2(\theta_{12})$. These oscillation parameter uncertainties are taken from the 2020
2₁₄₅ PDG measurements [72]. As described in chapter 4, each model parameter used
2₁₄₆ within this analysis requires a prior uncertainty. This is provided via separate
2₁₄₇ covariance matrices for each block. The covariance matrices can include prior
2₁₄₈ correlations between parameters within a single block, but the separate treatment
2₁₄₉ means prior correlations can not be included for parameters in different groups.
2₁₅₀ Some parameters in these models have no reasonably motivated uncertainties
2₁₅₁ and are assigned flat priors which do not modify the likelihood penalty. In
2₁₅₂ practice, these flat prior parameters are actually assigned a Gaussian with a
2₁₅₃ very large width to ensure the covariance matrix is positive definite. They are
2₁₅₄ then checked at run time to determine if they contribute to the likelihood. The
2₁₅₅ flux, neutrino interaction, and detector modeling simulations have already been
2₁₅₆ discussed in section 5.1 and section 5.2. The uncertainties invoked within each
2₁₅₇ of these models are described below.

2₁₅₈ 6.4.1 Beam Flux

2₁₅₉ The neutrino beam flux systematics are based upon the uncertainty in the model-
2₁₆₀ ing of the components of the beam simulation. This includes the model of hadron
2₁₆₁ production and reinteraction, the shape, intensity, and alignment of the beam
2₁₆₂ with respect to the target, and the uniformity of the magnetic field produced by
2₁₆₃ the horn, alongside other effects. The uncertainty, as a function of neutrino energy,
2₁₆₄ is illustrated in Figure 6.7 which includes a depiction of the total uncertainty as
2₁₆₅ well as the contribution from individual components. The uncertainty around

- ₂₁₆₆ ($E_\nu \sim 1.0\text{GeV}$) is dominated by uncertainties in the beam profile and alignment.
₂₁₆₇ Outside of this region, uncertainties on hadron production dominate the error.

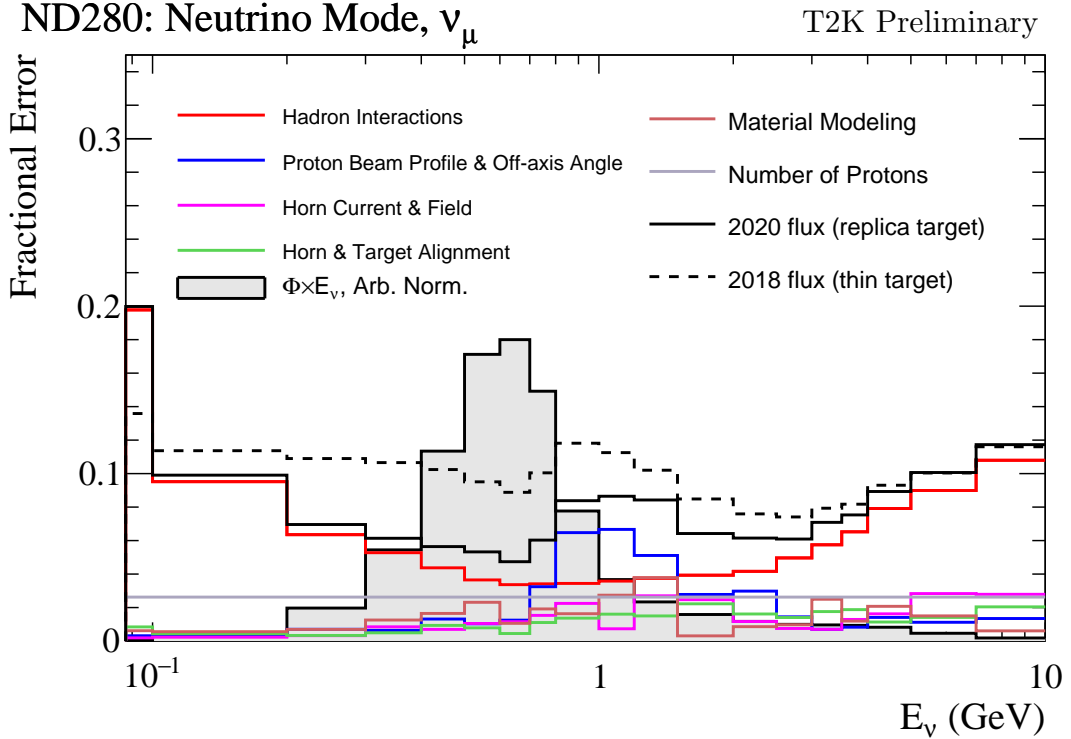


Figure 6.7: The total uncertainty evaluated on the near detector ν_μ flux prediction constrained by the replica-target data, illustrated as a function of neutrino energy. The solid(dashed) line indicates the uncertainty used within this analysis(the T2K 2018 analysis [190]). The solid histogram indicates the neutrino flux as a function of energy. Figure taken from [191].

₂₁₆₈ The beam flux uncertainties are described by one hundred parameters. They
₂₁₆₉ are split between the ND280 and SK detectors and binned by neutrino flavour:
₂₁₇₀ ν_μ , $\bar{\nu}_\mu$, ν_e and $\bar{\nu}_e$. The response is then broken down as a function of neutrino
₂₁₇₁ energy. The bin density in the neutrino energy is the same for the ν_μ in FHC
₂₁₇₂ and $\bar{\nu}_\mu$ in RHC beams, and narrows for neutrino energies close to the oscillation
₂₁₇₃ maximum of $E_\nu = 0.6\text{GeV}$. This binning is specified in Table 6.6. All of these
₂₁₇₄ systematic uncertainties are applied as normalisation parameters with Gaussian
₂₁₇₅ priors centered at 1.0 and error specified from a covariance matrix provided
₂₁₇₆ by the T2K beam group [191].

Neutrino Flavour	Sign	Neutrino Energy Bin Edges (GeV)
μ	Right	0., 0.4, 0.5, 0.6, 0.7, 1., 1.5, 2.5, 3.5, 5., 7., 30.
μ	Wrong	0., 0.7, 1., 1.5, 2.5, 30.
e	Right	0., 0.5, 0.7, 0.8, 1.5, 2.5, 4., 30.
e	Wrong	0., 2.5, 30.

Table 6.6: The neutrino energy binning for the different neutrino flavours. “Right” sign indicates neutrinos in the FHC beam and antineutrinos in the RHC beam. “Wrong” sign indicates antineutrinos in the FHC beam and neutrinos in the RHC beam. The binning of the detector response is identical for the FHC and RHC modes as well as at ND280 and SK.

2177 6.4.2 Atmospheric Flux

2178 The atmospheric neutrino flux is modeled by the HKKM model [50]. 16 systematic
 2179 uncertainties are applied to control the normalisation of each neutrino flavour,
 2180 energy, and direction. They are summarised below:

- 2181 • **Absolute Normalisation:** The overall normalisation of each neutrino flavour
 2182 is controlled by two independent systematic uncertainties, for $E_\nu < 1\text{GeV}$
 2183 and $E_\nu > 1\text{GeV}$, respectively. This is driven mostly by hadronic interaction
 2184 uncertainties for the production of pions and kaons [50]. The strength of
 2185 the response is dependent upon the neutrino energy. The uncertainty is
 2186 parameterized following Figure 11 in [50].
- 2187 • **Relative Normalisation:** Uncertainties on the ratio of $(\nu_\mu + \bar{\nu}_\mu) / (\nu_e + \bar{\nu}_e)$
 2188 are controlled by the difference between the HKKM model [50], FLUKA
 2189 [53] and Bartol models [49]. Three independent parameters are applied in
 2190 the energy ranges: $E_\nu < 1\text{GeV}$, $1\text{GeV} < E_\nu < 10\text{GeV}$, and $E_\nu > 10\text{GeV}$.
- 2191 • **$\nu/\bar{\nu}$ Normalisation:** The uncertainties in the π^+/π^- (and kaon equivalent)
 2192 production uncertainties in the flux of $\nu/\bar{\nu}$. The response is applied using
 2193 the same methodology as the relative normalisation parameters.
- 2194 • **Up/Down and Vertical/Horizontal Ratio:** Similar to the above two sys-
 2195 tematics, the difference between the HKKM, FLUKA, and Bartol model

2196 predictions, as a function of $\cos(\theta_Z)$, is used to control the normalisation of
 2197 events as a function of zenith angle.

- 2198 • **K/π Ratio:** Higher energy neutrinos ($E_\nu > 10\text{GeV}$) mostly originate in
 2199 kaon decay. Measurements of the ratio of K/π production [192] are used to
 2200 control the systematic uncertainty of the expected ratio of pion and kaon
 2201 production.
- 2202 • **Solar Activity:** As the 11-year solar cycle can affect the Earth's magnetic
 2203 field, the flux of primary cosmic rays varies across the same period. The
 2204 uncertainty is calculated by taking a ± 1 year variation, equating to a 10%
 2205 uncertainty for the SK-IV period.
- 2206 • **Atmospheric Density:** The height of the interaction of the primary cosmic
 2207 rays is dependent upon the atmospheric density. The HKKM assumes the
 2208 US standard 1976 [142] profile. This systematic controls the uncertainty in
 2209 that model.

2210 The total uncertainty is dominated by the absolute and relative normalisation
 2211 parameters. The effect of which is illustrated in Figure 6.8. Generally, the
 2212 uncertainty is large at low energy, reducing to $O(10\%)$ around the peak of the
 2213 flux distribution and then increasing once the neutrino energy exceeds 10GeV.

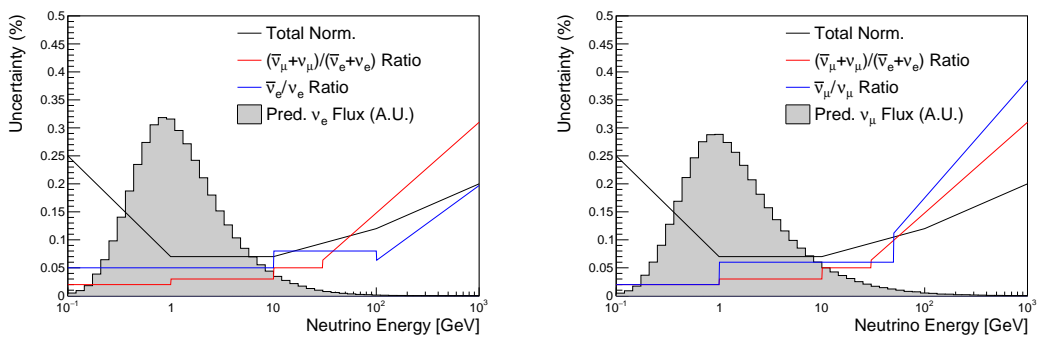


Figure 6.8: The uncertainty evaluated on the atmospheric ν_e (left) and ν_μ (right) flux predictions. The absolute normalisation and flavour ratio uncertainties are given. The solid histogram indicates the neutrino flux as a function of energy.

2214 Updates to the HKKM and Bartol models are underway [147] to use a similar
2215 tuning technique to that used in the beam flux predictions. After those updates,
2216 it may be possible to include correlations in the hadron production uncertainty
2217 systematics for beam and atmospheric flux predictions.

2218 **6.4.3 Neutrino Interaction**

2219 Neutrino interactions in the detectors are modeled by NEUT. The two indepen-
2220 dent oscillation analyses, T2K-only [193] and the SK-only [59], have developed
2221 separate interaction models. To maximise sensitivity out of this simultaneous
2222 beam and atmospheric analysis, a correlated interaction model has been defined
2223 in [182]. Where applicable, correlations allow the systematic uncertainties applied
2224 to the atmospheric samples to be constrained by near detector neutrino beam
2225 measurements. This can lead to stronger sensitivity to oscillation parameters
2226 as compared to an uncorrelated model.

2227 The low-energy T2K systematic model has a more sophisticated treatment
2228 of CCQE, 2p2h, and CCRES uncertainties, where extensive comparisons of
2229 this model have been performed to external data [193]. However, the model
2230 is not designed for high-energy atmospheric events, like those illustrated in
2231 Figure 5.11. Therefore the high energy systematic model from the SK-only
2232 analysis is implemented for the relevant multi-GeV, PC, and up- μ samples.

2233 The high energy systematic model includes parameters developed from
2234 comparisons of Nieves and Rein-Seghal models which affect resonant pion
2235 producing interactions, comparisons of the GRV98 and CKMT models which
2236 control DIS interactions, and hadron multiplicity measurements which modulate
2237 the normalisation of multi-pion producing events. The uncertainty on the ν_τ cross-
2238 section is particularly large and is controlled by a 25% normalisation uncertainty.
2239 These uncertainties are applied via normalisation or shape parameters. The
2240 former linearly scales the weight of all affected Monte-Carlo events, whereas
2241 the latter can increase or decrease a particular event's weight depending on its
2242 neutrino energy and mode of interaction. The response of the shape parameters is

defined by third-order polynomial splines which return a weight for a particular parameter variation. To reduce computational resources for the far detector fit, the response is binned by neutrino energy and sample binning: reconstructed lepton momentum and cosine zenith binning for atmospheric splined responses and reconstructed neutrino energy and direction binning for beam samples. In total, 17 normalisation and 15 shape parameters are included in the high-energy model within this analysis.

Figure 6.9 indicates the predicted neutrino energy distribution for both beam and subGeV atmospheric samples. There is clearly significant overlap in neutrino energy between the subGeV atmospheric and beam samples, allowing similar kinematics in the final state particles. Figure 6.10 illustrates the fractional contribution of the different interaction modes per sample.

Comparing beam and atmospheric samples which target CCQE interactions (S.G. e-like 0de, S.G. μ -like [0,1]de, [FHC,RHC] 1R μ -like and [FHC,RHC] 1R e-like samples), there is a very similar contribution of CCQE, CC 2p2h, and CC1 π^\pm interactions. The samples which target CC1 π^\pm interactions, (S.G. e-like 1de, S.G. μ -like 2de and FHC 1R+1d.e e-like) also consist of very similar mode interactions.

As a consequence of the similarity in energy and mode contributions, correlating the systematic model between the beam and subGeV atmospheric samples ensures that this analysis attains the largest sensitivity to oscillation parameters while still ensuring neutrino interaction systematics are correctly accounted for. Due to its more sophisticated CCQE and 2p2h model, the T2K systematic model was chosen as the basis of the correlated model. Separate low-energy (for beam and subGeV atmospheric samples) and high-energy (other atmospheric samples) CCQE dials have been implemented. The low-energy dials are constrained by the near detector measurements and are uncorrelated to their high-energy counterparts. The author of this thesis was responsible for implementing and validating the combined cross-section model as documented in [182, 194].

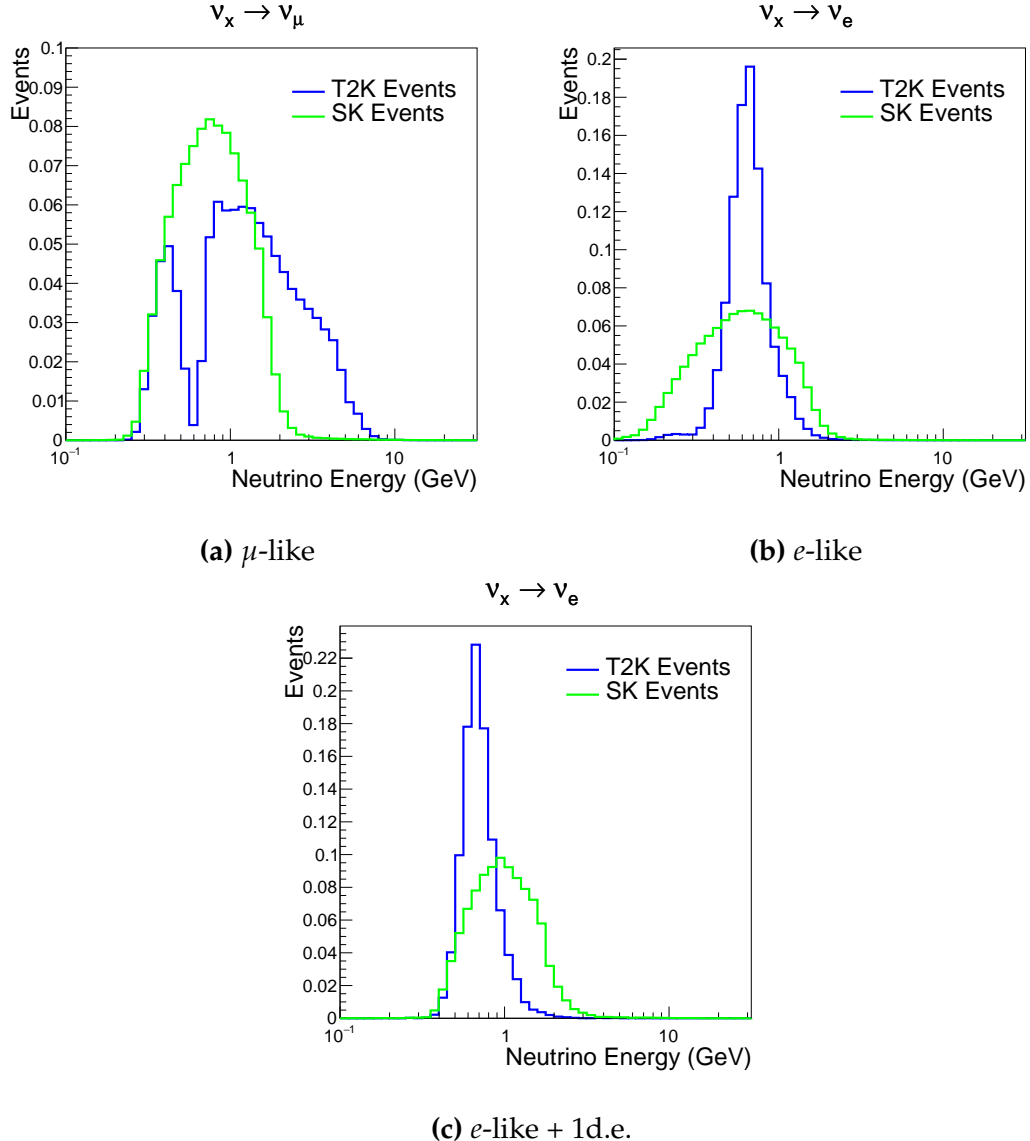


Figure 6.9: The predicted neutrino energy distribution for subGeV atmospheric and beam samples. FHC and RHC beam samples are summed together Asimov A oscillation parameters are assumed (given in Table 2.2). Beam and atmospheric samples with similar cuts are compared against one another.

The T2K systematic model [193] is applied in a similar methodology to the SK model parameters. It consists of 19 shape parameters and 24 normalisation parameters. Four additional parameters, which model the uncertainty in the binding energy, are applied in a way to shift the momentum of the lepton emitted from a nucleus. This controls the uncertainty specified on the 27MeV binding energy assumed within Equation 6.2. The majority of these parameters are assigned a

	CC QE	CC 2p2h	CC $1\pi^\pm$	CC $M\pi$	CC Other	NC $1\pi^0$	NC $1\pi^\pm$	NC $M\pi$	NC Coh.	NC Other
FHC 1R+1d.e. e-like	0.04	0.02	0.83	0.03	0.04	0.01	0.01	0.01	0.00	0.01
RHC 1R e-like	0.62	0.12	0.11	0.01	0.02	0.06	0.01	0.01	0.01	0.04
FHC 1R e-like	0.68	0.12	0.10	0.00	0.02	0.04	0.01	0.00	0.00	0.02
RHC 1R μ -like	0.62	0.13	0.17	0.02	0.03	0.00	0.02	0.00	0.00	0.00
FHC 1R μ -like	0.62	0.12	0.16	0.02	0.03	0.00	0.03	0.00	0.00	0.00
S.G. π^0 -like	0.05	0.01	0.02	0.00	0.01	0.68	0.06	0.07	0.06	0.04
S.G. μ -like 2de	0.04	0.01	0.80	0.10	0.04	0.00	0.00	0.00	0.00	0.00
S.G. μ -like 1de	0.72	0.11	0.12	0.01	0.02	0.00	0.01	0.00	0.00	0.00
S.G. μ -like 0de	0.68	0.11	0.10	0.01	0.02	0.01	0.05	0.01	0.00	0.02
S.G. e-like 1de	0.05	0.01	0.75	0.10	0.05	0.00	0.01	0.02	0.00	0.01
S.G. e-like 0de	0.73	0.11	0.10	0.01	0.02	0.02	0.00	0.00	0.00	0.00

Figure 6.10: The interaction mode contribution of each sample given as a fraction of the total event rate in that sample. Asimov A oscillation parameters are assumed (given in Table 2.2). The Charged Current (CC) modes are broken into quasi-elastic (QE), 2p2h, resonant charged pion production ($1\pi^\pm$), multi-pion production ($M\pi$), and other interaction categories. Neutral Current (NC) interaction modes are given in interaction mode categories: π^0 production, resonant charged pion production, multi-pion production, and others.

2278 Gaussian prior uncertainty. Those that have no reasonably motivated uncertainty,
2279 or those which have not been fit to external data, are assigned a flat prior.

2280 On top of the combination of the SK and T2K interaction models, several other
2281 parameters have been specifically developed for the joint oscillation analysis
2282 [182]. The majority of the atmospheric samples' δ_{CP} sensitivity comes from
2283 the normalisation of subGeV electron-like events. These are modeled using a
2284 spectral function to approximate the nuclear ground state. However, choosing
2285 an alternative model could affect the sensitivities. Therefore, an additional
2286 systematic is introduced which models an alternative Continous Random Phase
2287 Approximation (CRPA) nuclear ground state. This dial approximates the event
2288 weights if a CRPA model had been assumed rather than a spectral function.

2289 This dial only applies to ν_e and $\bar{\nu}_e$ as the near detector does not constraint ν_e
2290 cross-section measurements. It is applied as a shape parameter.

2291 Further additions to the model have been introduced due to the inclusion of
2292 the subGeV π^0 atmospheric sample. This particularly targets charged current and
2293 neutral current π^0 producing interactions. Therefore, an uncertainty that affects
2294 neutral current resonant π^0 production is incorporated into this analysis. Com-
2295 parisons of NEUT's NC resonant pion production predictions have been made to
2296 MiniBooNE [195] data and a consistent 16% to 21% underprediction is observed
2297 [182]. Consequently, a conservative 30% normalisation parameter is invoked.

2298 Down-going events are mostly insensitive to oscillation parameters and can
2299 act similar to the near detector within an accelerator experiment (as discussed in
2300 section 2.5 and section 5.1). This region of phase space can act as a sideband and
2301 allows the cross-section model and near detector constraint to be studied. The
2302 distribution of events in this region is calculated using the technique outlined in
2303 subsection 4.3.4. The results are illustrated in Figure 6.11. For CCQE-targeting
2304 samples, the application of the near detector constraint is well within the sta-
2305 tistical fluctuation of the down-going data. This means there is no significant
2306 tension observed between the data and the Monte Carlo prediction after the near
2307 detector constraint is applied. This is not the case for samples with target CCRES
2308 interactions. The electron-like data is consistent with the constrained prediction
2309 at high reconstructed momenta but diverges at lower momentum, whereas the
2310 muon-like sample is under-predicted throughout the range of momenta. To
2311 combat this disagreement, an additional cross-section systematic dial, specifically
2312 designed to inflate the low pion momentum systematics was developed in [182].
2313 This is a shape parameter implemented through a splined response.

2314 6.4.4 Near Detector

2315 The systematics applied due to uncertainties arising from the response of the near
2316 detector is documented in [122]. The response is described by 574 normalisation
2317 parameters binned in the selected sample as well as momentum and angle

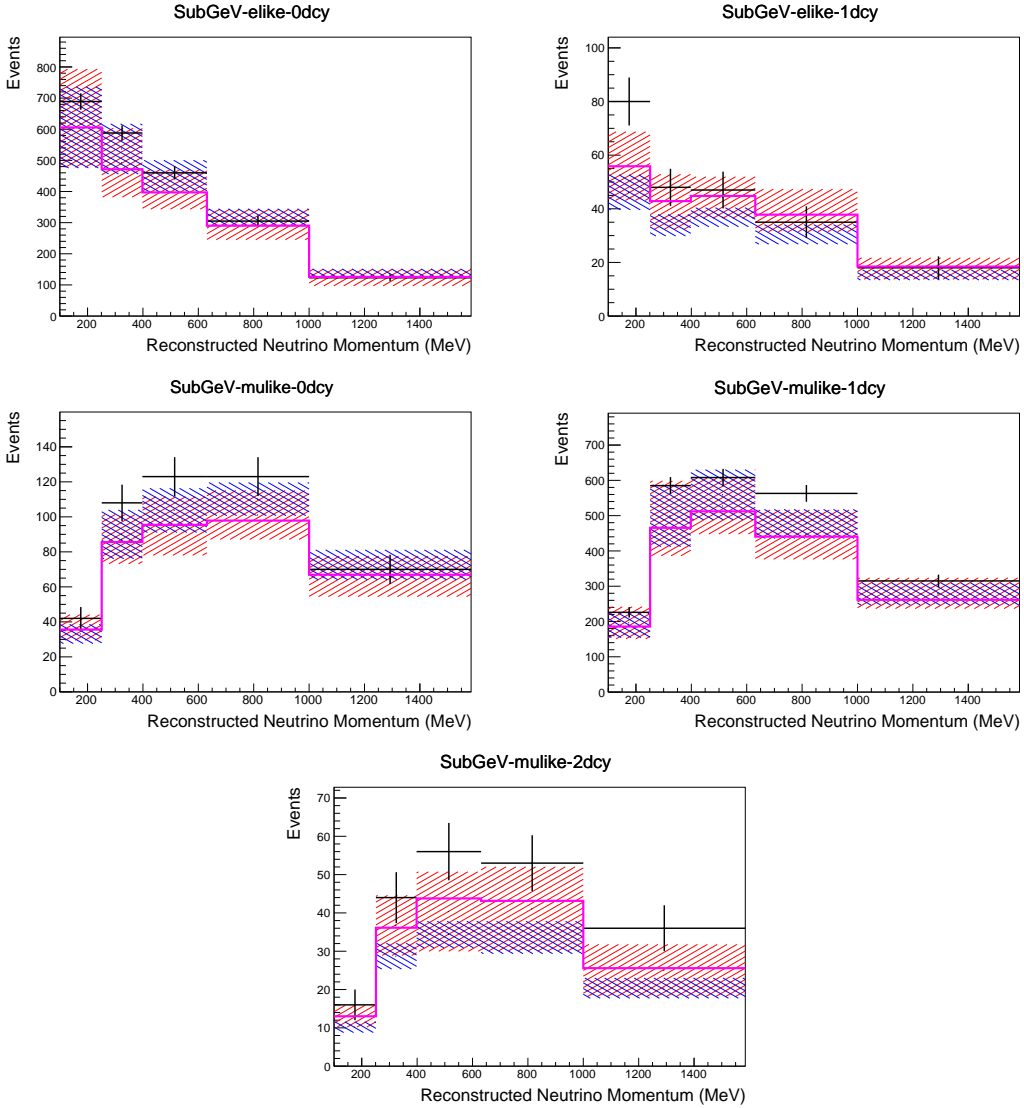


Figure 6.11: Down-going atmospheric subGeV single-ring samples comparing the mean and error of the pre-fit and post-fit Monte Carlo predictions in red and blue, respectively. The magenta histogram illustrates the Monte Carlo prediction using the generated dial values. The black points illustrate the down-going data with statistical errors given. The mean and errors of the Monte Carlo predictions are calculated by the techniques documented in subsection 4.3.4. The pre-fit spectrum is calculated by throwing the cross-section and atmospheric flux dial values from the pre-fit covariance matrix. The post-fit spectrum is calculated by sampling the cross-section dial values from an ND fit MCMC chain, whilst still throwing the atmospheric flux dials from the pre-fit covariance.

relative to the beam, P_μ and $\cos(\theta_\mu)$, of the final-state muon. These are applied via a covariance matrix with each parameter being assigned a Gaussian prior from that covariance matrix. These normalisation parameters are built from underlying systematics, e.g. pion secondary interaction systematics, which are

randomly thrown and the variation in each $P_\mu \times \cos(\theta_\mu)$ bin is determined. Two thousand throws are evaluated and a covariance matrix response is created. This allows significant correlations between FGD1 and FGD2 samples, as well as adjacent $P_\mu \times \cos(\theta_\mu)$ bins. Statistical uncertainties are accounted for by including fluctuations of each event's weight from a Poisson distribution.

Similar to the cross-section systematics, MaCh3 and BANFF are used to constrain the uncertainty of these systematics through independent validations. Each fitter generates a post-fit covariance matrix which is compared and passed to the far-detector oscillation analysis working group. As the analysis presented within this thesis uses the MaCh3 framework, a joint oscillation analysis fit of all three sets of samples and their respective systematics is performed.

6.4.5 Far Detector

Two configurations of the far detector systematic model implementation have been considered. Firstly, the far detector systematic uncertainties for beam and atmospheric samples are taken from their respective analysis inputs, denoted “official inputs” analysis, with no correlations assumed between the beam and atmospheric samples. The beam- and atmospheric-specific inputs are documented in subsubsection 6.4.5.1 and subsubsection 6.4.5.2. Secondly, an alternative detector model has been trialed which correlates the response of the SK detector systematics between the beam and low-energy atmospheric samples. Here, the distribution of parameters used for applying event cuts (e.g. electron-muon PID separation) is simultaneously fit alongside the oscillation parameters. It follows a similar methodology to the beam far detector systematics implementation but performs a joint fit of the beam and atmospheric data. This alternative concept is detailed in subsubsection 6.4.5.3.

6.4.5.1 Beam Samples

There are 45 systematics which describe the response of the far detector to beam events [175], split into 44 normalisation parameters and one energy scale

systematic. The energy scale systematic is applied as a multiplicative scaling of the reconstructed neutrino energy. It is estimated from data-to-Monte Carlo differences in the stopping muon sample and found to be 2.1% [59]. The normalisation parameters are assigned a Gaussian error centered at 1.0 with width taken from a covariance matrix. A detailed breakdown of the generation of the covariance matrix is found in [188]. To build the covariance matrix, a fit is performed on atmospheric data which has been selected using beam sample selection cuts. These cuts use the variables, L^i , where the index i is detailed in Table 6.7. Each L^i is modified by a smear, α , and shift, β parameter such that,

$$L_j^i \rightarrow \bar{L}_j^i = \alpha_j^i L_j^i + \beta_j^i. \quad (6.4)$$

Where L_j^i (\bar{L}_j^i) correspond to nominal(varied) PID cut parameters given in Table 6.7. The shift and smear parameters are nuisance parameters with no prior constraints. They are binned by final-state topology, j , where the binning is given in Table 6.8. The final-state topology binning is because the detector will respond differently to events that have one or multiple rings. For example, the detector will be able to distinguish single-ring events better than two overlapping ring events, resulting in different systematic uncertainty for one-ring events compared to two-ring events. This approach is used to allow the cut parameter distributions to be modified within the fit, allowing for better data to Monte Carlo agreement.

Cut Variable	Parameter Name
0	<code>fitQun e/μ PID</code>
1	<code>fitQun e/π⁰ PID</code>
2	<code>fitQun μ/π PID</code>
3	<code>fitQun Ring-Counting Parameter</code>

Table 6.7: List of cut variables that are included within the shift/smear fit documented in [188].

The mis-modeling of π^0 events is also considered. If one of the two rings from a π^0 event is missed, this will be reconstructed as a $CC\nu_e$ -like event. This is one of the largest systematics hindering the electron neutrino appearance analyses.

Category	Description
1e	Only one electron above Cherenkov threshold in the final state
1 μ	Only one muon above Cherenkov threshold in the final state
1e+other	One electron and one or more other charged particles above Cherenkov threshold in the final state
1 μ +other	One muon and one or more other charged particles above Cherenkov threshold in the final state
1 π^0	Only one π^0 in the final state
1 π^\pm or 1p	Only one hadron (typically charged pion or proton) in the final state
Other	Any other final state

Table 6.8: Reconstructed event topology categories on which the SK detector systematics [188] are based.

2371 Consequently, additional systematics have been introduced to constrain the
 2372 mis-modeling of π^0 events in SK, binned by reconstructed neutrino energy. To
 2373 evaluate this systematic uncertainty, a set of “hybrid- π^0 ” samples are constructed.
 2374 These events are built by overlaying one electron-like ring from the SK atmo-
 2375 spheric neutrino samples, or a decay electron ring from a stopping cosmic ray
 2376 muon, with a simulated photon ring. Both rings are chosen so that momenta and
 2377 opening angle follow the decay kinematics of NC π^0 events from the T2K-MC.
 2378 Hybrid- π^0 Monte Carlo samples with both rings from the SK Monte Carlo are
 2379 produced to compare with the hybrid- π^0 data samples and the difference in the
 2380 fraction of events that pass the ν_e selection criteria is used to assign the systematic
 2381 errors. In order to investigate any data to Monte Carlo differences that may
 2382 originate from either the higher energy ring or lower energy ring, two samples
 2383 are built: a sample in which the electron constitutes the higher energy ring from
 2384 the π^0 decay (called the primary sample) and another one in which it constitutes
 2385 the lower energy ring (called the secondary sample). The standard T2K ν_e fitQun
 2386 event selection criteria are used to select events.

2387 Final contributions to the covariance matrix are determined by supplemen-
 2388 tary uncertainties obtained by comparing stopping muon data to Monte Carlo
 2389 prediction, as first introduced in section 5.2. The efficiency of tagging decay
 2390 electrons is estimated by the stopping muon data to Monte Carlo differences by
 2391 comparing the number of one decay electron events to the number of events with

2392 one or fewer decay electrons. Similarly, the rate at which fake decay electrons
 2393 are reconstructed by `fitTQun` is estimated by comparing the number of two decay
 2394 electron events to the number of events with one or two reconstructed decay
 2395 electrons. The two sources of systematics are added in quadrature weighted by
 2396 the number of events with one true decay electron yielding a 0.2% systematic
 2397 uncertainty. A fiducial volume systematic of $\pm 2.5\text{cm}$ which corresponds to a 0.5%
 2398 shift in the normalisation of events is also applied. Additional normalisation
 2399 uncertainties based on neutrino flavour and interaction mode are also defined
 2400 in [175, 196, 197].

2401 Two additional sources of uncertainty are included: secondary and photo-
 2402 nuclear interactions. These are estimated by varying the underlying parameters
 2403 and building a distribution of sample event rates. These contributions are then
 2404 added in quadrature to the above covariance matrix. The final uncertainty on
 2405 the SK detector systematics are provided in Figure 6.12.

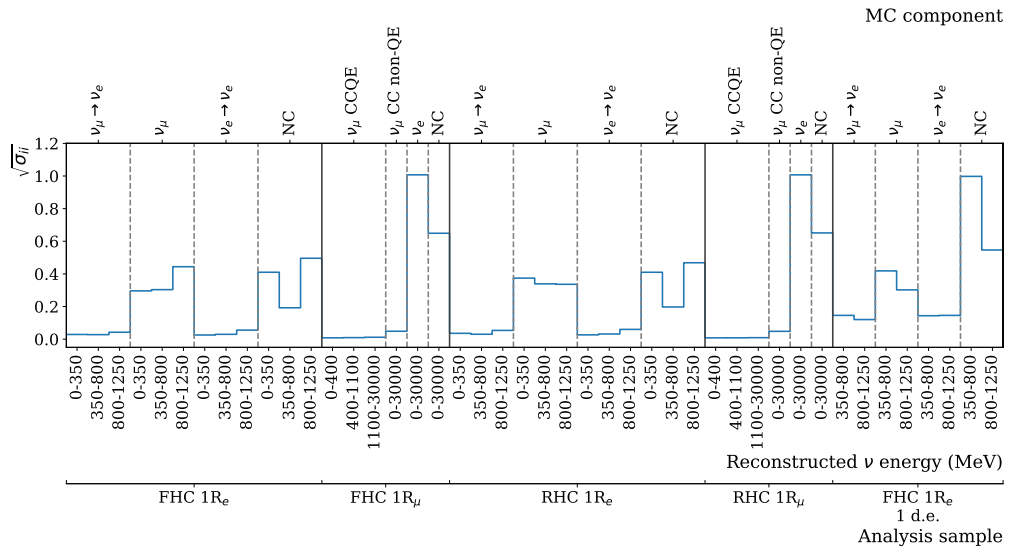


Figure 6.12: The fractional uncertainty on each of the 44 parameters describing the SK detector systematics (The energy scale systematic is neglected). The parameters are split by sample, oscillation channel, interaction mode and reconstructed neutrino energy.

2406 6.4.5.2 Atmospheric Samples

2407 The detector systematics for atmospheric samples, documented in [3], are split
 2408 into two sub-groups: those which are related to particle identification and ring

2409 counting systematics, and those which are related to calibration, separation,
2410 and reduction uncertainties.

2411 The particle identification systematics consist of five parameters. The ring sep-
2412 aration systematic enforces an anti-correlated response between the single-ring
2413 and multi-ring samples. This is implemented as a fractional increase/decrease
2414 in the overall normalisation of each sample, depending on the distance to the
2415 nearest wall from an event’s vertex. The coefficients of the normalisation are
2416 estimated prior to the fit and depend on the particular atmospheric sample. Two
2417 electron-muon separation systematics are included within this model which
2418 anti-correlates the response of the electron-like and muon-like samples: one for
2419 single-ring events and another for multi-ring events.

2420 The multiGeV multiring electron-like separation likelihood, discussed in
2421 section 6.1, encodes the ability of the detector to separate neutrino from anti-
2422 neutrino events. Two normalisation parameters vary the relative normalisation
2423 of multi-ring ν_e and $\bar{\nu}_e$ samples whilst keeping a consistent overall event rate.

2424 There are 22 systematics related to calibration measurements, including effects
2425 from backgrounds, reduction, and showering effects. They are documented in
2426 [3] and are briefly summarised in Table 6.9. They are applied via normalisation
2427 parameters, with the separation systematics requiring the conservation of event
2428 rate across all samples.

2429 6.4.5.3 Correlated Detector Model

2430 As an extension to the analysis, a conceptual implementation of correlated
2431 detector model, following the T2K-only model implementation documented in
2432 subsubsection 6.4.5.1, has been considered. It correlates the detector systematics
2433 between the far-detector beam and subGeV atmospheric samples due to their
2434 similar energies and interaction types. As there are no equivalent beam samples,
2435 the multi-GeV, multiring, PC, and Up- μ samples will be subject to the particle
2436 identification systematics implementation as described in subsubsection 6.4.5.2

Index	Description
0	Partially contained reduction
1	Fully contained reduction
2	Separation of fully contained and partially contained events
3	Separation of stopping and through-going partially contained events in top of detector
4	Separation of stopping and through-going partially contained events in barrel of detector
5	Separation of stopping and through-going partially contained events in bottom of detector
6	Background due to cosmic rays
7	Background due to flasher events
8	Vertex systematic moving events into and out of fiducial volume
9	Upward going muon event reduction
10	Separation of stopping and through-going in upward going muon events
11	Energy systematic in upward going muon events
12	Reconstruction of the path length of upward going muon events
13	Separation of showering and non-showering upward going muon events
14	Background of stopping upward going muon events
15	Background of non-showering through-going upward going muon events
16	Background of showering through-going upward going muon events
17	Efficiency of tagging two rings from π^0 decay
18	Efficiency of decay electron tagging
19	Background from downgoing cosmic muons
20	Asymmetry of energy deposition in tank
21	Energy scale deposition

Table 6.9: Sources of systematic errors specified within the grouped into the “calibration” systematics model.

²⁴³⁷ rather than using this correlated detector model. The calibration systematics also
²⁴³⁸ described in the aforementioned chapter still apply to all atmospheric samples.

²⁴³⁹ The correlated detector model concept utilises the same smear and shift
²⁴⁴⁰ parameters documented in subsubsection 6.4.5.1, split by final state topology.
²⁴⁴¹ Beyond this, the shift and smear parameters are split by visible energy deposited
²⁴⁴² within the detector, with binning specified in Table 6.10. This is because higher
²⁴⁴³ energy events are more likely to be better reconstructed due to fractionally less
²⁴⁴⁴ noise within the detector. As a result of the inclusion of visible energy binning,

²⁴⁴⁵ Equation 6.4 becomes

$$L_{jk}^i \rightarrow \bar{L}_{jk}^i = \alpha_{jk}^i L + \beta_{jk}^i, \quad (6.5)$$

²⁴⁴⁶ where k is the visible energy bin.

Index	Range (MeV)
0	$30 \geq E_{vis} > 300$
1	$300 \geq E_{vis} > 700$
2	$700 \geq E_{vis} > 1330$
3	$E_{vis} \geq 1330$

Table 6.10: Visible energy binning for which the correlated SK detector systematics are based

²⁴⁴⁷ The implementation of this systematic model takes the events reconstructed
²⁴⁴⁸ values of the cut parameters, modifies them by the particular shift and smear
²⁴⁴⁹ parameter for that event, and then re-applies event selection. This causes event
²⁴⁵⁰ migration, which is a new feature incorporated into the MaCh3 framework which
²⁴⁵¹ is only achievable due to the event-by-event reweighting scheme.

²⁴⁵² Particular care has to be taken when varying the ring counting parameter.
²⁴⁵³ This is because the number of rings is a finite value (one-ring, two-ring, etc.)
²⁴⁵⁴ which can not be continuously varied through this shift and smear technique.
²⁴⁵⁵ Consequently a continuous ring counting parameter, RC_i , is calculated for the
²⁴⁵⁶ i^{th} event, following the definition in [174]. The preferred likelihoods from all
²⁴⁵⁷ considered one-ring (L_{1R}) and two-ring (L_{2R}) fits are determined. The difference
²⁴⁵⁸ is computed as $\Delta_{LLH} = \log(L_{1R}) - \log(L_{2R})$. The ring counting parameter is
²⁴⁵⁹ then defined as

$$RC_i = \text{sgn}(\Delta_{LLH}) \times \sqrt{|\Delta_{LLH}|}, \quad (6.6)$$

²⁴⁶⁰ where $\text{sgn}(x) = x/|x|$. This ring counting parameter corresponds to an
²⁴⁶¹ intermediate likelihood value used within the `fitQun` algorithm to decide the
²⁴⁶² number of rings associated with a particular event. However, fake-ring merging
²⁴⁶³ algorithms are applied after this likelihood value is used. Consequently, this

2464 ring counting parameter does not always exactly correspond to the number of
2465 reconstructed rings. This can be seen in Figure 6.13.

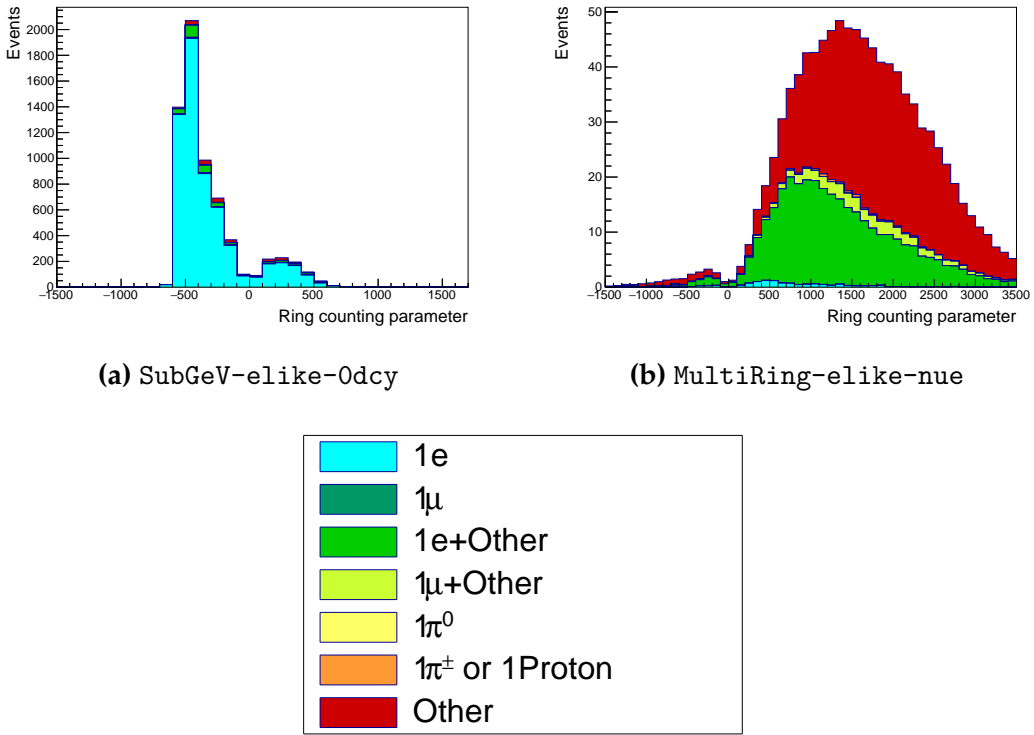


Figure 6.13: The ring counting parameter as defined in Equation 6.6 for the SubGeV-else-like-0dcy and MultiRing-else-like-nue samples.

2466 As the `fitQun` algorithm does not provide a likelihood value after the fake-
2467 ring algorithms have been applied, the ring counting parameter distribution is
2468 correlated to the final number of reconstructed rings through “maps”. These
2469 are two-dimensional distributions of the ring counting parameter and the final
2470 number of reconstructed rings. An example is illustrated in Figure 6.14. In
2471 principle, the `fitQun` reconstruction algorithm should be re-run after the variation
2472 in the ring counting parameter. However, this is not computationally viable.
2473 Therefore the “maps” are used as a reweighting template.

2474 The maps are split by final state topology and true neutrino flavour and
2475 all `fitQun`-reconstructed Monte Carlo events are used to fill them. The maps
2476 are row-normalised to represent the probability of X rings for a given RC_i
2477 value. Prior to the oscillation fit, an event’s nominal weight is calculated as

2478 $W^i(N_{Rings}^i, L_{jk}^i)$, where N_{Rings}^i is the reconstructed number of rings for the i^{th}
 2479 event and $W^i(x, y)$ is the bin content in map associated with the i^{th} event, where
 2480 x number of rings and y is ring counting parameter. Then during the fit, the
 2481 value of $R = W^i(N_{Rings}^i, \bar{L}_{jk}^i)/W^i(N_{Rings}^i, L_{jk}^i)$ is calculated as the event weight
 2482 for the i^{th} event. This is the only cut variable that uses a reweighting technique
 2483 rather than event migration.

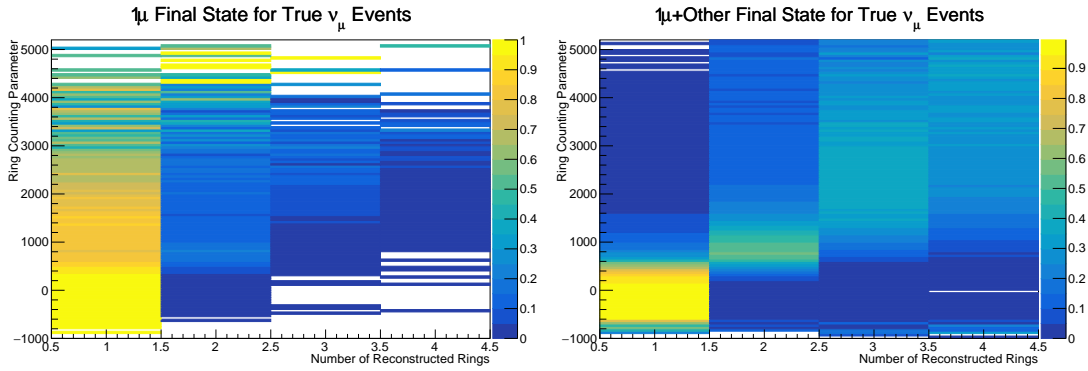


Figure 6.14: The ring counting parameter, defined in Equation 6.6, as a function of the number of reconstructed rings as found by the `fitQun` reconstruction algorithm. Left: true ν_μ events with only one muon above the Cherenkov threshold in the final state. Right: true ν_μ events with one muon and at least one other charged particle above the Cherenkov threshold in the final state.

2484 The π^0 systematics introduced in subsection 6.4.4 are applied via a covariance
 2485 matrix. This is not possible in the alternative model as no covariance matrix
 2486 is used. Thus, the implementation of the π^0 systematics has been modified.
 2487 The inputs from the hybrid π^0 sample are included via the use of “ χ^2 maps”,
 2488 which are two-dimensional histograms in α_{jk}^i and β_{jk}^i parameters over some
 2489 range. Illustrative examples of the χ^2 maps are given in Figure 6.15. Due to
 2490 their nature, the shift and smear parameters are typically very correlated. A
 2491 map is produced for each cut parameter given in Table 6.7 and for each visible
 2492 energy bin given in Table 6.10.

2493 The maps are filled through the χ^2 comparison of the hybrid π^0 Monte Carlo
 2494 and data in the particle identification parameters documented in Table 6.7. The
 2495 Monte Carlo distribution is modified by the α_{jk}^i and β_{jk}^i scaling, whilst cross-
 2496 section and flux nuisance parameters are thrown from their prior uncertainties.

2497 The χ^2 between the scaled Monte Carlo and data is calculated and the relevant
 2498 point in the χ^2 map is filled.

2499 The implementation within this alternative detector model is to add the bin
 2500 contents of the maps, for the relevant values of the α_{jk}^i and β_{jk}^i parameters, to
 2501 the likelihood penalty. Only $1\pi^0$ final state topology shift and smear parameters
 2502 use this prior uncertainty.

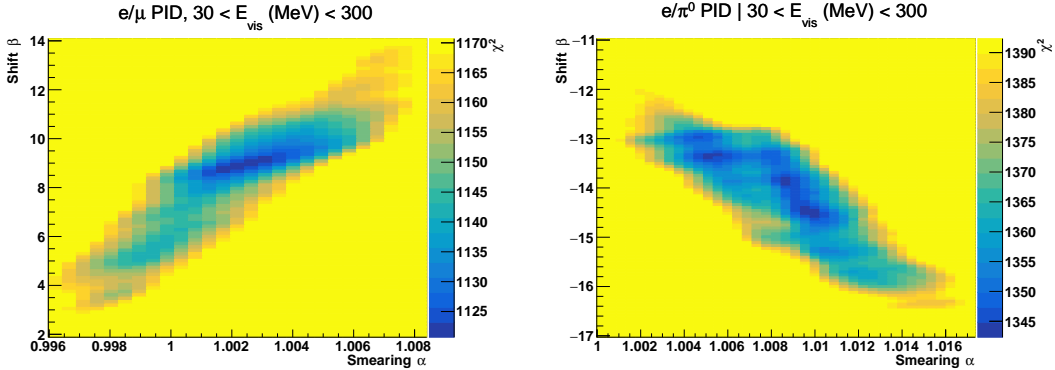


Figure 6.15: The χ^2 between the hybrid- π^0 Monte Carlo and data samples, as a function of smear (α) and shift (β) parameters, for events which have $1\pi^0$ final state topology. Left: Electron-muon separation PID parameter for events with $30 \leq E_{vis}(\text{MeV}) < 300$. Right: Electron- π^0 separation PID parameter for events with $30 \leq E_{vis}(\text{MeV}) < 300$.

2503 Similarly, the implementation of the supplementary systematics documented
 2504 in subsubsection 6.4.5.1 needs to be modified. A new framework [198] was built
 2505 in tandem between the author of this thesis and the T2K-SK working group [175]
 2506 so the additional parameters can be incorporated into the MaCh3 framework.
 2507 These are applied as normalisation parameters, depending on the particular
 2508 interaction mode, number of tagged decay electrons, and whether the primary
 2509 particle generated Cherenkov light. They are assigned Gaussian uncertainties
 2510 with widths described by a covariance matrix. Furthermore, the secondary
 2511 interaction and photo-nuclear effects need to be accounted for in this detector
 2512 model using a different implementation than that in subsubsection 6.4.5.1. This
 2513 was done by including a shape parameter for each of the secondary interaction
 2514 and the photo-nuclear systematic parameters.

2515 There are a total of 224 α_{jk}^i and β_{jk}^i parameters, of which 32 have prior
 2516 constraints from the hybrid π^0 samples.

2517 One final complexity of this correlated detector model is that the two sets of
 2518 samples, beam and subGeV atmospheric, use slightly different parameters to
 2519 distinguish electron and muon-like events. The T2K samples use the value of
 2520 $\ln(L_e/L_\mu)$ whereas the atmospheric samples use the value of $\ln(L_e/L_\pi)$, where
 2521 L_X is the likelihood for hypothesis X. This is because the T2K fits use single-ring
 2522 fitQun fitting techniques, whereas multi-ring fits are applied to the atmospheric
 2523 samples where only the electron and pion hypothesis are considered. The
 2524 correlation between the two likelihood ratios is illustrated in Figure 6.16. As
 2525 discussed in section 5.2, the pion hypothesis is a very good approximation of the
 2526 muon hypothesis due to their similar mass. Consequently, using the same shift
 2527 and smear parameters correlated between the beam and subGeV atmospheric
 2528 samples is deemed a good approximation.

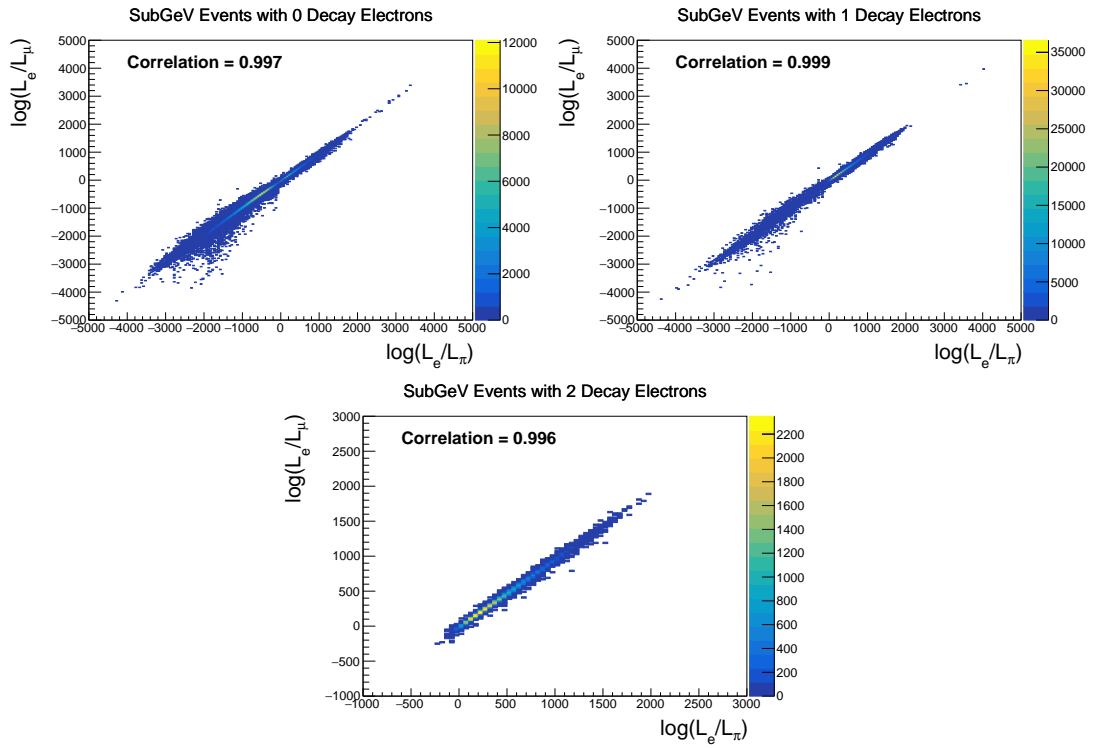


Figure 6.16: The distribution of $\log(L_e/L_\mu)$ compared to $\log(L_e/L_\pi)$ for subGeV events with zero (top left), one (top right) or two (bottom) decay electrons. The correlation in the distribution is calculated as 0.997, 0.999 and 0.996, respectively.

2529 6.5 Likelihood Calculation

2530 This analysis performs a joint oscillation parameter fit of the ND280 beam
2531 samples, the T2K far detector beam samples, and the SK atmospheric samples
2532 introduced in this chapter.

2533 Once the Monte Carlo predictions of each beam and atmospheric sample
2534 have been built, a likelihood needs to be constructed. This is done by comparing
2535 the binned Monte Carlo prediction to binned data. The Monte Carlo prediction
2536 is calculated at a particular point, $\vec{\theta}$, in the model parameter space such that
2537 $N_i^{MC} = N_i^{MC}(\vec{\theta})$, where N_i represents the bin content of the i^{th} bin. The data
2538 and Monte Carlo spectra are represented by N_i^D and N_i^{MC} , respectively. The bin
2539 contents for the beam near detector, beam far detector and atmospheric samples
2540 are denoted with ND , FD , and Atm , respectively. Taking the FHC1Rmu far detector
2541 sample as an example, the binning index runs over all the reconstructed neutrino
2542 energy bins. The likelihood calculation between the data and the Monte Carlo
2543 prediction for a particular bin follows a Poisson distribution, where the data
2544 is treated as a fluctuation of the simulation.

2545 The data can consist of either real data or an ‘Asimov’ Monte Carlo prediction,
2546 which is typically used for sensitivity studies and denoted ‘Asimov data’. The
2547 process for building Asimov data is as follows. The Monte Carlo prediction is
2548 reweighted using a particular set of oscillation parameters (potentially those
2549 listed in Table 2.2) and systematic parameter tune. The resulting spectra for each
2550 sample is then defined to be the Asimov data for that sample. Whilst this results
2551 in unphysical non-integer data predictions, it eliminates statistical fluctuations
2552 from the data. Therefore, the results of a fit to Asimov data should not include any
2553 biases from statistical fluctuations. Furthermore, these results should produce
2554 posterior probability distributions consistent with the parameters which were
2555 used to make the data prediction. That is to say, the fit results should return the
2556 known parameters. Any biases seen would be attributed to correlations between
2557 each oscillation parameter and correlations between oscillation and systematic

parameters. Consequently, Asimov fit results present the maximum precision at which the oscillation parameters could be measured to.

Following the T2K analysis presented in [2], the likelihood contribution for the near detector samples also includes a Monte Carlo statistical uncertainty term, derived from the Barlow and Beeston statistical treatment [199, 200]. It includes a contribution to the likelihood that treats the generated Monte Carlo prediction as a statistical fluctuation of the actual true simulation assuming an infinite amount of statistics had been created. The technical implementation of this additional likelihood term is documented in [183] and briefly summarised as follows. This additional term is defined as,

$$\frac{(\beta_i - 1)^2}{2\sigma_{\beta_i}^2}, \quad (6.7)$$

where β_i represents a scaling parameter for the i^{th} bin that relates the bin content for the amount of Monte Carlo actually generated N_i^{MC} to the bin content if an infinite amount of Monte Carlo statistics had been generated $N_{i,true}^{MC}$, such that $N_{i,true}^{MC} = \beta_i \times N_i^{MC}$. In the case where a sufficient amount of Monte Carlo statistics had been generated, $\beta_i = 1$ such that this additional terms tends to zero. An analytical solution for β_i is given in [183]. Additionally, $\sigma_{\beta_i} = \sqrt{\sum_i w_i^2 / N_i^{MC}}$ where $\sqrt{\sum_i w_i^2}$ represents the sum of the square of the weights of the Monte Carlo events which fall into bin i .

An additional contribution to the likelihood comes from the variation of the systematic model parameters. For those parameters with well-motivated uncertainty estimates, a covariance matrix, V , describes the prior knowledge of each parameter as well as any correlations between the parameters. Due to a technical implementation, a single covariance matrix describes each “block” of model parameters, e.g. beam flux systematics. The covariance matrix associated with the k^{th} block is denoted V^k . There are seven individual blocks of systematics ($N_b = 7$): oscillation parameters, beam flux systematics, atmospheric flux systematics, neutrino interaction systematics, near detector systematics, beam far detector systematics, and atmospheric far detector systematics. The

²⁵⁸⁶ number of parameters in the k^{th} block is defined as $n(k)$ and $\vec{\theta}^k$ represents the
²⁵⁸⁷ systematics associated with the k^{th} block.

²⁵⁸⁸ The equation for the likelihood \mathcal{L} includes all the terms discussed above,

$$\begin{aligned}
 -\ln(\mathcal{L}) = & \\
 & \sum_i^{\text{NDbins}} N_i^{\text{ND},MC}(\vec{\theta}) - N_i^{\text{ND},D} + N_i^{\text{ND},D} \times \ln \left[N_i^{\text{ND},D} / N_i^{\text{ND},MC}(\vec{\theta}) \right] + \frac{(\beta_i - 1)^2}{2\sigma_{\beta_i}^2} \\
 & + \sum_i^{\text{FDbins}} N_i^{\text{FD},MC}(\vec{\theta}) - N_i^{\text{FD},D} + N_i^{\text{FD},D} \times \ln \left[N_i^{\text{FD},D} / N_i^{\text{FD},MC}(\vec{\theta}) \right] \\
 & + \sum_i^{\text{Atmbins}} N_i^{\text{Atm},MC}(\vec{\theta}) - N_i^{\text{Atm},D} + N_i^{\text{Atm},D} \times \ln \left[N_i^{\text{Atm},D} / N_i^{\text{Atm},MC}(\vec{\theta}) \right] \\
 & + \frac{1}{2} \sum_k^{\text{N}_b} \sum_i^{n(k)} \sum_j^{n(k)} (\vec{\theta}^k)_i (V^k)_{ij}^{-1} (\vec{\theta}^k)_j.
 \end{aligned} \tag{6.8}$$

²⁵⁸⁹ The negative log-likelihood value is determined at each step of the MCMC
²⁵⁹⁰ to build the posterior distribution defined in chapter 4. This value is minimised
²⁵⁹¹ when the Monte Carlo prediction tends towards the data spectrum.

7

2592

2593

Oscillation Probability Calculation

2594 It is important to understand how and where the sensitivity to the oscillation parameters comes from for both atmospheric and beam samples. An
2595 overview of how these samples respond to changes in δ_{CP} , Δm_{32}^2 , and $\sin^2(\theta_{23})$
2596 is given in section 2.5. This section also explains the additional complexities
2597 involved when performing an atmospheric neutrino analysis as compared to
2598 a beam-only analysis.

2600 Without additional techniques, atmospheric sub-GeV upward-going neutrinos ($E_\nu < 1.33\text{GeV}, \cos(\theta_Z) < 0.$) can artificially inflate the sensitivity to δ_{CP} ,
2601 due to the quickly varying oscillation probability in this region. Therefore, a
2602 “sub-sampling” approach has been developed to reduce these biases ensuring
2603 accurate and reliable sensitivity measurements. This technique ensures that small-
2604 scale unresolvable features of the oscillation probability have been averaged
2605 over whilst the large-scale features in the oscillation probability are unaffected.
2606 The documentation and validation of this technique are found in section 7.1.
2607 The oscillation probability calculation is computationally intensive due to the
2608 large number of matrix multiplications needed. Consequently, the CUDAProb3
2609 implementation made within the fitting framework, as detailed in section 7.2,
2610 ensures that the analysis can be done in a timely manner.

Whilst the beam neutrinos are assumed to propagate through a constant density slab of material, the density variations through the Earth result in more complex oscillation patterns for atmospheric neutrinos. Furthermore, the uncertainty in the electron density can modify the oscillation probability for the denser core layers of the Earth. The model of the Earth used within this analysis is detailed in section 7.3. This includes information about the official SK-only methodology as well as improvements that have been made to remove some of the approximations used in that analysis. Another complexity of atmospheric neutrino oscillation studies is that the height of production in the atmosphere is not known on an event-by-event basis. An analytical averaging technique that approximates the uncertainty of the oscillation probability has been followed, with the author of this thesis being responsible for the implementation and validation. This implementation of an external technique is described in section 7.4.

7.1 Treatment of Fast Oscillations

As shown in Figure 7.1, atmospheric neutrino oscillations have a significantly more complex structure for upgoing neutrinos with energy below 1GeV. This is because the L/E dependence of the oscillation probability in this region induces rapid variations for small changes in L or E . As discussed in section 2.5, this is also the region in which atmospheric neutrinos have sensitivity to δ_{CP} . In practice, the direction of the neutrino is inferred from the direction of the final state particles traveling in the detector. The correlation between these two directions can be particularly weak for low-energy neutrino interactions. This creates a distinct difference from the beam neutrinos where the position of the source is very precisely known.

As a consequence of the unresolvable structure, an event rate consistent with the averaged oscillation probability is observed in the subGeV upgoing region. This creates a computational problem: A significantly large amount of Monte Carlo statistics would be required to accurately predict the number of events if Monte Carlo averaging was the only technique used. This section describes

2641 the ‘sub-sampling’ approach developed to mitigate these biases and compares
2642 it to the methodology used within the SK-only analysis.

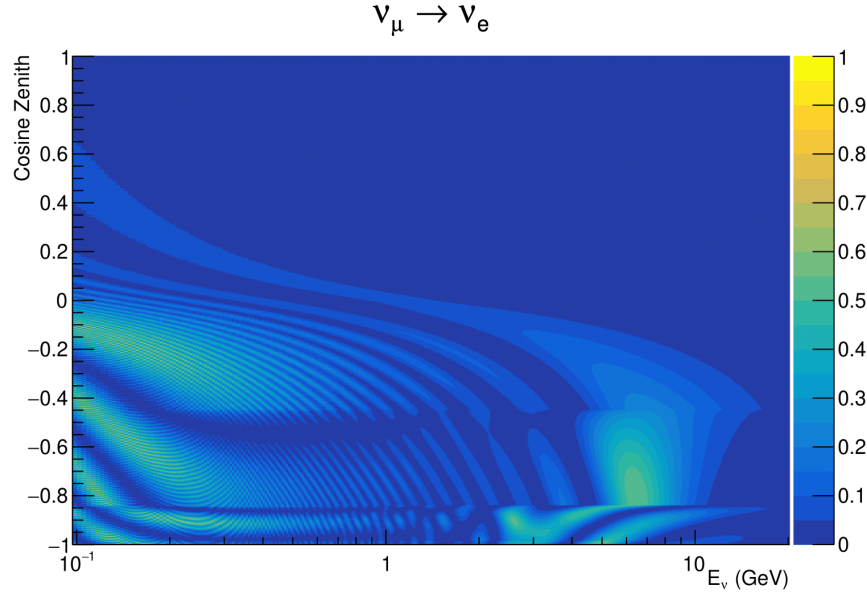


Figure 7.1: The oscillation probability $P(\nu_\mu \rightarrow \nu_e)$, given as a function of neutrino energy and zenith angle, which highlights an example of the “fast” oscillations in the sub-GeV upgoing region.

2643 The official SK-only analysis uses the osc3++ oscillation parameter fitter
2644 [76]. To perform the fast oscillation averaging, it uses a ‘nearest-neighbour’
2645 averaging technique. For a given Monte Carlo neutrino event, the nearest twenty
2646 Monte Carlo neighbours in reconstructed lepton momentum and zenith angle
2647 are found and a distribution of their neutrino energies is built. The RMS, σ , of
2648 this distribution is then used to compute an average oscillation probability for
2649 the given neutrino Monte Carlo event.

2650 For the i^{th} event, the oscillation weight is calculated as

$$W_i = \frac{1}{5}P(E_i, \bar{L}_i) + \frac{1}{5}\sum_{\beta=-1, -0.5, 0.5, 1} P(E_i + \beta\sigma_i, L_\beta), \quad (7.1)$$

2651 where $P(E, L)$ is the oscillation probability calculation for neutrino energy E
2652 and path length L and the two path lengths, \bar{L}_i and L_β are described below. All
2653 of the oscillation probability calculations are performed with a fixed zenith angle
2654 such that the same density profile is used. The uncertainty in the production

height is controlled by using an “average” production height, \bar{L}_i , which represents the average path length computed using twenty production heights taken from the Honda flux model’s prediction [52]. These inputs are provided in 5% intervals of the cumulative distribution function. The value of \bar{L}_i is calculated as:

$$\bar{L}_i = \frac{1}{20} \sum_{j=1}^{20} \sqrt{(R_E + h_j)^2 - R_E^2 (1 - \cos^2 \theta_i)} - R_E \cos \theta_i. \quad (7.2)$$

Where R_E is the Earth’s radius and θ_i is the zenith angle of the i^{th} event. The production heights h_j represent the $(j \times 5)^{th}$ percentile of the cumulative distribution function. L_β values (where the values of β are given in Equation 7.1) are similarly calculated but instead use different combinations of four production heights,

$$\begin{aligned} L_{-1.0} &= \frac{1}{4} L(45, 50, 55, 60), \\ L_{-0.5} &= \frac{1}{4} L(35, 40, 65, 70), \\ L_{+0.5} &= \frac{1}{4} L(25, 30, 75, 68), \\ L_{+1.0} &= \frac{1}{4} L(15, 20, 85, 89). \end{aligned} \quad (7.3)$$

Where $L(i, j, k, l)$ represents the sum of the path lengths with fixed zenith angle and production heights corresponding to the i^{th} , j^{th} , k^{th} and l^{th} percentile of the cumulative distribution function. The values that are taken as β (and values for L_β) are chosen to smooth the oscillation contours in Δm_{32}^2 without incurring loss of sensitivity [201].

This averaging technique works because of the inference between the zenith angle and the reconstructed direction of final state particles in the detector. For low-energy neutrinos, where the resolution of the true neutrino direction is poor, σ_i will be large, resulting in significant averaging effects. Contrary to this, the inferred direction of high-energy neutrinos will be much closer to the true value, meaning that σ_i will be smaller, culminating in small averaging effects.

In practice, these calculations are performed prior to the fit as only oscillation parameters at fixed points are considered. The MCMC technique used in this thesis requires oscillation probabilities to be evaluated at arbitrary parameter values, not known *a priori*. Calculating the five oscillation probabilities per event required by the SK technique is computationally infeasible, so a different averaging technique is used. However, the concept of the averaging technique can be taken from it.

To perform a similar averaging as the SK analysis, a sub-sampling approach using binned oscillograms has been devised. A coarsely binned oscillogram is defined in $\cos(\theta_Z)$ and E_ν . For a given set of oscillation parameters, a single oscillation probability will be assigned to each coarse bin. This value will then apply to all Monte Carlo events which fall into that bin. To assign these oscillation probabilities, the probability is calculated at $N \times N$ points on a grid within a particular bin. This ensemble of oscillation probabilities is averaged to define the coarse bin's oscillation probability, assuming a flat prior in E_ν and $\cos(\theta_Z)$ within the bin. Figure 7.2 illustrates the $N = 2$ example where the assigned value to a coarse bin is the average of the four fine bins which fall in that coarse bin. Whilst the coarse bin edges do not have to be linear on either axis, the sub-division of the fine bins is linear within the range of a coarse bin.

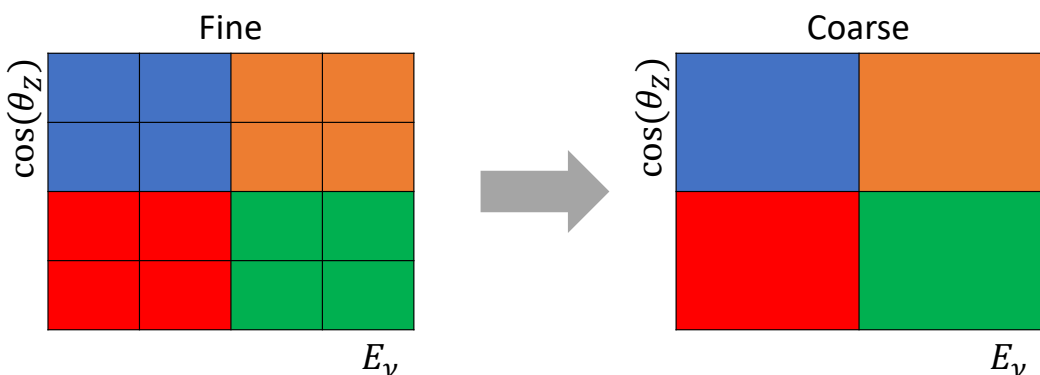


Figure 7.2: Illustration of the averaging procedure for $N = 2$. The oscillation probabilities calculated on the finer left binning are averaged to obtain the oscillation probabilities in the coarser right binning. These averaged oscillation probabilities with the coarser binning are then applied to each event during the fit.

2694 The coarse binning is defined with 67×52 bins in true neutrino energy \times
 2695 cosine zenith. It is picked to be identical to that provided in [201]. In general, the
 2696 binning is logarithmically spaced in neutrino energy but has some hand-picked
 2697 bin edges around the matter resonance to smoothly increase the bin density.
 2698 This is to avoid smearing this region which can be well sampled by the Monte
 2699 Carlo. The cosine zenith binning is approximately linearly spaced across the
 2700 allowable range but the values of layer transitions are hit precisely: -0.8376 (core-
 2701 mantle) and -0.4464 (mantle/transition zone). Bins are spread further apart for
 2702 downgoing events as this is a region unaffected by the fast oscillation wavelengths
 2703 and reduces the total number of calculations required to perform the calculation.

2704 The choice of N is justified based on two studies. Firstly, the variation of event
 2705 rates of each sample is studied as a function of N . For a given set of oscillation
 2706 parameters thrown from the PDG prior constraints (detailed in Table 2.1), the
 2707 oscillation probabilities are calculated using a given value of N . Each sample
 2708 is re-weighted and the event rate is stored. The value of N is scanned from
 2709 1, which corresponds to no averaging, to 19, which corresponds to the largest
 2710 computationally viable subdivision binning. The event rate of each sample at
 2711 large N is expected to converge to a stationary value due to the fine binning fully
 2712 sampling the small-scale structure. Figure 7.3 illustrates this behaviour for the
 2713 SubGeV_elike_0dcy sample for 9 different throws of the oscillation parameters.

2714 Denoting the event rate for one sample for a given throw t at each N by λ_t^N ,
 2715 the average over all considered N values ($\bar{\lambda}_t = \frac{1}{19} \sum_{N=1}^{19} \lambda_t^N$) is computed. The
 2716 variance in the event rate at each N is then calculated as

$$\text{Var}[\lambda^N] = \frac{1}{N_{\text{throws}}} \sum_{t=1}^{N_{\text{throws}}} \left(\lambda_t^N - \bar{\lambda}_t \right)^2 - \left[\frac{1}{N_{\text{throws}}} \sum_{t=1}^{N_{\text{throws}}} \left(\lambda_t^N - \bar{\lambda}_t \right) \right]^2. \quad (7.4)$$

2717 In practice, the following procedure is undertaken. For a particular throw,
 2718 the difference between the event rate at a particular choice of N and the mean
 2719 of the distribution is calculated. This is illustrated in Figure 7.4. This value
 2720 is then calculated for all the 2000 throws, generating a distribution of $\lambda_t^N - \bar{\lambda}_t$.

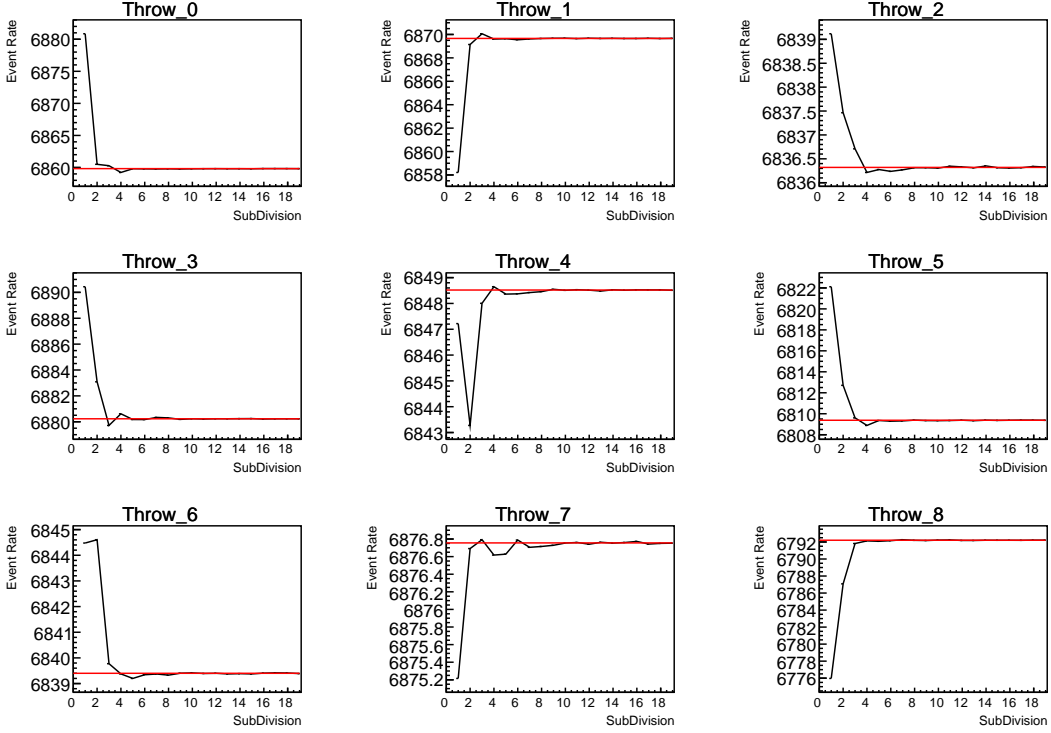


Figure 7.3: Event rate of the SubGeV_elike_0dcy sample as a function of the number of sub-divisions per coarse bin. Each subplot represents the event rate of the sample at a different oscillation parameter set thrown from the PDG priors detailed in Table 2.1. The red line in each subplot represents the mean of the event rate over the different values of sub-divisions for that particular oscillation parameter throw.

This is repeated for each of the values of N considered within this study. The distributions of this value, for $N = [1, 5]$, are given in Figure 7.5. As expected, the distribution gets narrower and tends towards zero for the higher values of N .

The aim of the study is to find the lowest value of N such that this variance is below 0.001. This is the typical threshold used by T2K fitters to validate systematic implementation so has been set as the same criteria. The results of this study for each atmospheric sample used within this thesis are illustrated in Figure 7.6 for 2000 throws of the oscillation parameters. As can be seen, the variance is below the threshold at $N = 10$, and is driven primarily by the SubGeV_mulike_1dcy and SubGeV_elike_0dcy samples.

The second study to determine the value of N is as follows. The likelihood for each sample is computed against an Asimov data set created with Asimov A

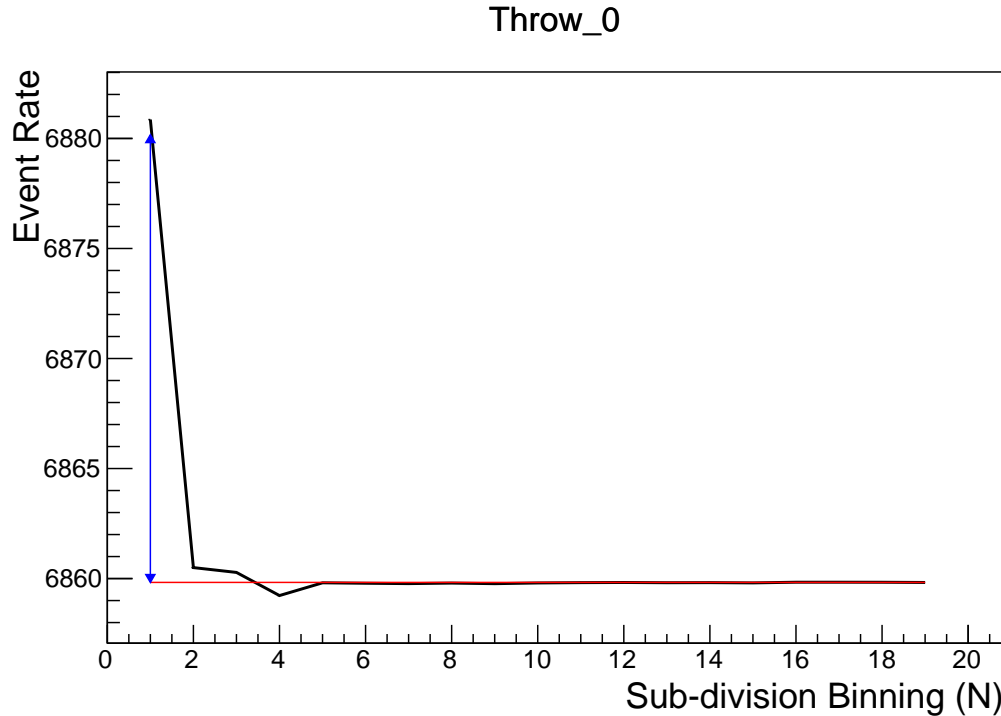


Figure 7.4: Event rate of the SubGeV_elike_0dcy sample, for a particular oscillation parameter throw, as a function of the number of sub-divisions, N , per coarse bin. The difference between the mean event rate (red), $\bar{\lambda}$, and the event rate at $N = 1$, $\lambda^{N=1}$ is defined as $\lambda^N - \bar{\lambda}$ and illustrated by the blue arrow.

oscillation parameters (Table 2.2). Following Equation 7.4, the variance of the log-likelihood over all considered N is computed. The results are shown in Figure 7.7.

A choice of $N = 10$ sub-divisions per coarse bin has a variance in both event rate and log-likelihood less than the required threshold of 0.001. The largest value of the log-likelihood variance is of order 10^{-7} , corresponding to an error on the log-likelihood of about 3×10^{-4} which is small enough to be negligible for the oscillation analysis.

Figure 7.8 illustrates the effect of the smearing using $N = 10$. The fast oscillations in the sub-GeV upgoing region have been replaced with a normalisation effect whilst the large matter resonance structure remains.

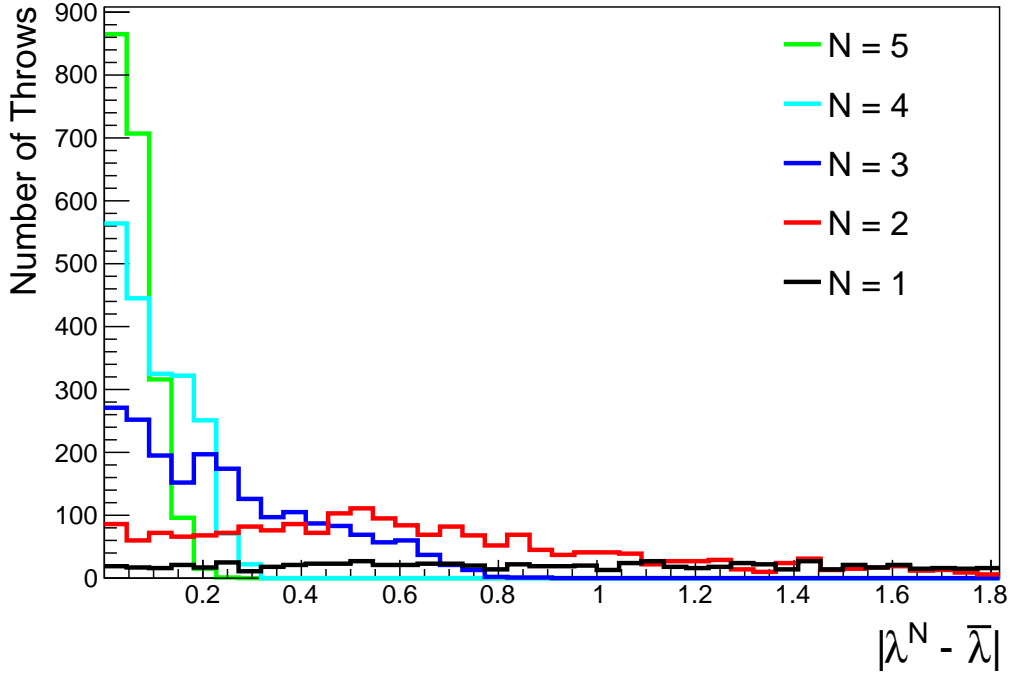


Figure 7.5: The distribution of $\lambda^N - \bar{\lambda}$ for various values of N . As expected, the distribution gets narrower for larger values of N .

2743 7.2 Calculation Engine

2744 As previously discussed in section 7.1, the calculation of oscillation probabilities
 2745 is performed at run-time. Consequently, the time per calculation is crucial for fit
 2746 performance. The initial fitting framework used for this analysis was developed
 2747 with ProbGPU [202]. This is a GPU-only implementation of the prob3 engine
 2748 [203]. It is primarily designed for neutrino propagation in a beam experiment
 2749 (single layer of constant density) with the atmospheric propagation code not
 2750 being used prior to the analysis in this thesis.

2751 Another engine, CUDAProb3 [204], has been interfaced with the fitting frame-
 2752 work used in this analysis. This interfacing was done by the author of this
 2753 thesis. It has been specifically optimised for atmospheric neutrino oscillation
 2754 calculation so does not contain the code to replace the beam oscillation calculation.
 2755 The engine utilises object-orientated techniques as compared to the functional
 2756 implementation of ProbGPU. This allows the energy and cosine zenith arrays to

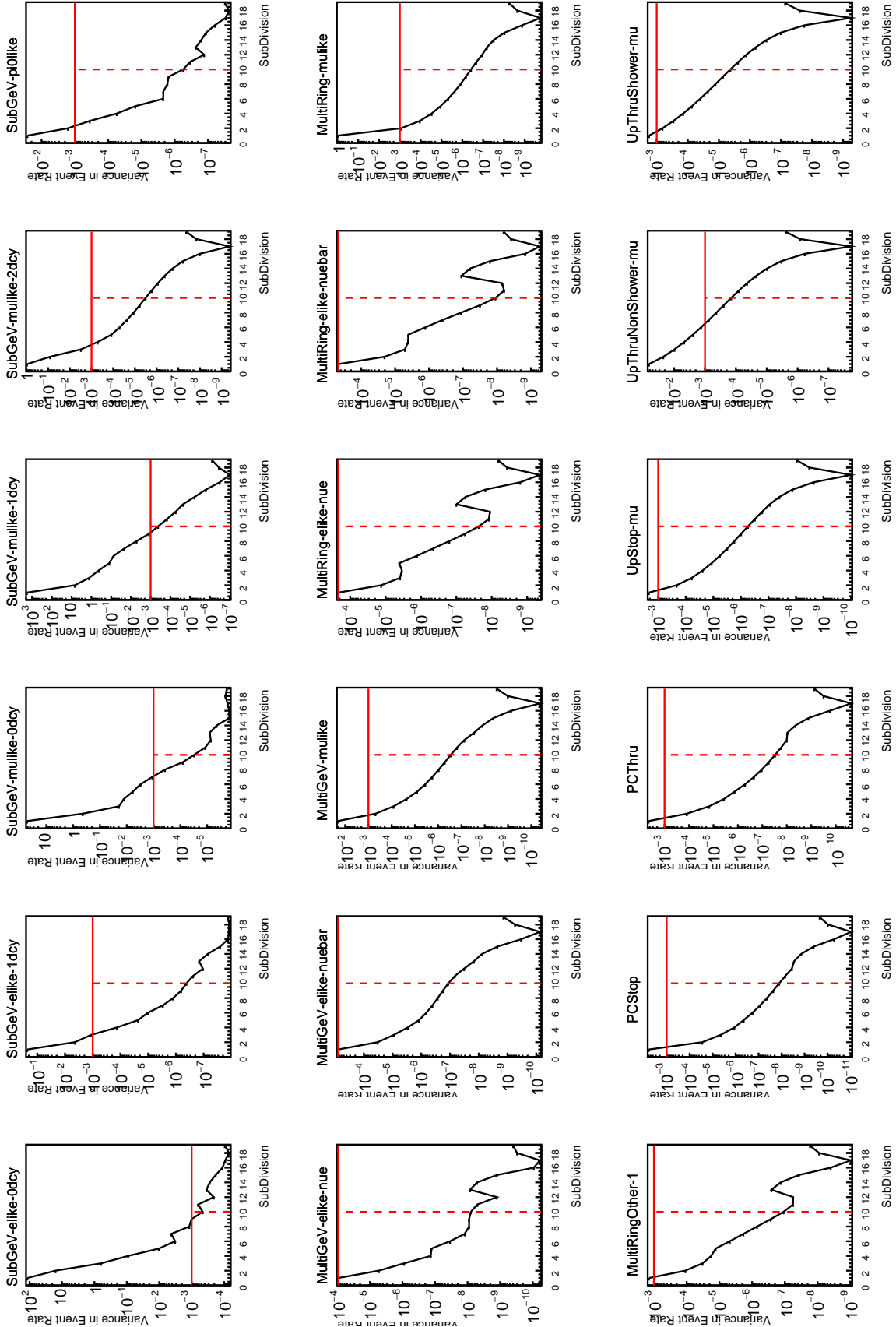


Figure 7.6: Variance of event rate for each atmospheric sample as a function of the number of sub-divisions per coarse bin. The solid red line indicates the 0.1% threshold and the dashed red line indicates the variance at a sub-division $N = 10$.

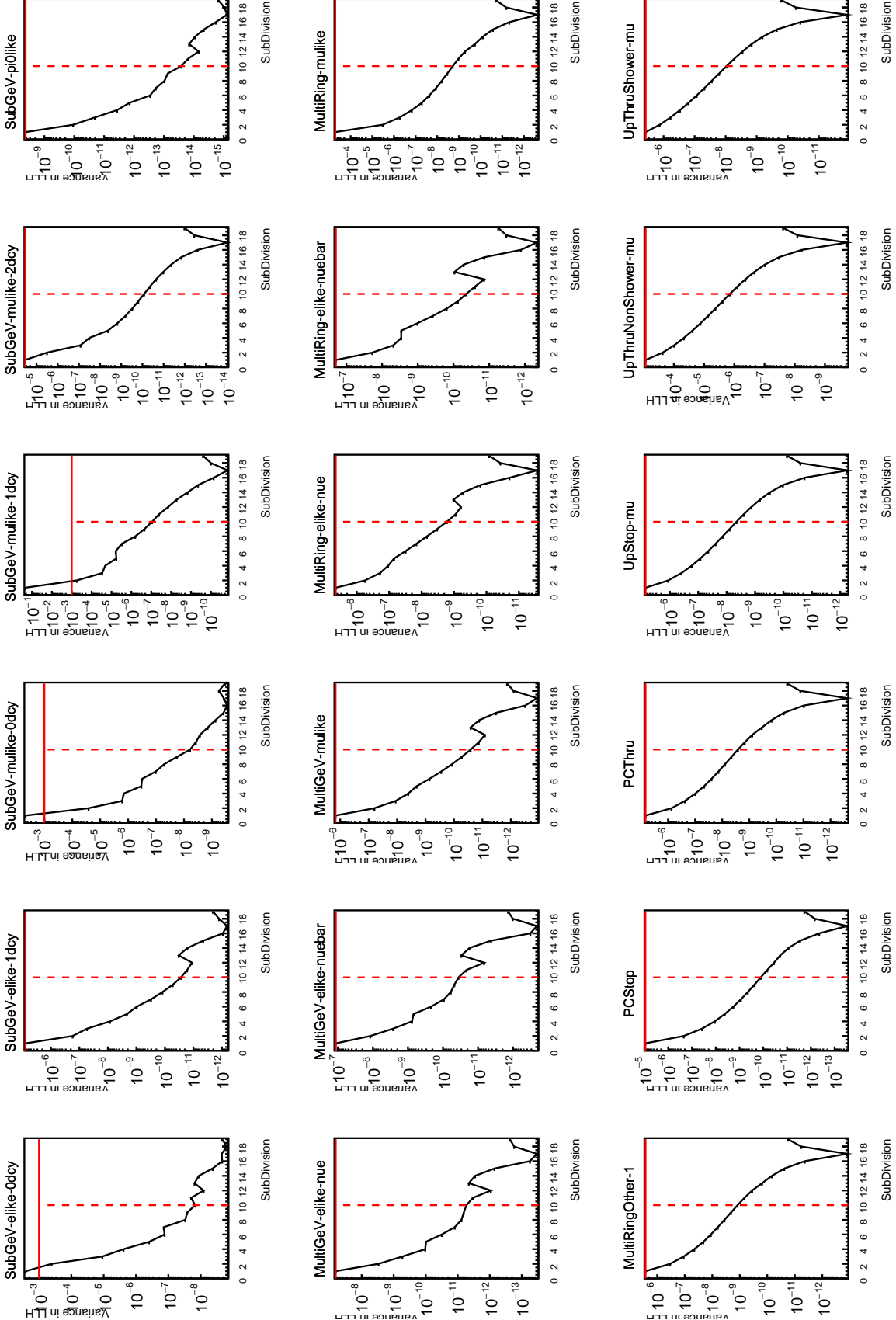


Figure 7.7: Variance of sample log-likelihood, when compared to 'Asimov data' set at Asimov A, for each atmospheric sample as a function of the number of sub-divisions per coarse bin. The solid red line indicates the 0.1% threshold and the dashed red line is a graphical indication of the variance at a sub-division $N = 10$.

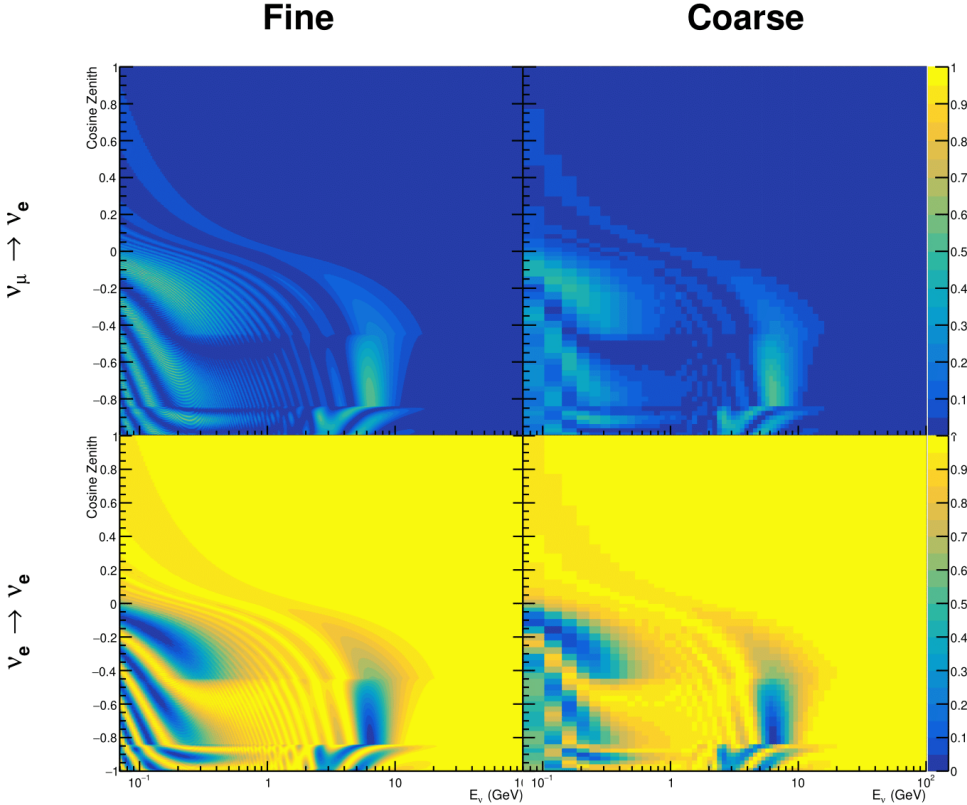


Figure 7.8: The oscillation probability, $P(\nu_\mu \rightarrow \nu_e)$ (top row) and $P(\nu_e \rightarrow \nu_e)$ (bottom row), given as a function of neutrino energy and zenith angle. The left column gives the “fine” binning used to calculate the oscillation probabilities and the right column illustrates the “coarse” binning used to reweight the Monte Carlo events. The fine binning choice is given with $N = 10$, which was determined to be below the threshold from Figure 7.6 and Figure 7.7.

2757 be kept on GPU memory, rather than having to load these arrays onto GPU
 2758 memory for each calculation. Reducing the memory transfer between CPU and
 2759 GPU significantly reduces the time required for calculation. This can be seen
 2760 in Figure 7.9, where the GPU implementation of CUDAProb3 is approximately
 2761 three times faster than the ProbGPU engine.

2762 Another significant advantage of CUDAProb3 is that it contains a CPU mul-
 2763 tithreaded implementation which is not possible with the ProbGPU or prob3
 2764 engines. This eliminates the requirement for GPU resources when submitting
 2765 jobs to batch systems. As illustrated in Figure 7.9, the calculation speed depends

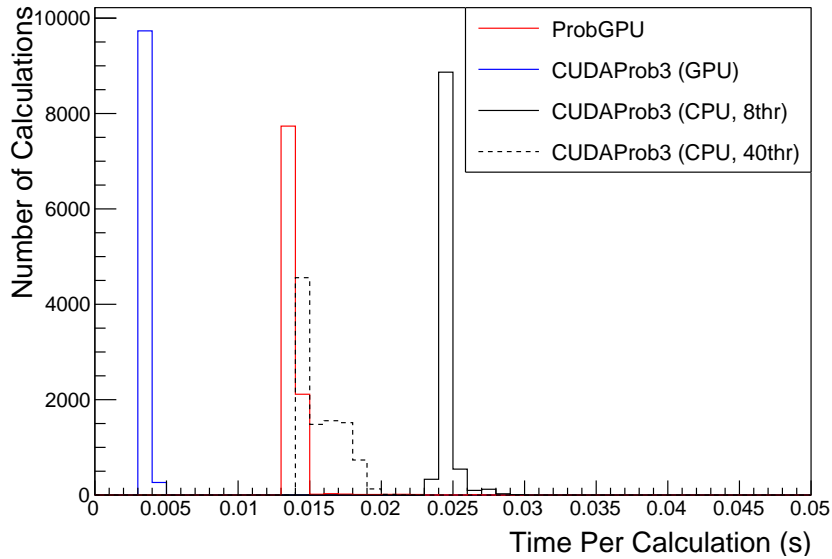


Figure 7.9: The calculation time taken to both calculate the oscillation probabilities and fill the “coarse” oscillograms, following the technique given in section 7.1, for the CUDAProb3 and ProbGPU (Red) calculation engines. CUDAProb3 has both a GPU (Blue) and CPU (Black) implementation, where the CPU implementation is multi-threaded. Therefore, 8-threads (solid) and 40-threads (dashed) configurations have been tested. Prob3, which is a CPU single-thread implementation has a mean step time of 1.142s.

2766 on the number of available threads. Using 8 threads (which is typical of the
 2767 batch systems being used) is approximately twice as slow as the ProbGPU engine
 2768 implementation, but would allow the fitting framework to be run on many more
 2769 resources. This fact is utilised for any SK-only fits but GPU resources are required
 2770 for any fits which include beam samples due to the ProbGPU requirement. Based
 2771 on the benefits shown by the implementation in this section, efforts are being
 2772 placed into including linear propagation for beam neutrino propagation into
 2773 the CUDAProb3 engine [205].

2774 7.3 Matter Density Profile

2775 For an experiment observing neutrinos propagating through the Earth, a model
 2776 of the Earth’s density profile is required. The model used within this analysis
 2777 is based on the Preliminary Reference Earth Model (PREM) [77], as illustrated
 2778 in Figure 2.8. Table 2.3 documents the density and radii of the layers used

within the constant density approximation used by the SK-only analysis [76]. The density measurements provided in the PREM model are provided in terms of mass density, whereas neutrino oscillations are sensitive to the electron number density. This value can be computed as the product of the chemical composition, or the Z/A value, and the mass density of each layer. Currently, the only way to measure the chemical composition value for layers close to the Earth's core is through neutrino oscillations. The chemical composition of the upper layers of the Earth's Mantle and the Transition zone is well known due to it being predominantly pyrolite which has a chemical composition value of 0.496 [206]. The chemical composition dial for the core layers is set to a value of 0.468, as calculated in [207]. As this value is less well known, it is assigned a Gaussian error with a standard deviation equivalent to the difference in chemical composition in core and mantle layers. Figure 7.10 illustrates the effect of moving from the $Z/A = 0.5$ method which is used in the official SK-only analysis to these more precise values.

The beam oscillation probability in this thesis uses a baseline of 295km, density $2.6\text{g}/\text{cm}^3$, and chemical composition 0.5 as is done by the official T2K-only analysis [208].

For a neutrino with given E_ν , $\cos(\theta_Z)$, the oscillation probability calculation engine must be passed a list of the matter regions that the neutrino traversed, with the path length and fixed density in each region. However, a neutrino passing through the earth experiences a range of radii, and thus a range of densities, in each region. In the SK-only analysis, the earth density model used is piecewise-constant, thereby ignoring this effect. For this thesis, the density values for the calculation engine are found by averaging the earth density along the neutrino's path in each layer,

$$\langle \rho \rangle_i = \frac{1}{t_{i+1} - t_i} \int_{t_i}^{t_{i+1}} \rho(t) dt, \quad (7.5)$$

where t_i are the intersection points between each layer and t is the path length of the trajectory across the layer. This leads to an improved approximation.

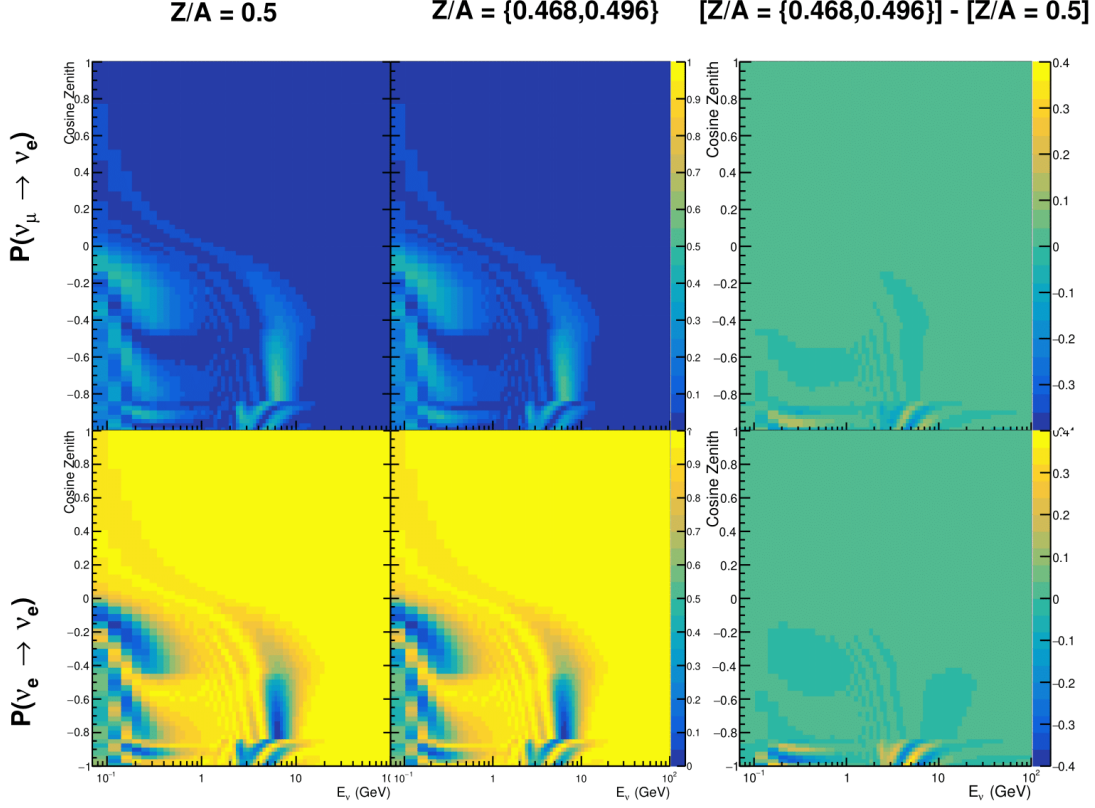


Figure 7.10: The oscillation probability, $P(\nu_\mu \rightarrow \nu_e)$ (top row) and $P(\nu_e \rightarrow \nu_e)$ (bottom row), given as a function of neutrino energy and zenith angle. The left column gives probabilities where the constant $Z/A = 0.5$ approximation which is used in the official SK-only analysis. The middle column gives the probabilities where $Z/A = [0.468, 0.498]$ values are used, as given in Table 2.3. The right column illustrates the difference in oscillation probability between the two different techniques.

For this averaging, the simplification of the PREM model developed in [209] is used. The layers of the prem model are combined into four to reduce calculation time, with a quadratic fit to each section. This fit was not performed by the author of the thesis and is documented in [201]. The coefficients of the quadratic fit to each layer are given in Table 7.1 with the final distribution illustrated in Figure 7.11. The quadratic approximation is clearly much closer to the PREM model as compared to the constant density approximation.

The effect of using the quadratic density per $\cos(\theta_Z)$ model is highlighted in Figure 7.12. The slight discontinuity in the oscillation probability around

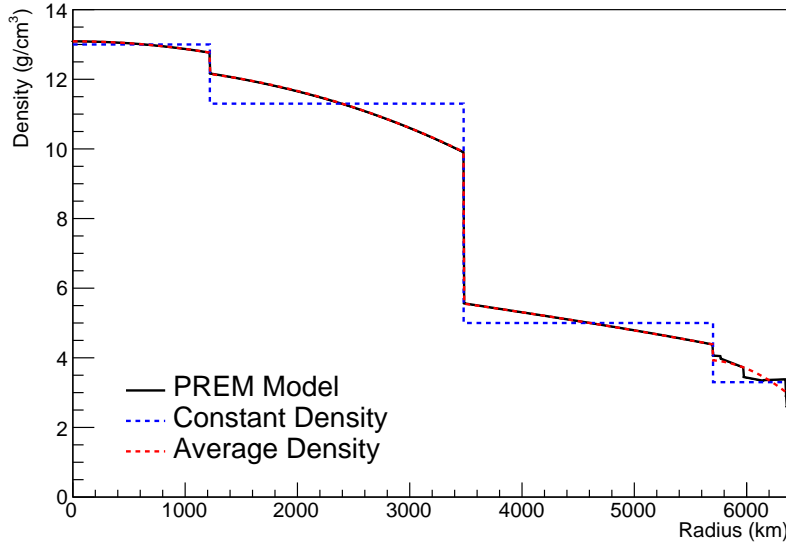


Figure 7.11: The density of the Earth given as a function of the radius, as given by the PREM model (Black), the constant density four-layer approximation (Blue), as used in the official SK-only analysis, and the quadratic approximation of the PREM model (Red).

Layer	Outer Radius [km]	Density [g/cm ³]
Inner Core	1220	$13.09 - 8.84x^2$
Outer Core	3480	$12.31 + 1.09x - 10.02x^2$
Lower Mantle	5701	$6.78 - 1.56x - 1.25x^2$
Transition Zone	6371	$-50.42 + 123.33x - 69.95x^2$

Table 7.1: The quadratic polynomial fits to the PREM model for four assumed layers of the PREM model. The fit to calculate the coefficients is given in [201], where $x = R / R_{Earth}$.

2816 $\cos(\theta_Z) \sim -0.45$ in the fixed density model, which is due to the transition to
 2817 mantle layer boundary, has been reduced. This is expected as the difference in
 2818 the density across this boundary is significantly smaller in the quadratic density
 2819 model as compared to the constant density model. Whilst the difference in
 2820 density across the other layer transitions is reduced, there is still a significant
 2821 difference. This means the discontinuities in the oscillation probabilities remain.
 2822 However, as the quadratic density approximation matches the PREM model
 2823 well in this region, these discontinuities are due to the Earth model rather than
 2824 an artifact of the oscillation calculation.

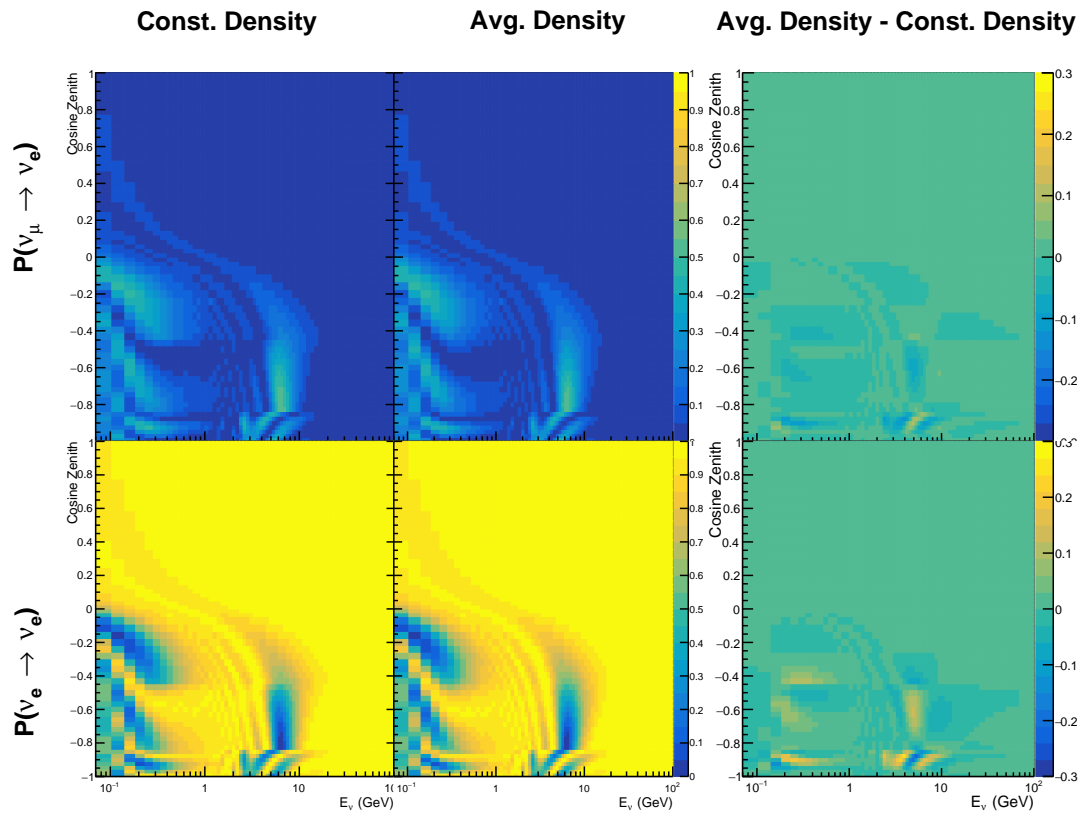


Figure 7.12: The oscillation probability, $P(\nu_\mu \rightarrow \nu_e)$ (top row) and $P(\nu_e \rightarrow \nu_e)$ (bottom row), given as a function of neutrino energy and zenith angle. The left column gives probabilities where the four-layer constant density approximation is used. The middle column gives the probabilities where the density is integrated over the trajectory, using the quadratic PREM approximation, for each $\cos(\theta_Z)$ is used. The right column illustrates the difference in oscillation probability between the two different techniques.

2825 7.4 Production Height Averaging

2826 As discussed in section 2.5, the height at which the cosmic ray flux interacts
 2827 in the atmosphere is not known on an event-by-event basis. The production
 2828 height can vary from the Earth’s surface to $\sim 50\text{km}$ above that. The SK-only
 2829 analysis methodology (described in section 7.1) for including the uncertainty
 2830 on the production height is to include variations from the Honda model when
 2831 pre-calculating the oscillation probabilities prior to the fit. This technique is not
 2832 possible for this analysis which uses continuous oscillation parameters that can
 2833 not be known prior to the fit. Consequently, an analytical averaging technique
 2834 was developed in [201]. The author of this thesis was not responsible for the
 2835 derivation of the technique but has performed the implementation and validation
 2836 of the technique for this analysis.

2837 Using the 20 production heights per Monte Carlo neutrino event, provided
 2838 as 5% percentiles from the Honda flux model, a production height distribution
 2839 $p_j(h|E_\nu, \cos \theta_Z)$ is built for each neutrino flavour $j = \nu_e, \bar{\nu}_e, \nu_\mu, \bar{\nu}_\mu$. In practice, a
 2840 histogram is filled with 20 evenly spaced bins in production height h between
 2841 0 and 50km. The neutrino energy and cosine zenith binning of the histogram
 2842 are the same as that provided in section 7.1. The average production height,
 2843 $\bar{h} = \int dh \frac{1}{4} \sum_j p_j(h|E_\nu, \cos(\theta_Z))$, is calculated. This assumes a linear average over
 2844 the four flavours of neutrino which are considered to be generated in cosmic
 2845 ray showers. The production height binning of this histogram is then translated
 2846 into $\delta t(h) = t(\bar{h}) - t(h)$, where $t(x)$ is the distance travelled along the trajectory
 2847 in the atmosphere from some production height, x .

2848 For the i^{th} traversed layer, the transition amplitude, $D_i(t_{i+1}, t_i)$, is computed.
 2849 The time-ordered product of these is then used as the overall transition amplitude
 2850 via

$$A(t_{n+1}, t_0) = D_n(t_{n+1}, t_n) \dots D_1(t_2, t_1) D_0(t_1, t_0), \quad (7.6)$$

2851 where,

$$\begin{aligned} D_n(t_{n+1}, t_n) &= \exp[-iH_n(t_{n+1} - t_n)] \\ &= \sum_{k=1}^3 C_k \exp[ia_k(t_{n+1} - t_n)] \end{aligned} \quad (7.7)$$

2852 is expressed as a diagonalised time-dependent solution to the Schrodinger
 2853 equation. The 0th layer is the propagation through the atmosphere and is the
 2854 only term that depends on the production height. Using the substitution $t_0 =$
 2855 $t(\bar{h}) - \delta t(h)$, it can be shown that

$$D_0(t_1, t_0) = D_0(t_1, \bar{h})D_0(\delta t). \quad (7.8)$$

2856 Thus Equation 7.6 becomes

$$\begin{aligned} A(t_{n+1}, t_0) &= D_n(t_{n+1}, t_n) \dots D_1(t_2, t_1)D_0(t_1, \bar{h})D(\delta t) \\ &= A(t_{n+1}, \bar{h}) \sum_{k=1}^3 C_k \exp[ia_k \delta t], \\ &= \sum_{k=1}^3 B_k \exp[ia_k \delta t]. \end{aligned} \quad (7.9)$$

2857 The oscillation probability averaged over production height is then calculated
 2858 as

$$\begin{aligned} \bar{P}(\nu_j \rightarrow \nu_i) &= \int d(\delta t) p_j(\delta t | E_\nu, \cos \theta_Z) P(\nu_j \rightarrow \nu_i) \\ &= \int d(\delta t) p_j(\delta t | E_\nu, \cos \theta_Z) A(t_{n+1}, t_0) A^*(t_{n+1}, t_0) \\ &= \sum_{km} (B_k)_{ij} (B_m)_{ij}^* \int d(\delta t) p_j(\delta t | E_\nu, \cos \theta_Z) \exp[i(a_k - a_m) \delta t]. \end{aligned} \quad (7.10)$$

2859 It is important to note that the exact value of \bar{h} used does not matter as the
 2860 values of δt would change to compensate for any modification to the value of \bar{h} .

2861 In practice, implementation in CUDAProb3 [204] is relatively straightforward
 2862 as the majority of these terms are already calculated in the standard oscillation
 2863 calculation. Figure 7.13 illustrates the results of the production height averaging.

2864 As expected, the main effect is observed in the low-energy downward-going
 2865 and horizontal-going events. Upward-going events have to travel the radius
 2866 of the Earth, $R_E = 6371\text{km}$, where the production height uncertainty is a small
 2867 fraction of the total path length.

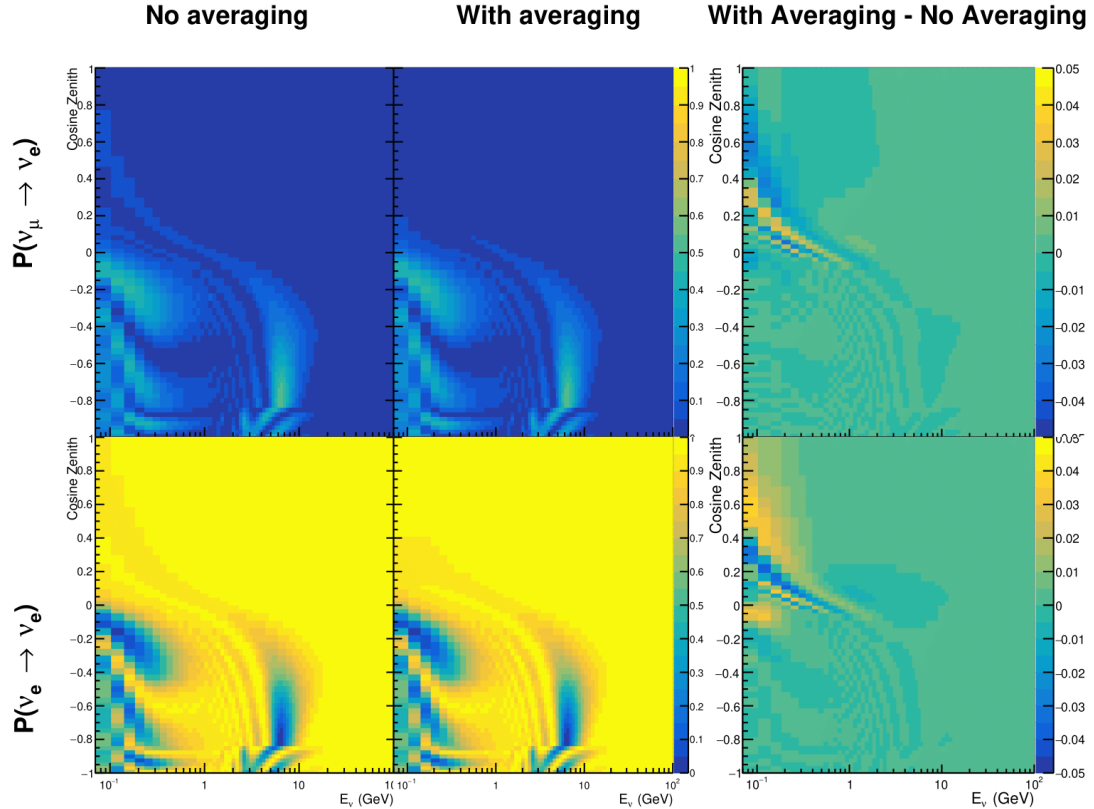


Figure 7.13: The oscillation probability, $P(\nu_\mu \rightarrow \nu_e)$ (top row) and $P(\nu_e \rightarrow \nu_e)$ (bottom row), given as a function of neutrino energy and zenith angle. The left column gives probabilities where a fixed production height of 25km is used. The middle column gives the probabilities where the production height is analytically averaged. The right column illustrates the difference in oscillation probability between the two different techniques.

8

2868

2869

Oscillation Analysis

2870 Using the samples and systematics defined in chapter 6, this chapter documents
2871 a simultaneous beam and atmospheric oscillation analysis from the T2K and SK
2872 experiments. The MaCh3 Bayesian MCMC framework introduced in chapter 4
2873 is used for all studies performed within this thesis.

2874 The MaCh3 framework has been validated through many tests. The code that
2875 handles the beam far detector samples was developed by the author and validated
2876 by comparison to the 2020 T2K analysis [2]. The sample event rates and likelihood
2877 evaluations of beam samples generated by the framework used within this thesis
2878 were compared to those from the 2020 T2K analysis by the author of this thesis.
2879 Variations of the sample predictions were compared at $\pm 1\sigma$ and $\pm 3\sigma$ and good
2880 agreement was found in all cases. A similar study, led by Dr. C. Wret was used
2881 to validate the near detector portion of the code [194]. The implementation of
2882 the atmospheric samples within MaCh3 was completed and cross-checked by the
2883 author of this thesis against the P-Theta framework (introduced in section 3.2).
2884 Both fitters are provided with the same inputs and can therefore cross-validate
2885 each other. These validations compared the event rates and likelihood calculation.
2886 Documentation of all the above validations can be found in [194]. These stringent
2887 validations ensure that the code is doing as intended.

2888 8.1 Monte Carlo Prediction

- 2889 Using the three sets of dial values (generated, pre-fit, and post-fit tunes) defined
 2890 in subsection 6.4.3, the predicted event rates for each sample are given in Table 8.1.
 2891 The oscillated and un-oscillated event rates are calculated for each tune.

Sample	Total Predicted Events					
	Generated		Pre-fit		Post-fit	
	Osc	UnOsc	Osc	UnOsc	Osc	UnOsc
SubGeV- <i>elike</i> -0dcy	7121.0	7102.6	6556.8	6540.0	7035.2	7015.7
SubGeV- <i>elike</i> -1dcy	704.8	725.5	693.8	712.8	565.7	586.0
SubGeV- <i>mulike</i> -0dcy	1176.5	1737.2	1078.6	1588.1	1182.7	1757.1
SubGeV- <i>mulike</i> -1dcy	5850.7	8978.1	5351.7	8205.1	5867.0	9009.9
SubGeV- <i>mulike</i> -2dcy	446.9	655.2	441.6	647.7	345.9	505.6
SubGeV- <i>pi0like</i>	1438.8	1445.4	1454.9	1461.1	1131.1	1136.2
MultiGeV- <i>elike</i> -nue	201.4	195.6	201.1	195.3	202.6	196.7
MultiGeV- <i>elike</i> -nuebar	1141.5	1118.3	1060.7	1039.5	1118.5	1095.7
MultiGeV- <i>mulike</i>	1036.7	1435.8	963.1	1334.1	1015.2	1405.9
MultiRing- <i>elike</i> -nue	1025.1	982.2	1026.8	984.3	1029.8	986.4
MultiRing- <i>elike</i> -nuebar	1014.8	984.5	991.0	962.0	1008.9	978.5
MultiRing- <i>mulike</i>	2510.0	3474.4	2475.6	3425.8	2514.6	3480.4
MultiRingOther-1	1204.5	1279.1	1205.8	1280.3	1207.4	1281.0
PCStop	349.2	459.2	338.4	444.7	346.8	456.1
PCThrus	1692.8	2192.5	1661.5	2149.8	1689.2	2187.8
UpStop-mu	751.2	1295.0	739.7	1271.6	750.4	1293.0
UpThruNonShower-mu	2584.4	3031.6	2577.9	3019.4	2586.8	3034.0
UpThruShower-mu	473.0	488.6	473.2	488.7	473.8	489.4
FHC1Rmu	328.0	1409.2	301.1	1274.7	345.1	1568.0
RHC1Rmu	133.0	432.3	122.7	396.2	135.0	443.9
FHC1Re	84.6	19.2	77.4	18.2	93.7	19.7
RHC1Re	15.7	6.4	14.6	6.1	15.9	6.3
FHC1Re1de	10.5	3.2	10.3	3.1	8.8	2.9

Table 8.1: The Monte Carlo predicted event rate of each far detector sample used within this analysis. Three model parameter tunes are considered, as defined in subsection 6.4.3. Un-oscillated and oscillated predictions are given, where the oscillated predictions assume Asimov A oscillation parameters provided in Table 2.2.

- 2892 Generally, the samples that target CCQE interaction modes observe a decrease
 2893 in prediction when comparing the generated values with the pre-fit dial values.
 2894 This is in accordance with the Monte Carlo being produced at $M_A^{QE} = 1.21\text{GeV}$
 2895 [153] whilst the pre-fit dial value is set to $M_A^{QE} = 1.03\text{GeV}$ as suggested by [193].

Furthermore, the predicted event rates of samples that target CCRES interaction modes are significantly reduced when considering the post-BANFF fit. This follows the observations in subsection 6.4.3. The strength of the accelerator neutrino experiment can be seen in the remarkable difference between the oscillated and unoscillated predictions in the FHC1Rmu and RHC1Rmu samples. There is a very clear decrease in the expected event rate between the oscillated and un-oscillated predictions which is not as obvious as in the atmospheric samples. This is due to the fact that the beam energy is tuned to the maximum disappearance probability, which is not the case for the naturally generated atmospheric neutrinos.

8.2 Likelihood Scans

Using the definition of the likelihood presented in section 6.5, the contribution of each sample to the likelihood from a variation of a particular parameter can be studied. This process identifies which samples drive the determination of the oscillation parameters in the joint fit. Figure 8.1 presents the variation of all the samples (beam and atmospheric) at the far detector to the oscillation parameters of interest: δ_{CP} , $\sin^2(\theta_{13})$, $\sin^2(\theta_{23})$, and Δm_{32}^2 . These plots are colloquially called ‘likelihood scans’ (or ‘log-likelihood scans’). The process of making these plots is as follows. An Asimov data set is built using the AsimovA oscillation parameters and pre-fit systematic tune. The Monte Carlo is then reweighted using the value of the oscillation parameter at each point on the x-axis of the scan. The likelihood is then calculated between the Asimov data and Monte Carlo prediction and plotted.

Due to the caveat of fixed systematic parameters and the correlations between oscillation parameters being ignored when creating these likelihood scans, the value of $\chi^2 = 1$ (or $-2 \times \ln(\text{Likelihood}) = 1$) does not equate to the typical 1σ sensitivity. However, it does give an indication of which samples respond most strongly to variations in a particular oscillation parameter. The point at

2924 which the likelihood tends to zero illustrates the value of the parameter used
 2925 to build the Asimov data prediction.

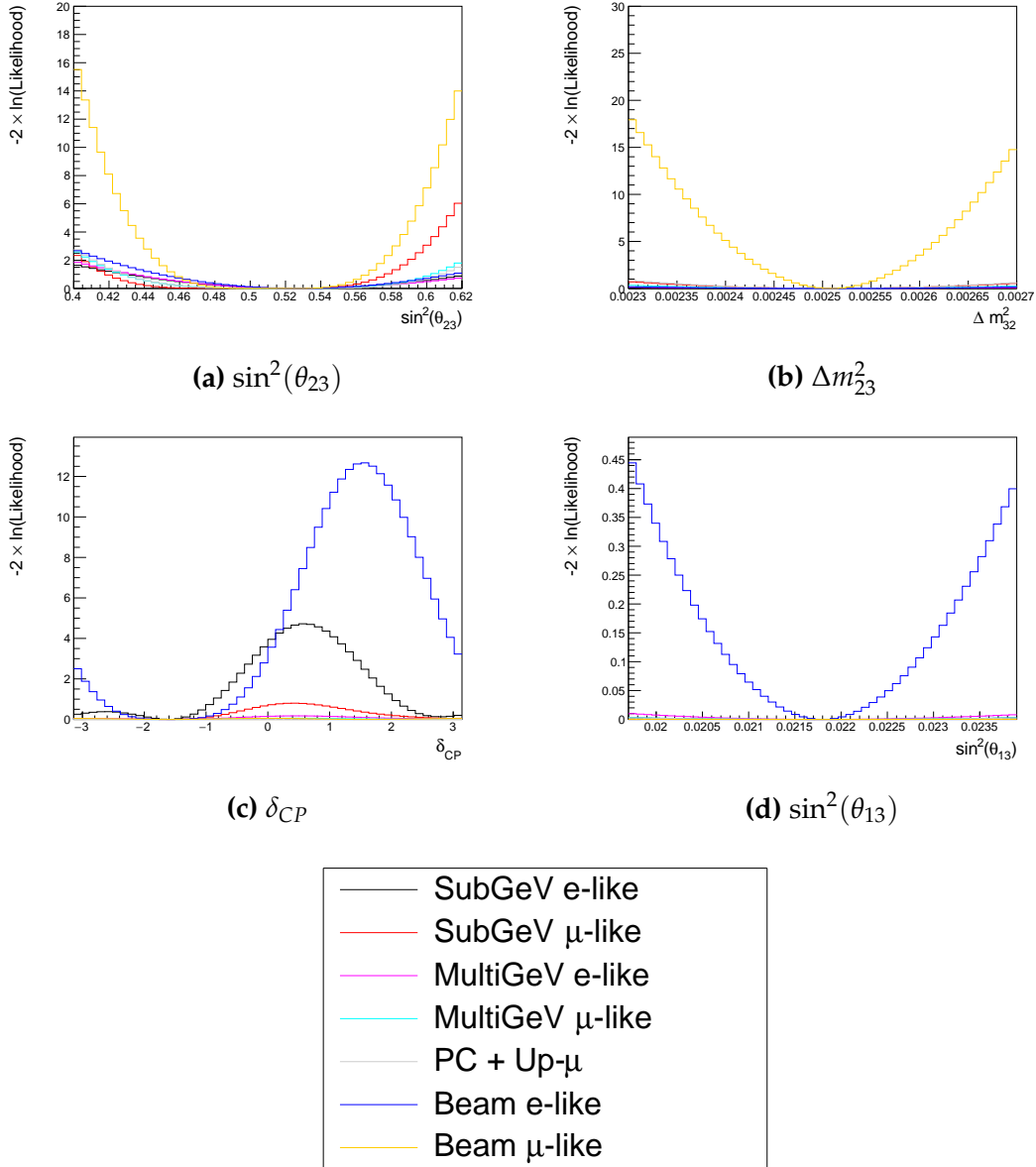


Figure 8.1: The response of the likelihood, as defined in section 6.5, illustrating the response of the samples to a variation of an oscillation parameter.

2926 The sensitivity to $\sin^2(\theta_{23})$ is mostly dominated by the beam muon-like
 2927 samples. The response of an individual atmospheric sample is small but non-
 2928 negligible such that the summed response over all atmospheric samples becomes
 2929 comparable to that of the muon-like beam samples. Consequently, the sensitivity

of the joint fit to $\sin^2(\theta_{23})$ would be expected to be greater than the beam-only analysis. The only sample that responds to the $\sin^2(\theta_{13})$ oscillation parameter is the electron-like beam sample. Consequently, no increase in sensitivity beyond that of the T2K-only analysis would be expected from the joint fit. Regardless, the sensitivity of the beam sample is significantly weaker than the external reactor constraint so prior knowledge will dominate any sensitivity to $\sin^2(\theta_{13})$ which is included within this thesis. The Δm_{21}^2 and $\sin^2(\theta_{12})$ parameters are not considered as there is simply no sensitivity in any sample considered within this analysis. The response to Δm_{32}^2 is completely dominated by the beam muon-like samples. This is because the beam neutrino energy is specifically tuned to match the maximal disappearance probability. Despite this, improvements to the $|\Delta m_{32}^2|$ sensitivity may be expected due to additional mass hierarchy determination added by the atmospheric samples.

Two-dimensional scans of the appearance ($\sin^2(\theta_{13}) - \delta_{CP}$) and disappearance ($\sin^2(\theta_{23}) - \Delta m_{32}^2$) parameters are illustrated in Figure 8.2 and Figure 8.3, respectively. The caveat of fixed systematic parameters and correlations between other oscillation parameters being neglected still apply.

The appearance log-likelihood scans show the distinct difference in how the beam and atmospheric samples respond. The beam samples have an approximately constant width of the 2σ and 3σ contours, throughout all ranges of δ_{CP} . Whereas, the response of the atmospheric samples to $\sin^2(\theta_{13})$ is very strongly correlated to the value of δ_{CP} . At higher values of $\sin^2(\theta_{13})$, two lobes appear around $\delta_{CP} \sim -\pi/2$ and $\delta_{CP} \sim 2.4$. Consequently, this difference allows some of the degeneracy in a beam-only fit to be broken. Comparing the beam-only and joint fit likelihood scans, the 2σ continuous contour in δ_{CP} for beam samples becomes closed when the atmospheric samples are added. This may result in a stronger sensitivity to δ_{CP} . Similarly, the width of the 3σ contours also becomes dependent upon the value of δ_{CP} . Furthermore, atmospheric samples have little sensitivity to $\sin^2(\theta_{13})$ on their own, as evidenced in Figure 8.1, but may improve sensitivity to the parameter when combined within the simultaneous

2960 fit. It is important to remember that these likelihood scans are not sensitivity
2961 measurements as the systematic parameters are fixed and the correlation between
2962 oscillation parameters is neglected. However, they are a very encouraging result
2963 for the joint fit.

2964 The disappearance log-likelihood scans in $\sin^2(\theta_{23}) - \Delta m_{32}^2$ space (Figure 8.3)
2965 show the expected behaviour when considering the one-dimensional scans
2966 already discussed. The uncertainty on the width of $|\Delta m_{32}^2|$ is mostly driven by the
2967 beam samples. However, the width of this contour in the inverted mass region
2968 ($\Delta m_{32}^2 < 0$) is significantly reduced due to the ability of the atmospheric samples
2969 to select the correct (normal) mass hierarchy. The width of the uncertainty
2970 in $\sin^2(\theta_{23})$ is also reduced compared to the beam-only sensitivities, with a
2971 further decrease in the inverted hierarchy region due to the better mass hierarchy
2972 determination.

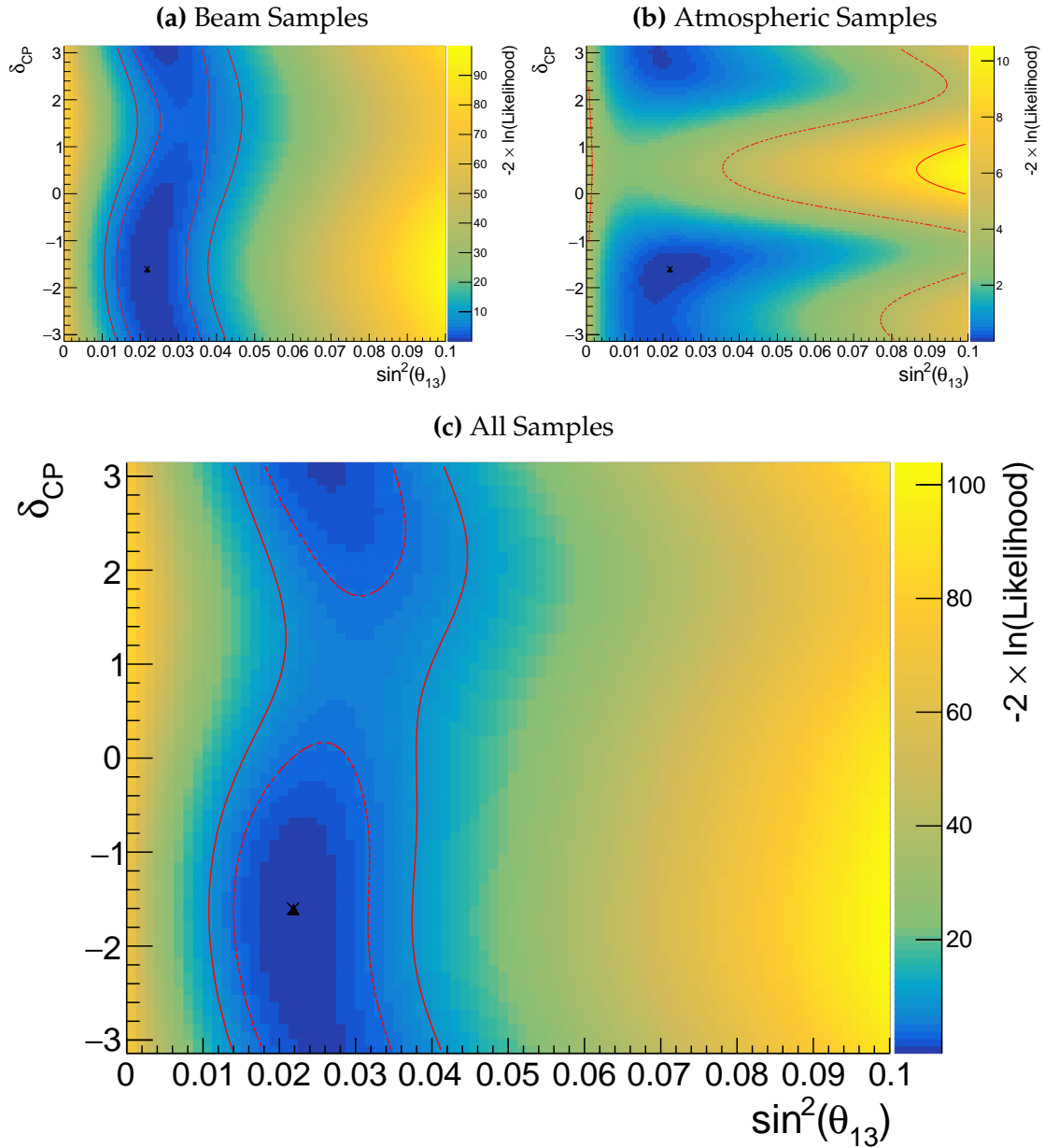


Figure 8.2: Two-dimensional log-likelihood scan of the appearance ($\sin^2(\theta_{13})-\delta_{CP}$) parameters showing the response of the beam samples (top left), atmospheric samples (top right) and the summed response (bottom). The Asimov A oscillation parameters, defined in Table 2.2, are known to be the true point (Black Cross). The position of the smallest log-likelihood is highlighted with the triangle. Prior uncertainty terms of the oscillation parameters are neglected. The two(three) sigma contour levels are illustrated with the dashed(solid) red line.

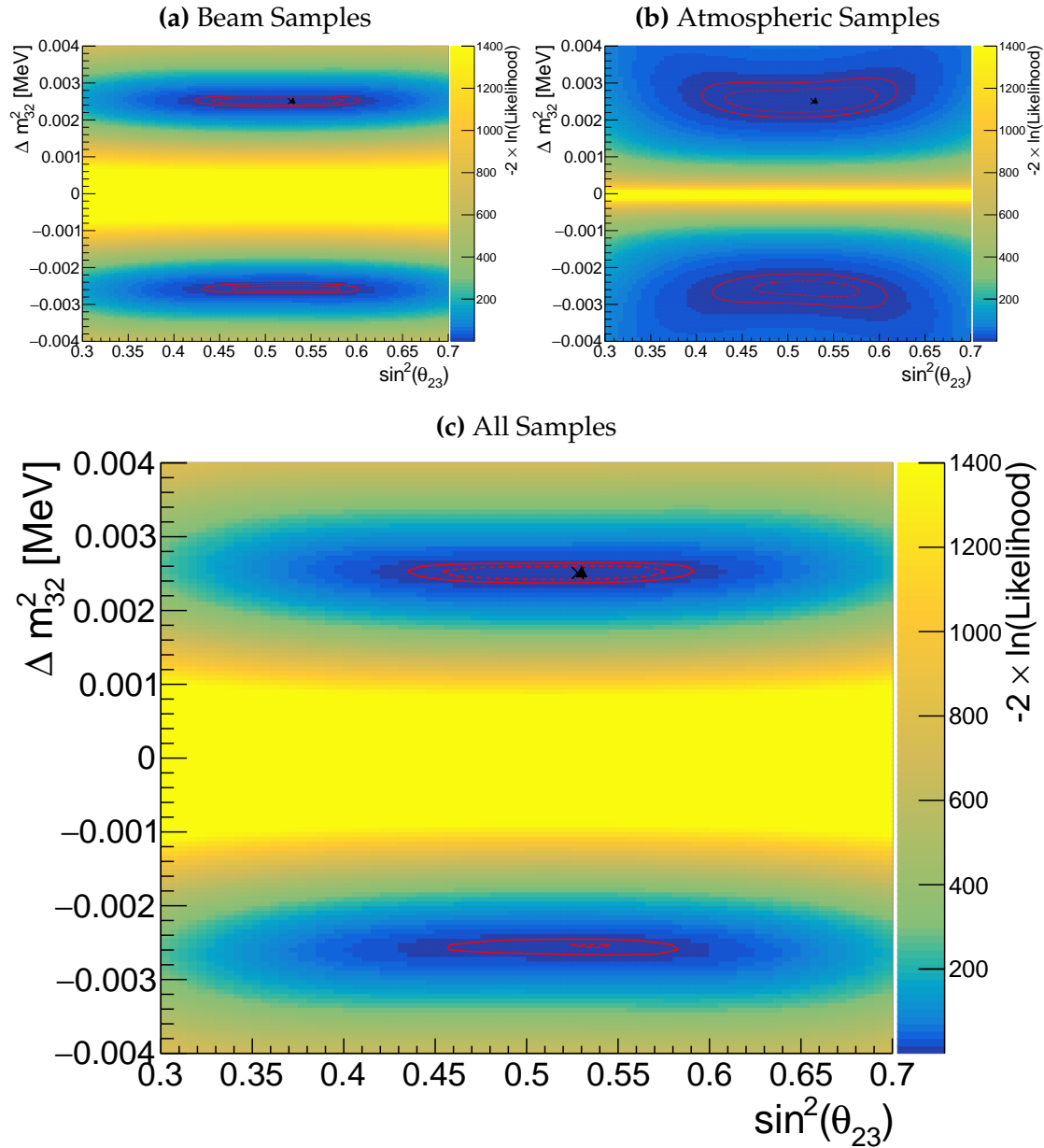


Figure 8.3: Two-dimensional log-likelihood scan of the disappearance ($\sin^2(\theta_{23}) - \Delta m_{32}^2$) parameters showing the response of the beam samples (top left), atmospheric samples (top right) and the summed response (bottom). The Asimov A oscillation parameters, defined in Table 2.2, are known to be the true point (Black Cross). The position of the smallest log-likelihood is highlighted with the triangle. Prior uncertainty terms of the oscillation parameters are neglected. The two(three) sigma contour levels are illustrated with the dashed(solid) red line.

The likelihood scans illustrated thus far only consider the sensitivity of this analysis for a fixed set of true oscillation parameters, namely Asimov A defined in Table 2.2. Whilst computationally infeasible to run many fits at different parameter sets, it is possible to calculate the likelihood response to different Asimov data sets. Figure 8.4 and Figure 8.5 illustrate how the sensitivity changes for differing true values of δ_{CP} and $\sin^2(\theta_{23})$, respectively. For both of these plots, the other oscillation parameters are fixed at their Asimov A values. Consequently, the caveat of fixed systematic parameters and correlations between other oscillation parameters being neglected still applies.

To explain how these plots are made, consider Figure 8.4. This plot is built by considering multiple one-dimensional log-likelihood scans, each creating an Asimov data set with the value of δ_{CP} taken from the x-axis. The likelihood to this particular Asimov data set is calculated after reweighting the Monte Carlo prediction to each value of δ_{CP} on the y-axis.

Figure 8.4 illustrates the sensitivity to δ_{CP} . To interpret this plot, larger contours result in more parameter space being excluded from the 1σ region. The 1σ intervals contain regions where the beam and atmospheric samples have discontinuous contours. For example, for the x-axis value of $\delta_{CP} = 0$, the beam samples sensitivity would include two discontinuous regions excluded from the 1σ interval: $\delta_{CP} \sim 0$ and $\delta_{CP} \sim \pi$. This behaviour is also seen in atmospheric samples response but at a value of $\delta_{CP} \sim -1$. This difference allows the joint fit to have increased sensitivity to these regions. Consequently, the difference between the beam-only and joint beam-atmospheric fit should be studied using multiple Asimov data sets.

Despite the increased sensitivity at 1σ , the 2σ intervals from the joint fit are more similar to the two independent sensitivities and the off-diagonal degeneracies mostly remain. This indicates that the joint fit has the strength to aid parameter determination but can not entirely break the degeneracies in δ_{CP} at higher confidence levels.

Figure 8.5 illustrates a similar analysis as above, although the value of $\sin^2(\theta_{23})$ is varied whilst δ_{CP} is fixed to the Asimov A parameter value. Due to the beam parameters and baseline being tuned to specifically target this oscillation parameter, the average sensitivity of the beam samples is stronger than the atmospheric samples. However, the degeneracy around maximal mixing ($\sin^2(\theta_{23}) = 0.5$) is significantly more peaked in the beam samples compared to the atmospheric samples. This means that a value of $\sin^2(\theta_{23}) \sim 0.56$ would be contained within the 1σ confidence interval for a true value of $\sin^2(\theta_{23}) \sim 0.46$ if using the beam-only analysis, whereas it would be excluded in the joint analysis. Given the caveat of only considering likelihood scans, the joint analysis would mostly eliminate the discontinuous intervals in these regions. This means that the joint fit could feasibly have an increased preference for the correct octant hypothesis.

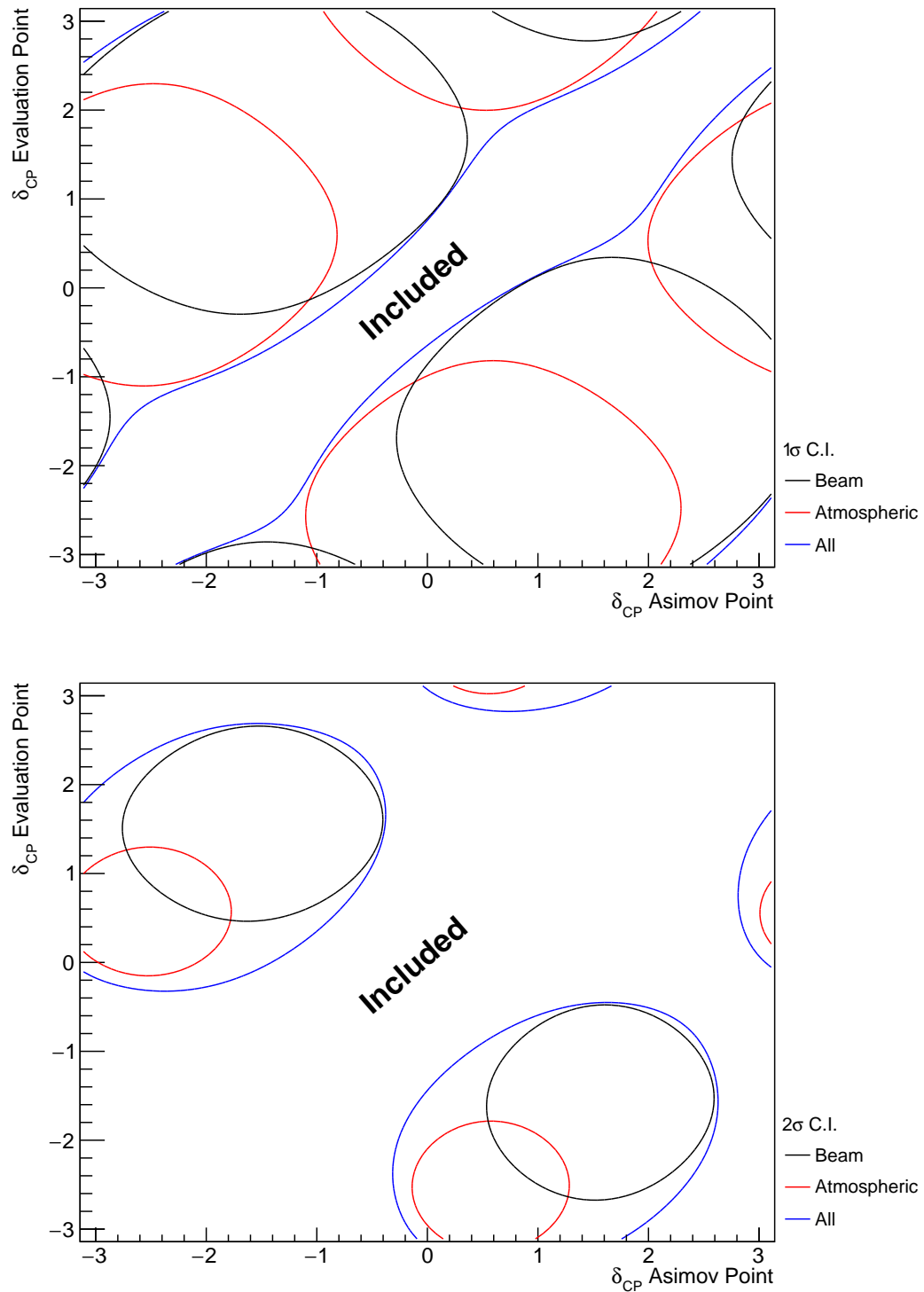


Figure 8.4: A series of one-dimensional likelihood scans over δ_{CP} , where an Asimov data set is built for each value of δ_{CP} on the x-axis and the likelihood is evaluated for each value of δ_{CP} on the y-axis. The diagonal represents the minimum log-likelihood and defines the region included within the 1σ (Top) and 2σ (Bottom) confidence intervals. The beam (black) and atmospheric (red) samples are individually plotted and the joint fit (blue) is the sum of the two.

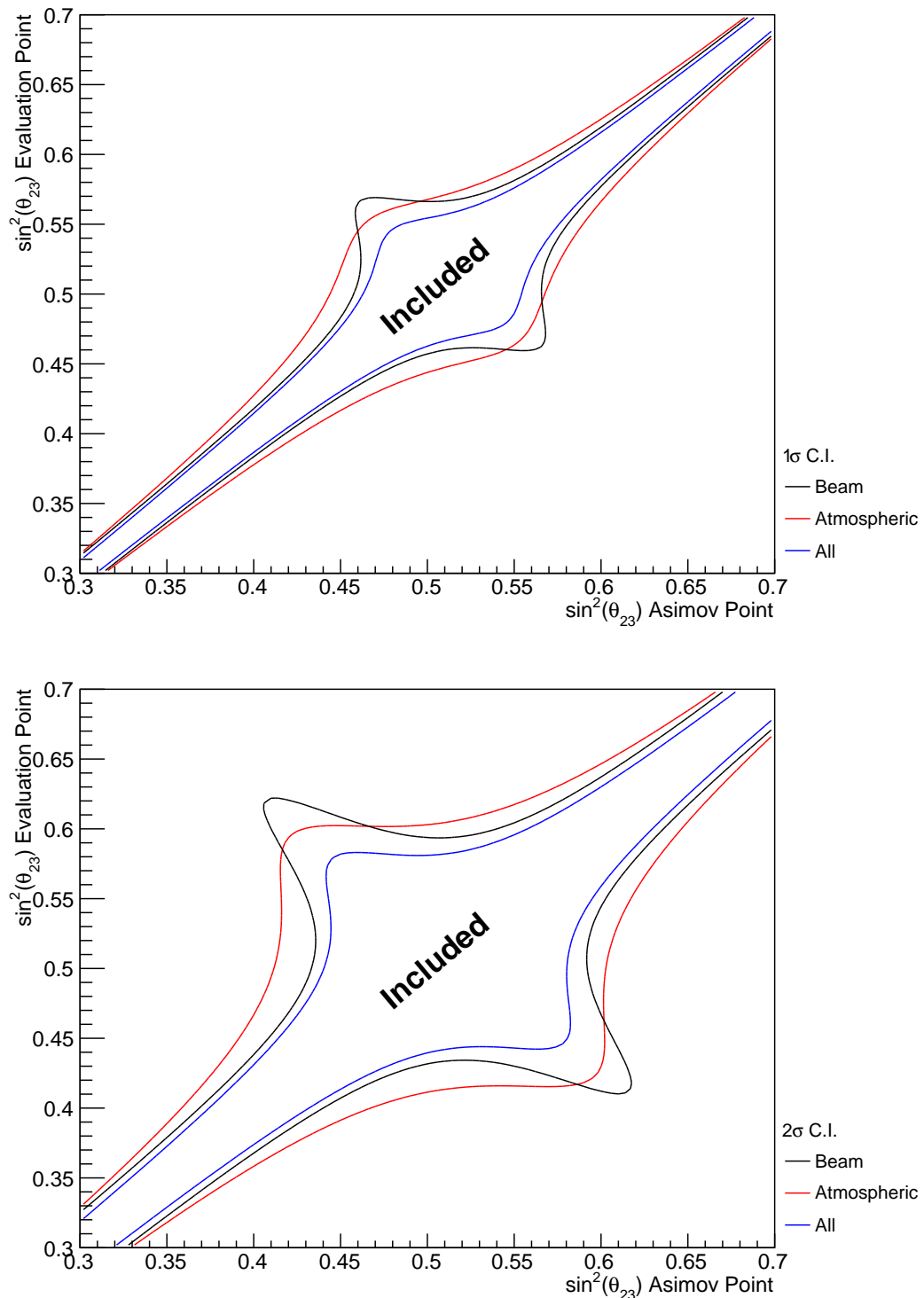


Figure 8.5: A series of one-dimensional likelihood scans over $\sin^2(\theta_{23})$, where an Asimov data set is built for each value of $\sin^2(\theta_{23})$ on the x-axis and the likelihood is evaluated for each value of $\sin^2(\theta_{23})$ on the y-axis. The diagonal represents the minimum log-likelihood and defines the region included within the 1σ (Top) and 2σ (Bottom) confidence intervals. The beam (black) and atmospheric (red) samples are individually plotted and the joint fit (blue) is the sum of the two.

Alongside oscillation parameters (Figure 8.1), the sensitivity to systematic parameters can also be studied for the joint fit. As some of these parameters are correlated between the beam and atmospheric events, the response of the atmospheric samples can modify the post-fit constraint. This means the systematics can have additional constraints than they would from a beam-only analysis. Therefore, the response from the beam and the atmospheric samples to various systematic parameters has been compared in Figure 8.6. The Asimov data set has been created using the AsimovA oscillation parameter and the pre-fit systematic tune.

The systematic parameter controlling the effective axial mass coupling in CCQE interactions, M_A^{QE} , is clearly dominated by the ND constraint. An example where the response of the atmospheric sample is approximately similar to the near detector constraint is the 2p2h CtoO normalisation systematic. This systematic models the scaling of the 2p2h interaction cross-section on a carbon target to an oxygen target. There are also systematics that have no near detector constraint. For example, the systematic parameters which describe the normalisation of the NC1Gamma and NCOther interaction modes. The atmospheric and beam samples can have similar sensitivity to these systematics due to their similar composition in energy and interaction mode. As an example of how including atmospheric samples can help constrain systematic parameters used within the beam analysis, these NC background events in beam electron-like samples will be more constrained with the additional sensitivity of atmospheric samples. This would be expected to reduce the overall uncertainty of the beam electron-like event rates in the joint analysis compared to the beam-only studies. This could modify the sensitivity of the beam samples due to the more constrained background events.

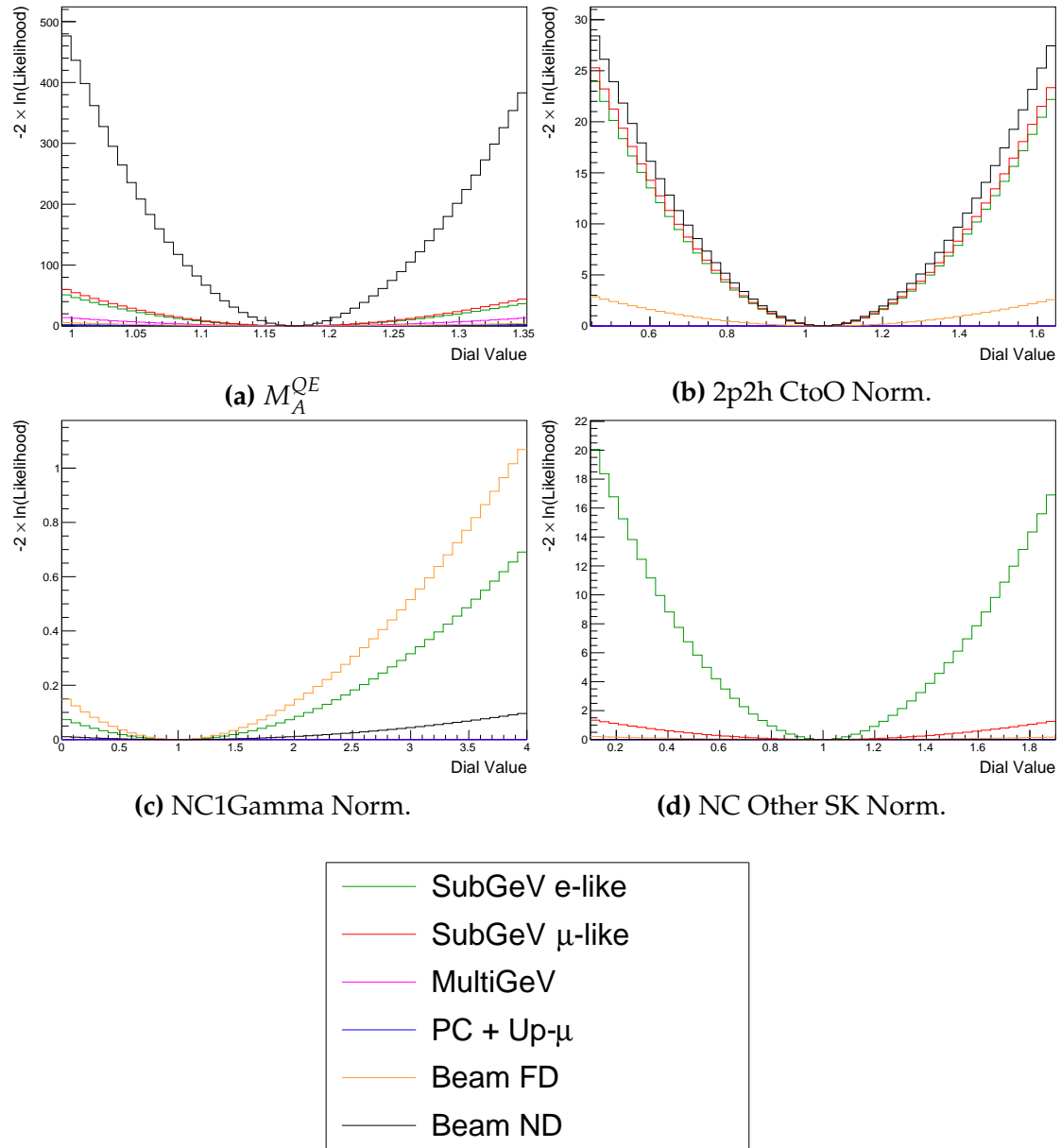


Figure 8.6: The response of the likelihood, as defined in section 8.2, illustrating the response of the samples to the various cross-section systematic parameters.

3040 8.3 Sensitivity Studies

3041 The sensitivities of the joint T2K and SK oscillation analysis are presented in
3042 the form of Asimov fits. These fits consider beam samples from the near and
3043 far detector alongside atmospheric samples at SK. This technique builds an
3044 Asimov data set (following section 6.5) using the AsimovA oscillation parameters
3045 and post-BANFF systematic tune, which is then fit. This technique eliminates
3046 statistical fluctuations from the data, therefore, providing the maximum sen-
3047 sitivity of the analysis.

3048 In practice, the Asimov fits presented within this analysis are modified from
3049 the above definition. An Asimov prediction of both beam and atmospheric far
3050 detector samples is fit whilst the true data is used for near detector samples.
3051 These modifications mean that the results are equivalent to performing a far
3052 detector Asimov fit using inputs from the BANFF data fit. Consequently, this
3053 allows the results to be cross-checked with the results from the P-Theta analysis.
3054 The comparison has been performed and is documented in [210]. No significant
3055 discrepancies were found between the fitters.

3056 This section proceeds with the following studies. Firstly, the sensitivity
3057 of the atmospheric samples using the correlated detector model is detailed in
3058 subsection 8.3.1. This includes studying the choice of applying the 2020 PDG
3059 reactor constraint [72] to the atmospheric samples, which is documented in
3060 subsection 8.3.2. Additionally, the effect of applying the near-detector constraints
3061 onto the atmospheric samples is discussed in subsection 8.3.3. The main result is
3062 the sensitivity of the simultaneous beam and atmospheric fit. The sensitivities,
3063 both with and without the application of the reactor constraint, are presented
3064 in subsection 8.3.4 and subsection 8.3.5, respectively. To indicate the benefit
3065 of the joint analysis, the sensitivities are compared to the 2020 T2K beam-only
3066 sensitivities [2, 211] in subsection 8.3.6 and subsection 8.3.7. The T2K analysis
3067 is used as a reference as it uses the same samples and a similar systematic
3068 model. As shown in section 8.2, the response of the beam and atmospheric

samples change depending upon the true set of oscillation parameters assumed. Therefore, subsection 8.3.8 documents the sensitivities at an alternative oscillation parameter set.

8.3.1 Atmospheric-Only Sensitivity Without Reactor Constraint

This section presents the results of an Asimov fit using samples from the near detector and only atmospheric samples from the far detector. The results are presented as one-dimensional or two-dimensional histograms which have been marginalised over all other parameters using the technique outlined in subsection 4.3.1. Each histogram displays the posterior probability density and illustrates the credible intervals, calculated using the technique in subsection 4.3.2. For this fit, a flat prior is used for $\sin^2(\theta_{13})$ meaning that the reactor constraint is not applied. The Asimov data is generated assuming the AsimovA oscillation parameter set defined in Table 2.2 and the post-BANFF systematic parameter tune.

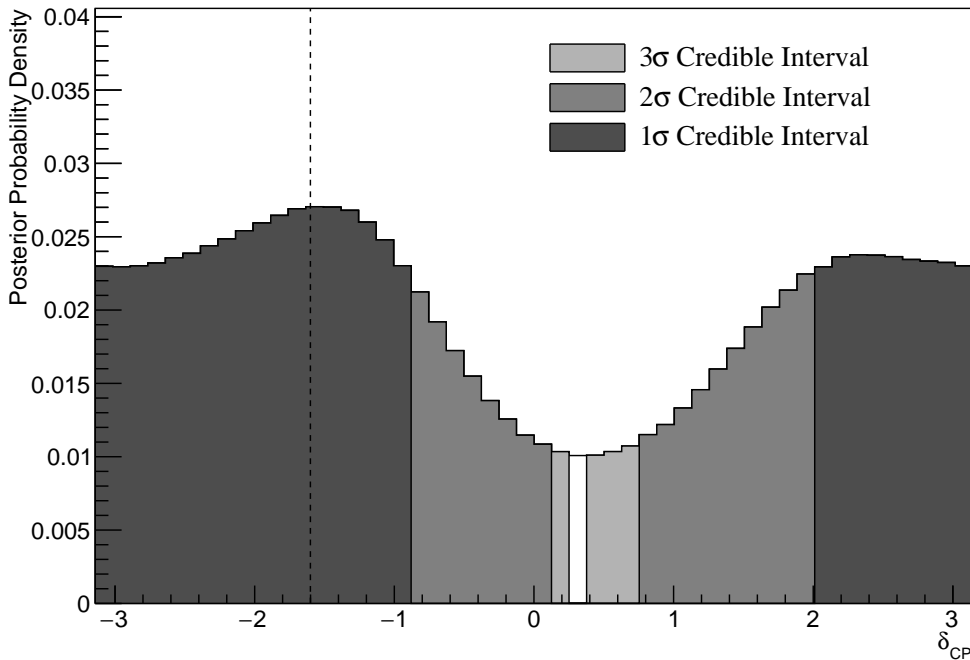


Figure 8.7: The one-dimensional posterior probability density distribution in δ_{CP} , marginalised over both hierarchies, from the SK atmospheric-only fit. The reactor constraint is not applied. The vertical dashed line represents the known value of δ_{CP} .

3082 Figure 8.7 illustrates the posterior probability density for δ_{CP} , marginalised
 3083 over both hierarchies. The fit favours the known oscillation parameter ($\delta_{CP} =$
 3084 -1.601) although the posterior probability is very flat through the range of
 3085 $-\pi < \delta_{CP} < -1$ and $2 < \delta_{CP} < \pi$. There is also a region around $\delta_{CP} \sim 0.4$
 3086 which is disfavoured at 2σ . This indicates that the SK samples can rule out some
 3087 parts of the CP conserving parameter space reasonably well, near $\delta_{CP} \sim 0.4$,
 3088 when the true value of $\delta_{CP} \sim -\pi/2$.

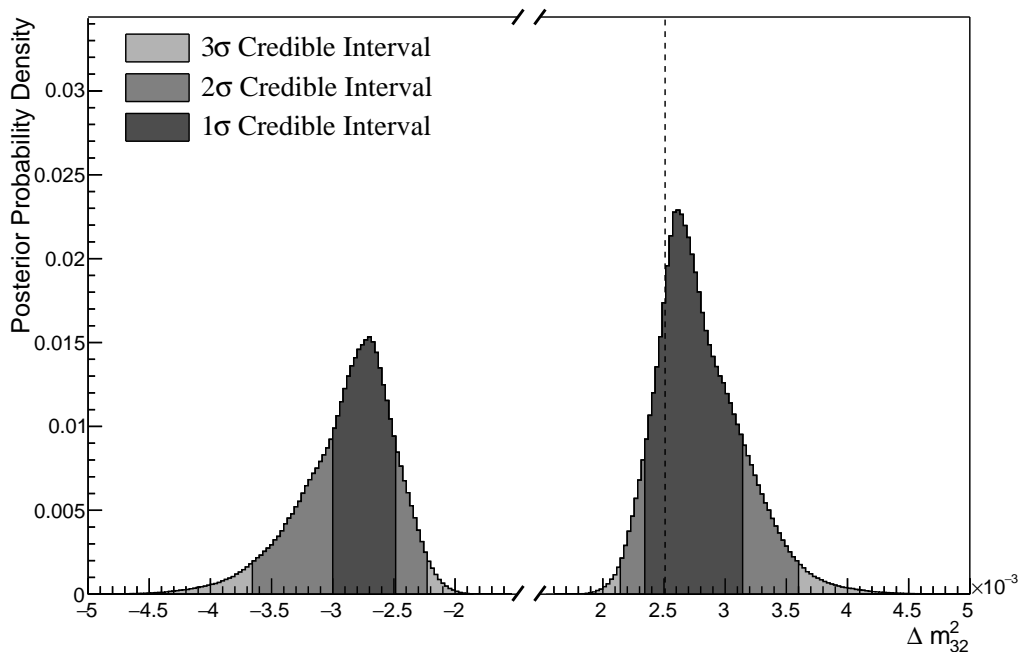


Figure 8.8: The one-dimensional posterior probability density distribution in Δm_{32}^2 , marginalised over both hierarchies, from the SK atmospheric-only fit. The reactor constraint is not applied. The vertical dashed line represents the known value of Δm_{32}^2 .

3089 The posterior probability density in Δm_{32}^2 is given in Figure 8.8. This distribu-
 3090 tion includes steps in both the normal hierarchy (NH, $\Delta m_{32}^2 > 0$) and the inverse
 3091 hierarchy (IH, $\Delta m_{32}^2 < 0$). The highest posterior probability density is found
 3092 within the NH 1σ credible interval, which agrees with the known oscillation
 3093 parameter value, $2.509 \times 10^{-3} \text{ eV}^2$. However, all of the credible intervals span
 3094 both of the hierarchy hypotheses.

	LO ($\sin^2 \theta_{23} < 0.5$)	UO ($\sin^2 \theta_{23} > 0.5$)	Sum
NH ($\Delta m_{32}^2 > 0$)	0.17	0.40	0.58
IH ($\Delta m_{32}^2 < 0$)	0.13	0.29	0.42
Sum	0.31	0.69	1.00

Table 8.2: The distribution of steps in an SK atmospheric-only fit, presented as the fraction of steps in the upper (UO) and lower (LO) octants and the normal (NH) and inverted (IH) hierarchies. The reactor constraint is not applied. The Bayes factors are calculated as $B(\text{NH}/\text{IH}) = 1.37$ and $B(\text{UO}/\text{LO}) = 2.24$.

Following the discussion in subsection 4.3.3, the Bayes factor for hierarchy preference can be calculated by determining the fraction of steps that fall into the NH and the IH regions, as an equal prior is placed on both hypotheses. A similar calculation can be performed by calculating the fraction of steps which fall in the lower octant (LO, $\sin^2 \theta_{23} < 0.5$) or upper octant (UO, $\sin^2 \theta_{23} > 0.5$). The fraction of steps, broken down by hierarchy and octant, are given in Table 8.2. The Bayes factor for preferred hierarchy hypothesis is $B(\text{NH}/\text{IH}) = 1.37$. Jeffrey's scale, given in Table 4.1, states this value of the Bayes factor indicates a weak preference for the normal hierarchy hypothesis which is correct given the known oscillation parameters. The Bayes factor for choice of octant is $B(\text{UO}/\text{LO}) = 2.24$. This is also identifying the correct hypothesis (UO) albeit with a strength classified as a weak preference. Both of these show that the fit is returning the correct choice of hypotheses (NH and UO) for the known Asimov A oscillation parameters defined in Table 2.2.

The 1σ credible intervals, broken down by hierarchy, and position in parameter space of the highest posterior probability density is given in Table 8.3. These are taken from the one-dimensional projections of the oscillation parameters, marginalised over all other parameters within the fit. As the distribution is binned, the highest posterior density is presented as the center of the bin with the highest posterior density with an error equal to the bin width. For the known Asimov value of $\delta_{CP} = -1.601$, the 1σ credible interval rules out a region between $\delta_{CP} = -0.88$ and $\delta_{CP} = 2.01$, when marginalising over both hierarchies. The

Parameter	Interval	HPD
δ_{CP} , (BH)	$[-\pi, -0.88], [2.01, \pi]$	-1.57 ± 0.07
δ_{CP} , (NH)	$[-\pi, -0.88], [1.88, \pi]$	-1.57 ± 0.07
δ_{CP} , (IH)	$[-\pi, -0.88], [2.01, \pi]$	-1.57 ± 0.07
Δm_{32}^2 (BH) [$\times 10^{-3}\text{eV}^2$]	$[-3.00, -2.49], [2.34, 3.14]$	2.61 ± 0.02
Δm_{32}^2 (NH) [$\times 10^{-3}\text{eV}^2$]	$[2.41, 3.04]$	2.59 ± 0.03
Δm_{32}^2 (IH) [$\times 10^{-3}\text{eV}^2$]	$[-3.11, -2.41]$	-2.73 ± 0.03
$\sin^2(\theta_{23})$ (BH)	$[0.476, 0.584]$	0.542 ± 0.006
$\sin^2(\theta_{23})$ (NH)	$[0.488, 0.596]$	0.554 ± 0.006
$\sin^2(\theta_{23})$ (IH)	$[0.476, 0.584]$	0.542 ± 0.006

Table 8.3: The position of the highest posterior probability density (HPD) and width of the 1σ credible interval for the SK atmospheric-only fit. The reactor constraint is not applied. The values are presented by which hierarchy hypothesis is assumed: marginalised over both hierarchies (BH), normal hierarchy only (NH), and inverted hierarchy only (IH).

position of the highest posterior density is $\delta_{CP} = -1.57 \pm 0.07$ which is clearly compatible with the known oscillation parameter value.

The sensitivity of the atmospheric samples to $\sin^2(\theta_{13})$ is presented in Figure 8.9. The likelihood scans presented in Figure 8.1 suggest that the sensitivity to $\sin^2(\theta_{13})$ will be small. This behaviour is also seen in the fit results, where the width of the 1σ credible intervals span the region of $\sin^2(\theta_{13}) = [0.008, 0.08]$. This is more than an order of magnitude worse than the constraint from reactor experiments [72].

As previously discussed, the correlations between oscillation parameters are also important to understand how the atmospheric samples respond. Figure 8.10 illustrates the two dimensional $\sin^2(\theta_{13})-\delta_{CP}$ sensitivity, marginalised over all other parameters. The shape of the 1σ credible interval shows that the constraining power of the fit on δ_{CP} is dependent upon the value of $\sin^2(\theta_{13})$. Whilst the atmospheric samples do not strongly constrain the value of $\sin^2(\theta_{13})$, the value of $\sin^2(\theta_{13})$ does impact the atmospheric samples' sensitivity to δ_{CP} . Furthermore, they show a strong resemblance to the likelihood scans illustrated in Figure 8.2.

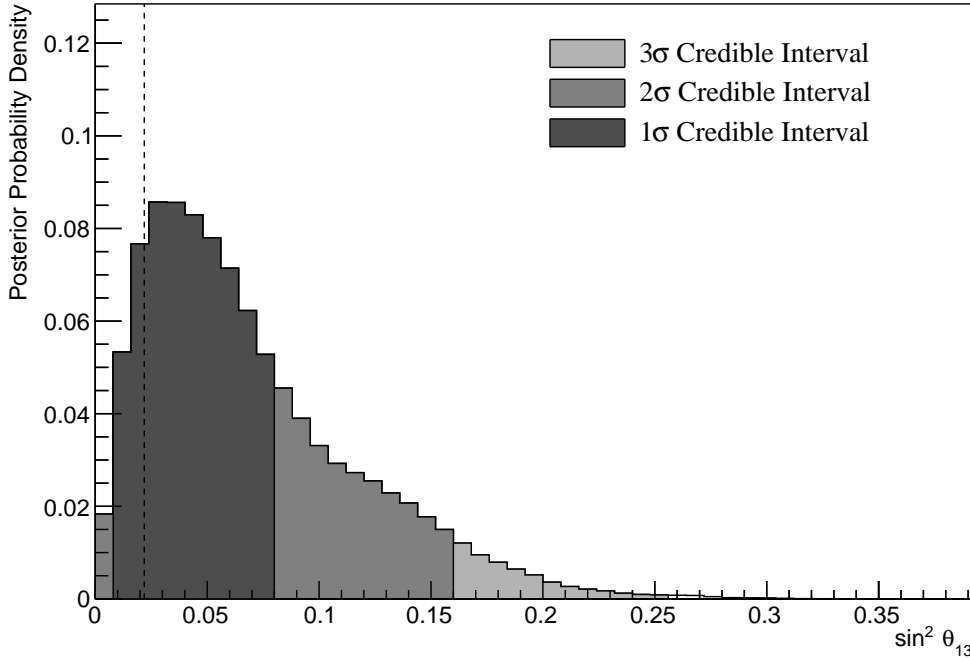


Figure 8.9: The one-dimensional posterior probability density distribution in $\sin^2(\theta_{13})$, marginalised over both hierarchies, from the SK atmospheric-only fit. The reactor constraint is not applied. The vertical dashed line represents the known value of $\sin^2(\theta_{13})$.

3133 The $\sin^2(\theta_{23})-\Delta m_{32}^2$ disappearance contours are illustrated in Figure 8.11. As
 3134 expected, the area contained in the inverted hierarchy 1σ credible interval is
 3135 slightly smaller than that in the normal hierarchy. This follows from the Bayes
 3136 factor showing a weak preference for NH meaning that more of the steps will exist
 3137 in the $\Delta m_{32}^2 > 0$ region. The known oscillation parameters of $\sin^2(\theta_{23}) = 0.528$
 3138 and $\Delta m_{32}^2 = 2.509 \times 10^{-3} \text{ eV}^2$ are contained within the 1σ credible interval.

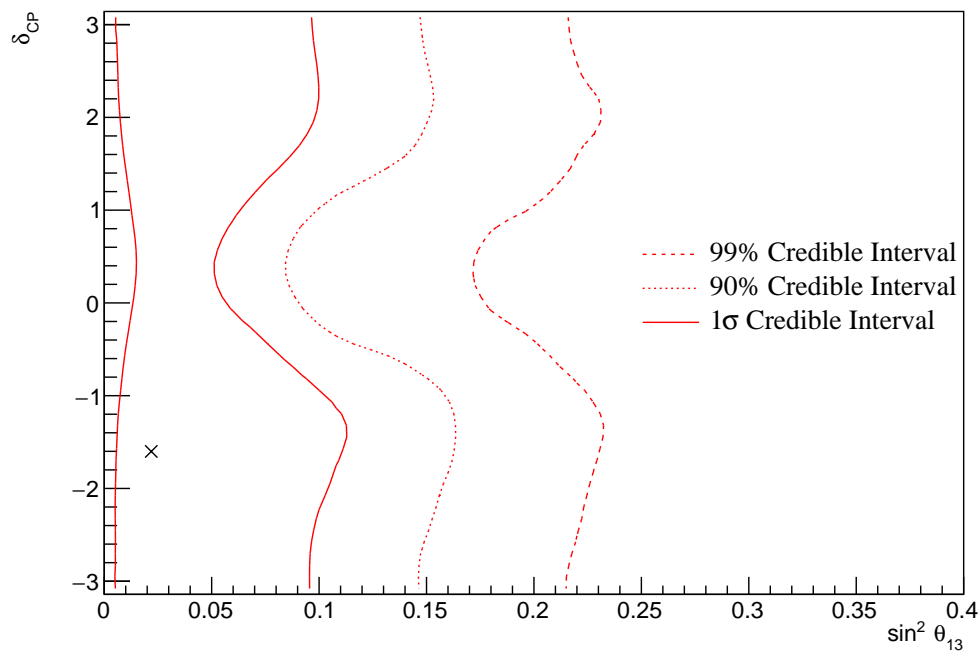


Figure 8.10: The two-dimensional posterior probability density distribution in δ_{CP} – $\sin^2(\theta_{13})$, marginalised over both hierarchies, from the SK atmospheric-only fit. The reactor constraint is not applied. The marker represents the input value.

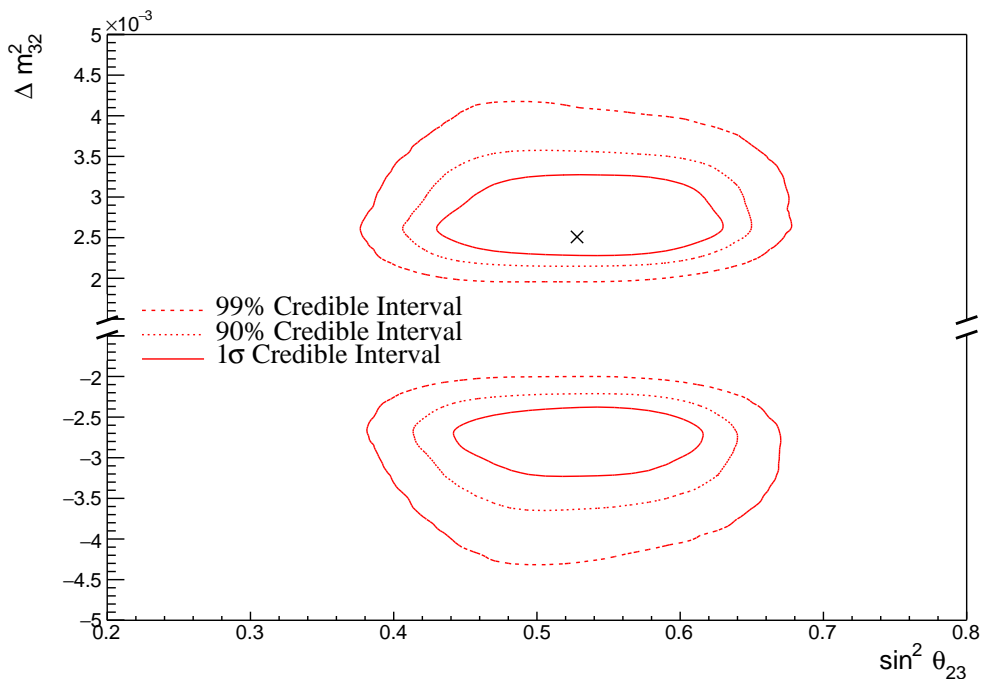


Figure 8.11: The two-dimensional posterior probability density distribution in Δm_{32}^2 – $\sin^2(\theta_{23})$, marginalised over both hierarchies, from the SK atmospheric-only fit. The reactor constraint is not applied. The marker represents the input value.

3139 Figure 8.12 illustrates the two-dimensional projections for each permutation of
3140 oscillation parameters which this analysis is sensitive to: δ_{CP} , $\sin^2(\theta_{13})$, $\sin^2(\theta_{23})$,
3141 and Δm_{32}^2 . The purpose of this plot is to illustrate the correlations between
3142 the oscillation parameters. The contours are calculated whilst marginalising
3143 over both hierarchies, however, only the NH is illustrated when plotting the
3144 Δm_{32}^2 parameter. As expected the correlations play a significant role in these
3145 sensitivity measurements, especially the choice of the $\sin^2(\theta_{13})$ constraint. Most
3146 notably, the application of reactor constraint would be expected to alter both the
3147 width and position of the Δm_{32}^2 intervals due to the strong correlation between
3148 the parameters.

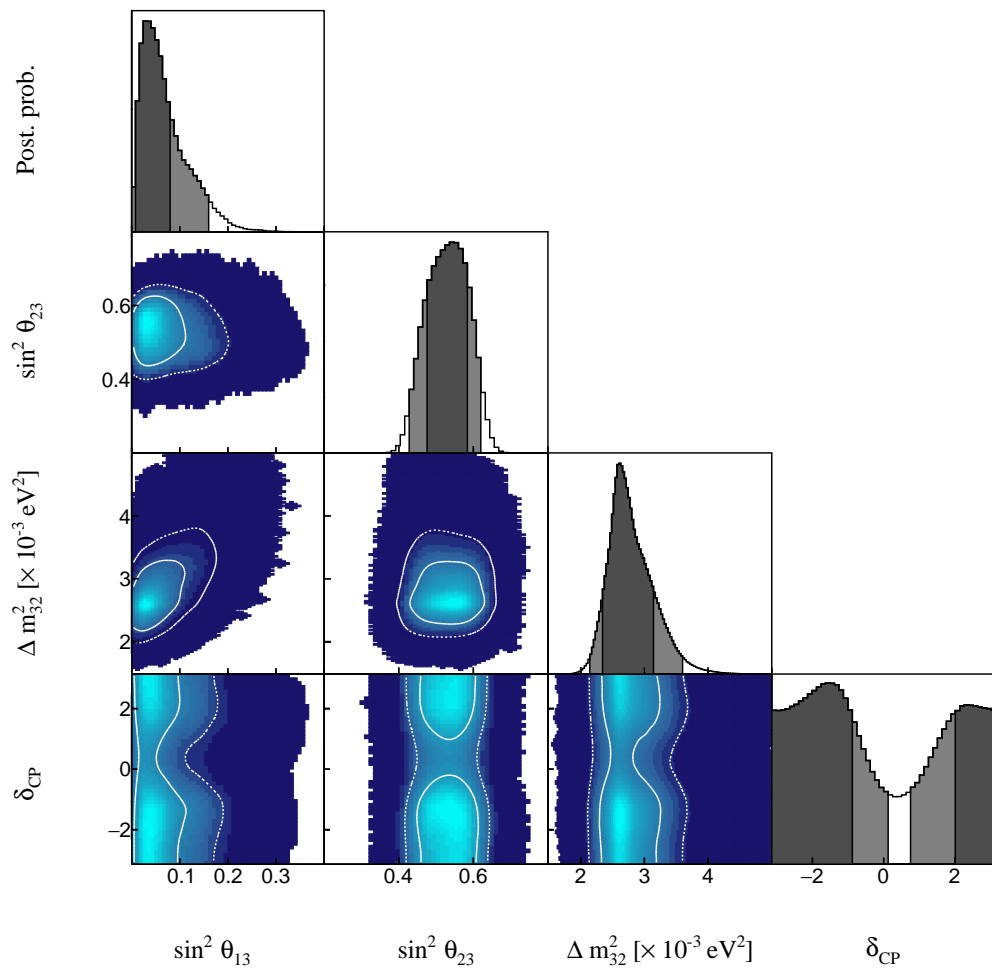


Figure 8.12: The posterior probability density distribution from the SK atmospheric-only fit. The reactor constraint is not applied. The distribution is given for each two-dimensional permutation of the oscillation parameters of interest. The one-dimensional distribution of each parameter is also given.

3149 8.3.2 Atmospheric-Only Sensitivity With Reactor Constraint

3150 The results in subsection 8.3.1 discuss the atmospheric sensitivity when the
 3151 reactor constraint is not applied. The correlations illustrated in Figure 8.12
 3152 indicate that the marginalisation effects could contribute to differing sensitivities
 3153 when the external reactor constraint is applied. Using the technique discussed
 3154 in subsection 4.1.1, the posterior distribution of the fit in subsection 8.3.1 can be
 3155 reweighted to include the reactor constraint of $\sin^2(\theta_{13}) = (2.18 \pm 0.08) \times 10^{-2}$
 3156 [72]. This section documents the sensitivities of the atmospheric-only fit after
 3157 the reactor constraint has been applied.

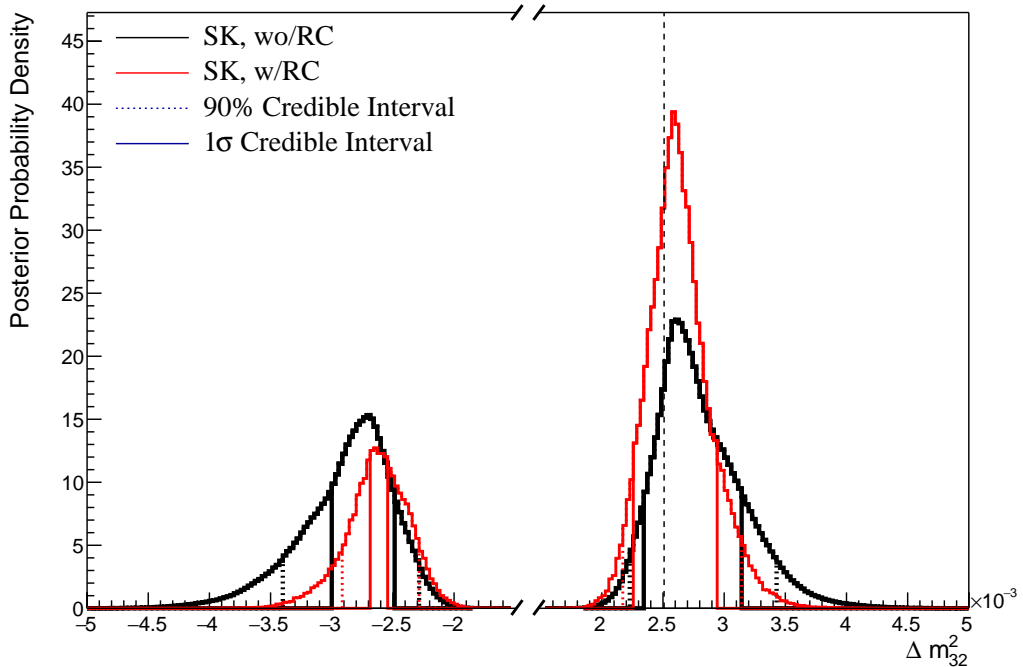


Figure 8.13: The one-dimensional posterior probability density distribution in Δm_{32}^2 compared between the SK atmospheric-only fit (Black) and the SK atmospheric fit with the reactor constraint applied (Red). The distributions are marginalised over both hierarchies. The vertical dashed line represents the known value of Δm_{32}^2 .

3158 The reactor constraint increases the sensitivity of the atmospheric samples to
 3159 Δm_{32}^2 as illustrated in Figure 8.13. The 1σ credible interval in Δm_{32}^2 is determined
 3160 to be $[-2.69, -2.54] \times 10^{-3}\text{eV}^2$ and $[2.25, 2.94] \times 10^{-3}\text{eV}^2$. The width of the IH
 3161 credible interval is reduced by $\sim 70\%$ when the reactor constraint is applied. Due

to the marginalisation effects observed in Figure 8.12, the favoured region of Δm_{32}^2 moves closer to zero for both hierarchies. A clear explanation of this behaviour is illustrated in Figure 8.14, which shows the posterior distribution in the $\Delta m_{32}^2 - \sin^2(\theta_{13})$ parameters. The correlation between Δm_{32}^2 and $\sin^2(\theta_{13})$ is such that lower values of $\sin^2(\theta_{13})$ tend towards lower values of $|\Delta m_{32}^2|$. Therefore the application of the reactor constraint moves the posterior distribution towards the known oscillation parameter.

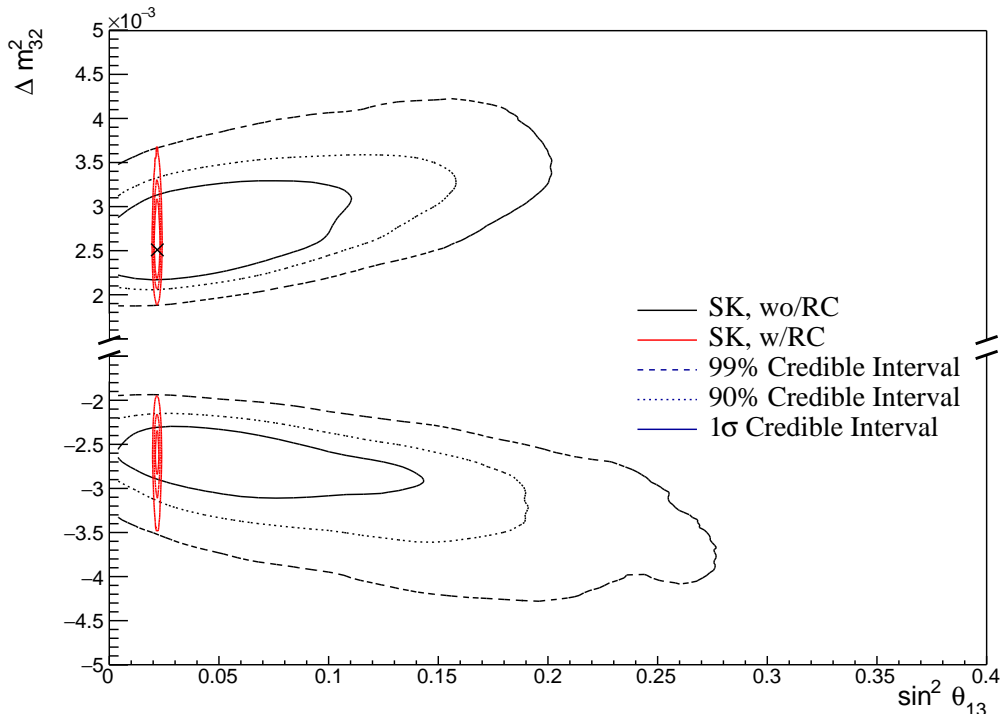


Figure 8.14: The two-dimensional posterior probability density distribution in $\Delta m_{32}^2 - \sin^2(\theta_{13})$ compared between the SK atmospheric-only fit (Black) and the SK atmospheric fit with the reactor constraint (Red). The distributions are marginalised over both hierarchies. The marker represents the known value of $\Delta m_{32}^2 - \sin^2(\theta_{13})$.

Table 8.4 presents the fraction of steps in each hierarchy and octant model for the fit after the reactor constraint has been applied. The reactor constraint significantly increases the preference for the correct hierarchy, increasing the Bayes factor from $B(\text{NH}/\text{IH}) = 1.37$ to $B(\text{NH}/\text{IH}) = 2.85$ when the reactor constraint is applied. This is still defined as a weak preference for the NH hypothesis according to Jeffrey's scale, however, it is a much stronger preference

	LO ($\sin^2 \theta_{23} < 0.5$)	UO ($\sin^2 \theta_{23} > 0.5$)	Sum
NH ($\Delta m_{32}^2 > 0$)	0.21	0.53	0.74
IH ($\Delta m_{32}^2 < 0$)	0.08	0.18	0.26
Sum	0.29	0.71	1.00

Table 8.4: The distribution of steps in an SK atmospheric with reactor constraint fit, presented as the fraction of steps in the upper (UO) and lower (LO) octants and the normal (NH) and inverted (IH) hierarchies. The Bayes factors are calculated as $B(\text{NH}/\text{IH}) = 2.85$ and $B(\text{UO}/\text{LO}) = 2.39$.

³¹⁷⁵ than when the constraint is not applied. The preference for the correct octant
³¹⁷⁶ model is also slightly increased by the application of the reactor constraint.

3177 8.3.3 Impact of Near Detector Constraints for Atmospheric Sam- 3178 ples

3179 The choice of applying the near detector constraints to the low-energy atmo-
3180 spheric samples was introduced in subsection 6.4.3. This subsection illustrates the
3181 effect of removing the ND constraint on the sensitivity of the atmospheric samples
3182 to the oscillation parameters. To do this, the fit presented in subsection 8.3.1 has
3183 been compared to another fit where the constraints from the near detector have
3184 not been included. This is the only case where the near detector constraints are
3185 neglected throughout this chapter. For both fits, the Asimov data was generated
3186 assuming the ‘AsimovA’ oscillation parameter set defined in Table 2.2 and the
3187 post-BANFF systematic parameter tune.

3188 The change in sensitivity on δ_{CP} is given in Figure 8.15. The reactor constraint
3189 is not applied in either of the fits within this comparison. The fit which includes
3190 the near detector constraint is slightly more peaked at the known oscillation
3191 parameter value. The width of the 1σ credible intervals are approximately the
3192 same (identical to within a bin width) and the same conclusion holds for the
3193 higher credible intervals. The change in sensitivity to other oscillation parameters
3194 has been studied and no significant discrepancies were found. This shows that
3195 the exact choice of constraint does not significantly affect the physics conclusions
3196 one would make from this analysis.

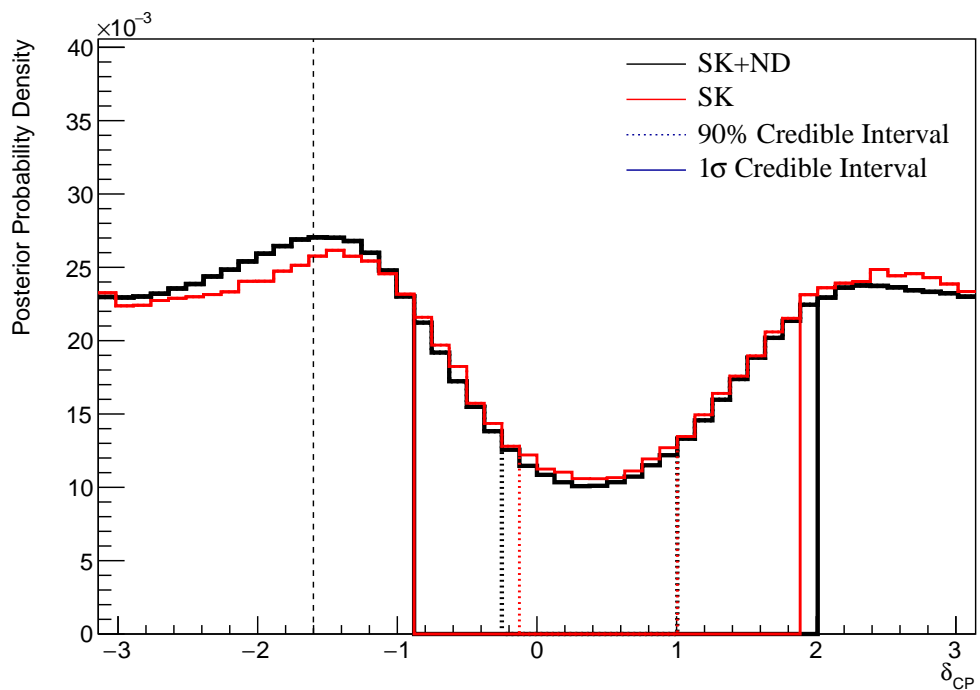


Figure 8.15: The one-dimensional posterior probability density distribution in δ_{CP} compared between the SK atmospheric-only fit where the near detector constraint is (Black) and is not (Red) applied. The distributions are marginalised over both hierarchies. The reactor constraint is not applied in either fit. The vertical dashed line represents the known value of δ_{CP} .

3197 8.3.4 Atmospheric and Beam Sensitivity without Reactor Con- 3198 straint

3199 This section presents the sensitivities of the simultaneous beam and atmospheric
 3200 analysis where the reactor constraint is not applied. Similar to the previous
 3201 studies, the Asimov data is built assuming the post-BANFF systematic tune and
 3202 Asimov A oscillation parameters defined in Table 2.2. This fit uses all 18 near
 3203 detector beam samples, 5 far detector beam samples, and 18 atmospheric samples.

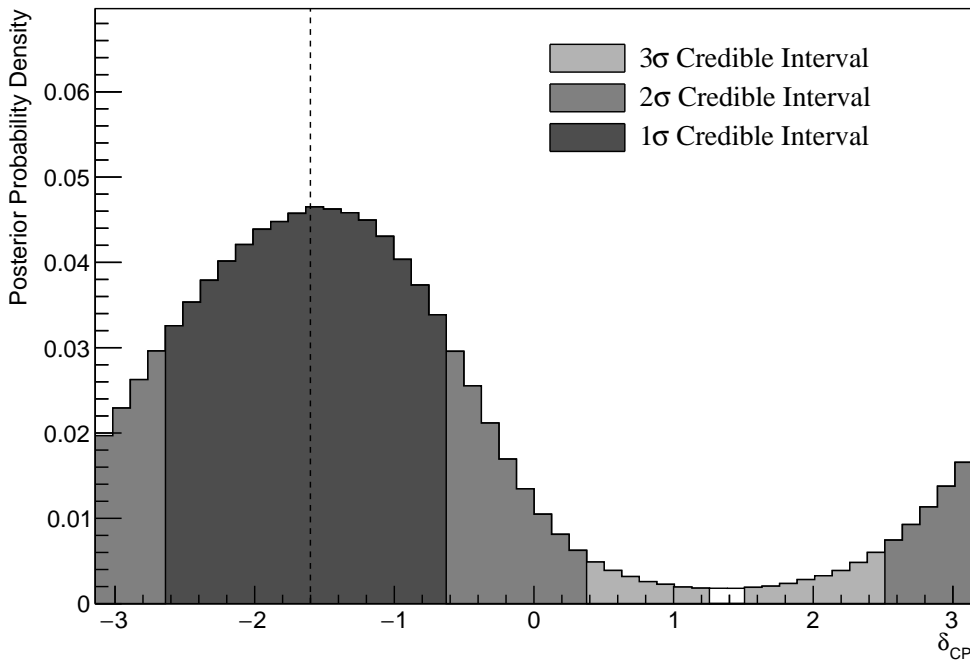


Figure 8.16: The one-dimensional posterior probability density distribution in δ_{CP} , marginalised over both hierarchies, from the joint beam-atmospheric fit. The reactor constraint is not applied. The vertical dashed line represents the known value of δ_{CP} .

3204 The sensitivity to δ_{CP} , marginalised over both hierarchies, is given in Fig-
 3205 ure 8.16. The credible intervals and highest posterior distribution for each
 3206 oscillation parameter is given in Table 8.5. The highest posterior probability
 3207 density is $\delta_{CP} = -1.57 \pm 0.07$ and is compatible with the known value of
 3208 $\delta_{CP} = -1.601$. The CP-conserving values of $\delta_{CP} = 0, \pm\pi$ are disfavoured at
 3209 1 σ credible interval. There is also a region around $\delta_{CP} = 1.4$ which is disfavoured
 3210 at more than 3 σ . Whilst these conclusions can only be made at this particular

3211 Asimov point, it does show that if the true value of δ_{CP} were CP-violating,
3212 this joint analysis would be able to disfavour CP conserving values at over 1σ
3213 without any external constraints.

Parameter	Interval	HPD
δ_{CP} , (BH)	$[-2.64, -0.63]$	-1.57 ± 0.07
δ_{CP} , (NH)	$[-2.76, -0.63]$	-1.45 ± 0.07
δ_{CP} , (IH)	$[-2.39, -0.88]$	-1.57 ± 0.07
Δm_{32}^2 (BH) [$\times 10^{-3}\text{eV}^2$]	[2.45, 2.58]	2.51 ± 0.01
Δm_{32}^2 (NH) [$\times 10^{-3}\text{eV}^2$]	[2.47, 2.56]	2.51 ± 0.01
Δm_{32}^2 (IH) [$\times 10^{-3}\text{eV}^2$]	$[-2.60, -2.51]$	-2.55 ± 0.01
$\sin^2(\theta_{23})$ (BH)	[0.480, 0.545]	0.518 ± 0.003
$\sin^2(\theta_{23})$ (NH)	[0.480, 0.545]	0.508 ± 0.003
$\sin^2(\theta_{23})$ (IH)	[0.480, 0.545]	0.513 ± 0.003

Table 8.5: The position of the highest posterior probability density (HPD) and width of the 1σ credible interval for the joint beam-atmospheric fit. The reactor constraint is not applied. The values are presented by which hierarchy hypothesis is assumed: marginalised over both hierarchies (BH), normal hierarchy only (NH), and inverted hierarchy only (IH).

3214 The sensitivity to Δm_{32}^2 is illustrated in Figure 8.17. Notably, the 1σ credible
3215 interval is entirely contained within the NH region, as further evidenced by
3216 Table 8.5. This illustrates good sensitivity to the mass hierarchy as it is correctly
3217 selecting the known hypothesis. This is reflected in the 1σ credible intervals being
3218 approximately the same when they are constructed considering both hierarchies
3219 and when considering only the NH region. The NH distribution favours this
3220 region surrounding the known Asimov point, $\Delta m_{32}^2 = 2.509 \times 10^{-3}\text{eV}^2$, where
3221 the highest posterior probability density is at $\Delta m_{32}^2 = (2.51 \pm 0.01) \times 10^{-3}\text{eV}^2$.

3222 The fraction of steps in each of the mass hierarchy regions and octants of
3223 $\sin^2(\theta_{23})$ is given in Table 8.6. The Bayes factors are determined to be $B(\text{NH}/\text{IH}) =$
3224 3.67 and $B(\text{UO}/\text{LO}) = 1.74$. Jeffrey's scale states that this value of the mass
3225 hierarchy Bayes factor illustrates substantial evidence for the NH hypothesis.

3226 This corresponds to the correct hypothesis given the known oscillation parameters
 3227 and is a stronger statement than the atmospheric-only analysis can provide. It
 3228 is important to note that this substantial preference requires no external con-
 3229 straints on $\sin^2(\theta_{13})$. The Bayes factor for octant determination represents a weak
 3230 preference for the upper octant, therefore, selecting the correct octant hypothesis.

	LO ($\sin^2 \theta_{23} < 0.5$)	UO ($\sin^2 \theta_{23} > 0.5$)	Sum
NH ($\Delta m_{32}^2 > 0$)	0.29	0.50	0.79
IH ($\Delta m_{32}^2 < 0$)	0.08	0.13	0.21
Sum	0.37	0.63	1.00

Table 8.6: The distribution of steps in a joint beam-atmospheric fit, presented as the fraction of steps in the upper (UO) and lower (LO) octants and the normal (NH) and inverted (IH) hierarchies. The reactor constraint is not applied. The Bayes factors are calculated as $B(\text{NH}/\text{IH}) = 3.67$ and $B(\text{UO}/\text{LO}) = 1.74$.

3231 The sensitivity to $\sin^2(\theta_{23})$ is presented in Figure 8.18. There is a clear
 3232 preference for the upper octant but the peak of the distribution is relatively
 3233 flat. It peaks at $\sin^2(\theta_{23}) = 0.509 \pm 0.003$ which is in the region of the known
 3234 value of $\sin^2(\theta_{23}) = 0.528$. The difference in the highest posterior distribution
 3235 and the width of the credible interval is relatively unchanged when consid-
 3236 ering different hierarchy hypotheses showing no strong correlation between
 3237 $\sin^2(\theta_{23})$ and $|\Delta m_{32}^2|$.

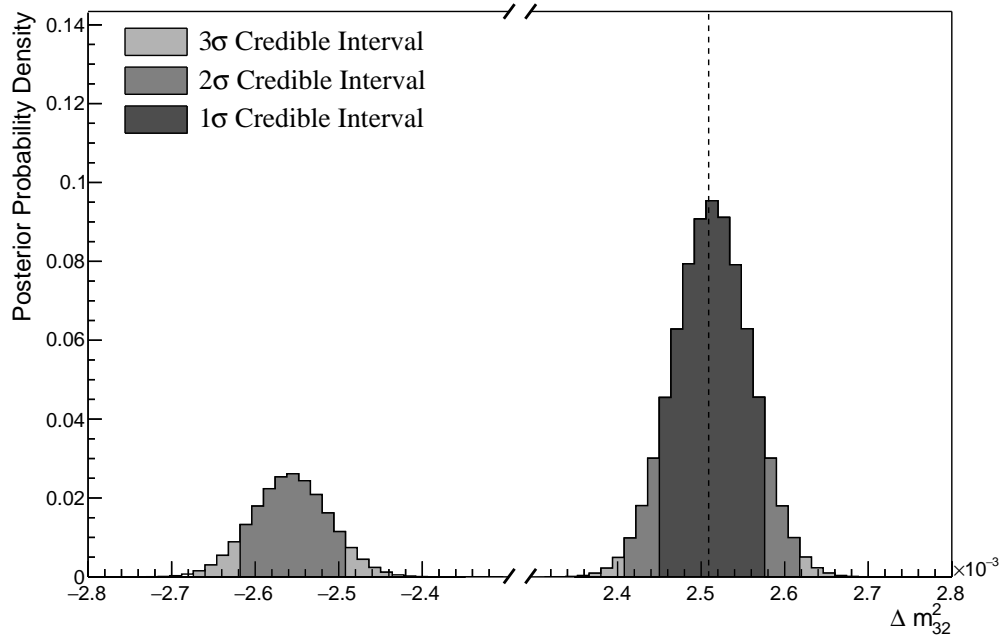


Figure 8.17: The one-dimensional posterior probability density distribution in Δm_{32}^2 , marginalised over both hierarchies, from the joint beam-atmospheric fit. The reactor constraint is not applied. The vertical dashed line represents the known value of Δm_{32}^2 .

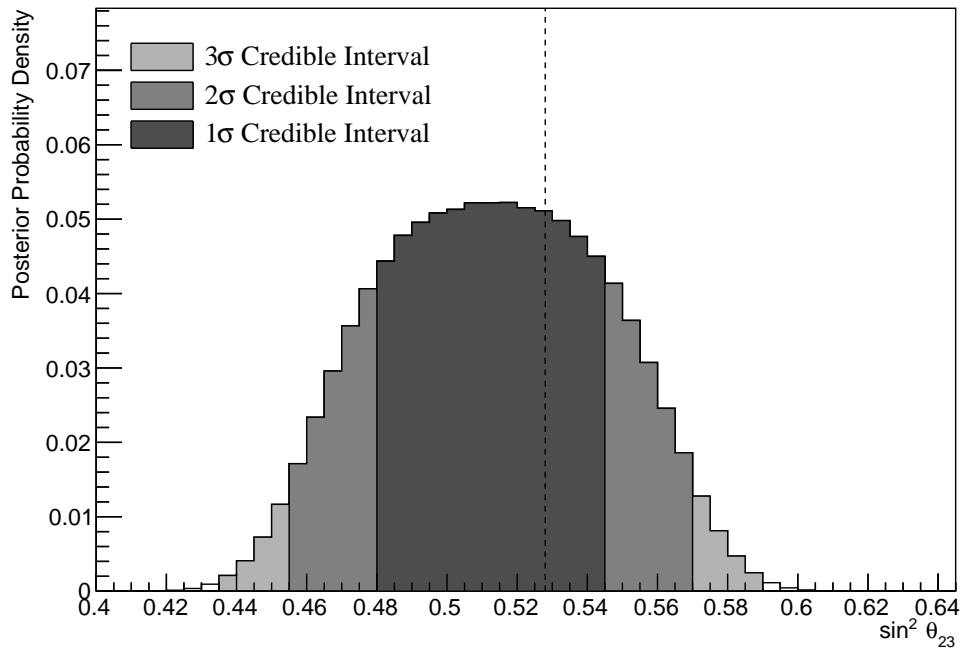


Figure 8.18: The one-dimensional posterior probability density distribution in $\sin^2(\theta_{23})$, marginalised over both hierarchies, from the joint beam-atmospheric fit. The reactor constraint is not applied. The vertical dashed line represents the known value of $\sin^2(\theta_{23})$.

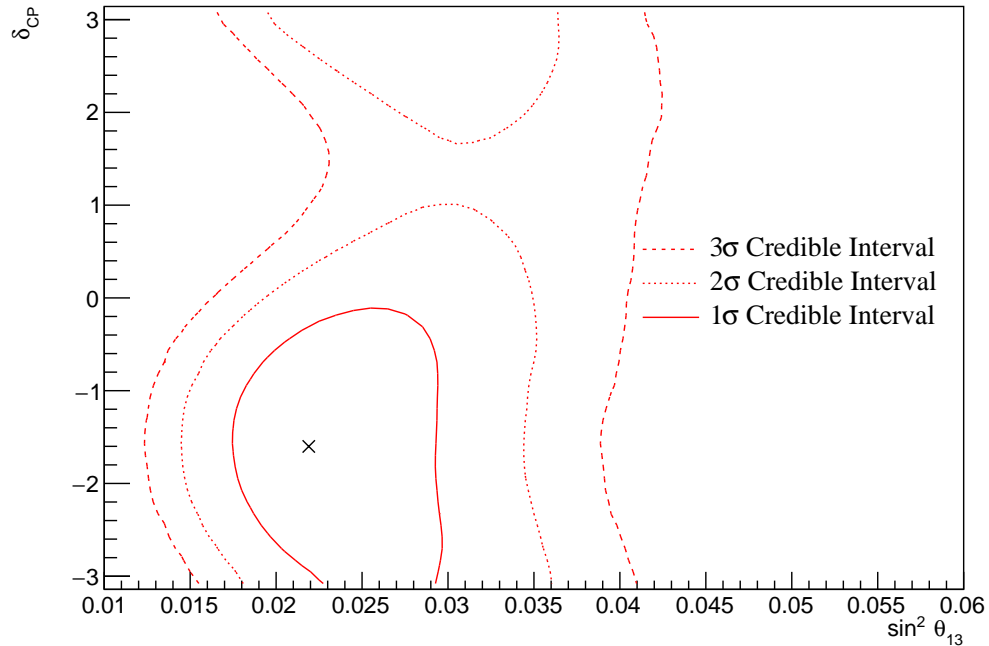


Figure 8.19: The two-dimensional posterior probability density distribution in δ_{CP} – $\sin^2(\theta_{13})$, marginalised over both hierarchies, from the joint beam-atmospheric fit. The reactor constraint is not applied. The marker represents the input value.

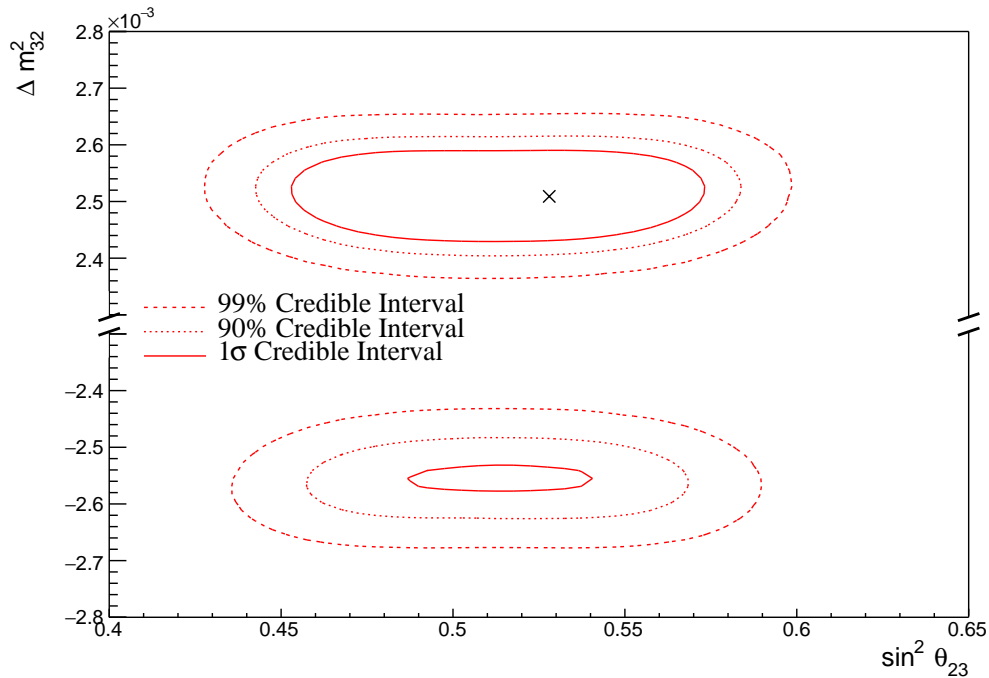


Figure 8.20: The two-dimensional posterior probability density distribution in Δm_{32}^2 – $\sin^2(\theta_{23})$, marginalised over both hierarchies, from the joint beam-atmospheric fit. The reactor constraint is not applied. The marker represents the input value.

3238 The sensitivity presented as a function of the appearance parameters ($\sin^2(\theta_{13}) - \delta_{CP}$)
 3239 is given in Figure 8.19. As expected, the contours follow the likelihood shape
 3240 given in Figure 8.2, where the 2σ credible intervals have a closed contour exclud-
 3241 ing the region around $\delta_{CP} \sim 1.2$. The width of the 3σ credible interval in $\sin^2(\theta_{13})$
 3242 is dependent upon the value of δ_{CP} . Close to the Asimov point, $\delta_{CP} = -1.601$, the
 3243 width of the 3σ credible interval approximately spans $\sin^2(\theta_{13}) = [0.013, 0.04]$.
 3244 This is reduced to a region of $\sin^2(\theta_{13}) = [0.023, 0.042]$ at the most disfavoured
 3245 value of δ_{CP} . The 1σ credible interval is consistent with the known oscillation
 3246 parameter. Application of the reactor constraint would be expected to decrease
 3247 the width of the 1σ credible intervals in δ_{CP} due to the triangular shape of the
 3248 posterior probability around the known value.

3249 The sensitivity in terms of the disappearance parameters, $\sin^2(\theta_{23}) - \Delta m_{32}^2$, is
 3250 given in Figure 8.20. The area contained within the IH contours is significantly
 3251 smaller than the area within the NH contours. The IH credible intervals are
 3252 also notably tighter in the $\sin^2(\theta_{23})$ dimension. No significant correlation is
 3253 observed between $\sin^2(\theta_{23})$ and $|\Delta m_{32}^2|$.

3254 The two-dimensional posterior distribution for each permutation of the oscil-
 3255 lation parameters of interest is given in Figure 8.21. The most notable observation
 3256 is that the $\sin^2(\theta_{13})$ and $\sin^2(\theta_{23})$ are anti-correlated. If the value of $\sin^2(\theta_{13})$ was
 3257 constrained closer to the known oscillation parameter value, the preferred value
 3258 of $\sin^2(\theta_{23})$ would increase. This would move the highest posterior probability
 3259 closer in line with the known value and could lead to an increase in the preference
 3260 for the correct octant hypothesis (UO).

3261 Furthermore, the δ_{CP} and $|\Delta m_{32}^2|$ oscillation parameters are anti-correlated,
 3262 such that higher values of $|\Delta m_{32}^2|$ prefer lower values of δ_{CP} . Whilst this is
 3263 an interesting result on its own, the width of the Δm_{32}^2 contours also depend
 3264 on $\sin^2(\theta_{13})$. This introduces another correlation effect that could modify the
 3265 sensitivity to δ_{CP} once the reactor constraint is applied.

3266 The correlation between $\sin^2(\theta_{13})$ and Δm_{32}^2 can be seen in Figure 8.22. A
 3267 much larger fraction of the posterior distribution is contained in the NH for lower

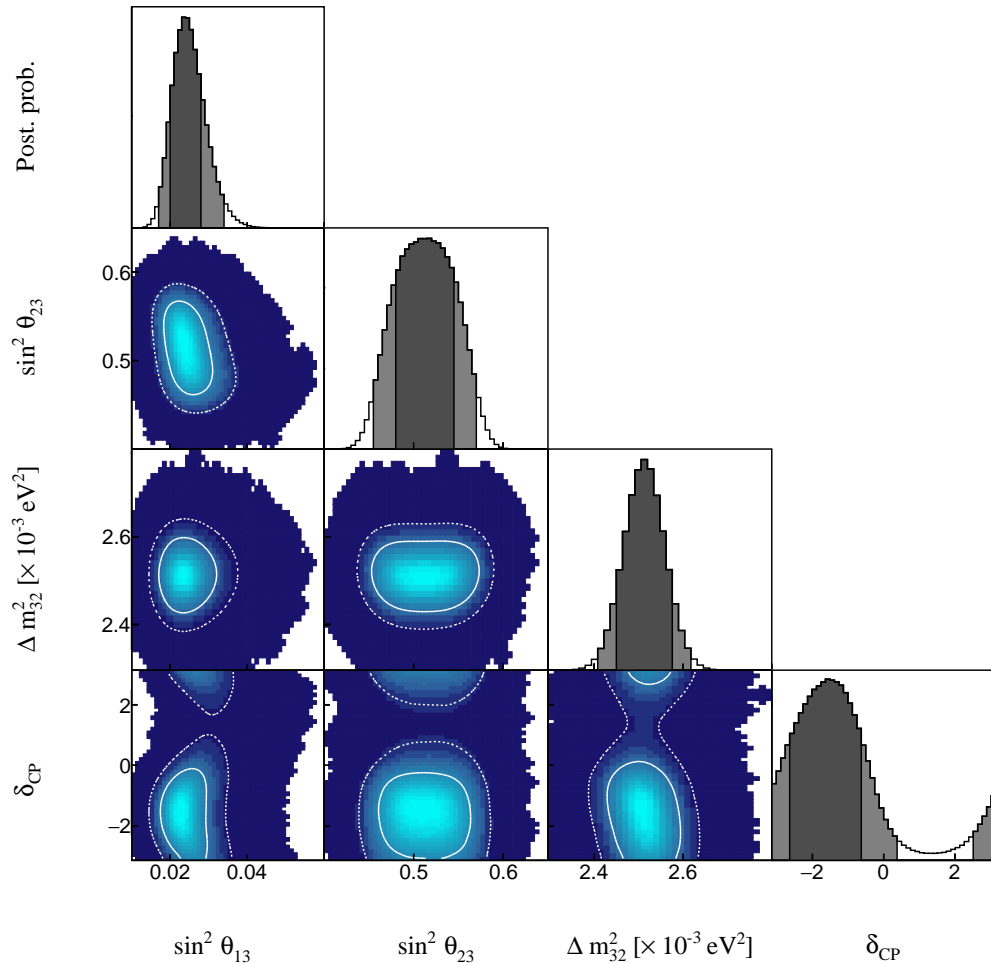


Figure 8.21: The posterior probability density distribution from the joint beam-atmospheric fit. The reactor constraint is not applied. The distribution is given for each two-dimensional permutation of the oscillation parameters of interest. The one-dimensional distribution of each parameter is also given.

3268 values of $\sin^2(\theta_{13})$. Consequently, the application of the reactor constraint would
 3269 be expected to significantly increase the preference for NH.

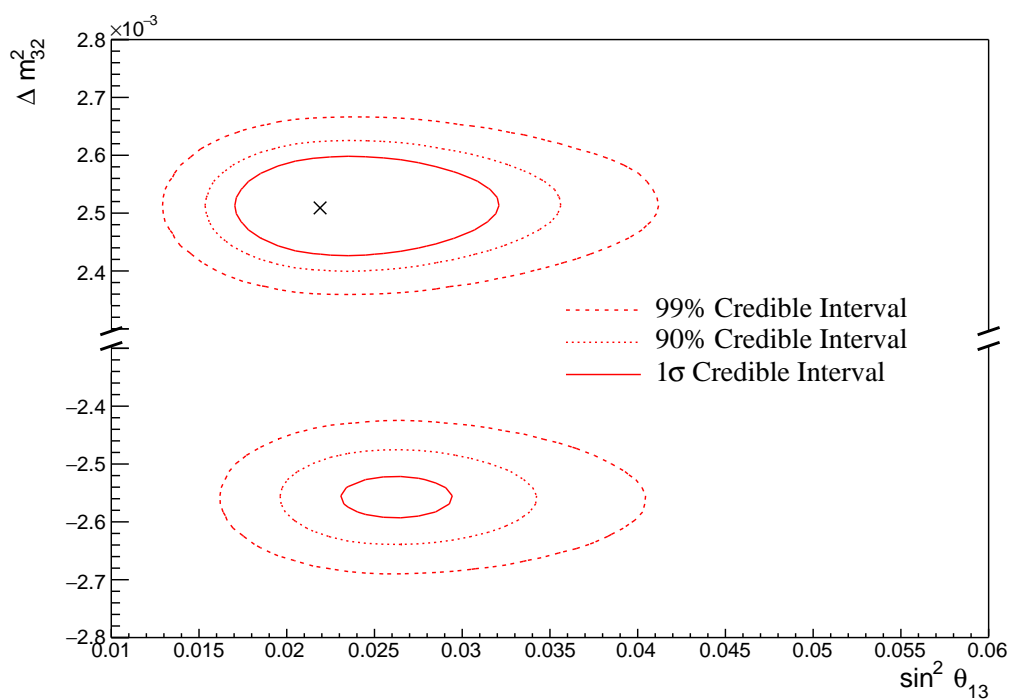


Figure 8.22: The two-dimensional posterior probability density distribution in $\Delta m_{32}^2 - \sin^2(\theta_{13})$, marginalised over both hierarchies, from the joint beam-atmospheric fit. The reactor constraint is not applied. The marker represents the known value of $\Delta m_{32}^2 - \sin^2(\theta_{13})$.

3270 8.3.5 Atmospheric and Beam Sensitivity with Reactor Constraint

3271 This section presents the sensitivities of the joint beam-atmospheric fit when
3272 the reactor constraint is applied to $\sin^2(\theta_{13})$. As with the previous studies, the
3273 Asimov data is made using the AsimovA oscillation parameter set defined in
3274 Table 2.2 and the post-BANFF systematic parameter tune.

3275 Figure 8.23 illustrates the sensitivity to δ_{CP} , marginalised over both hierarchies.
3276 The CP-conserving value of $\delta_{CP} = 0$ is disfavoured at 2σ whilst the value of $\delta_{CP} =$
3277 $\pm\pi$ is very close to being disfavoured at 2σ . Furthermore, the 3σ credible interval
3278 excludes the region of $\delta_{CP} = [0.63, 2.39]$, thus clearly disfavouring the region of
3279 $\delta_{CP} = \pi/2$ at more than 3σ for this particular set of known oscillation parameters.
3280 The width of the 1σ credible intervals and the position of the highest posterior
3281 probability density is given in Table 8.7. The highest posterior probability density
3282 in δ_{CP} is calculated as $\delta_{CP} = -1.57 \pm 0.07$ showing no significant biases in the
3283 determination of the known oscillation parameters.

3284 The effect of applying the reactor constraint for δ_{CP} in the joint beam-atmospheric
3285 fit is presented in Figure 8.24. The reactor constraint significantly improves the
3286 ability of the fit to select the known parameter value. This behaviour is evidenced
3287 by the tightening of the 1σ and 90% credible intervals and the disfavoured region,
3288 centered at $\delta_{CP} \sim \pi/2$, becoming wider when the reactor constraint is applied.
3289 This follows from the correlations shown in Figure 8.19, where a lower value
3290 of $\sin^2(\theta_{13})$ results in tighter constraints on δ_{CP} .

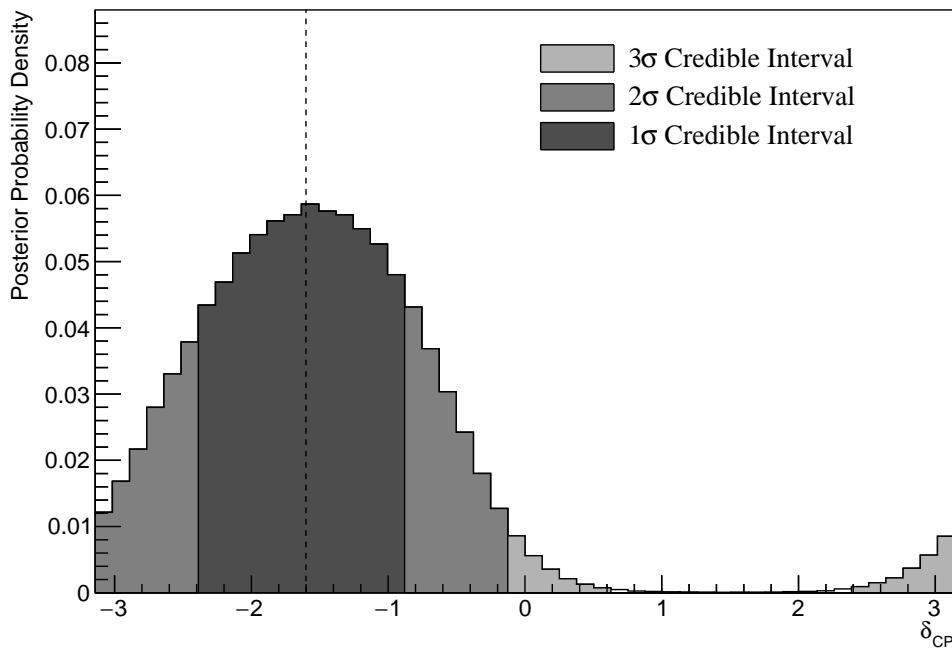


Figure 8.23: The one-dimensional posterior probability density distribution in δ_{CP} , marginalised over both hierarchies, from the joint beam-atmospheric fit where the reactor constraint is applied. The vertical dashed line represents the known value.

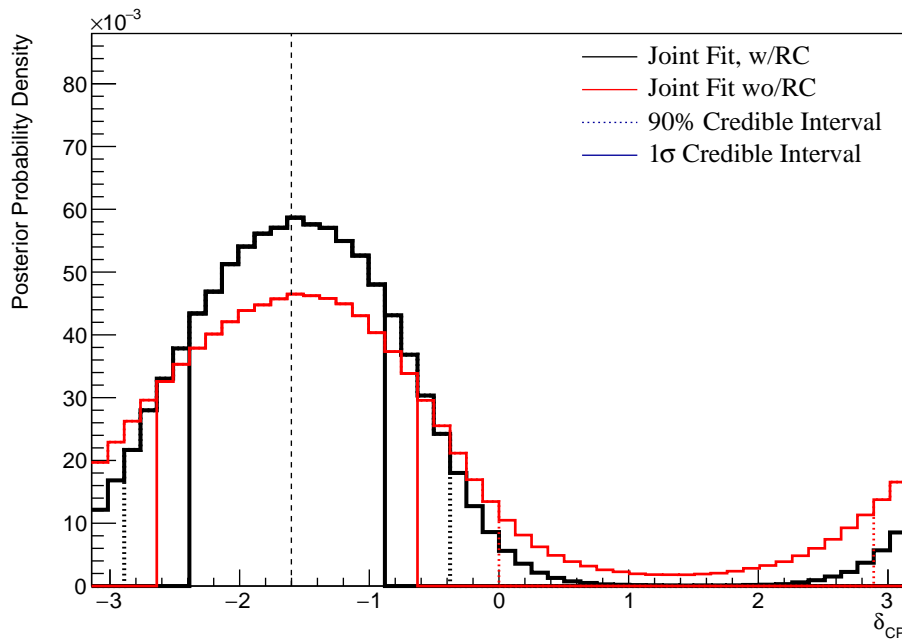


Figure 8.24: The one-dimensional posterior probability density distribution in δ_{CP} compared between the joint beam-atmospheric fit (Red) and the joint beam-atmospheric fit with the reactor constraint (Black). The distributions are marginalised over both hierarchies. The vertical dashed line represents the known value.

Parameter	Interval	HPD
δ_{CP} , (BH)	$[-2.39, -0.88]$	-1.57 ± 0.07
δ_{CP} , (NH)	$[-2.39, -0.75]$	-1.57 ± 0.07
δ_{CP} , (IH)	$[-2.14, -1.01]$	-1.57 ± 0.07
Δm_{32}^2 (BH) [$\times 10^{-3}\text{eV}^2$]	[2.45, 2.56]	2.51 ± 0.01
Δm_{32}^2 (NH) [$\times 10^{-3}\text{eV}^2$]	[2.47, 2.56]	2.51 ± 0.01
Δm_{32}^2 (IH) [$\times 10^{-3}\text{eV}^2$]	$[-2.60, -2.51]$	-2.55 ± 0.01
$\sin^2(\theta_{23})$ (BH)	[0.490, 0.555]	0.528 ± 0.03
$\sin^2(\theta_{23})$ (NH)	[0.490, 0.555]	0.528 ± 0.03
$\sin^2(\theta_{23})$ (IH)	[0.500, 0.560]	0.538 ± 0.03

Table 8.7: The position of the highest posterior probability density (HPD) and width of the 1σ credible interval for the joint beam-atmospheric fit where the reactor constraint is applied. The values are presented by which hierarchy hypothesis is assumed: marginalised over both hierarchies (BH), normal hierarchy only (NH), and inverted hierarchy only (IH).

The sensitivity to $\sin^2(\theta_{23})$, marginalised over both hierarchies, is given in Figure 8.25. The highest posterior probability density is located at $\sin^2(\theta_{23}) = 0.528 \pm 0.03$ which agrees with the known value of $\sin^2(\theta_{23}) = 0.528$. The distribution clearly favours the UO with almost the entirety of the 1σ credible interval being contained in that region. Figure 8.26 highlights the sensitivity of the joint fit both with and without the reactor constraint. The fit where the reactor constraint is applied selects the known value much better. This is a result of the marginalisation effects between the $\sin^2(\theta_{13})$ and $\sin^2(\theta_{23})$ parameters, as observed in Figure 8.21.

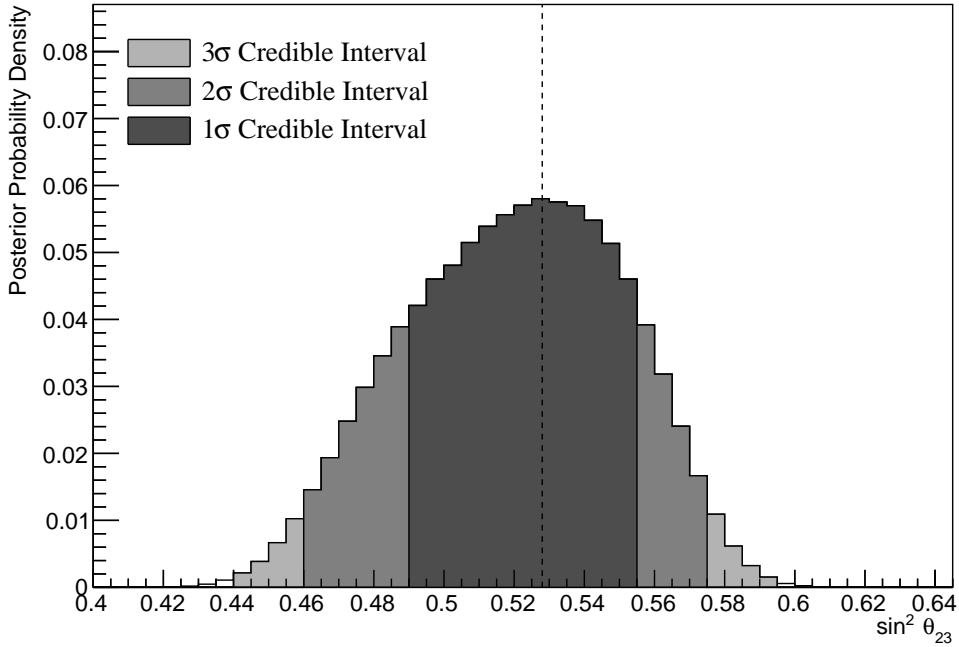


Figure 8.25: The one-dimensional posterior probability density distribution in $\sin^2(\theta_{23})$, marginalised over both hierarchies, from the joint beam-atmospheric fit where the reactor constraint is applied. The vertical dashed line represents the known value.

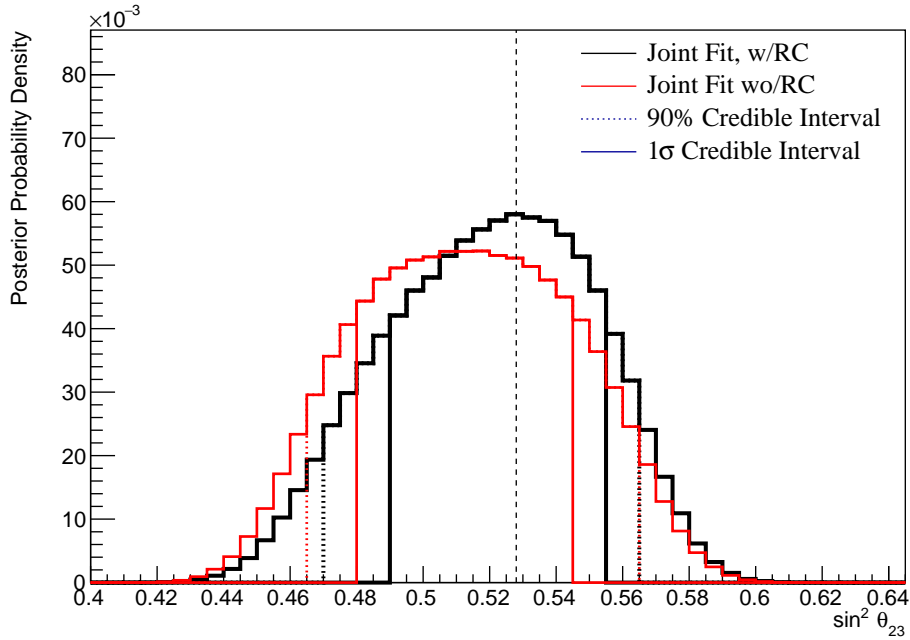


Figure 8.26: The one-dimensional posterior probability density distribution in $\sin^2(\theta_{23})$ compared between the joint beam-atmospheric fit (Red) and the joint beam-atmospheric fit with the reactor constraint (Black). The distributions are marginalised over both hierarchies. The vertical dashed line represents the known value.

3300 The fraction of steps from the joint fit, after the reactor constraint is applied, is
 3301 given in Table 8.8 and split by the two hierarchy and two octant hypotheses. The
 3302 reactor constraint significantly reduces the fraction of steps that are contained
 3303 within the IH-LO region from 0.08 to 0.03, whilst significantly increasing the
 3304 fraction of steps within the NH-UO region from 0.50 to 0.62. The application
 3305 of the reactor constraint increases the Bayes factor from $B(\text{NH}/\text{IH}) = 3.67$ to
 3306 $B(\text{NH}/\text{IH}) = 6.47$. There is a very clear preference for the correct hypothesis,
 3307 with the Jeffreys scale stating a substantial preference for both fits. The Bayes
 3308 factor for selecting the correct octant is calculated as $B(\text{UO}/\text{LO}) = 2.64$. Whilst
 3309 still a weak preference, this is certainly a stronger statement than the sensitivity
 3310 when the reactor constraint is not applied.

	LO ($\sin^2 \theta_{23} < 0.5$)	UO ($\sin^2 \theta_{23} > 0.5$)	Sum
NH ($\Delta m_{32}^2 > 0$)	0.24	0.62	0.87
IH ($\Delta m_{32}^2 < 0$)	0.03	0.10	0.13
Sum	0.27	0.73	1.00

Table 8.8: The distribution of steps in a joint beam-atmospheric with the reactor constraint fit applied, presented as the fraction of steps in the upper (UO) and lower (LO) octants and the normal (NH) and inverted (IH) hierarchies. The Bayes factors are calculated as $B(\text{NH}/\text{IH}) = 6.47$ and $B(\text{UO}/\text{LO}) = 2.64$.

3311 The sensitivity of the joint beam-atmospheric fit to Δm_{32}^2 , with the reactor
 3312 constraint applied, is presented in Figure 8.27. The 1σ credible interval is
 3313 entirely contained within the NH region and the position of the highest posterior
 3314 probability density is given as $(2.51 \pm 0.01) \times 10^{-3}\text{eV}^2$. This illustrates no bias
 3315 between the fit results and the known oscillation parameters. The application
 3316 of the reactor constraint does not significantly move the position or width of
 3317 the credible intervals.

3318 The sensitivity to the appearance parameters ($\sin^2(\theta_{13}) - \delta_{CP}$) is given in Fig-
 3319 ure 8.28. The distribution is mostly uncorrelated between the two parameters
 3320 and is centered at the known oscillation parameters. The 1σ contours exclude

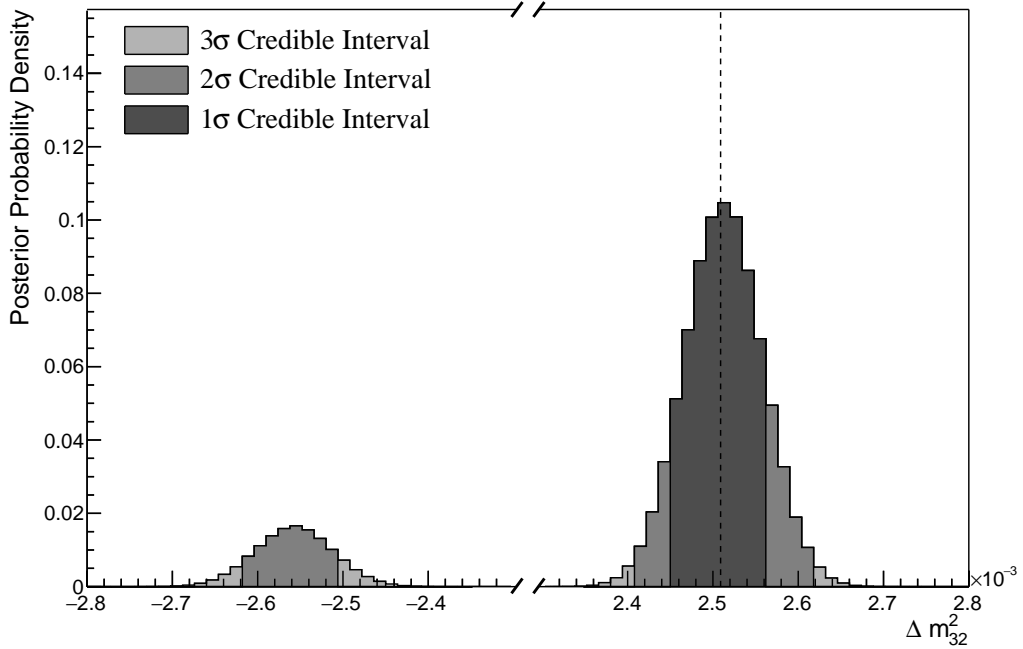


Figure 8.27: The one-dimensional posterior probability density distribution in Δm_{32}^2 from the joint beam-atmospheric fit where the reactor constraint is applied. The vertical dashed line represents the known value of Δm_{32}^2 .

values of $\delta_{CP} = 0$ and $\delta_{CP} = \pm\pi$. Furthermore, the 3σ contours exclude the region of $\delta_{CP} = \pi/2$.

The sensitivity to the disappearance parameters ($\sin^2(\theta_{23}) - \Delta m_{32}^2$) is illustrated in Figure 8.29. The 1σ contour is entirely contained within the NH region reflecting the same results as the one-dimensional marginalised results in Figure 8.27. Both the NH and IH regions favour the UO, with a visually similar preference in both hierarchies. The width of the 1σ contour, in Δm_{32}^2 , does not significantly depend upon the value or octant of $\sin^2(\theta_{23})$. This shows that there are no strong correlations between these two parameters.

Figure 8.30 illustrates the posterior distribution for each permutation of two oscillation parameters of interest. The application of the reactor constraint significantly reduces the correlations previously seen in Figure 8.21.

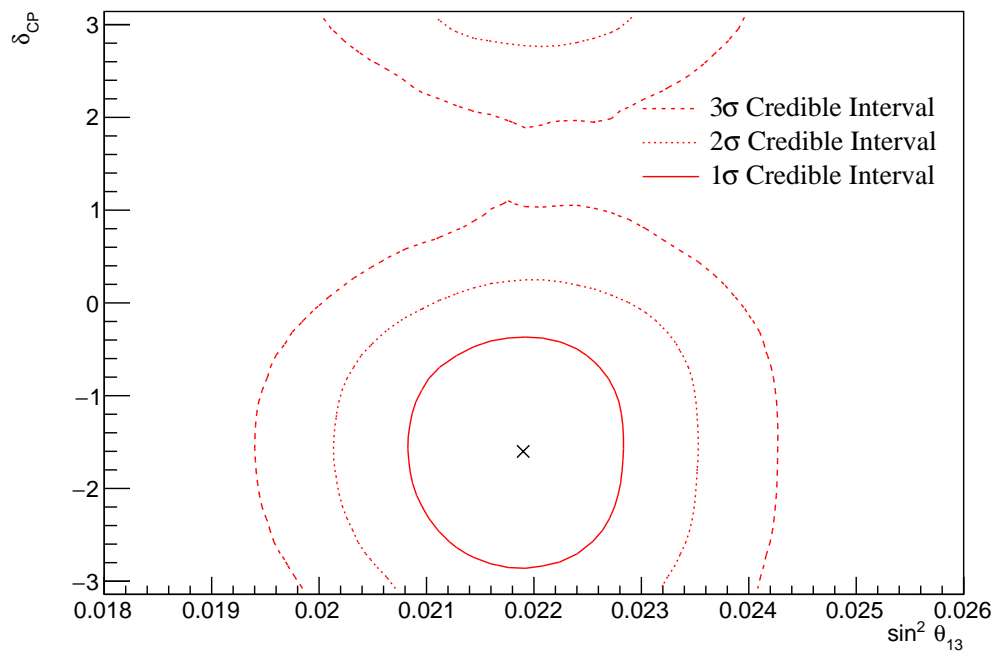


Figure 8.28: The two-dimensional posterior probability density distribution in δ_{CP} – $\sin^2(\theta_{13})$, marginalised over both hierarchies, from the joint beam-atmospheric fit where the reactor constraint is applied. The marker represents the known value.

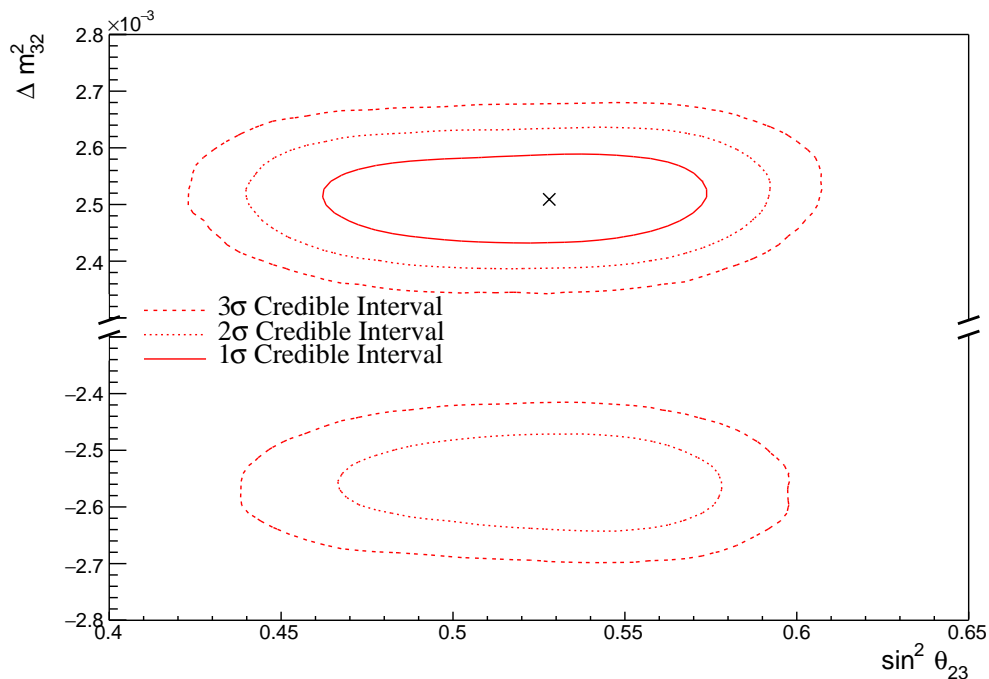


Figure 8.29: The two-dimensional posterior probability density distribution in Δm_{32}^2 – $\sin^2(\theta_{23})$, marginalised over both hierarchies, from the joint beam-atmospheric fit where the reactor constraint is applied. The marker represents the known value.

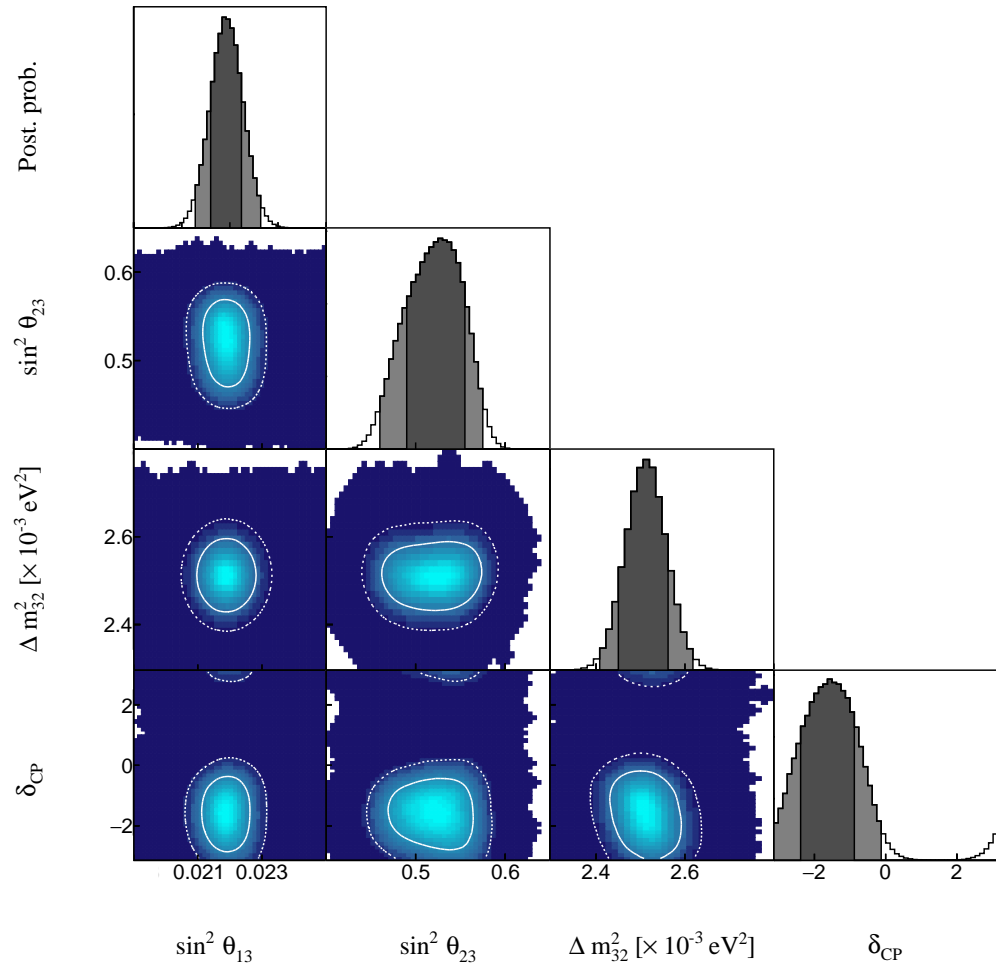


Figure 8.30: The posterior probability density distribution from the joint beam-atmospheric fit where the reactor constraint is applied. The distribution is given for each two-dimensional permutation of the oscillation parameters of interest. The one-dimensional distribution of each parameter is also given.

3333 8.3.6 Comparison to Latest T2K Sensitivities without Reactor 3334 Constraint

3335 The benefits of the joint beam-atmospheric analysis can be determined by compar-
 3336 ing the sensitivities to the beam-only analysis presented in [2, 211]. This section
 3337 presents those comparisons for sensitivities built using the Asimov A oscillation
 3338 parameters defined in Table 2.2 and the post-BANFF systematic tune. The reactor
 3339 constraint is not applied within either of the fits used in these comparisons.

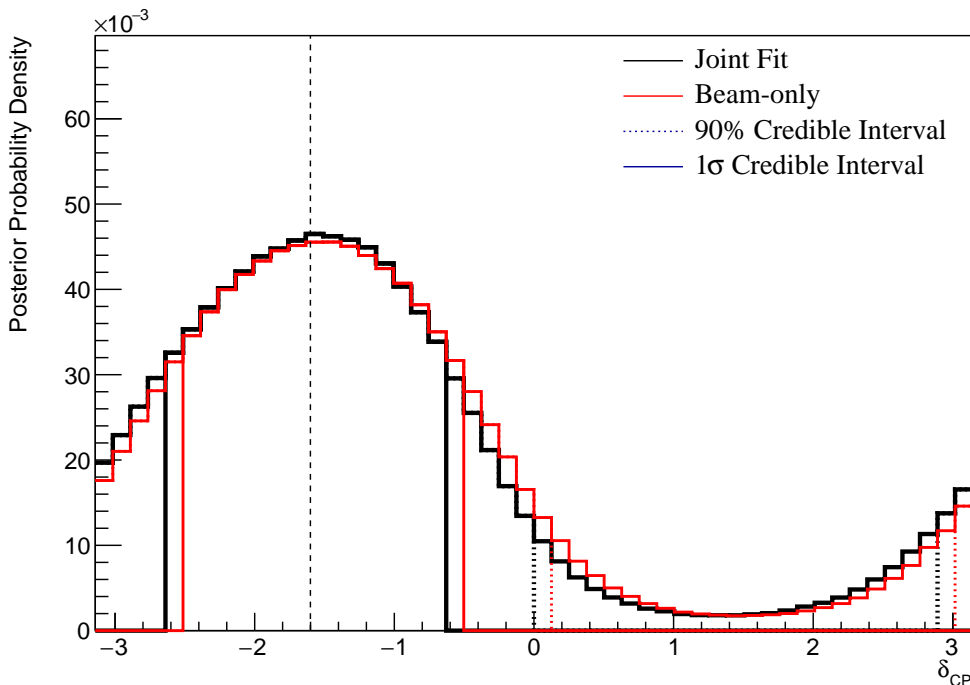


Figure 8.31: The one-dimensional posterior probability density distribution in δ_{CP} compared between the joint beam-atmospheric fit (Black) and the latest T2K sensitivities (Red) [2, 211]. The reactor constraint is not applied in either fit. The distributions are marginalised over both hierarchies. The vertical dashed line represents the known value of δ_{CP} .

3340 The sensitivity, marginalised over both hierarchies, to δ_{CP} from the joint beam-
 3341 atmospheric and beam-only fits is presented in Figure 8.31. As expected from the
 3342 likelihood scans (Figure 8.4), the sensitivity to δ_{CP} is not significantly increased.
 3343 This is because the known oscillation parameter value lies at the position where
 3344 the beam samples dominate the sensitivity compared to the SK samples.

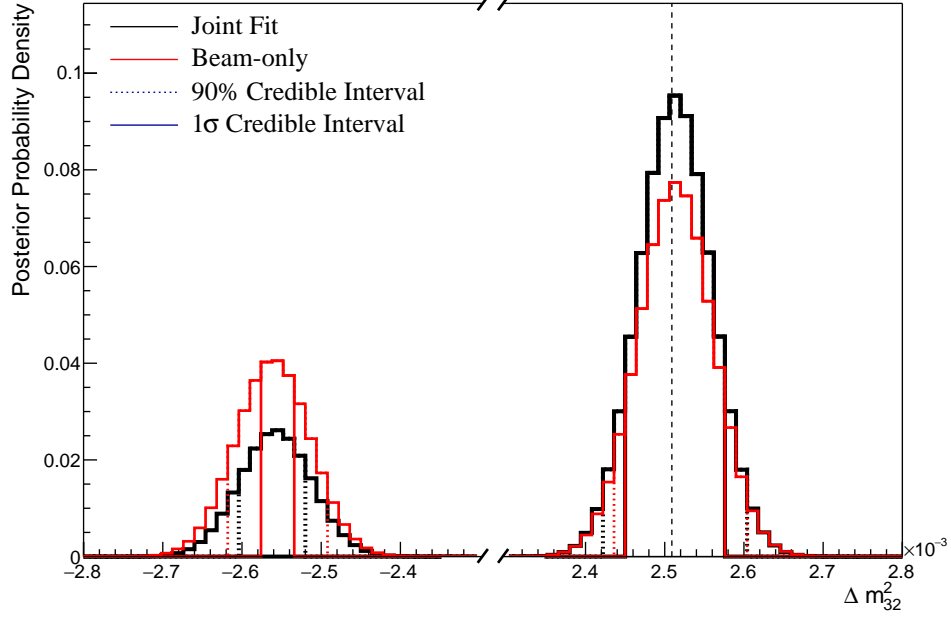


Figure 8.32: The one-dimensional posterior probability density distribution in Δm_{32}^2 compared between the joint beam-atmospheric fit (Black) and the latest T2K sensitivities (Red) [2, 211]. The reactor constraint is not applied in either fit. The vertical dashed line represents the known value.

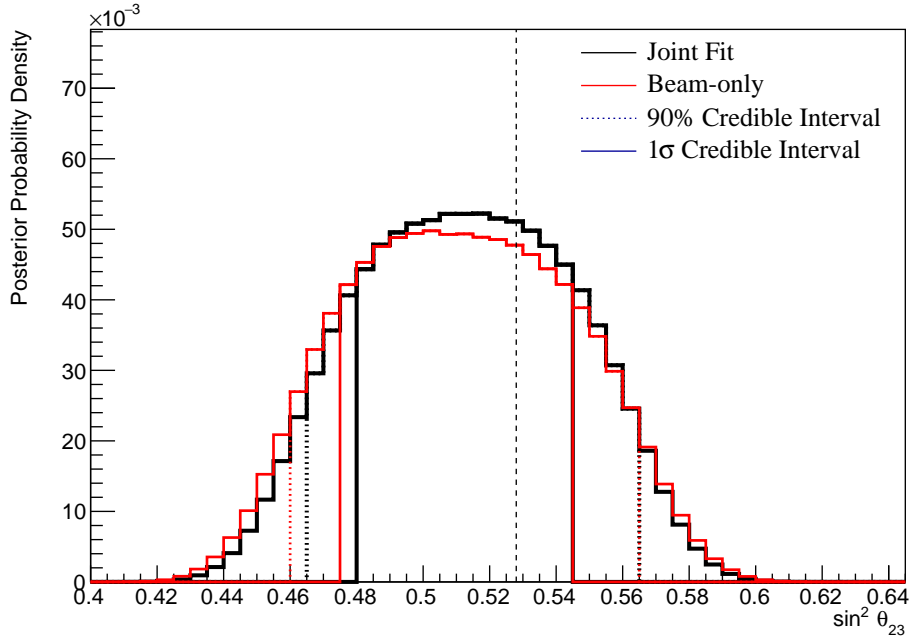


Figure 8.33: The one-dimensional posterior probability density distribution in $\sin^2(\theta_{23})$ compared between the joint beam-atmospheric fit (Black) and the latest T2K sensitivities (Red) [2, 211]. The reactor constraint is not applied in either fit. The distributions are marginalised over both hierarchies. The vertical dashed line represents the known value.

3345 The sensitivity to Δm_{32}^2 is compared between the joint beam-atmospheric fit
 3346 and beam-only fit in Figure 8.32. The 1σ credible interval of the joint beam-
 3347 atmospheric fit is entirely contained within the NH region. This shows the
 3348 significant increase in the ability of the fit to determine the correct mass hierarchy,
 3349 compared to the beam-only analysis. This is further evidenced by the fact that the
 3350 90% credible intervals from the joint fit are also tighter in the IH region compared
 3351 to the beam-only analysis. The Bayes factor for mass hierarchy determination
 3352 for the beam-only and joint beam-atmospheric fits are $B(\text{NH}/\text{IH}) = 1.91$ and
 3353 $B(\text{NH}/\text{IH}) = 3.67$, respectively. According to Jeffrey's scale, the beam-only
 3354 analysis represents a weak preference for the correct hierarchy whereas the
 3355 joint fit returns a substantial preference for the NH hypothesis. Notably, this
 3356 conclusion does not require any external constraints and clearly illustrates the
 3357 benefit of the joint analysis.

3358 The sensitivity to $\sin^2(\theta_{23})$, marginalised over both hierarchies, for both the
 3359 beam-only and joint beam-atmospheric analysis are presented in Figure 8.33. The
 3360 peak of the posterior distribution from the joint analysis is more aligned with the
 3361 known value of $\sin^2(\theta_{23}) = 0.528$ compared to the beam-only analysis. The Bayes
 3362 factors for the beam-only and joint beam-atmospheric fit are $B(\text{UO}/\text{LO}) = 1.56$
 3363 and $B(\text{UO}/\text{LO}) = 1.74$, respectively. Therefore, the joint beam-atmospheric
 3364 fit does prefer the UO, which is the correct octant, more strongly than the
 3365 beam-only analysis.

3366 Whilst the beam-only and joint beam-atmospheric fits have similar sensi-
 3367 tivity to δ_{CP} and $\sin^2(\theta_{23})$ when projected in one-dimension, the benefit of the
 3368 joint analysis becomes more obvious when the sensitivities are presented in
 3369 two-dimensions. The sensitivity of the two fits to the appearance parameters
 3370 ($\delta_{CP}-\sin^2(\theta_{13})$) is illustrated in Figure 8.34. The width of the 99% joint fit contour
 3371 in $\sin^2(\theta_{13})$ is squeezed in the region of $\delta_{CP} \sim 0$ compared to the beam-only anal-
 3372 ysis. This is the same behaviour that is seen in the appearance likelihood scans
 3373 presented in Figure 8.2. The 1σ and 90% also exhibit slightly tighter constraints
 3374 on δ_{CP} . This is most prevalent in the region of $\delta_{CP} \sim 0$ and $\sin^2(\theta_{13}) \sim 0.03$.

Whilst the atmospheric samples do not have significant sensitivity to $\sin^2(\theta_{13})$ (as shown in Figure 8.1), they aid in breaking the degeneracy between the oscillation parameters allowing for tighter constraints.

The sensitivity to the disappearance parameters $\sin^2(\theta_{23})-\Delta m_{32}^2$ is presented in Figure 8.35 for both the beam-only and joint beam-atmospheric fits. Whilst the one-dimensional sensitivity comparisons considered so far show the improvements of the joint fit, the two-dimensional projection really shows the benefit of adding the atmospheric samples to the beam samples. The area contained within the IH contours is drastically reduced in the joint fit. This follows from the better determination of the mass hierarchy seen in the Bayes factor comparisons. Even in the NH region, the width of the contour in $\sin^2(\theta_{23})$ decreases, albeit to a smaller extent.

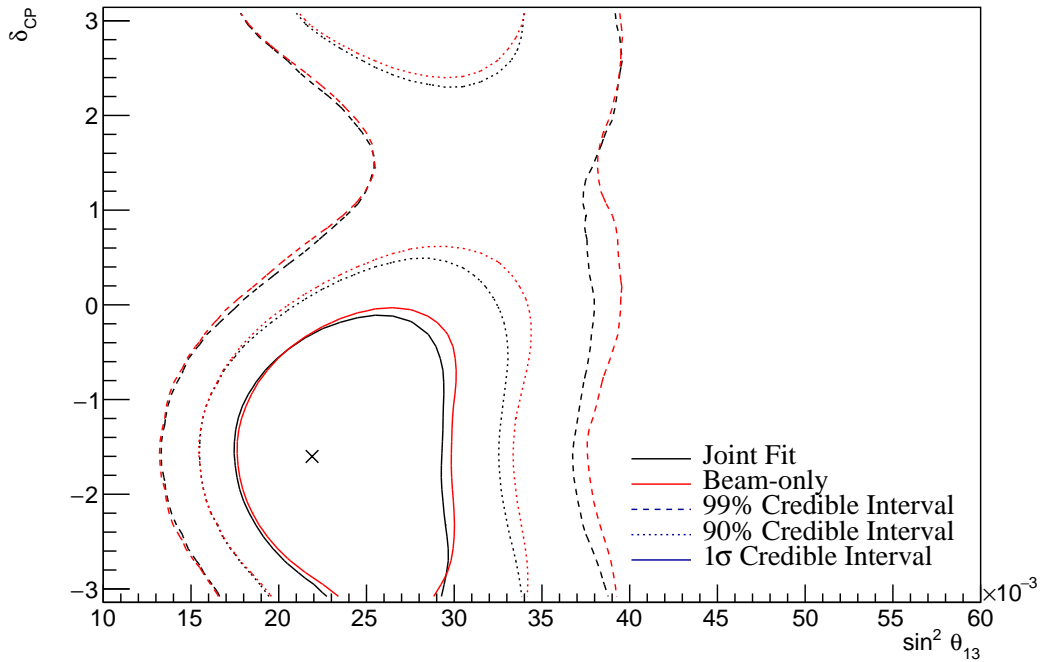


Figure 8.34: The two-dimensional posterior probability density distribution in $\delta_{CP}-\sin^2(\theta_{13})$ compared between the joint beam-atmospheric fit (Black) and the latest T2K sensitivities (Red) [2, 211]. The reactor constraint is not applied in either fit. The distributions are marginalised over both hierarchies. The marker represents the known value of $\delta_{CP}-\sin^2(\theta_{13})$.

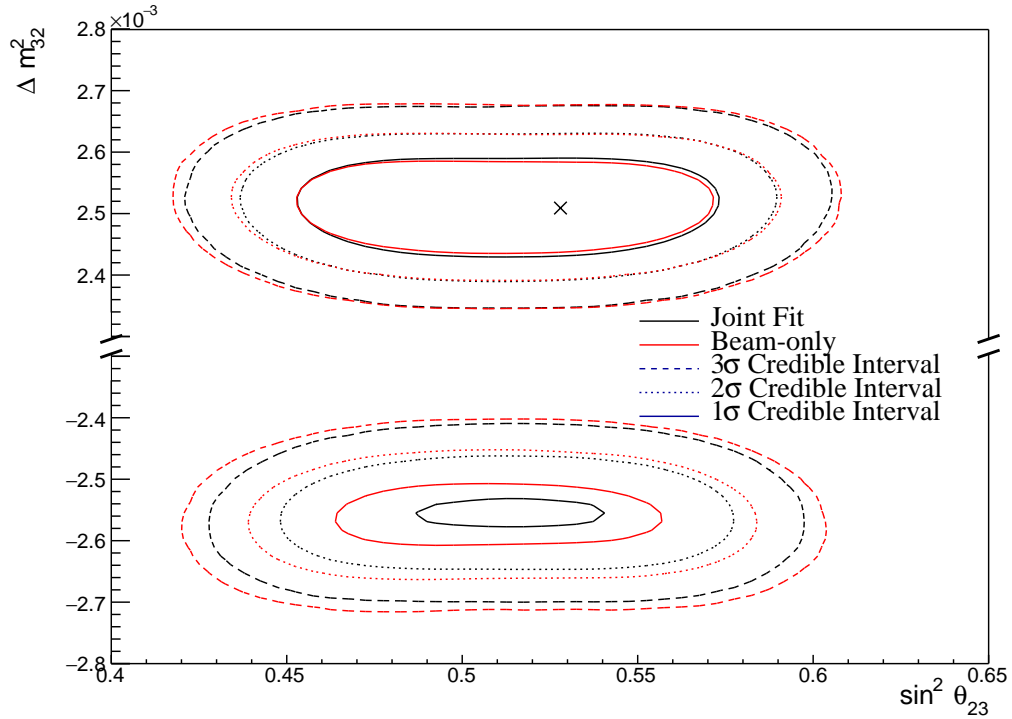


Figure 8.35: The two-dimensional posterior probability density distribution in $\Delta m_{32}^2 - \sin^2(\theta_{23})$ compared between the joint beam-atmospheric fit (Black) and the latest T2K sensitivities (Red) [2, 211]. The reactor constraint is not applied in either fit. The marker represents the known value of $\Delta m_{32}^2 - \sin^2(\theta_{23})$.

3387 The comparison in sensitivity to $\delta_{CP} - \Delta m_{32}^2$ is illustrated in Figure 8.36. The
 3388 contours from the joint beam-atmospheric fit are much smaller in the IH region
 3389 as compared to the beam-only analysis. This culminates in a region around
 3390 $\delta_{CP} \sim \pi/2$ in the IH region which is excluded at 3σ . This behaviour is not
 3391 present within the beam-only analysis. Consistent with the previous observations,
 3392 the area contained within the IH credible intervals is significantly reduced in
 3393 comparison to the beam-only analysis.

3394 The sensitivity to Δm_{32}^2 , as a function of $\sin^2(\theta_{13})$, is presented in Figure 8.37.
 3395 Similar to previous observations, the Δm_{32}^2 contours within IH region of the joint
 3396 fit are much smaller than the beam-only analysis. Notably, the joint fit IH 1σ
 3397 contour excludes the region around the reactor constraint. This suggests that the
 3398 application of the reactor constraint would further increase the preference for
 3399 NH in the joint fit compared to its effect on the beam-only analysis.

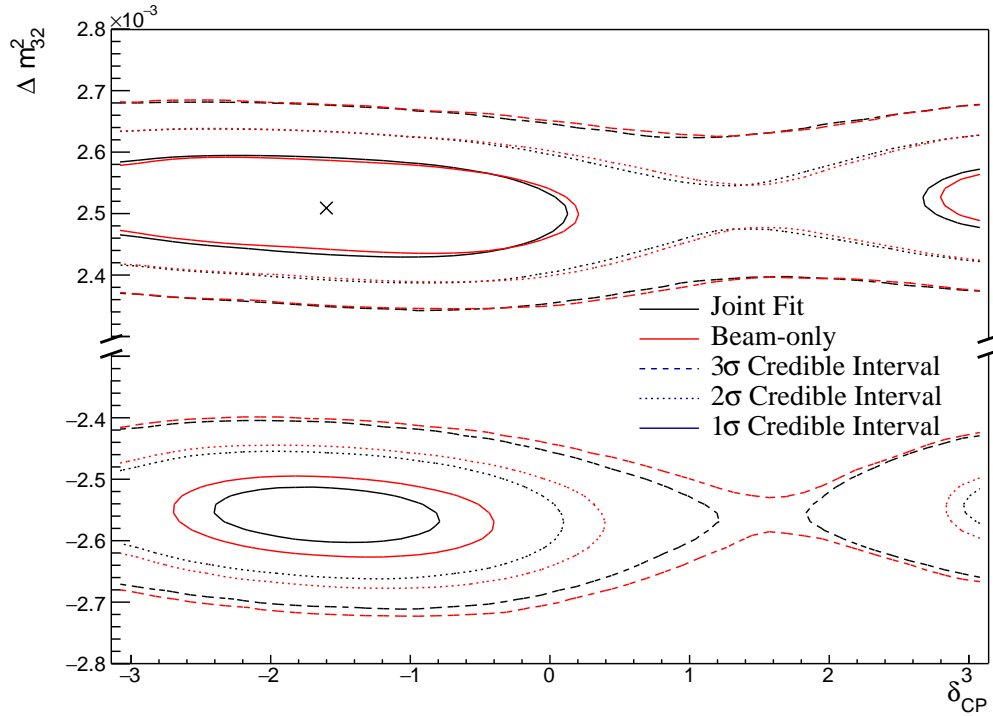


Figure 8.36: The two-dimensional posterior probability density distribution in $\Delta m_{32}^2 - \Delta_{CP}$ compared between the joint beam-atmospheric fit (Black) and the latest T2K sensitivities (Red) [2, 211]. The reactor constraint is not applied in either fit. The marker represents the known value of $\Delta m_{32}^2 - \Delta_{CP}$.

3400 The beam-only and joint beam-atmospheric fits have a slightly different
 3401 contour shape between the $\sin^2(\theta_{13})$ and $\sin^2(\theta_{23})$ parameters, as illustrated
 3402 by Figure 8.38. The joint analysis disfavours the wrong octant hypothesis more
 3403 strongly in the region of high $\sin^2(\theta_{13})$. This change in correlation means that the
 3404 application of the reactor constraint could affect the two analyses differently.

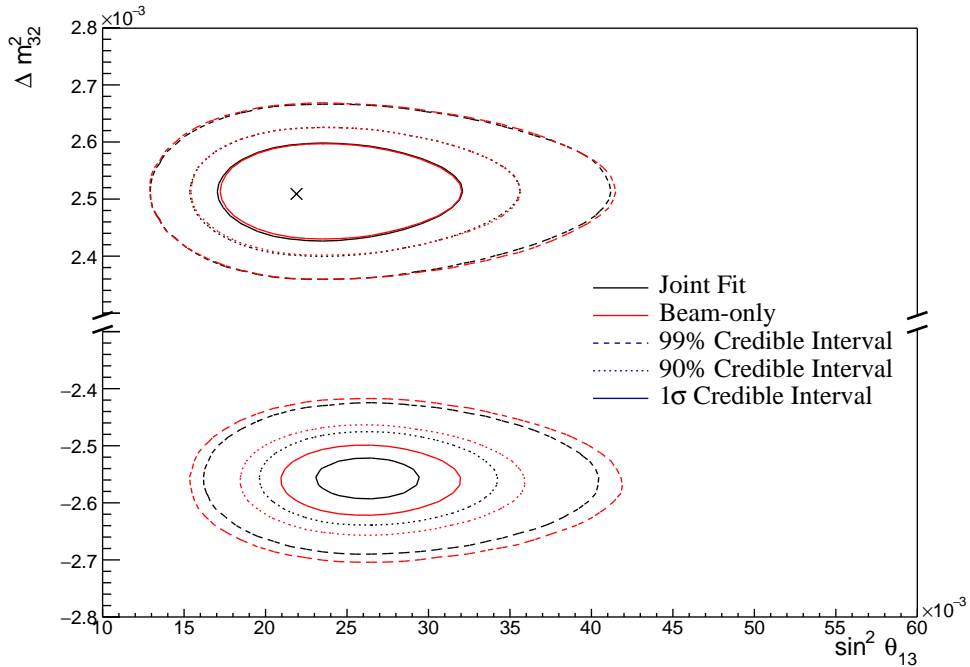


Figure 8.37: The posterior probability density distribution in $\Delta m_{32}^2 - \sin^2(\theta_{23})$ compared between the joint beam-atmospheric fit (Black) and the latest T2K sensitivities (Red) [2, 211]. The reactor constraint is not applied in either fit. The marker represents the known value.

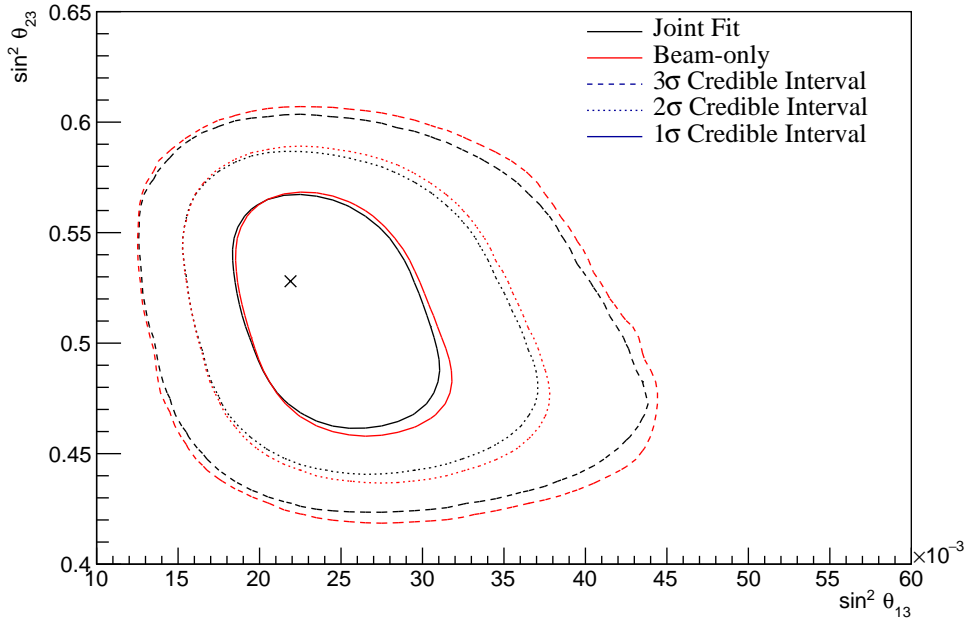


Figure 8.38: The posterior probability density distribution in $\sin^2(\theta_{23}) - \sin^2(\theta_{13})$ compared between the joint beam-atmospheric fit (Black) and the latest T2K sensitivities (Red) [2, 211]. The reactor constraint is not applied in either fit. The distributions are marginalised over both hierarchies. The marker represents the known value.

3405 8.3.7 Comparison to Latest T2K Sensitivities with Reactor Con- 3406 straint

3407 This section illustrates the comparison between the joint beam-atmospheric and
 3408 beam-only fits when the reactor constraint is applied. As shown in Figure 8.37,
 3409 the application of the reactor constraint is expected to significantly increase
 3410 the joint fit's preference for the NH hypothesis, compared to the beam-only
 3411 analysis. Figure 8.39 illustrates the sensitivities of the two fits to the disappearance
 3412 parameters ($\sin^2(\theta_{23}) - \Delta m_{32}^2$). This plot further illustrates the benefit of the joint
 3413 beam-atmospheric analysis. The 1σ contour in the IH region is entirely removed
 3414 in the joint analysis but not for the beam-only analysis.

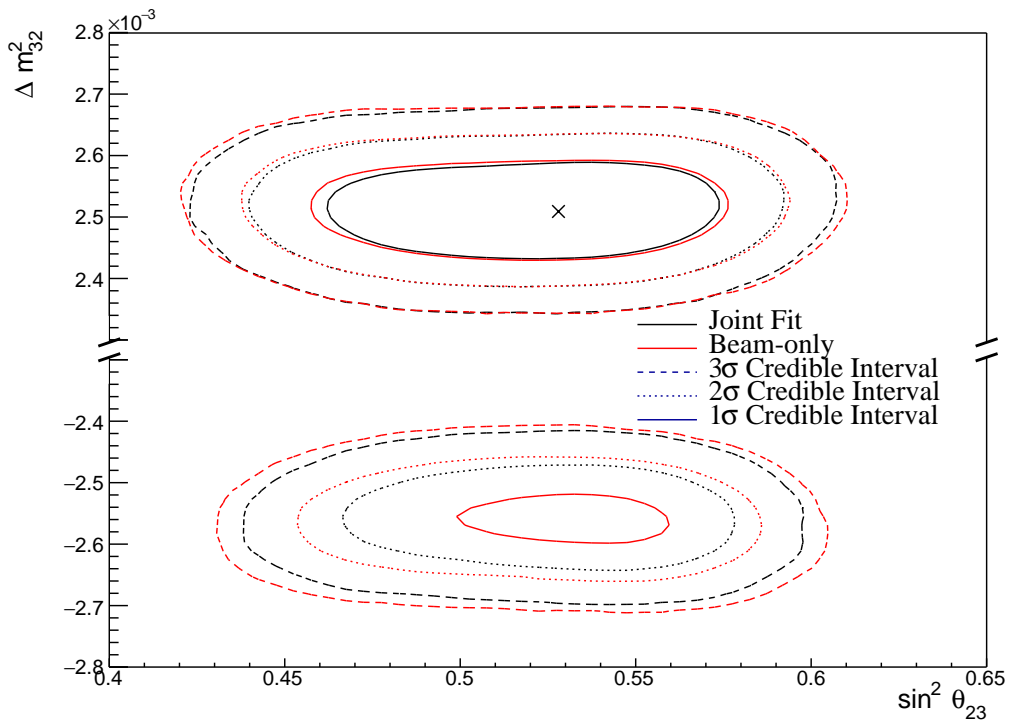


Figure 8.39: The two-dimensional posterior probability density distribution in $\Delta m_{32}^2 - \sin^2(\theta_{23})$ compared between the joint beam-atmospheric fit (Black) and the latest T2K sensitivities (Red) [2, 211]. The reactor constraint is applied in both fits. The marker represents the known value of $\Delta m_{32}^2 - \sin^2(\theta_{23})$.

3415 The contours of the joint fit are also tighter in the $\sin^2(\theta_{23})$ dimension than the
 3416 beam-only analysis in both mass hierarchy regions. This shows that beyond the
 3417 ability of the joint fit to prefer the NH more strongly than the beam-only analysis,

3418 the precision to which it can measure $\sin^2(\theta_{23})$ is also improved. The Bayes factor
3419 for NH preference is calculated as $B(\text{NH}/\text{IH}) = 6.47$ and $B(\text{NH}/\text{IH}) = 3.09$ for
3420 the joint beam-atmospheric and beam-only analysis, respectively. This important
3421 conclusion illustrates that the joint beam-atmospheric analysis can provide a
3422 substantial preference for the correct hypothesis (NH) whilst the beam-only
3423 analysis can not.

3424 The Bayes factors for UO preference which are $B(\text{UO}/\text{LO}) = 2.86$ and
3425 $B(\text{UO}/\text{LO}) = 2.47$ for the joint beam-atmospheric and beam-only analysis,
3426 respectively. Both of these represent a mild preference for the correct octant
3427 (UO) but a stronger preference is observed in the joint analysis.

3428 The sensitivity of the beam-only and joint beam-atmospheric analyses, to
3429 the appearance parameters ($\delta_{CP} - \sin^2(\theta_{13})$), are compared in Figure 8.40. These
3430 results are marginalised over both hierarchies. For this particular set of known
3431 oscillation parameters (AsimovA defined in Table 2.2), the beam-only analysis
3432 dominates the sensitivity. The joint fit does slightly increase the sensitivity to δ_{CP}
3433 but it does not change any conclusions that would be made. As expected, the
3434 prior knowledge dominates any sensitivity either fit would have on $\sin^2(\theta_{13})$.

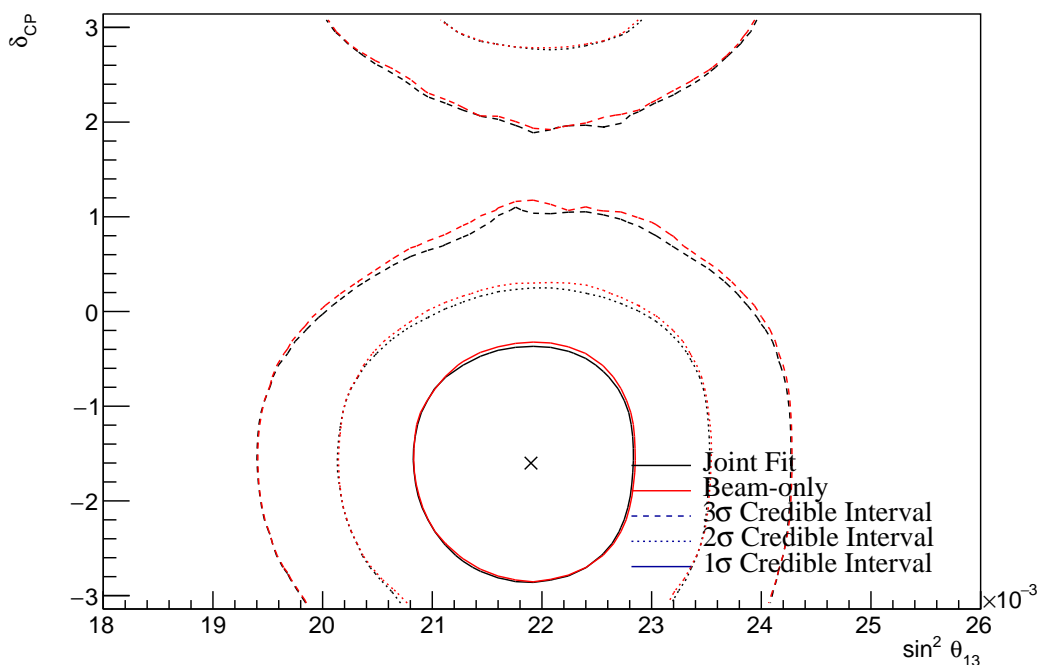


Figure 8.40: The two-dimensional posterior probability density distribution in δ_{CP} – $\sin^2(\theta_{13})$ compared between the joint beam-atmospheric fit (Black) and the latest T2K sensitivities (Red) [2, 211]. The reactor constraint is applied in both fits. The distributions are marginalised over both hierarchies. The marker represents the known value of δ_{CP} – $\sin^2(\theta_{13})$.

3435 8.3.8 Alternate Asimov Parameter Set

3436 Figure 8.4 and Figure 8.5 show that the choice of the parameter set at which the
 3437 Asimov data is made can affect the sensitivities. ‘AsimovA’ oscillation parameters
 3438 are defined at a region of δ_{CP} which is preferred by the T2K experiment. This
 3439 explains why the addition of the atmospheric samples does not significantly in-
 3440 crease the sensitivity to δ_{CP} , as illustrated in subsection 8.3.6 and subsection 8.3.7.
 3441 This section presents the sensitivities when ‘AsimovB’ oscillation parameters,
 3442 as defined in Table 2.2, are assumed (alongside the post-BANFF tune) when
 3443 building the Asimov data.

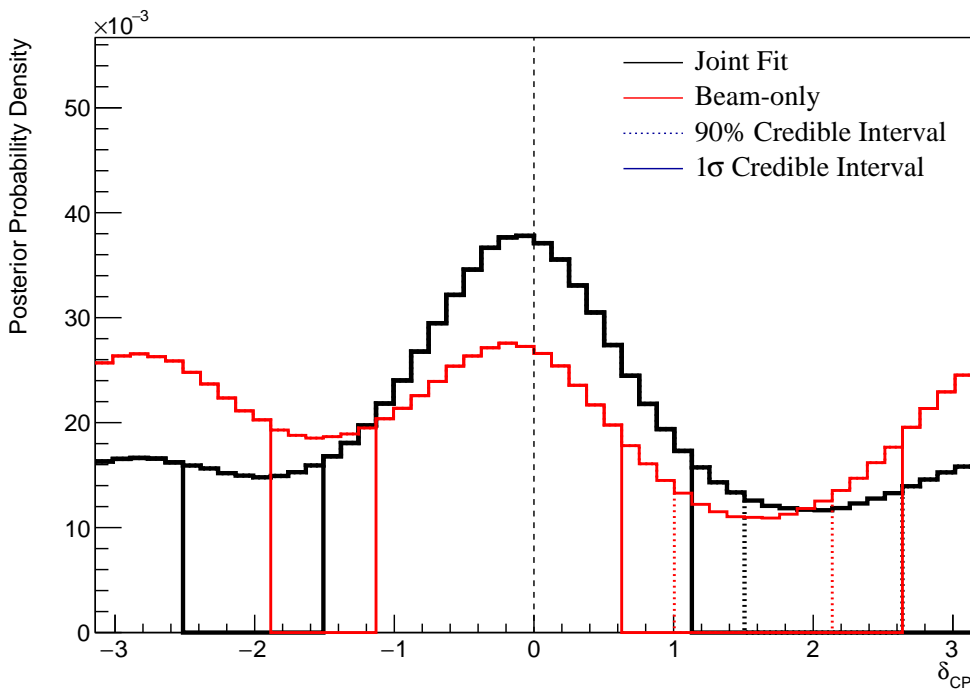


Figure 8.41: The one-dimensional posterior probability density distribution in δ_{CP} compared between the joint beam-atmospheric fit (Black) and the latest T2K sensitivities (Red) [2, 211]. The reactor constraint is not applied in either fit. The distributions are marginalised over both hierarchies. The vertical dashed line represents the known value of δ_{CP} .

3444 The sensitivity to δ_{CP} for the joint beam-atmospheric fit is presented in
 3445 Figure 8.41. The results are compared to those from the beam-only analysis
 3446 in [2, 211]. The reactor constraint is not applied in either of the fits. The

shape of the posterior distribution from the joint analysis is more peaked at the known oscillation parameter value compared to the beam-only analysis, which has approximately the same posterior probability density at $\delta_{CP} = 0$ and $\delta_{CP} = \pm\pi$. This shows the ability of the joint analysis to better determine the correct phase of δ_{CP} if the true value were CP-conserving. The 1σ credible intervals and the position of the highest posterior probability density are given in Table 8.9. The highest posterior density for the joint beam-atmospheric analysis is $\delta_{CP} = -0.06 \pm 0.06$ which is consistent with the known value.

Parameter	Interval	HPD
δ_{CP} , (BH)	$[-\pi, -2.51], [-1.51, 1.13]$	-0.06 ± 0.06
δ_{CP} , (NH)	$[-1.13, 1.63]$	0.06 ± 0.06
δ_{CP} , (IH)	$[-3.02, -1.88], [-1.76, 0.13]$	-0.44 ± 0.06
Δm_{32}^2 (BH) [$\times 10^{-3}\text{eV}^2$]	$[-2.60, -2.52], [2.46, 2.56]$	2.51 ± 0.01
Δm_{32}^2 (NH) [$\times 10^{-3}\text{eV}^2$]	$[2.47, 2.56]$	2.52 ± 0.01
Δm_{32}^2 (IH) [$\times 10^{-3}\text{eV}^2$]	$[-2.61, -2.52]$	-2.57 ± 0.01
$\sin^2(\theta_{23})$ (BH)	$[0.430, 0.480], [0.545, 0.585]$	0.453 ± 0.003
$\sin^2(\theta_{23})$ (NH)	$[0.430, 0.485], [0.550, 0.580]$	0.453 ± 0.003
$\sin^2(\theta_{23})$ (IH)	$[0.435, 0.480], [0.540, 0.585]$	0.568 ± 0.003

Table 8.9: The position of the highest posterior probability density (HPD) and width of the 1σ credible interval for the joint beam-atmospheric fit. The reactor constraint is not applied. The values are presented by which hierarchy hypothesis is assumed: marginalised over both hierarchies (BH), normal hierarchy only (NH) and inverted hierarchy only (IH).

Naively, if just the 1σ credible interval were considered without observing the shape of the distribution, it would appear that the joint analysis would have a worse sensitivity to δ_{CP} due to the larger interval around $\delta_{CP} = 0$. However, the 1σ credible interval for the beam-only analysis is given as the range $\delta_{CP} = [-\pi, -1.88], [-1.13, 0.63]$ and $[2.64, \pi]$ which contains 56% of all values of δ_{CP} . Whereas, the joint beam-atmospheric analysis contains 52% of all δ_{CP} values within the 1σ credible interval. Therefore, if the area within the 1σ credible

3462 interval were to be compared between the two fits, the joint analysis would
3463 be shown to have better precision.

3464 This apparent contradiction stems from the methodology in which the credible
3465 interval is calculated. The technique used in this analysis (documented in
3466 subsection 4.3.2) fills the credible interval by selecting bins in order of probability
3467 density until 68% of the posterior density is contained. If instead, the credible
3468 interval were calculated by expanding around the highest posterior probability,
3469 the benefits of the joint fit would be more obvious. In the case where the shape
3470 of the posterior was uni-modal, these two techniques would be equivalent to
3471 statistical fluctuations.

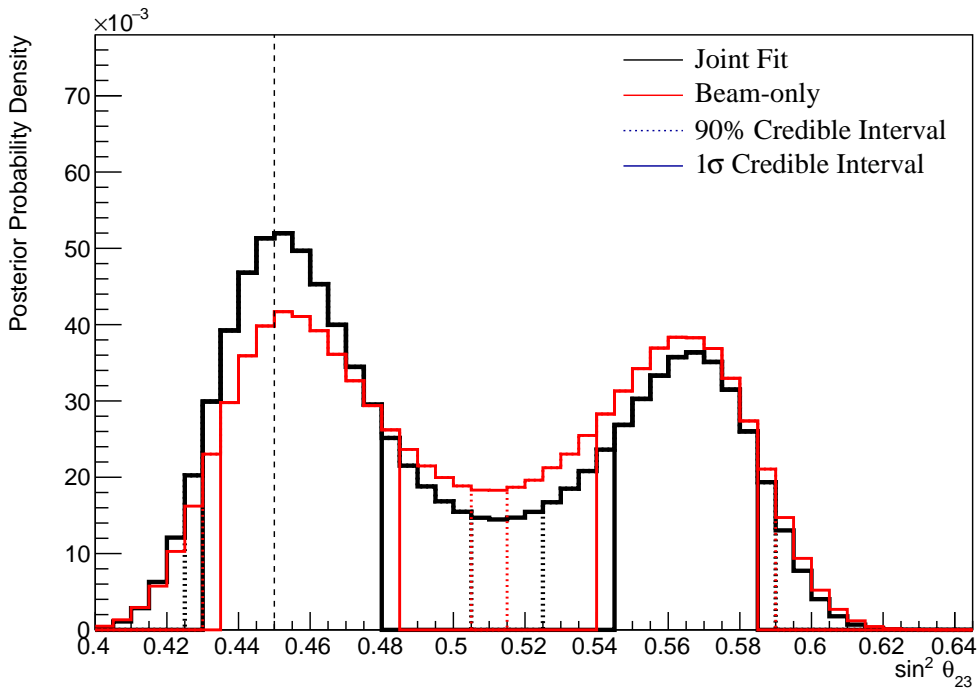


Figure 8.42: The one-dimensional posterior probability density distribution in $\sin^2(\theta_{23})$ compared between the joint beam-atmospheric fit (Black) and the latest T2K sensitivities (Red) [2, 211]. The reactor constraint is not applied in either fit. The distributions are marginalised over both hierarchies. The vertical dashed line represents the known value of $\sin^2(\theta_{23})$.

3472 The sensitivity of the joint beam-atmospheric fit to $\sin^2(\theta_{23})$ is presented in
3473 Figure 8.42. The sensitivity is compared to that of the beam-only analysis in [2,
3474 211]. The reactor constraint is not applied in either of the fits being compared.

3475 The joint beam-atmospheric fit has a much larger probability density in the region
 3476 surrounding the known oscillation parameter, $\sin^2(\theta_{23}) = 0.45$. This shows the
 3477 better octant determination of the joint analysis compared to the beam-only fit.
 3478 The ratio of the posterior density at the peak of the lower octant to the peak of
 3479 the upper octant from the joint fit is 1.43 compared to 1.09 from the beam-only
 3480 analysis. The area contained within the 1σ credible interval for the joint analysis
 3481 is $\sin^2(\theta_{23}) = [0.430, 0.480]$ and $\sin^2(\theta_{23}) = [0.545, 0.585]$, whereas the beam-
 3482 only analysis includes $\sin^2(\theta_{23}) = [0.435, 0.485]$ and $\sin^2(\theta_{23}) = [0.540, 0.585]$.
 3483 This corresponds to a $\sim 5\%$ (binning dependent) increase in precision from
 3484 the joint analysis.

	LO ($\sin^2 \theta_{23} < 0.5$)	UO ($\sin^2 \theta_{23} > 0.5$)	Sum
NH ($\Delta m_{32}^2 > 0$)	0.35	0.24	0.59
IH ($\Delta m_{32}^2 < 0$)	0.19	0.22	0.41
Sum	0.54	0.46	1.00

Table 8.10: The distribution of steps in a joint beam-atmospheric fit, presented as the fraction of steps in the upper (UO) and lower (LO) octants and the normal (NH) and inverted (IH) hierarchies. The reactor constraint is not applied. The Bayes factors are calculated as $B(\text{NH}/\text{IH}) = 1.43$ and $B(\text{LO}/\text{UO}) = 1.19$.

3485 The distribution of steps, split by hierarchy and octant hypothesis, is presented
 3486 in Table 8.10. The Bayes factor for hierarchy and octant determination are
 3487 $B(\text{NH}/\text{IH}) = 1.43$ and $B(\text{LO}/\text{UO}) = 1.19$, respectively. These values compare
 3488 to $B(\text{NH}/\text{IH}) = 1.08$ and $B(\text{LO}/\text{UO}) = 0.91$ from the beam-only analysis.
 3489 This evidences the joint analysis's ability to better select the correct octant and
 3490 hierarchy hypothesis. Comparisons to the AsimovA Bayes factors presented in
 3491 Table 8.6 show how the preferences for the correct octant and hierarchy depend
 3492 on the true value of δ_{CP} and $\sin^2(\theta_{23})$.

3493 The sensitivity of the beam-only and joint beam-atmospheric analysis to
 3494 Δm_{32}^2 is given in Figure 8.43. The joint analysis has a stronger preference for the
 3495 correct hierarchy (NH) which is shown by the higher Bayes factor compared
 3496 to the beam-only analysis. This is further evidenced by the width of the 90%

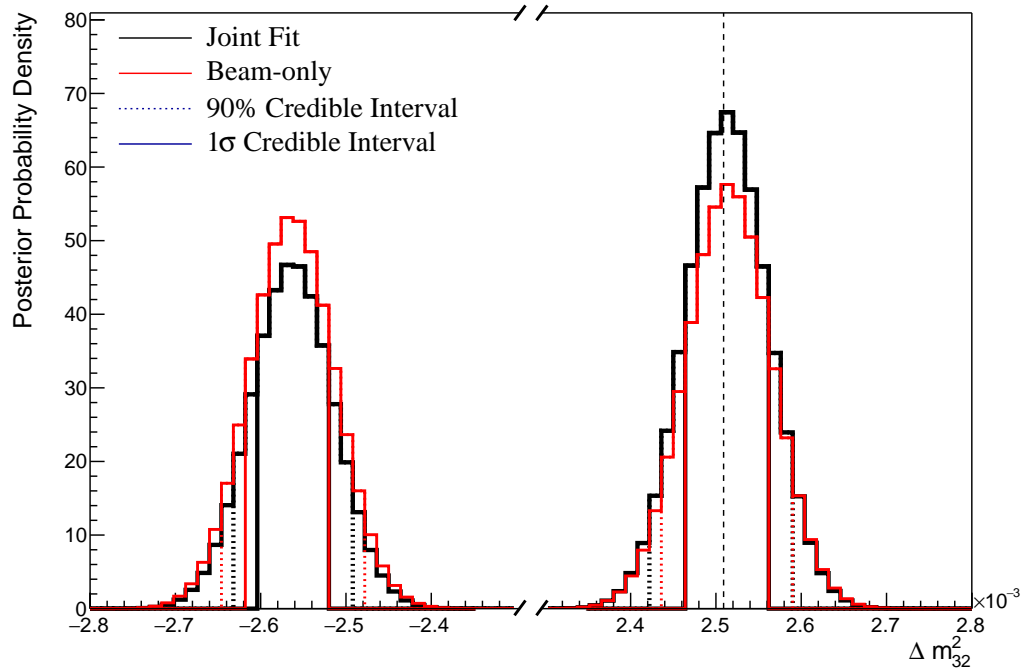


Figure 8.43: The one-dimensional posterior probability density distribution in Δm_{32}^2 compared between the joint beam-atmospheric fit (Black) and the latest T2K sensitivities (Red) [2, 211]. The reactor constraint is not applied in either fit. The vertical dashed line represents the known value of Δm_{32}^2 .

credible interval in the IH region being tighter in the joint analysis compared
 to the beam-only analysis.

3497

3498

3499 8.3.9 Effect of Systematics

3500 The effect of systematics on each sample used in this analysis is calculated using
3501 the posterior predictive method documented in subsection 4.3.4. The distribution
3502 of each sample’s spectrum has been generated by sampling 2000 steps from the
3503 posterior distribution of the joint beam-atmospheric fit. This technique reweights
3504 the Monte Carlo prediction using the systematic values given by a particular
3505 step, stores the sample spectra, and repeats for the desired number of steps.
3506 The oscillation parameters are always fixed at Asimov A values to only study
3507 the effect of systematic parameters.

3508 Figure 8.44 illustrates the distribution for the SubGeV-*elike-0dcy* atmospheric
3509 sample. The fit being sampled is detailed in subsection 8.3.4. The post-fit
3510 distribution closely resembles the Asimov data spectrum. This would be expected
3511 from an Asimov fit where the Monte Carlo is fit to itself but gives more credibility
3512 to the results of the fit.

3513 The total event rate for each sample from each of the sampled steps is calcu-
3514 lated and the percentage uncertainty, $\Delta N_i / N_i$ where N_i is the event rate of the i^{th}
3515 sample, is calculated. These values are presented in Table 8.11. In general, the
3516 impact of the systematics has a $\sim 3\%$ uncertainty on the event rate of atmospheric
3517 samples, where CC1 π -targeting samples have slightly larger uncertainties than
3518 the CCQE-like samples. The fractional uncertainties on the beam samples are
3519 compared to those from the beam-only analysis presented in [2, 211]. The
3520 uncertainties on the one-ring muon samples are mostly unchanged, whereas
3521 the uncertainties on the one-ring electron samples are different. As discussed in
3522 section 8.2, the atmospheric samples should be able to add constraints on the NC
3523 background events present in the FHC1Re and RHC1Re samples. The uncertainty
3524 reduction seen in those samples is due to those additional constraints. The reason
3525 why the FHC1Re1de sample has a higher uncertainty in this analysis is due to the
3526 additional systematic introduced for CC1 π interactions (see subsection 6.4.3).

3527 Beyond the impact of the uncertainty on each sample’s event rate, the post-
3528 fit constraint on each systematic parameter should be checked. Figure 8.45

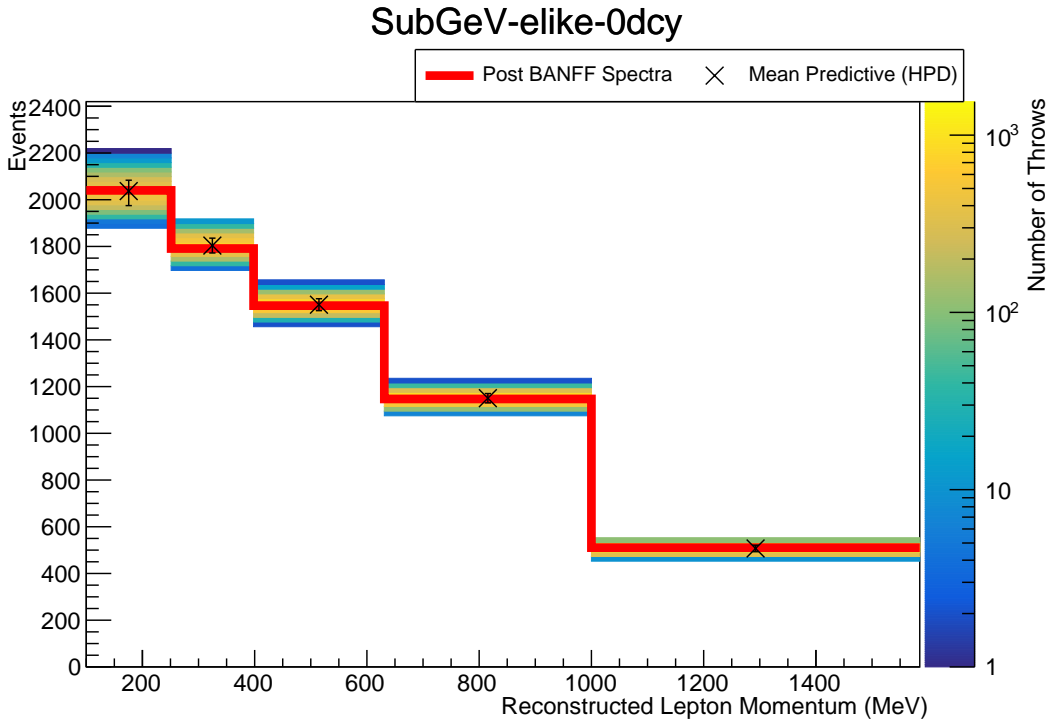


Figure 8.44: Result of the posterior predictive method for the SubGeV_elike_0dcy sample after sampling 2000 steps from the joint beam-atmospheric chain detailed in subsection 8.3.4 (Coloured histogram). The mean and uncertainty is presented for each bin. The Asimov data prediction (denoted ‘Post BANFF Spectra’, Red) assumes the post-BANFF tune and Asimov A oscillation parameters.

3529 illustrates the central value and uncertainty on a select group of interaction
 3530 systematics, for both the joint beam-atmospheric (from subsection 8.3.4) and
 3531 the beam-only analysis. From the discussion in section 8.2, the uncertainty
 3532 on systematics which are strongly constrained by the near detector should not
 3533 significantly change when adding the atmospheric analysis. This behaviour is
 3534 evidenced by the fact that the ratio of constraints between the two fits are very
 3535 similar (within a few %) for almost all systematics. The only systematic which
 3536 is significantly more constrained in the joint beam-atmospheric analysis is the
 3537 $NCOtherSK$ normalisation parameter, which has a $O(10\%)$ tighter constraint. As
 3538 expected, the atmospheric samples have been able to constrain this systematic
 3539 which leads to the reduction in uncertainty for the beam electron-like samples.

Sample	Percentage Uncertainty (%)	
	Joint Analysis	Beam-only Analysis
SubGeV-elike-0dcy	2.53	-
SubGeV-elike-1dcy	3.28	-
SubGeV-mulike-0dcy	2.62	-
SubGeV-mulike-1dcy	2.23	-
SubGeV-mulike-2dcy	3.96	-
SubGeV-pi0like	2.84	-
MultiGeV-elike-nue	5.14	-
MultiGeV-elike-nuebar	2.79	-
MultiGeV-mulike	2.99	-
MultiRing-elike-nue	2.94	-
MultiRing-elike-nuebar	2.83	-
MultiRing-mulike	2.89	-
MultiRingOther-1	2.70	-
PCStop	3.22	-
PCThrus	2.99	-
UpStop-mu	2.95	-
UpThruNonShower-mu	2.70	-
UpThruShower-mu	3.19	-
FHC1Rmu	2.49	2.33
RHC1Rmu	2.89	2.93
FHC1Re	4.12	4.57
RHC1Re	5.15	5.65
FHC1Re1de	13.38	11.51

Table 8.11: The percentage uncertainty, $\Delta N / N$, as calculated from sampling 2000 throws from a joint beam-atmospheric chain. The same values for the beam samples are provided from the beam-only analysis [2, 211]. These uncertainties consider all systematic parameters to be sampled from the fit whilst the oscillation parameters are fixed at the Asimov A oscillation set.

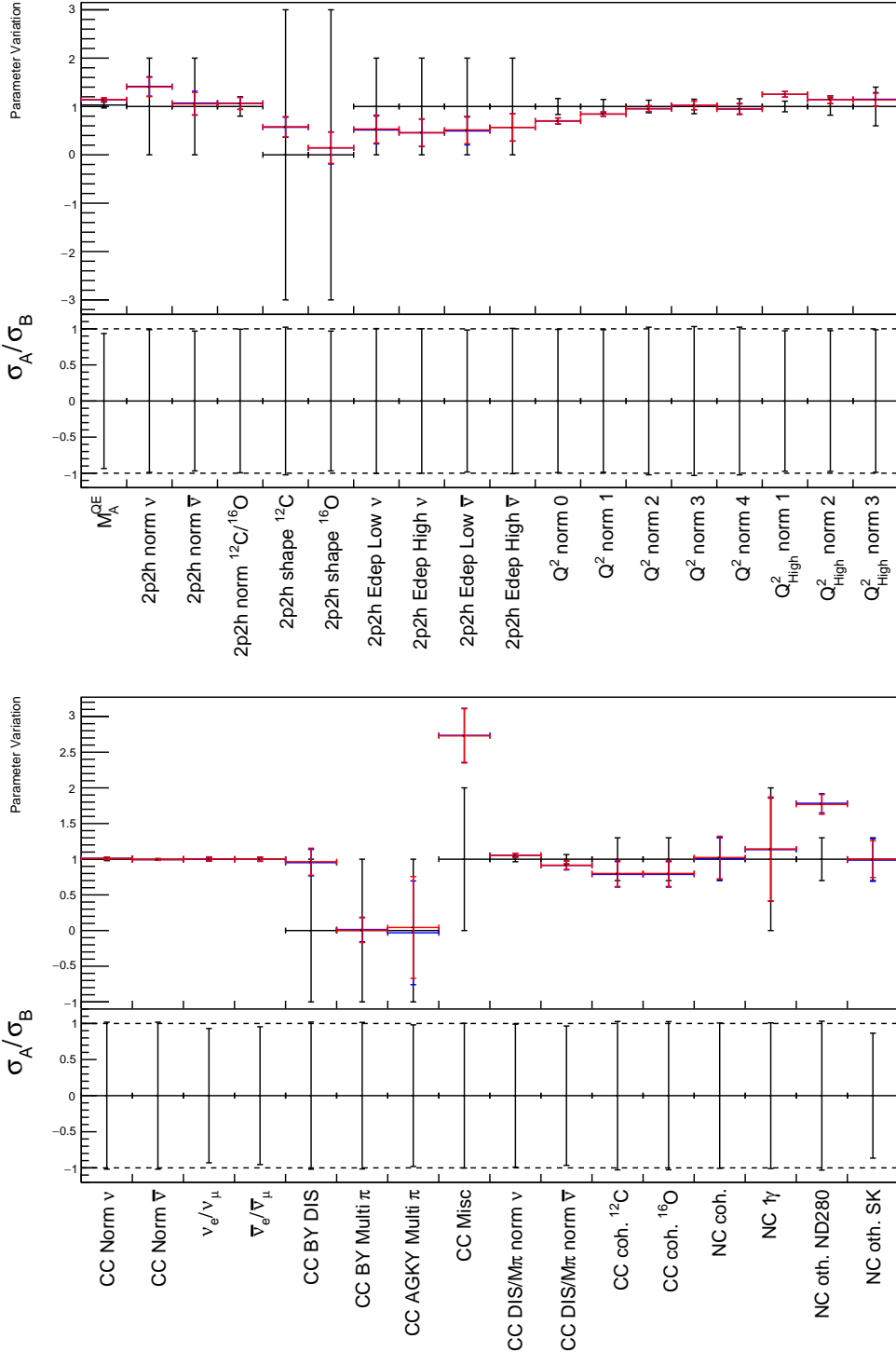


Figure 8.45: Central values and 1σ uncertainties for a select group of interaction systematics. The constraints from the prior uncertainty (Black), joint atmospheric-beam fit given in subsection 8.3.4 (Red) and beam-only analysis [2, 211] (Blue) are presented. The top part of each plot presents the parameter variation and the bottom part represents the ratio of the uncertainty between the joint beam-atmospheric and beam-only fits, where a value below 1.0 means the joint fit has a tighter constraint than the beam-only analysis.

3540 8.3.10 Alternative Detector Model Concept

3541 As a plausible extension to the analysis already presented, this section considers
 3542 the joint beam-atmospheric fit results when the correlated detector model doc-
 3543 umented in subsubsection 6.4.5.3 is used instead of the inputs provided by the
 3544 two experiments. The results shown here should be considered preliminary as
 3545 the results need further investigation to ensure their reliability.

3546 This technique fits the detector systematics simultaneously with the sample
 3547 spectra so the definition of the likelihood, given in section 6.5, needs to be
 3548 modified. Following the method outlined in DB: Xiaoyue's thesis, an additional
 3549 term needs to be added to the likelihood. This additional term is,

$$\frac{1}{2} \sum_s^{\text{Samples}} \sum_k^{E_k \text{bins}} \left(\rho(R_s | E_k, \vec{\theta}) \rho(P_s^{e/\mu} | E_k, \vec{\theta}) \rho(P_s^{e/\pi^0} | E_k, \vec{\theta}) \rho(P_s^{\mu/\pi^+} | E_k, \vec{\theta}) \right). \quad (8.1)$$

3550 This fits the ring counting R_s , electron-muon $P^{e/\mu}$, electron-neutral pion P^{e/π^0}
 3551 and muon-charged pion P^{μ/π^+} particle identification parameters, in bins of
 3552 visible energy E_k , of the s^{th} SubGeV atmospheric or beam sample. The visible
 3553 energy binning can be found in Table 6.10. In the situation where infinite
 3554 Monte Carlo statistics were generated, a many-dimensional spectra could be
 3555 determined, e.g. reconstructed lepton momentum and direction along with the
 3556 four particle identification parameters for the atmospheric samples. However,
 3557 there is limited Monte Carlo statistics so the standard spectra (e.g. reconstructed
 3558 lepton momentum and direction for atmospheric samples) is fit along with four
 3559 one-dimensional distributions of each particle identification parameter. To avoid
 3560 double counting events, shape-likelihoods are used for the likelihood associated
 3561 with each particle identification parameter,

$$\rho(X | E_k, \vec{\theta}) = \sum_{i=0}^j \left[N_i^d \times \log \left(\frac{N_i^p(\vec{\theta})}{\sum_{i=0}^X N_i^p(\vec{\theta})} \right) \right]. \quad (8.2)$$

3562 Where X refers to a particle identification parameter, $N_i^p(N_i^d)$ refers to the i^{th}
 3563 bin value from the predicted MC distribution (data distribution) and j represents
 3564 the total bin number of the X distribution.

3565 The post-fit distribution, using the posterior predictive method documented
 3566 in subsection 4.3.4, of the four particle identification parameters provided in
 3567 Table 6.7 are illustrated in Figure 8.46. Only the distributions for the first energy
 3568 bin ($0 \leq E_{vis}(\text{MeV}) \leq 300$) are plotted but similar distributions exist for each
 3569 of the energy bins listed in Table 6.10. The fit is returning a distribution of
 3570 each parameter that is consistent with the Asimov data (denoted ‘post-BANFF’)
 3571 illustrating that the modified likelihood is functioning as intended.

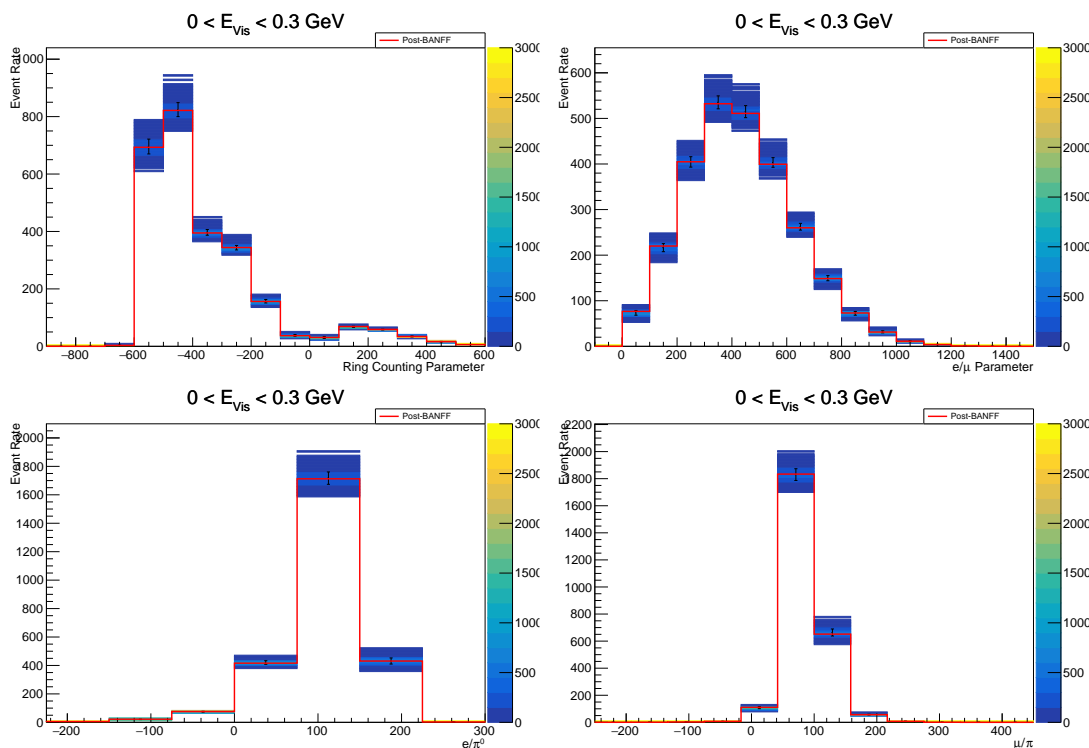


Figure 8.46

3572 The sensitivity to δ_{CP} using this alternative correlated detector model concept
 3573 is presented in Figure 8.47. It is compared against the previous result presented in
 3574 subsection 8.3.4. This alternative fit appears to have slightly stronger sensitivity to
 3575 δ_{CP} than the standad analysis, and still finds has the highest posterior distribution
 3576 at the known value. Regardless, this correlated detector modelling method

³⁵⁷⁷ should be further developed and more rigourously tested before any conclusions
³⁵⁷⁸ should be made.

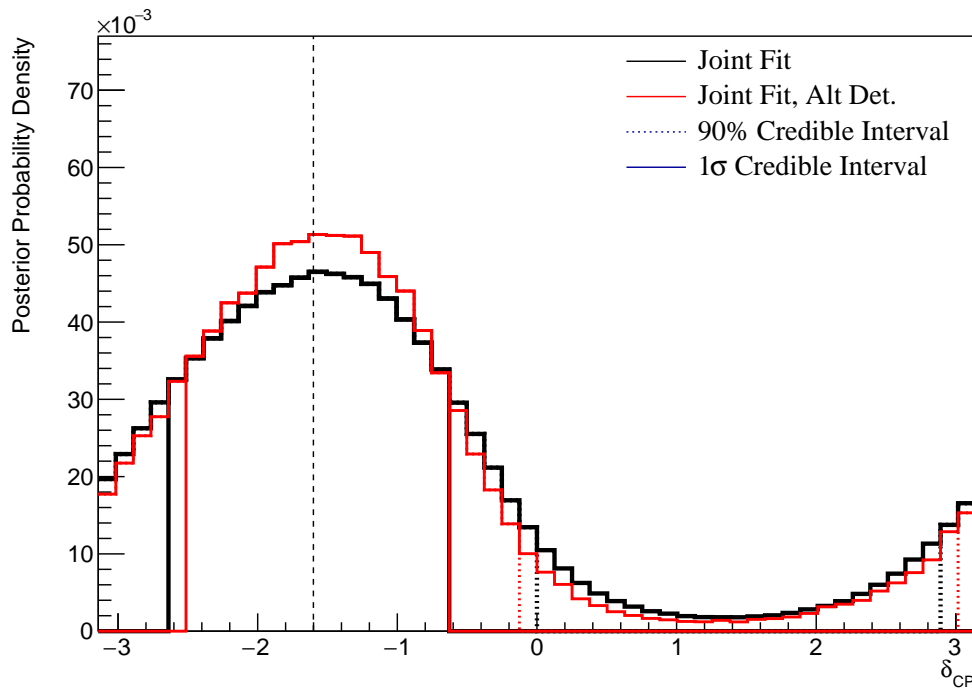


Figure 8.47

3579 8.4 Summary of Sensitivity Studies

3580 The sensitivities to each oscillation parameter from the joint beam-atmospheric
 3581 and beam-only fits, which use the Asimov A oscillation parameter set, are
 3582 summarised in Table 8.12. As the posterior distribution to δ_{CP} is cyclical, only
 3583 the position of the highest posterior density (HPD) is given. The uncertainty
 3584 corresponds to the width of the bin in which the HPD is located. That means
 3585 the Δm_{32}^2 reported values only consider the NH credible interval region. The full
 3586 discussion can be found in subsection 8.3.6 and subsection 8.3.7.

Fit	δ_{CP} (HPD)	$\Delta m_{32}^2 [\times 10^{-3}\text{eV}^2]$	$\sin^2(\theta_{23})$	$\sin^2(\theta_{13}) [\times 10^{-2}]$
Asimov A	-1.601	2.509	0.528	2.19
Beam	-1.45 ± 0.06	$2.51^{+0.07}_{-0.06}$	$0.501^{+0.044}_{-0.026}$	$2.45^{+0.45}_{-0.35}$
Beam w/RC	-1.57 ± 0.06	$2.51^{+0.08}_{-0.06}$	$0.533^{+0.022}_{-0.043}$	$2.19^{+0.06}_{-0.07}$
Joint	-1.57 ± 0.06	$2.51^{+0.07}_{-0.06}$	$0.518^{+0.027}_{-0.038}$	$2.35^{+0.45}_{-0.35}$
Joint w/RC	-1.57 ± 0.06	$2.51^{+0.05}_{-0.06}$	$0.528^{+0.027}_{-0.038}$	$2.18^{+0.07}_{-0.06}$

Table 8.12: A comparison of the sensitivity to each oscillation parameter of interest, from the beam-only [2, 211] and joint atmospheric-beam fits discussed within this thesis. The results are illustrated both with and without the reactor constraint (RC). The best-fit values are taken from the highest posterior density (HPD) and the error comes from the width of the one-dimensional 1σ credible interval that contains the HPD. As the posterior distribution in δ_{CP} is cyclical, the highest posterior distribution is given instead.

3587 The Bayes factors from the beam-only and joint atmospheric-beam analyses
 3588 are presented in Table 8.13. The strength of each preference, from Jeffrey's
 3589 scale (Table 4.1), is also given.

3590 To summarise this information, the joint fit prefers a tighter 1σ credible
 3591 interval in $\sin^2(\theta_{23})$ along with a stronger Bayes factor for preferring the correct
 3592 octant hypothesis. The increase in sensitivity to $|\Delta m_{32}^2|$ between the two fits is
 3593 negligible but the joint analysis substantially prefers the correct mass hierarchy
 3594 hypothesis. It does not require any external constraints on $\sin^2(\theta_{13})$ to make
 3595 this statement. This is a stronger preference than any statement made by the
 3596 beam-only analysis. The joint fit also produces a value of $\sin^2(\theta_{13})$ closer to the

Fit	$B(\text{NH}/\text{IH})$		$B(\text{UO}/\text{LO})$	
	Value	Strength	Value	Strength
Asimov A				
Beam	1.91	Weak	1.56	Weak
Beam w/RC	3.09	Weak	2.47	Weak
Joint	3.67	Substantial	1.74	Weak
Joint w/RC	6.47	Substantial	2.64	Weak
Asimov B				
Beam	1.08	Weak	0.91	Weak
Beam w/RC	0.98	Weak	1.15	Weak
Joint	1.43	Weak	1.19	Weak
Joint w/RC	1.36	Weak	1.52	Weak

Table 8.13: A comparison of the Bayes factors for mass hierarchy and $\sin^2(\theta_{23})$ octant hypotheses, from the beam-only [2, 211] and joint atmospheric-beam fits discussed within this thesis. The results are illustrated both with and without the reactor constraint (RC). The strength of the preference for the normal mass hierarchy and upper octants are provided by Jeffrey's scale Table 4.1.

known value compared to the beam-only analysis. When the reactor constraint is applied, the preference for the correct hierarchy and octant (NH and UO) hypotheses increase but does not change the statement which would be made.

The fits from the Asimov B comparisons (subsection 8.3.9) show the improved ability for the joint analysis to more precisely select the true value of δ_{CP} if it were CP-conserving, compared to the beam-only analysis. This is evidenced by the area contained within the 1σ credible interval decreasing by $\sim 4\%$. Furthermore, the joint fit is able to better determine the octant of $\sin^2(\theta_{23})$ when the true value is moved further away from the boundary as evidenced by the larger Bayes factor. There is also a $\sim 5\%$ reduction of area contained within the 1σ credible interval in $\sin^2(\theta_{23})$.

9

3608

3609

Conclusions and Outlook

3610 This thesis has presented a joint beam and atmospheric neutrino oscillation
3611 analysis from the Tokai-to-Kamioka (T2K) and Super-Kamiokande (SK) collab-
3612 orations. It reports the sensitivities of the analysis, with the intention for the
3613 two collaborations to publish a data analysis in the near-future. It combines
3614 the two independent analyses presented by the collaborations [2, 3] and uses
3615 3244.4 days of SK livetime and 1.97×10^{21} (1.63×10^{21}) POT recorded at the far
3616 detector in the neutrino(antineutrino) beam operating mode. The ND280 near
3617 detector is used within this analysis to constrain the beam flux and cross-section
3618 systematics. It uses 1.15×10^{21} POT and 8.34×10^{20} POT in the neutrino and
3619 antineutrino running modes, respectively.

3620 This analysis uses a Bayesian Markov Chain Monte Carlo fitting technique
3621 implemented within the MaCh3 framework. This work has significantly developed
3622 the fitting framework, both in terms of technical features and performance.
3623 This includes supporting new samples, systematics, and oscillation channels.
3624 These developments have become the foundation of the fitter's expansion into
3625 other neutrino oscillation experiments. Beyond these improvements, a novel
3626 technique for calculating the atmospheric neutrino oscillation probabilities has
3627 been developed. This calculation uses a sub-sampling linear-averaging approach
3628 to ensure that the sensitivities being calculated are not biased due to insufficient

3629 Monte Carlo statistics in a region of rapidly varying probability. It illustrates a
3630 computationally feasible method of reliably calculating oscillation probabilities
3631 that can be utilised within any fitting framework.

3632 The sensitivity of the joint beam-atmospheric analysis is presented in Table 9.1,
3633 and compared to the beam-only analysis [2]. The sensitivities are evaluated
3634 using a set of known oscillation parameter values close to the results from a
3635 previous T2K analysis [75] (denoted AsimovA in Table 9.1). The joint analysis
3636 has a stronger sensitivity to $\sin^2(\theta_{23})$, as evidenced by the tighter 1σ credible
3637 intervals when the constraints from reactor experiments are not applied. The
3638 joint fit's sensitivity to δ_{CP} is marginally stronger than beam-only analysis. Whilst
3639 the sensitivity to $|\Delta m_{32}^2|$ is mostly unchanged between the two analyses, the
3640 sensitivity to select the correct hierarchy is significantly improved. This follows
3641 from a substantial preference for the normal hierarchy hypothesis presented
3642 within the joint analysis, as classified by Jeffrey's scale [130], which is the correct
3643 hierarchy for the known values. This is notable as the beam-only analysis
3644 cannot make this statement, either with or without the application of the reactor
3645 constraint on $\sin^2(\theta_{13})$. The joint fit's preference for the correct hierarchy increases
3646 once the reactor constraint is applied. The preference for selecting the correct
3647 octant of $\sin^2(\theta_{23})$ is classified as weak by Jeffrey's scale but is still stronger than
3648 the statement made by the beam-only analysis.

3649 The sensitivities of the beam-only and joint atmospheric-beam fit have also
3650 been compared at a set of known oscillation parameters which are CP-conserving
3651 and in the lower octant of $\sin^2(\theta_{23})$. The joint analysis has a $\sim 5\%$ improved abil-
3652 ity to select the known values more precisely compared to the beam-only analysis.

3653 Whilst this analysis provides the first sensitivities of a joint beam and atmo-
3654 spheric analysis, there are more improvements that could be made. Since this
3655 analysis began, the T2K collaboration has released an updated oscillation analysis
3656 with additional near and far detector samples alongside a more sophisticated
3657 interaction model [4]. The overall change in oscillation parameter measurement

Fit	δ_{CP} (HPD)	Δm_{32}^2 [$\times 10^{-3}$ eV 2]	$\sin^2(\theta_{23})$	$B(\text{NH/IH})$	$B(\text{UO/LO})$
Asimov A	-1.601	2.509	0.528	NH	UO
Beam	$-1.45^{+0.06}_{-0.06}$	$2.51^{+0.07}_{-0.06}$	$0.501^{+0.044}_{-0.026}$	1.91	1.56
Beam w/RC	$-1.57^{+0.06}_{-0.06}$	$2.51^{+0.08}_{-0.06}$	$0.533^{+0.022}_{-0.043}$	3.09	2.47
Joint	$-1.57^{+0.06}_{-0.06}$	$2.51^{+0.07}_{-0.06}$	$0.518^{+0.027}_{-0.038}$	3.67	1.74
Joint w/RC	$-1.57^{+0.06}_{-0.06}$	$2.51^{+0.05}_{-0.06}$	$0.528^{+0.027}_{-0.038}$	6.47	2.64

Table 9.1: A comparison of the sensitivity to each oscillation parameter of interest, from the beam-only [2, 211] and joint atmospheric-beam fits discussed within this thesis. The results are illustrated both with and without the reactor constraint (RC). The best-fit values are taken from the highest posterior density (HPD) and the error comes from the width of the one-dimensional 1σ credible intervals. As the posterior distribution in δ_{CP} is cyclical, the highest posterior distribution is given instead. The Bayes factors are provided for the mass hierarchy preference: normal hierarchy (NH) and inverse hierarchy (IH), and $\sin^2(\theta_{23})$ octant preference: upper octant (UO) and lower octant (LO).

3658 observed by T2K is relatively minor but the stronger constraints on the systemat-
 3659 ics could impact this joint analysis to a larger extent. Further developments could
 3660 consider the effect of correlating the beam and atmospheric flux uncertainties
 3661 relating to hadron production, where updates of the Bartol and Honda models
 3662 may allow this to be studied [147].

3663 Beyond these model improvements, more data is available than what is
 3664 assumed for this analysis. The T2K experiment has accumulated an additional
 3665 1.78×10^{20} POT in neutrino mode. Similarly, there are several early SK periods
 3666 that have not been considered within this analysis as the reconstruction software
 3667 has not been validated for those periods. SK will also continue to accumulate
 3668 statistics with Gadolinium doping. Developments in the atmospheric sample
 3669 selections may also benefit from the Gadolinium dopants as neutron capture
 3670 will aid in neutrino/antineutrino separation leading to better mass hierarchy
 3671 sensitivity. This would require including interaction systematics for neutron
 3672 capture of Gadolinium which has already started [212].

3673 This analysis shows the increased sensitivity to oscillation parameters from
 3674 the combination of beam and atmospheric samples. It has developed the MaCh3

3675 fitting framework and has laid the foundations of the fitter's expansion into other
3676 neutrino oscillation experiments. The sensitivities presented in this thesis, and
3677 the techniques that were used to generate them, are significant to the future of
3678 neutrino oscillation physics which will likely perform similar analyses. As such,
3679 they have been presented by the T2K and SK collaborations at the Neutrino 2022
3680 conference [4]. Moving towards the next generation of neutrino experiments,
3681 this analysis has the potential to become the basis of the oscillation analysis
3682 for the future Hyper-Kamiokande experiment which aims to make conclusive
3683 statements about CP-violation in the neutrino sector.

Bibliography

- [1] Andrei D Sakharov. "Violation of CP invariance, C asymmetry, and baryon asymmetry of the universe". In: *Soviet Physics Uspekhi* 34.5 (May 1991), pp. 392–393. URL: <https://doi.org/10.1070/pu1991v034n05abeh002497>.
- [2] P. Dunne. "Latest Neutrino Oscillation Results from T2K". In: *Neutrino 2020* (2020). URL: <https://zenodo.org/record/3959557>.
- [3] M. Jiang et al. "Atmospheric neutrino oscillation analysis with improved event reconstruction in Super-Kamiokande IV". en. In: *Prog. Theor. Exp. Phys.* 2019.5 (May 2019).
- [4] C. Bronner. "Accelerator Neutrino I Recent results from T2K". In: *Neutrino 2022* (2022). URL: <https://zenodo.org/record/6683821>.
- [5] J. Chadwick. "Intensitätsverteilung im magnetischen Spectrum der β -Strahlen von radium B + C". In: *Verhandl. Dtsc. Phys. Ges.* 16 (1914), p. 383. URL: <http://cds.cern.ch/record/262756>.
- [6] C. D. Ellis and W. A. Wooster. "The average energy of disintegration of radium E". en. In: *Proc. R. Soc. Lond. A Math. Phys. Sci.* 117.776 (Dec. 1927), pp. 109–123.
- [7] W. Pauli. "Dear radioactive ladies and gentlemen". In: *Phys. Today* 31N9 (1978), p. 27.
- [8] E. Fermi. "An attempt of a theory of beta radiation. 1." In: *Z. Phys.* 88 (1934), pp. 161–177.
- [9] F. Reines and C. L. Cowan. "Detection of the Free Neutrino". In: *Phys. Rev.* 92 (3 1953), pp. 830–831. URL: <https://link.aps.org/doi/10.1103/PhysRev.92.830>.
- [10] C. L. Cowan et al. "Detection of the Free Neutrino: a Confirmation". In: *Science* 124.3212 (1956), pp. 103–104. URL: <http://science.sciencemag.org/content/124/3212/103>.
- [11] G. Danby et al. "Observation of High-Energy Neutrino Reactions and the Existence of Two Kinds of Neutrinos". In: *Phys. Rev. Lett.* 9 (1 1962), pp. 36–44. URL: <https://link.aps.org/doi/10.1103/PhysRevLett.9.36>.
- [12] K. Kodama et al. "Observation of tau neutrino interactions". In: *Physics Letters B* 504.3 (2001), pp. 218 –224. URL: <http://www.sciencedirect.com/science/article/pii/S0370269301003070>.
- [13] A. Aguilar-Arevalo et al. "Evidence for neutrino oscillations from the observation of anti-neutrino(electron) appearance in a anti-neutrino(muon) beam". In: *Phys. Rev.* D64 (2001), p. 112007. arXiv: [hep-ex/0104049 \[hep-ex\]](https://arxiv.org/abs/hep-ex/0104049).

- [14] A. A. Aguilar-Arevalo et al. "Improved Search for $\bar{\nu}_\mu \rightarrow \bar{\nu}_e$ Oscillations in the MiniBooNE Experiment". In: *Phys. Rev. Lett.* 110 (16 2013), p. 161801. URL: <https://link.aps.org/doi/10.1103/PhysRevLett.110.161801>.
- [15] Planck Collaboration. "Planck 2018 results. VI. Cosmological parameters". In: *aap* 641 (Sept. 2020).
- [16] J. A. Bagger et al. "Precision electroweak measurements on the Z resonance". In: *Physics Reports* 427.5 (2006), pp. 257–454. URL: <http://www.sciencedirect.com/science/article/pii/S0370157305005119>.
- [17] B. Pontecorvo. "Neutrino Experiments and the Problem of Conservation of Leptonic Charge". In: *Sov. Phys. JETP* 26 (1968). [Zh. Eksp. Teor. Fiz. 53, 1717(1967)], pp. 984–988.
- [18] B. Pontecorvo. "Inverse beta processes and nonconservation of lepton charge". In: *Sov. Phys. JETP* 7 (1958). [Zh. Eksp. Teor. Fiz. 34, 247(1957)], pp. 172–173.
- [19] M. Kobayashi and T. Maskawa. "CP-Violation in the Renormalizable Theory of Weak Interaction". In: *Progress of Theoretical Physics* 49.2 (1973), pp. 652–657. URL: <http://dx.doi.org/10.1143/PTP.49.652>.
- [20] N. Cabibbo. "Unitary Symmetry and Leptonic Decays". In: *Phys. Rev. Lett.* 10 (12 1963), pp. 531–533. URL: <https://link.aps.org/doi/10.1103/PhysRevLett.10.531>.
- [21] A. Maio et al. "Search for Majorana neutrinos with the SNO+ detector at SNOLAB". In: *Journal of Physics: Conference Series* 587 (2015), p. 012030. URL: <https://doi.org/10.1088/1742-6596/587/1/012030>.
- [22] A. Y. Smirnov. "The MSW effect and Solar Neutrinos". In: *ArXiv* (2003). URL: <https://arxiv.org/abs/hep-ph/0305106>.
- [23] S. P. Mikheyev and A. Y. Smirnov. "Resonance enhancement of oscillations in matter and solar neutrino spectroscopy". In: *Soviet Journal of Nuclear Physics* 42 (6 1985), pp. 913–917.
- [24] L. Wolfenstein. "Neutrino oscillations in matter". In: *Phys. Rev. D* 17 (9 1978), pp. 2369–2374. URL: <https://link.aps.org/doi/10.1103/PhysRevD.17.2369>.
- [25] V. D. Barger et al. "Matter Effects on Three-Neutrino Oscillations". In: *Phys. Rev. D* 22 (1980), p. 2718.
- [26] Y. Ashie et al. "Evidence for an Oscillatory Signature in Atmospheric Neutrino Oscillations". In: *Phys. Rev. Lett.* 93 (10 2004), p. 101801. URL: <https://link.aps.org/doi/10.1103/PhysRevLett.93.101801>.
- [27] Q. R. Ahmad et al. "Direct Evidence for Neutrino Flavor Transformation from Neutral-Current Interactions in the Sudbury Neutrino Observatory". In: *Phys. Rev. Lett.* 89 (1 2002), p. 011301. URL: <https://link.aps.org/doi/10.1103/PhysRevLett.89.011301>.
- [28] Nobel Prize. *2015 Nobel prize in Physics as listed by Nobelprize.org*. https://www.nobelprize.org/nobel_prizes/physics/laureates/2015/. Accessed: 22-06-2022.
- [29] J. A. Formaggio and G. P. Zeller. "From eV to EeV: Neutrino Cross Sections Across Energy Scales". In: *Rev. Mod. Phys.* 84 (2012), pp. 1307–1341. arXiv: 1305.7513 [hep-ex].

- 3763 [30] A. Oralbaev, M. Skorokhvatov, and O. Titov. "The inverse beta decay: a study of
3764 cross section". In: *Journal of Physics: Conference Series* 675.1 (2016), p. 012003. URL:
3765 <https://doi.org/10.1088/1742-6596/675/1/012003>.
- 3766 [31] A. Bellerive. "Review of solar neutrino experiments". en. In: *Int. J. Mod. Phys. A*
3767 19.08 (Mar. 2004), pp. 1167–1179.
- 3768 [32] R. Davis, D. S. Harmer, and K. C. Hoffman. "Search for Neutrinos from the Sun".
3769 In: *Phys. Rev. Lett.* 20 (21 1968), pp. 1205–1209. URL:
3770 <https://link.aps.org/doi/10.1103/PhysRevLett.20.1205>.
- 3771 [33] N. Vinyoles et al. "A new generation of standard solar models". In: *Astrophys. J.*
3772 835.2 (Jan. 2017), p. 202.
- 3773 [34] V. Gribov and B. Pontecorvo. "Neutrino astronomy and lepton charge". en. In:
3774 *Phys. Lett. B* 28.7 (Jan. 1969), pp. 493–496.
- 3775 [35] K. S. Hirata et al. "Observation of ${}^8\text{B}$ solar neutrinos in the Kamiokande-II
3776 detector". In: *Phys. Rev. Lett.* 63 (1 1989), pp. 16–19. URL:
3777 <https://link.aps.org/doi/10.1103/PhysRevLett.63.16>.
- 3778 [36] W. Hampel et al. "GALLEX solar neutrino observations: results for GALLEX IV".
3779 en. In: *Phys. Lett. B* 447.1-2 (Feb. 1999), pp. 127–133.
- 3780 [37] J. N. Abdurashitov et al. "Measurement of the solar neutrino capture rate with
3781 gallium metal". In: *Phys. Rev. C* 60 (5 1999), p. 055801. URL:
3782 <https://link.aps.org/doi/10.1103/PhysRevC.60.055801>.
- 3783 [38] K. Abe et al. "T2K neutrino flux prediction". In: *Phys. Rev. D* 87 (1 2013),
3784 p. 012001. URL: <https://link.aps.org/doi/10.1103/PhysRevD.87.012001>.
- 3785 [39] D. G. Michael et al. "Observation of Muon Neutrino Disappearance with the
3786 MINOS Detectors in the NuMI Neutrino Beam". In: *Phys. Rev. Lett.* 97 (19 2006),
3787 p. 191801. URL:
3788 <https://link.aps.org/doi/10.1103/PhysRevLett.97.191801>.
- 3789 [40] M. H. Ahn et al. "Measurement of neutrino oscillation by the K2K experiment".
3790 In: *Phys. Rev. D* 74 (7 2006), p. 072003. eprint:
3791 <https://link.aps.org/doi/10.1103/PhysRevD.74.072003>.
- 3792 [41] M. A. Acero et al. "First measurement of neutrino oscillation parameters using
3793 neutrinos and antineutrinos by NOvA". In: *Phys. Rev. Lett.* 123 (15 2019),
3794 p. 151803. URL:
3795 <https://link.aps.org/doi/10.1103/PhysRevLett.123.151803>.
- 3796 [42] K. Abe et al. "The T2K experiment". In: *Nuclear Instruments and Methods in Physics*
3797 *Research Section A* 659.1 (2011), pp. 106–135. eprint:
3798 <http://www.sciencedirect.com/science/article/pii/S0168900211011910>.
- 3799 [43] B. Abi et al. "Long-baseline neutrino oscillation physics potential of the DUNE
3800 experiment". en. In: *Eur. Phys. J. C Part. Fields* 80.10 (Oct. 2020).
- 3801 [44] Hyper-Kamiokande Proto-Collaboration. "Physics potential of a long-baseline
3802 neutrino oscillation experiment using a J-PARC neutrino beam and
3803 Hyper-Kamiokande". In: *Prog. Theor. Exp. Phys.* 2015.5 (May 2015), pp. 53C02–0.

- 3804 [45] C. Blanco, D. Hooper, and P. Machado. "Constraining sterile neutrino
3805 interpretations of the LSND and MiniBooNE anomalies with coherent neutrino
3806 scattering experiments". In: *Phys. Rev. D* 101.7 (2020). URL:
3807 <https://doi.org/10.1103/2Fphysrevd.101.075051>.
- 3808 [46] MicroBooNE Collaboration. "Search for an Excess of Electron Neutrino
3809 Interactions in MicroBooNE Using Multiple Final State Topologies". In: *arXiv*
3810 (2021). URL: <https://arxiv.org/abs/2110.14054>.
- 3811 [47] B. Armbruster et al. "Upper limits for neutrino oscillations $\bar{\nu}_\mu \rightarrow \bar{\nu}_e$ from muon
3812 decay at rest". In: *Phys. Rev. D* 65 (11 2002), p. 112001. URL:
3813 <https://link.aps.org/doi/10.1103/PhysRevD.65.112001>.
- 3814 [48] T. K. Gaisser and M. Honda. "Flux of Atmospheric Neutrinos". In: *Annual Review
3815 of Nuclear and Particle Science* 52.1 (2002), pp. 153–199. URL:
3816 <https://doi.org/10.1146%2Fannurev.nucl.52.050102.090645>.
- 3817 [49] G. D. Barr et al. "Three-dimensional calculation of atmospheric neutrinos". In:
3818 *Phys. Rev. D* 70.2 (2004). URL: <https://doi.org/10.1103/physrevd.70.023006>.
- 3819 [50] M. Honda et al. "Calculation of atmospheric neutrino flux using the interaction
3820 model calibrated with atmospheric muon data". In: *Phys. Rev. D* 75.4 (2007). URL:
3821 <https://doi.org/10.1103/physrevd.75.043006>.
- 3822 [51] M. Honda et al. "New calculation of the atmospheric neutrino flux in a
3823 three-dimensional scheme". In: *Phys. Rev. D* 70 (4 2004), p. 043008. URL:
3824 <https://link.aps.org/doi/10.1103/PhysRevD.70.043008>.
- 3825 [52] M. Honda et al. "Improvement of low energy atmospheric neutrino flux
3826 calculation using the JAM nuclear interaction model". In: *Phys. Rev. D* 83 (12
3827 2011), p. 123001. URL:
3828 <https://link.aps.org/doi/10.1103/PhysRevD.83.123001>.
- 3829 [53] A. Fassò et al. *FLUKA: Status and Prospects for Hadronic Applications*. Ed. by
3830 Andreas Kling et al. Berlin, Heidelberg: Springer Berlin Heidelberg, 2001,
3831 pp. 955–960.
- 3832 [54] Y. Ashie et al. "Measurement of atmospheric neutrino oscillation parameters by
3833 Super-Kamiokande I". In: *Phys. Rev. D* 71.11 (2005). URL:
3834 <https://doi.org/10.1103/physrevd.71.112005>.
- 3835 [55] F. Reines et al. "Evidence for high-energy cosmic-ray neutrino interactions". In:
3836 *Phys. Rev. Lett.* 15.9 (Aug. 1965), pp. 429–433.
- 3837 [56] D. Casper et al. "Measurement of atmospheric neutrino composition with the
3838 IMB-3 detector". In: *Phys. Rev. Lett.* 66 (20 1991), pp. 2561–2564. URL:
3839 <https://link.aps.org/doi/10.1103/PhysRevLett.66.2561>.
- 3840 [57] K. S. Hirata et al. "Observation of a small atmospheric ν_μ/ν_e ratio in
3841 Kamiokande". en. In: *Phys. Lett. B* 280.1-2 (Apr. 1992), pp. 146–152.
- 3842 [58] Z. Li et al. "Measurement of the tau neutrino cross section in atmospheric
3843 neutrino oscillations with Super-Kamiokande". In: *Phys. Rev. D* 98.5 (2018). URL:
3844 <https://doi.org/10.1103/physrevd.98.052006>.
- 3845 [59] K. Abe et al. "Atmospheric neutrino oscillation analysis with external constraints
3846 in Super-Kamiokande I-IV". In: *Phys. Rev. D* 97 (7 2018), p. 072001. URL:
3847 <https://link.aps.org/doi/10.1103/PhysRevD.97.072001>.

- 3848 [60] T2K Collaboration. "Constraint on the matter-antimatter symmetry-violating
3849 phase in neutrino oscillations". en. In: *Nature* 580.7803 (Apr. 2020), pp. 339–344.
- 3850 [61] M. A. Acero et al. "First measurement of neutrino oscillation parameters using
3851 neutrinos and antineutrinos by NOvA". en. In: *Phys. Rev. Lett.* 123.15 (Oct. 2019),
3852 p. 151803.
- 3853 [62] M. G. Aartsen et al. "Measurement of atmospheric neutrino oscillations at 6–56
3854 GeV with IceCube DeepCore". In: *Phys. Rev. Lett.* 120.7 (Feb. 2018).
- 3855 [63] P. Adamson et al. "Combined analysis of $\nu\mu$ Disappearance
3856 and $\nu\mu \rightarrow \nu e$ Appearance in MINOS using accelerator and atmospheric neutrinos".
3857 In: *Phys. Rev. Lett.* 112.19 (May 2014).
- 3858 [64] M. Sajjad Athar et al. "Status and perspectives of neutrino physics". In: *Progress
3859 in Particle and Nuclear Physics* 124 (2022), p. 103947. URL:
3860 <https://doi.org/10.1016/Fj.pnpp.2022.103947>.
- 3861 [65] S. B. Kim, T. Lasserre, and Y. Wang. "Reactor Neutrinos". In: *Adv. High Energy
3862 Phys.* 2013 (2013), pp. 1–34.
- 3863 [66] K Abe et al. "First gadolinium loading to Super-Kamiokande". en. In: *Nucl.
3864 Instrum. Methods Phys. Res. A* 1027.166248 (Mar. 2022), p. 166248.
- 3865 [67] F. P. An et al. "Observation of Electron-Antineutrino Disappearance at Daya Bay".
3866 In: *Phys. Rev. Lett.* 108 (17 2012), p. 171803. URL:
3867 <https://link.aps.org/doi/10.1103/PhysRevLett.108.171803>.
- 3868 [68] J. K. Ahn et al. "Observation of Reactor Electron Antineutrinos Disappearance in
3869 the RENO Experiment". In: *Phys. Rev. Lett.* 108 (19 2012), p. 191802. URL:
3870 <https://link.aps.org/doi/10.1103/PhysRevLett.108.191802>.
- 3871 [69] Y. Abe et al. "Indication of Reactor $\bar{\nu}_e$ Disappearance in the Double Chooz
3872 Experiment". In: *Phys. Rev. Lett.* 108 (13 2012), p. 131801. URL:
3873 <https://link.aps.org/doi/10.1103/PhysRevLett.108.131801>.
- 3874 [70] M. P. Decowski. "KamLAND's precision neutrino oscillation measurements". en.
3875 In: *Nucl. Phys. B*. 908 (July 2016), pp. 52–61.
- 3876 [71] A. Gando et al. "Constraints on θ_{13} from a three-flavor oscillation analysis of
3877 reactor antineutrinos at KamLAND". In: *Phys. Rev. D* 83 (5 2011), p. 052002. URL:
3878 <https://link.aps.org/doi/10.1103/PhysRevD.83.052002>.
- 3879 [72] Particle Data Group. "Review of particle physics". en. In: *Prog. Theor. Exp. Phys.*
3880 2020.8 (Aug. 2020).
- 3881 [73] K. Abe et al. "Constraint on the matter-antimatter symmetry-violating phase in
3882 neutrino oscillations". In: *Nature* 580.7803 (Apr. 2020), pp. 339–344.
- 3883 [74] R. L. Workman et al. "Review of Particle Physics". In: *PTEP* 2022 (2022),
3884 p. 083C01.
- 3885 [75] K. Abe et al. "Precise Measurement of the Neutrino Mixing Parameter θ_{23} from
3886 Muon Neutrino Disappearance in an Off-Axis Beam". In: *Phys. Rev. Lett.* 112 (18
3887 2014), p. 181801. URL:
3888 <https://link.aps.org/doi/10.1103/PhysRevLett.112.181801>.
- 3889 [76] R. Wendell. "Three Flavor Oscillation Analysis of Atmospheric Neutrinos in
3890 Super-Kamiokande". PhD thesis. University of North Carolina, 2008.

- 3891 [77] A. M. Dziewonski and D. L. Anderson. "Preliminary reference Earth model". en.
3892 In: *Phys. Earth Planet. Inter.* 25.4 (June 1981), pp. 297–356.
- 3893 [78] K. Abe et al. "Improved constraints on neutrino mixing from the T2K experiment
3894 with 3.13×10^{21} protons on target". en. In: *Phys. Rev. D.* 103.11 (June 2021).
- 3895 [79] Y. Fukuda et al. "Evidence for oscillation of atmospheric neutrinos". In: *Phys. Rev.*
3896 *Lett.* 81.8 (Aug. 1998), pp. 1562–1567.
- 3897 [80] K. Abe et al. "Calibration of the Super-Kamiokande detector". In: *Nuclear*
3898 *Instruments and Methods in Physics Research Section A* 737 (2014), pp. 253–272. URL:
3899 <https://doi.org/10.1016/j.nima.2013.11.081>.
- 3900 [81] L. Wan. "Atmospheric Neutrino Super-K". In: *Neutrino* 2022 (2022). URL:
3901 <https://zenodo.org/record/6694761>.
- 3902 [82] M. Jiang. "Study of the neutrino mass hierarchy with the atmospheric neutrino
3903 data collected in Super-Kamiokande IV". PhD thesis. Kyoto University, 2019.
- 3904 [83] S. Fukuda et al. "The super-kamiokande detector". en. In: *Nucl. Instrum. Methods*
3905 *Phys. Res. A* 501.2-3 (Apr. 2003), pp. 418–462. eprint:
3906 <http://www.sciencedirect.com/science/article/pii/S016890020300425X>.
- 3907 [84] Y. Itow et al. "The JHF-Kamioka neutrino project". In: *arXiv* (2001).
- 3908 [85] H. Kume et al. "20 inch diameter photomultiplier". In: *Nuclear Instruments and*
3909 *Methods in Physics Research* 205.3 (1983), pp. 443–449. URL:
3910 <https://www.sciencedirect.com/science/article/pii/0167508783900078>.
- 3911 [86] A. Suzuki et al. "Improvement of 20 in. diameter photomultiplier tubes". In:
3912 *Nuclear Instruments and Methods in Physics Research Section A* 329.1-2 (May 1993),
3913 pp. 299–313. URL: [https://doi.org/10.1016/0168-9002\(93\)90949-i](https://doi.org/10.1016/0168-9002(93)90949-i).
- 3914 [87] Y. Nakano et al. "Measurement of the radon concentration in purified water in
3915 the Super-Kamiokande IV detector". en. In: *Nucl. Instrum. Methods Phys. Res. A*
3916 977.164297 (Oct. 2020), p. 164297.
- 3917 [88] Hamamatsu. *Hamamatsu Photonics Photomultiplier Tubes Handbook*. URL:
3918 https://www.hamamatsu.com/content/dam/hamamatsu-photonics/sites/documents/99_SALES_LIBRARY/etd/PMT_handbook_v4E.pdf.
- 3919 [89] J. F. Beacom and M. R. Vagins. "Antineutrino Spectroscopy with Large Water
3920 Čerenkov Detectors". In: *Phys. Rev. Lett.* 93 (17 2004), p. 171101. URL:
3921 <https://link.aps.org/doi/10.1103/PhysRevLett.93.171101>.
- 3922 [90] L. Marti et al. "Evaluation of gadolinium's action on water Cherenkov detector
3923 systems with EGADS". en. In: *Nucl. Instrum. Methods Phys. Res. A* 959.163549
3924 (Apr. 2020), p. 163549.
- 3925 [91] M. Vagins. "Solar/DSNB Neutrino SK-Gd". In: *Neutrino* 2022 (2022). URL:
3926 <https://zenodo.org/record/6696210>.
- 3927 [92] J. Focht. "Dark Noise Calibration of the Super-Kamiokande Outer Detector".
3928 PhD thesis. Massachusetts Institute of Technology, 2004.
- 3929 [93] T. Tanimori et al. "Design and performance of semi-custom analog IC including
3930 two TACs and two current integrators for 'Super-Kamiokande'". In: *IEEE*
3931 *Transactions on Nuclear Science* 36.1 (1989), pp. 497–501.

- 3933 [94] J. Hosaka et al. "Solar neutrino measurements in Super-Kamiokande-I". In: *Phys.*
3934 *Rev. D* 73 (11 2006), p. 112001.
- 3935 [95] H. Nishino et al. "High-speed charge-to-time converter ASIC for the
3936 Super-Kamiokande detector". en. In: *Nucl. Instrum. Methods Phys. Res. A* 610.3
3937 (Nov. 2009), pp. 710–717.
- 3938 [96] S. Yamada et al. "New online system without hardware trigger for the
3939 Super-Kamiokande experiment". In: *2007 IEEE Nuclear Science Symposium*
3940 *Conference Record*. Honolulu, HI, USA: IEEE, Oct. 2007.
- 3941 [97] G. Carminati. "The new wide-band solar neutrino trigger for super-kamiokande".
3942 In: *Phys. Procedia* 61 (2015), pp. 666–672.
- 3943 [98] P. A. Čerenkov. "Visible radiation produced by electrons moving in a medium
3944 with velocities exceeding that of light". In: *Phys. Rev.* 52.4 (Aug. 1937),
3945 pp. 378–379.
- 3946 [99] I. Frank and I. Tamm. "Coherent visible radiation of fast electrons passing
3947 through matter". In: *Selected Papers*. Berlin, Heidelberg: Springer Berlin
3948 Heidelberg, 1991, pp. 29–35.
- 3949 [100] The T2K Collaboration. "Letter of Intent: Neutrino Oscillation Experiment at
3950 JHF". In: *KEK Proposal* (2001). eprint:
3951 <http://neutrino.kek.jp/jhfnu/loi/loi.v2.030528.pdf>.
- 3952 [101] The K2K Collaboration and S. H. Ahn. "Detection of Accelerator-Produced
3953 Neutrinos at a Distance of 250 km". In: (Feb. 2001). arXiv: [hep-ex/0103001](https://arxiv.org/abs/hep-ex/0103001)
3954 [[hep-ex](#)].
- 3955 [102] The T2K Collaboration. "Tokai-to-Kamioka (T2K) Long Baseline Neutrino
3956 Oscillation Experiment Proposal". In: *KEK Proposal* (2006). eprint: [http://j-](http://j-parc.jp/researcher/Hadron/en/pac\0606/pdf/p11-Nishikawa.pdf)
3957 [parc.jp/researcher/Hadron/en/pac\0606/pdf/p11-Nishikawa.pdf](http://j-parc.jp/researcher/Hadron/en/pac\0606/pdf/p11-Nishikawa.pdf).
- 3958 [103] K. Abe et al. "Observation of Electron Neutrino Appearance in a Muon Neutrino
3959 Beam". In: *Phys. Rev. Lett.* 112 (6 2014), p. 061802. eprint:
3960 <https://link.aps.org/doi/10.1103/PhysRevLett.112.061802>.
- 3961 [104] T. Fukuda et al. "Proposal for precise measurement of neutrino-water
3962 cross-section in NINJA physics run". Proposal for J-PARC and KEK. 2017.
- 3963 [105] T. Ovsianikova et al. "New experiment WAGASCI to measure cross sections of
3964 neutrino interactions in water and hydrocarbon using J-PARC beam". In: *Physics*
3965 *of Particles and Nuclei* 48.6 (2017), pp. 1014–1017. eprint:
3966 <https://doi.org/10.1134/S1063779617060478>.
- 3967 [106] M. Antonova et al. "Baby MIND: a magnetized segmented neutrino detector for
3968 the WAGASCI experiment". In: *Journal of Instrumentation* 12.07 (2017), p. C07028.
3969 eprint: <http://stacks.iop.org/1748-0221/12/i=07/a=C07028>.
- 3970 [107] K. Abe et al. "First measurement of the charged current $\bar{\nu}_\mu$ double differential
3971 cross section on a water target without pions in the final state". In: *Phys. Rev. D*
3972 102 (1 2020), p. 012007. URL:
3973 <https://link.aps.org/doi/10.1103/PhysRevD.102.012007>.

- 3974 [108] K. Abe et al. "Measurements of $\bar{\nu}_\mu$ and $\bar{\nu}_\mu + \nu_\mu$ charged-current cross-sections
3975 without detected pions or protons on water and hydrocarbon at a mean
3976 anti-neutrino energy of 0.86 GeV". In: *Progress of Theoretical and Experimental*
3977 *Physics* 2021.4 (Mar. 2021). URL: <https://doi.org/10.1093/ptep/ptab014>.
- 3978 [109] K. Matsuoka et al. "Design and performance of the muon monitor for the T2K
3979 neutrino oscillation experiment". In: *Nuclear Instruments and Methods in Physics*
3980 *Research Section A* 624.3 (2010), pp. 591–600. eprint:
3981 <http://www.sciencedirect.com/science/article/pii/S016890021002098X>.
- 3982 [110] T. Vladisavljevic. *Predicting the T2K neutrino flux and measuring oscillation*
3983 *parameters*. 1st ed. Springer theses. Cham, Switzerland: Springer Nature, Sept.
3984 2020.
- 3985 [111] D. Beavis, A. Carroll, and I. Chiang. "Long baseline neutrino oscillation
3986 experiment at the AGS. Physics design report". In: *Office of Scientific and Technical*
3987 *Information (OSTI)* (Apr. 1995).
- 3988 [112] P.-A. Amaudruz et al. "The T2K fine-grained detectors". In: *Nuclear Instruments*
3989 *and Methods in Physics Research Section A: Accelerators, Spectrometers, Detectors and*
3990 *Associated Equipment* 696 (Dec. 2012), pp. 1–31. URL:
3991 <https://doi.org/10.1016/j.nima.2012.08.020>.
- 3992 [113] N. Abgrall et al. "Time projection chambers for the T2K near detectors". In:
3993 *Nuclear Instruments and Methods in Physics Research Section A: Accelerators,*
3994 *Spectrometers, Detectors and Associated Equipment* 637.1 (May 2011), pp. 25–46. URL:
3995 <https://doi.org/10.1016/j.nima.2011.02.036>.
- 3996 [114] S. Assylbekov et al. "The T2K ND280 off-axis pi-zero detector". In: *Nuclear*
3997 *Instruments and Methods in Physics Research Section A: Accelerators, Spectrometers,*
3998 *Detectors and Associated Equipment* 686 (Sept. 2012), pp. 48–63. URL:
3999 <https://doi.org/10.1016/j.nima.2012.05.028>.
- 4000 [115] D. Allan et al. "The electromagnetic calorimeter for the T2K near detector
4001 ND280". In: *Journal of Instrumentation* 8.10 (2013), P10019–P10019. URL:
4002 <https://doi.org/10.1088%2F1748-0221%2F8%2F10%2Fp10019>.
- 4003 [116] CERN Courier. *UA1 magnet sets off for a second new life*. 2008. URL: <https://cerncourier.com/a/ua1-magnet-sets-off-for-a-second-new-life/>.
- 4005 [117] F. Vannucci. "The NOMAD Experiment at CERN". In: *Advances in High Energy*
4006 *Physics* 2014 (2014), pp. 1–20. URL: <https://doi.org/10.1155/2014/129694>.
- 4007 [118] S. Aoki et al. "The T2K Side Muon Range Detector (SMRD)". In: *Nuclear*
4008 *Instruments and Methods in Physics Research Section A: Accelerators, Spectrometers,*
4009 *Detectors and Associated Equipment* 698 (Jan. 2013), pp. 135–146. URL:
4010 <https://doi.org/10.1016/j.nima.2012.10.001>.
- 4011 [119] K. Suzuki et al. "Measurement of the muon beam direction and muon flux for the
4012 T2K neutrino experiment". In: *Progress of Theoretical and Experimental Physics*
4013 2015.5 (2015), pp. 53C01–0. URL: <https://doi.org/10.1093/ptep/ptv054>.
- 4014 [120] S. Brooks et al. *Handbook of Markov Chain Monte Carlo*. CRC Press, 2011.
- 4015 [121] W. R. Gilks, S. Richardson, and D. J. Spiegelhalter. *Markov Chain Monte Carlo in*
4016 *Practice*. Chapman & Hall/CRC Interdisciplinary Statistics, 1995.

- 4017 [122] C. Wret. "Minimising systematic uncertainties in the T2K experiment using
4018 near-detector and external data". PhD thesis. Imperial College London, 2018.
- 4019 [123] K. E. Duffy. "Measurement of the Neutrino Oscillation Parameters $\sin^2 \theta_{23}$, Δm_{32}^2 ,
4020 $\sin^2 \theta_{13}$, and δ_{CP} in Neutrino and Antineutrino Oscillation at T2K". PhD thesis.
4021 Oriel College, University of Oxford, 2016.
- 4022 [124] C. Bojechko and A. Kabooth. "Muon neutrino disappearance simultaneous fit of
4023 ND280 and SK with Run 1+2+3 data using Markov Chain Monte Carlo Analysis".
4024 In: *T2K Technical Note* 140 (2013).
- 4025 [125] T. Bayes. "An essay toward solving a problem in the doctrine of chances". In: *Phil.*
4026 *Trans. Roy. Soc. Lond.* 53 (1764), pp. 370–418.
- 4027 [126] A. Sztuc. "Standard and Non-Standard Neutrino-Antineutrino Oscillation
4028 Analyses and Event Reconstruction Studies using Markov Chain Monte Carlo
4029 Methods at T2K". PhD thesis. Imperial College London, 2021.
- 4030 [127] N. Metropolis et al. "Equation of State Calculations by Fast Computing
4031 Machines". In: *Journal of Chemical Physics* 21.6 (1970).
- 4032 [128] W. K. Hastings. "Monte Carlo Sampling Methods Using Markov Chains and
4033 Their Applications". In: *Biometrika* 57.1 (1970).
- 4034 [129] J. Dunkley et al. "Fast and reliable Markov chain Monte Carlo technique for
4035 cosmological parameter estimation". en. In: *Mon. Not. R. Astron. Soc.* 356.3 (Jan.
4036 2005), pp. 925–936.
- 4037 [130] H. Jeffreys. *The Theory of Probability*. Oxford Classic Texts in the Physical Sciences.
4038 1939.
- 4039 [131] R. E. Kass and A. E. Raftery. "Bayes factors". en. In: *J. Am. Stat. Assoc.* 90.430
4040 (June 1995), pp. 773–795.
- 4041 [132] T.T. Böhlen et al. "The FLUKA Code: Developments and Challenges for High
4042 Energy and Medical Applications". In: *Nuclear Data Sheets* 120 (2014), pp. 211
4043 –214. eprint:
4044 <http://www.sciencedirect.com/science/article/pii/S0090375214005018>.
- 4045 [133] R. Brun et al. *GEANT: Detector Description and Simulation Tool; Oct 1994*. CERN
4046 Program Library. Long Writeup W5013. Geneva: CERN, 1993. eprint:
4047 <http://cds.cern.ch/record/1082634>.
- 4048 [134] C. Zeitnitz and T.A. Gabriel. "The GEANT-CALOR interface and benchmark
4049 calculations of ZEUS test calorimeters". In: *Nuclear Instruments and Methods in*
4050 *Physics Research Section A* 349.1 (1994), pp. 106 –111. eprint:
4051 <http://www.sciencedirect.com/science/article/pii/0168900294906130>.
- 4052 [135] A. Fiorentini et al. "Flux Prediction and Uncertainty Updates with NA61 2009
4053 Thin Target Data and Negative Focussing Mode Predictions". In: *T2K Technical*
4054 *Note* 217 (2017).
- 4055 [136] N. Abgrall et al. "Measurements of cross sections and charged pion spectra in
4056 proton-carbon interactions at 31 GeV". In: *Phys. Rev. C* 84.3 (2011). URL:
4057 <https://doi.org/10.1103%2Fphysrevc.84.034604>.
- 4058 [137] N. Abgrall et al. "Measurement of production properties of positively charged
4059 kaons in proton-carbon interactions at 31 GeV". In: *Phys. Rev. C* 85.3 (2012). URL:
4060 <https://doi.org/10.1103%2Fphysrevc.85.035210>.

- 4061 [138] N. Abgrall et al. "Pion emission from the T2K replica target: Method, results and
4062 application". In: *Nuclear Instruments and Methods in Physics Research Section A* 701
4063 (2013), pp. 99–114. eprint:
4064 <http://www.sciencedirect.com/science/article/pii/S016890021201234X>.
- 4065 [139] M. Apollonio et al. "Forward production of charged pions with incident protons
4066 on nuclear targets at the CERN Proton Synchrotron". In: *Phys. Rev. C* 80 (3 2009),
4067 p. 035208. eprint: <https://link.aps.org/doi/10.1103/PhysRevC.80.035208>.
- 4068 [140] B. Blau et al. "The superconducting magnet of AMS-02". In: *Nuclear Physics B -
4069 Proceedings Supplements* 113.1-3 (Dec. 2002), pp. 125–132. URL:
4070 [https://doi.org/10.1016/s0920-5632\(02\)01831-5](https://doi.org/10.1016/s0920-5632(02)01831-5).
- 4071 [141] S. Haino et al. "Measurements of primary and atmospheric cosmic-ray spectra
4072 with the BESS-TeV spectrometer". In: *Physics Letters B* 594.1-2 (July 2004),
4073 pp. 35–46. URL: <https://doi.org/10.1016/j.physletb.2004.05.019>.
- 4074 [142] NASA. *U.S. Standard Atmosphere, 1976*. 1976. URL: <https://ntrs.nasa.gov/api/citations/19770009539/downloads/19770009539.pdf>.
- 4075 [143] S. Roesler, R. Engel, and J. Ranft. "The Monte Carlo Event Generator
4076 DPMJET-III". In: *Advanced Monte Carlo for Radiation Physics, Particle Transport
4077 Simulation and Applications*. Springer Berlin Heidelberg, 2001, pp. 1033–1038. URL:
4078 https://doi.org/10.1007/978-3-642-18211-2_166.
- 4079 [144] K. Niita et al. "PHITS—a particle and heavy ion transport code system". In:
4080 *Radiation Measurements* 41.9-10 (Oct. 2006), pp. 1080–1090. URL:
4081 <https://doi.org/10.1016/j.radmeas.2006.07.013>.
- 4082 [145] T. Sanuki et al. "Measurements of atmospheric muon spectra at mountain
4083 altitude". In: *Physics Letters B* 541.3-4 (2002), pp. 234–242. URL:
4084 <https://doi.org/10.1016%2Fs0370-2693%2802%2902265-7>.
- 4085 [146] P. Achard et al. "Measurement of the atmospheric muon spectrum from 20 to
4086 3000 GeV". In: *Physics Letters B* 598.1-2 (2004), pp. 15–32. URL:
4087 <https://doi.org/10.1016%2Fj.physletb.2004.08.003>.
- 4088 [147] K. Sato. "Atmospheric Neutrino Reviews on neutrino fluxes (low E atm nu)". In:
4089 *Neutrino 2022* (2022). URL: <https://zenodo.org/record/6695711>.
- 4090 [148] Y. Hayato and L. Pickering. "The NEUT neutrino interaction simulation program
4091 library". In: *The European Physical Journal Special Topics* 230.24 (Oct. 2021),
4092 pp. 4469–4481. URL: <https://doi.org/10.1140/epjs/s11734-021-00287-7>.
- 4093 [149] Y. Hayato. "A Neutrino Interaction Simulation Program Library NEUT". In: *Acta
4094 Physica Polonica B* 40.9 (2009).
- 4095 [150] C. H. Llewellyn Smith. "Neutrino reactions at accelerator energies". In: *Physics
4096 Reports* 3.5 (1972), pp. 261–379. eprint:
4097 <http://www.sciencedirect.com/science/article/pii/0370157372900105>.
- 4098 [151] O. Benhar, A. Fabrocini, and S. Fantoni. "The nucleon spectral function in infinite
4099 nuclear matter". In: *Nuclear Physics A* 497 (June 1989), pp. 423–430. URL:
4100 [https://doi.org/10.1016/0375-9474\(89\)90484-3](https://doi.org/10.1016/0375-9474(89)90484-3).

- 4102 [152] R. Bradford et al. "A New Parameterization of the Nucleon Elastic Form Factors".
4103 In: *Nuclear Physics B - Proceedings Supplements* 159 (2006). Proceedings of the 4th
4104 International Workshop on Neutrino-Nucleus Interactions in the Few-GeV
4105 Region, pp. 127–132. eprint:
4106 <http://www.sciencedirect.com/science/article/pii/S0920563206005184>.
- 4107 [153] A. A. Aguilar-Arevalo et al. "First measurement of the muon neutrino charged
4108 current quasielastic double differential cross section". In: *Phys. Rev. D* 81.9 (2010).
4109 URL: <https://doi.org/10.1103%2Fphysrevd.81.092005>.
- 4110 [154] R. Gran et al. "Neutrino-nucleus quasi-elastic and 2p2h interactions up to 10
4111 GeV". In: *Phys. Rev. D* 88 (11 2013), p. 113007. eprint:
4112 <https://link.aps.org/doi/10.1103/PhysRevD.88.113007>.
- 4113 [155] C. Berger and L. M. Sehgal. "Lepton mass effects in single pion production by
4114 neutrinos". In: *Phys. Rev. D* 76 (11 2007), p. 113004. URL:
4115 <https://link.aps.org/doi/10.1103/PhysRevD.76.113004>.
- 4116 [156] C. Berger and L. M. Sehgal. "Partially conserved axial vector current and
4117 coherent pion production by low energy neutrinos". In: *Phys. Rev. D* 79 (5 2009),
4118 p. 053003. eprint: <https://link.aps.org/doi/10.1103/PhysRevD.79.053003>.
- 4119 [157] T. Sjöstrand. "High-energy-physics event generation with PYTHIA 5.7 and
4120 JETSET 7.4". In: *Computer Physics Communications* 82.1 (Aug. 1994), pp. 74–89.
4121 URL: [https://doi.org/10.1016/0010-4655\(94\)90132-5](https://doi.org/10.1016/0010-4655(94)90132-5).
- 4122 [158] C. Bronner and M. Hartz. "Tuning of the Charged Hadrons Multiplicities for
4123 Deep Inelastic Interactions in NEUT". In: *Proceedings of the 10th International
4124 Workshop on Neutrino-Nucleus Interactions in Few-GeV Region (NuInt15)*. Journal of
4125 the Physical Society of Japan, Dec. 2016. URL:
4126 <https://doi.org/10.7566/jpsc.12.010041>.
- 4127 [159] M. Glück, E. Reya, and A. Vogt. "Dynamical parton distributions revisited". In:
4128 *The European Physical Journal C* 5.3 (1998), pp. 461–470. URL:
4129 <https://doi.org/10.1007%2Fs100529800978>.
- 4130 [160] A. Bodek and U. Yang. "Axial and Vector Structure Functions for Electron- and
4131 Neutrino- Nucleon Scattering Cross Sections at all Q^2 using Effective Leading
4132 order Parton Distribution Functions". In: *arXiv* (2010). URL:
4133 <https://arxiv.org/abs/1011.6592>.
- 4134 [161] A. Bodek and U. Yang. "Update to the Bodek-Yang Unified Model for Electron-
4135 and Neutrino- Nucleon Scattering Cross Sections". In: *arXiv* (2010). URL:
4136 <https://arxiv.org/abs/1012.0261>.
- 4137 [162] S. Gollapinni. "Neutrino Cross section Future". In: *arXiv* (2016). URL:
4138 <https://arxiv.org/abs/1602.05299>.
- 4139 [163] E. S. Pinzon Guerra et al. "Using world π^\pm -nucleus scattering data to constrain
4140 an intranuclear cascade model". In: *Phys. Rev. D* 99 (5 2019), p. 052007.
- 4141 [164] S. Agostinelli et al. "GEANT4: A Simulation toolkit". In: *Nucl. Instrum. Meth.*
4142 A506 (2003), pp. 250–303.
- 4143 [165] R. Brun et al. "GEANT3". In: *Cern Document Server* (Sept. 1987). URL:
4144 <https://cds.cern.ch/record/1119728/>.

- 4145 [166] A. Himmel et al. "Super-Kamiokande events and data quality studies for T2K
4146 Runs 5 and 6". In: *T2K Technical Note* 219 (2015).
- 4147 [167] S. Berkman et al. "fiTQun: A New Reconstruction Algorithm for Super-K". In:
4148 *T2K Technical Note* 146 (2013).
- 4149 [168] R.B. Patterson et al. "The extended-track event reconstruction for MiniBooNE".
4150 In: *Nuclear Instruments and Methods in Physics Research Section A* 608.1 (2009),
4151 pp. 206–224. URL: <https://doi.org/10.1016/j.nima.2009.06.064>.
- 4152 [169] M. Shiozawa. "Reconstruction algorithms in the Super-Kamiokande large water
4153 Cherenkov detector". In: *Nuclear Instruments and Methods in Physics Research*
4154 *Section A: Accelerators, Spectrometers, Detectors and Associated Equipment* 433.1-2
4155 (Aug. 1999), pp. 240–246.
- 4156 [170] K. Abe et al. "Search for CP Violation in Neutrino and Antineutrino Oscillations
4157 by the T2K Experiment with 2.2×10^{21} Protons on Target". In: *Phys. Rev. Lett.*
4158 121.17 (Oct. 2018). URL: <https://doi.org/10.1103/physrevlett.121.171802>.
- 4159 [171] K. Abe et al. "Measurements of neutrino oscillation in appearance and
4160 disappearance channels by the T2K experiment with 6.6×10^{20} protons on
4161 target". In: *Phys. Rev. D* 91.7 (Apr. 2015).
- 4162 [172] F. James. "MINUIT Function Minimization and Error Analysis". In: *Reference*
4163 *Manual, Version 94.1, CERN Program Library Long Writeup D506 D.506* (1994).
4164 eprint:
4165 <https://root.cern.ch/sites/d35c7d8c.web.cern.ch/files/minuit.pdf>.
- 4166 [173] X. Li and M. Wilking. "FiTQun Event Selection Optimization". In: *T2K Technical*
4167 *Note* 319 (2017).
- 4168 [174] S. Tobayama. "An Analysis of the Oscillation of Atmospheric Neutrinos".
4169 PhD thesis. British Columbia U., 2016.
- 4170 [175] D. Barrow et al. "Super-Kamiokande Data Quality, MC, and Systematics in Run
4171 10". In: *T2K Technical Note* 399 (2020).
- 4172 [176] A. Maghrabi, A. Aldosari, and M. Almutairi. "Correlation analyses between solar
4173 activity parameters and cosmic ray muons between 2002 and 2012 at high cutoff
4174 rigidity". In: *Advances in Space Research* 68.7 (Oct. 2021), pp. 2941–2952.
- 4175 [177] J. Beringer et al. "Review of Particle Physics". In: *Phys. Rev. D* 86 (1 2012),
4176 p. 010001. URL: <https://link.aps.org/doi/10.1103/PhysRevD.86.010001>.
- 4177 [178] S. Nakayama K. Iyogi and Y. Obayashi. "T2K data acquisition and FC event
4178 selection at Super-Kamiokande". In: *T2K Technical Note* 027 (2011).
- 4179 [179] L. K. Pik. "Study of the neutrino mass hierarchy with the atmospheric neutrino
4180 data observed in Super-Kamiokande". PhD thesis. Tokyo University, 2012.
- 4181 [180] R. Wendell et al. "Atmospheric neutrino oscillation analysis with subleading
4182 effects in Super-Kamiokande I, II, and III". In: *Phys. Rev. D* 81 (9 2010), p. 092004.
- 4183 [181] J. Hosaka et al. "Three flavor neutrino oscillation analysis of atmospheric
4184 neutrinos in Super-Kamiokande". In: *Phys. Rev. D* 74 (3 2006), p. 032002.
- 4185 [182] D. Barrow et al. "Flux and interaction models for the initial T2K-SK atmospheric
4186 joint fit studies". In: *T2K Technical Note* 422 (2022).

- 4187 [183] L. Munteanu et al. "Constraining the Flux and Cross Section Models with Data
4188 from ND280 using FGD1 and FGD2 for the 2020 Oscillation Analysis". In: *T2K*
4189 *Technical Note* 395 (2020).
- 4190 [184] P. Bartet et al. " ν_μ CC event selections in the ND280 tracker using Run 2+3+4
4191 data". In: *T2K Technical Note* 212 (2015).
- 4192 [185] W. Parker. "Constraining Systematic Uncertainties at T2K using Near Detector
4193 Data". PhD thesis. Royal Holloway University of London, 2020.
- 4194 [186] V. Berardi et al. " $\bar{\nu}_\mu$ event selection in the ND280 tracker using Run 5c and Run 6
4195 anti-neutrino beam data". In: *T2K Technical Note* 246 (2015).
- 4196 [187] B. Kirby J. Kim and M. Wilking. "Michel Electron Tagging in FGD1". In: *T2K*
4197 *Technical Note* 104 (2012).
- 4198 [188] J. Missert. "TN-318: Fit to Super-K Atmospheric Neutrino Data for Optimization
4199 of the fiTQun Fiducial Volume Cuts and Estimation of Detector Uncertainties".
4200 In: *T2K Technical Note* 318 (2017).
- 4201 [189] J. Chakrani et al. "NIWG model and uncertainties for 2021 oscillation analysis".
4202 In: *T2K Technical Note* 414 (2022).
- 4203 [190] M. Wascko. "T2K Status, Results, And Plans". In: *Neutrino 2018* (2018). URL:
4204 <https://zenodo.org/record/1286752>.
- 4205 [191] T. Vladislavljevic et al. "Flux Prediction and Uncertainty with NA61/SHINE 2009
4206 Replica-Target Data (TN354 version 3.3)". In: *T2K Technical Note* 354 (2020).
- 4207 [192] G. Ambrosini et al. "K/ π production ratios from 450 GeV/c protons on
4208 beryllium". en. In: *Phys. Lett. B* 420.1-2 (Feb. 1998), pp. 225–232.
- 4209 [193] E. Atkin et al. "NIWG model and uncertainties for 2019-2020 oscillation analysis".
4210 In: *T2K Technical Note* 344 (2019).
- 4211 [194] D. Barrow et al. "SK atmospheric T2K beam joint fit technical note, MaCh3
4212 details". In: *T2K Technical Note* 426 (2022).
- 4213 [195] A. A. Aguilar-Arevalo et al. "Measurement of ν_μ and $\bar{\nu}_\mu$ induced neutral current
4214 single π^0 production cross sections on mineral oil at $E_\nu \sim \mathcal{O}(1 \text{ GeV})$ ". In: *Phys.*
4215 *Rev. D* 81 (1 2010), p. 013005.
- 4216 [196] P. Perio and J. Imber. "Super-K Systematic Uncertainties for RUN1-4 Joint ν_e and
4217 ν_μ Analyses". In: *T2K Technical Note* 186 (2014).
- 4218 [197] P. Perio and J. Imber. "Update of SK ν_e systematic error for 2012a oscillation
4219 analysis". In: *T2K Technical Note* 107 (2012).
- 4220 [198] D. Barrow and C. Vilela. *T2K-SK Detector Matrix Uncertainties - MaCh3 Integration*.
4221 <https://git.t2k.org/t2k-sk/t2ksk-detcovmat/-/tree/feature/MaCh3Integration>. Accessed: 22-06-2022.
- 4223 [199] R. Barlow and C. Beeston. "Fitting using finite Monte Carlo samples". en. In:
4224 *Comput. Phys. Commun.* 77.2 (Oct. 1993), pp. 219–228.
- 4225 [200] J. S. Conway. "Incorporating Nuisance Parameters in Likelihoods for Multisource
4226 Spectra". In: *arXiv* (2011). URL: <https://arxiv.org/abs/1103.0354>.
- 4227 [201] D. Barrow et al. "Oscillation probability calculation for the T2K+SK atmospheric
4228 joint fit". In: *T2K Technical Note* 425 (2022).

- 4229 [202] R. G. Calland, A. C. Kaboth, and D. Payne. "Accelerated event-by-event neutrino
4230 oscillation reweighting with matter effects on a GPU". In: *IOP Journal of*
4231 *Instrumentation* 9.04 (Apr. 2014), P04016–P04016.
- 4232 [203] R. Wendell. *Prob3++ Oscillation Probability Calculation*. URL:
4233 <http://www.phy.duke.edu/~raw22/public/Prob3++/>.
- 4234 [204] F. Kallenborn et al. "Massively parallel computation of atmospheric neutrino
4235 oscillations on CUDA-enabled accelerators". In: *Computer Physics Communications*
4236 234 (2019), pp. 235–244.
- 4237 [205] L. Warsame. *MaCh3 Analysis Progress*. Implementation of CUDAProb3 in MaCh3
4238 for DUNE. URL: https://indico.fnal.gov/event/50217/contributions/241232/attachments/155318/202209/MaCh3ProgressforDUNELBL_May17%20%282%29.pdf.
- 4241 [206] S. Bourret et al. "Neutrino oscillation tomography of the Earth with
4242 KM3NeT-ORCA". In: *Journal of Physics: Conference Series* 888 (2017), p. 012114.
- 4243 [207] C. Rott, A. Taketa, and D. Bose. "Spectrometry of the Earth using Neutrino
4244 Oscillations". In: *Scientific Reports* 5.1 (Oct. 2015). URL:
4245 <https://doi.org/10.1038/srep15225>.
- 4246 [208] K. Hagiwara, N. Okamura, and K. Senda. "The earth matter effects in neutrino
4247 oscillation experiments from Tokai to Kamioka and Korea". In: *Journal of High*
4248 *Energy Physics* 2011.9 (Sept. 2011).
- 4249 [209] D. Typinski. *Earth Gravity*.
4250 <http://www.typnet.net/Essays/EarthGravGraphics/EarthGrav.pdf>.
4251 Accessed: 24-06-2022.
- 4252 [210] D. Barrow. *T2K Beam + SK Atmospheric Joint Fit*. Plenary Slides for May 2022 T2K
4253 Collaboration Meeting. 2022. URL:
4254 https://t2k.org/meet/collab/CM_May_2022/Talks/Friday/T2KSKPlenary.
- 4255 [211] E. Atkin et al. "Measuring PMNS parameters in a joint ND280-SK analysis using
4256 MCMC". In: *T2K Technical Note* 393 (2020).
- 4257 [212] K. Abe et al. "Neutron Tagging following Atmospheric Neutrino Events in a
4258 Water Cherenkov Detector". In: *arXiv* (2022). URL:
4259 <https://arxiv.org/abs/2209.08609>.